Modeling of Blood Circulation and Biochemical Signaling

Ananta Kumar Nayak

THÈSE

Pour obtenir le grade de

DOCTEUR DE L'UNIVERSITÉ GRENOBLE ALPES

École doctorale : PHYS - Physique
Spécialité : Physique pour les Sciences du Vivant
Unité de recherche : Laboratoire Interdisciplinaire de Physique

Modélisation de la circulation sanguine et signalisation biochimique

Modeling of Blood Circulation and Biochemical Signaling

Présentée par :

Ananta Kumar NAYAK

Direction de thèse :

Chaouqi MISBAH DIRECTEUR DE RECHERCHE, CNRS DELEGATION ALPES	Directeur de thèse
Sovan LAL DAS ASSOCIATE PROFESSOR, INDIAN INSTITUTE OF TECHNOLOGY, PALAKKAD	Co-directeur de thèse

Rapporteurs :

MARC LEONETTI
DIRECTEUR DE RECHERCHE, CNRS DELEGATION PROVENCE ET CORSE
BADR KAOUI
CHARGE DE RECHERCHE HDR, CNRS DELEGATION HAUTS-DE-FRANCE

Thèse soutenue publiquement le **18 décembre 2023**, devant le jury composé de :

MARC LEONETTI DIRECTEUR DE RECHERCHE, CNRS DELEGATION PROVENCE ET CORSE	Rapporteur
BADR KAOUI CHARGE DE RECHERCHE HDR, CNRS DELEGATION HAUTS-DE-FRANCE	Rapporteur
MARCO CANEPARI CHARGE DE RECHERCHE HDR, INSERM DELEGATION AUVERGNE-RHONE-ALPES	Examinateur
IRINA MIHALCESCU PROFESSEURE DES UNIVERSITES, UNIVERSITE GRENOBLE ALPES	Présidente

Modeling of Blood Circulation and Biochemical Signaling

Ananta Kumar Nayak

Laboratoire Interdisciplinaire de Physique Grenoble

Université Grenoble Alpes

A thesis submitted for the degree of

Doctor of Physics

December 18, 2023

"*Land and water are not really separate things, but they are separate words, and we perceive through words*"— David Rains Wallace

Dedicated this thesis to my family

Acknowledgements

Firstly, I would like to express my gratitude to my thesis supervisor Chaouqi Misbah for his unwavering support and encouragement throughout this four-year journey. Although I have a lot to say about him, it is not possible to list everything. From the beginning of my PhD, for example, I remember he was more concerned about my thesis progress during the COVID-19 period than I was. He constantly monitored and provided the right direction on what and how to solve a problem, guiding me like a baby just starting to discover new things on Earth. I recall that when I began learning about biochemical signaling, he was himself very enthusiastic and attentive to learn new things. He was always available to help me connect with researchers working in my area of research. He supported, encouraged, and motivated me to be an independent thinker. He displayed great patience while I implemented something new in the numerical code and waited for results for several months. Additionally, I always enjoyed scientific discussions with him, learning many new things, such as how to explain physics in a simple mathematical equation and how to present findings to people not familiar with my research area, using humorous and layman's terms. I also appreciated his group meeting presentations; each one taught me something new. I consider myself fortunate to have had a supervisor like him.

Secondly, I would like to express my gratitude to my PhD co-supervisor, Sovan Lal Das, for introducing me to an intriguing subject in biophysics to carry out research within Chaouqi's group. This PhD journey would not have been possible without his constant guidance and mentorship. He was always available to dedicate time whenever I asked to discuss my research. He always provided me with the freedom to think and analyze problems, exploring their solutions by delving into their roots. Additionally, my connection with him dates back to the time when I took admission for my PhD in Applied Mechanics under his supervision and undertook teaching assistantship at IIT Kharagpur, before joining Chaouqi's group at LiPhy Grenoble. During this period, my interest in teaching blossomed as I attended his classes, where he adeptly explained complex concepts in simple and minimalistic ways to classes of 100-200 undergraduate students. I would also like to thank him for creating interests in continuum mechanics, tensor calculus, Cosserat shell theory (taught me this subject in a detailed manner, using pen and paper), and mechanobiology during my stay at IIT Kharagpur.

Thirdly, I would like to express my gratitude to the members of the Comité de Suivi Individuel des Doctorants (CSI), including Aurélie Dupont, Philippe Peyla, and

Marco Canepari, for dedicating their valuable time to review my PhD thesis progress, providing feedback to enhance the thesis manuscript, and guiding me in planning for the post-PhD phase. Special mention to Marco Canepari for helping and guiding me at the beginning of my PhD while I was developing Ca^{2+} and NO dynamics models. The discussions with him always provided me with the opportunity to gain new insights from his experience in biochemical pathways modeling. I would also like to thank Marc Leonetti, Badr Kaoui, and Irina Mihalcescu for agreeing to be part of my PhD thesis jury. Once again, I express my gratitude to Marc Leonetti and Badr Kaoui for reviewing my thesis and providing comments that significantly improved the final manuscript. I would like to express my sincere gratitude to Alexander Farutin, the leader of the EcCel group, for the opportunity to work with him for a short period of time and gain real insights into applied mathematics in biophysics. I would also like to thank my collaborator Abdul I. Barakat for sharing his experiences during the development of the Ca^{2+} model.

Penultimately, while it is not feasible to mention each friend individually, their steadfast support, encouragement, and weekend conversations significantly eased the challenges of my PhD journey. I want to express my deep appreciation to Rishbah, Aniket, Rajat, and Santanu for the insightful discussions we had over the weekend on a variety of topics. Special thanks to Zhe Gou, who greatly assisted me in understanding numerical code, and I appreciate many stimulating discussions with him on current and future research topics in biophysics. Many thanks to my friends in India for their constant support and understanding, which played a crucial role in making my PhD experience smoother and more rewarding. This part would be incomplete if I did not mention Edith, who supported me whenever I needed her help. I would also like to thank Sabine Gustave and Chantal Reignier for making my life easier by speeding up the administrative processes. In addition, I would like to thank my funding agencies - CNRS, Living Fluids, and Campus France - for their financial support and resources, which enabled me to complete my PhD without any difficulties.

Lastly, this thesis would not have been completed without the constant, unconditional love from my family, including my father, mother, brothers, sister, sister-in-laws, brother-in-law, father-in-law, mother-in-law, grandmother, Piusa, Piusi, and other family members. A special mention goes to my mother, father, brothers, and sister; their unwavering support and sacrifices played a pivotal role in helping me reach this point. Thanks to Gulu, Puchu, and Satyaranjan for your laughter, innocence, and for being a wonderful part of my journey during the high-stress times of my PhD. Last but not least, I would like to express my gratitude to my wife, Satabdy,

for bearing with me and for her unconditional love, encouragement, and support over the past three years. She was always there for me whenever I needed her help. I would also like to express my regret for not being able to spend enough time together after our marriage, as we lived 7,000 km apart while pursuing our PhD studies.

Abstract

In our body, red blood cells (RBCs) are primarily involved in transporting oxygen and nutrients to the tissues, and conversely, they become the transporter of metabolic excreta such as carbon dioxide from the tissues. In addition to these passive processes, RBCs are actively participated in communication with the vascular wall. This communication is mediated by a signalling molecule, adenosine triphosphate (ATP), which is released as a result of the shear stress experienced by the RBC membrane. ATP is known as an energy carrier, and the energy it releases by hydrolysis of the phosphate bond is used to carry out cellular functions. However, the ATP released to the plasma by RBCs triggers a cascade of biochemical reactions in endothelial cells (ECs), resulting in the release of sequestered Ca^{2+} from the endoplasmic reticulum (ER). Ca^{2+} is a ubiquitous ion responsible for numerous cellular functions such as vasodilation, cell proliferation and gene transcription. In particular, Ca^{2+} regulates the synthesis of nitric oxide (NO), an important vasodilator, in the vascular wall. NO molecules act on smooth muscle cells (SMCs), a layer located beneath the endothelium layer, to relax the vessel wall diameter. As a result, increased vessel diameter results in improved blood supply to the area where metabolic needs are high. Nevertheless, the concentration of NO available for SMC relaxation is also affected by RBCs, as they act as scavengers by converting it into other metabolites such as nitrites and nitrates. Because of the aforementioned importance of RBC dynamics and its impact on biochemical signalling in the vascular wall, it is necessary to understand the fundamentals of local blood perfusion control and progression of vascular diseases. This thesis is mainly devoted to the coupling of RBC dynamics and biochemical signalling occurring in the vascular wall using immersed boundary lattice Boltzmann method (IBLBM). More specifically, we investigated the effect of RBC dynamics in a two-dimensional straight channel (2-D) with changes in parameters such as flow strength, channel width, and RBC concentration

on the Ca^{2+} and NO dynamics. More elaborately, firstly, we developed a minimal homeostatic Ca^{2+} dynamics model that ensures the return of intracellular Ca^{2+} concentrations from their non-physiological concentrations to the physiological concentrations in the presence of an agonist (ATP). Secondly, we explicitly integrated ATP released from RBCs and ECs that triggers Ca^{2+} signalling in the endothelium. This study sheds light on the upstream control of blood perfusion in a vascular network due to the propagation of Ca^{2+} signals from a region of higher ATP concentration to region of lower ATP concentration. Lastly, we further modelled both ATP and shear stress-dependent NO synthesis in ECs. This model is extended to explicitly incorporate the scavenging of NO by RBCs in order to understand NO availability in blood vessels with a 2-D numerical setting. This study highlights the fact that the concentration of NO in the vascular wall strongly depends on the concentration of RBCs.

Keywords: Homeostasis; Receptor Desensitization; ATP; RBCs; NO; Calcium; LBM; Endothelial Cells

Résumé

Au sein de notre corps, les globules rouges (GR) sont principalement impliqués dans le transport de l'oxygène et des nutriments vers les tissus, et inversement, ils deviennent le transporteur des excréments métaboliques tels que le dioxyde de carbone des tissus. En plus de ces processus passifs, les GR participent activement à la communication avec la paroi vasculaire. Cette communication est assurée par une molécule de signalisation, l'adénosine triphosphate (ATP), qui est libérée sous l'effet de la contrainte de cisaillement subie par la membrane des GR. L'ATP est connue comme un transporteur d'énergie, et l'énergie qu'il libère par hydrolyse de la liaison phosphate est utilisée pour assurer les fonctions cellulaires. Cependant, l'ATP libéré dans le plasma par les GR déclenche une cascade de réactions biochimiques dans les cellules endothéliales (CE), entraînant la libération du Ca^{2+} séquestré dans le réticulum endoplasmique (ER). Le Ca^{2+} est un ion ubiquitaire responsable de nombreuses fonctions cellulaires telles que la vasodilatation, la prolifération cellulaire et la transcription des gènes. En particulier, le Ca^{2+} régule la synthèse de l'oxyde nitrique (NO), un important vasodilatateur, dans la paroi vasculaire. Les molécules de NO agissent sur les cellules musculaires lisses (CML), une couche située sous la couche d'endothélium, pour détendre le diamètre de la paroi du vaisseau. Par conséquent, l'augmentation du diamètre des vaisseaux améliore l'apport sanguin dans la zone où les besoins métaboliques sont élevés. Néanmoins, la concentration de NO disponible pour la relaxation des CML est également affectée par les GR, qui agissent comme des piégeurs en le convertissant en d'autres métabolites tels que les nitrites et les nitrates. En raison de l'importance susmentionnée de la dynamique des GR et de son impact sur la signalisation biochimique dans la paroi vasculaire, il est nécessaire de comprendre les principes fondamentaux du contrôle de la perfusion sanguine locale et de la progression des maladies vasculaires. Cette thèse est principalement consacrée au couplage de la dynamique des GR et de la signalisation biochimique dans la paroi vasculaire en utilisant

la méthode de Boltzmann sur réseau à frontière immergée (IBLBM). Plus précisément, nous avons étudié l'effet de la dynamique des GR dans un canal droit bidimensionnel (2-D) avec des changements de paramètres tels que la force du flux, la largeur du canal et la concentration des GR sur la dynamique du Ca^{2+} et du NO. Plus en détail, nous avons tout d'abord développé un modèle homéostatique minimal de dynamique du Ca^{2+} qui assure le retour des concentrations intracellulaires de Ca^{2+} vers la concentration physiologique (retour à l'homéostasie) en présence d'un agoniste (ATP). Deuxièmement, nous avons explicitement intégré l'ATP libéré par les GR et les CE qui déclenche la signalisation du Ca^{2+} dans l'endothélium. Cette étude met en lumière le contrôle en amont de la perfusion sanguine dans un réseau vasculaire grâce à la propagation des signaux Ca^{2+} d'une région à forte concentration d'ATP vers une région à faible concentration d'ATP. Enfin, nous avons modélisé la synthèse de NO dépendante de l'ATP et de la contrainte de cisaillement dans les CE. Ce modèle est généralisé pour incorporer explicitement le piégeage du NO par les GR afin de comprendre la disponibilité du NO dans les vaisseaux sanguins dans un cadre numérique bidimensionnel. Cette étude met en évidence le fait que la concentration de NO dans la paroi vasculaire dépend fortement de la concentration de globules rouges.

Mots clés : Homéostasie ; Désensibilisation des Récepteurs ; ATP ; Globules Rouges ; NO ; Calcium ; LBM ; Cellules Endothéliales

Contents

List of Figures

List of Tables

Chapter 1

Introduction

The human cardiovascular system is a closed and complex system. The main functions of the cardiovascular system are to transport nutrients, oxygen, hormones, and neurotransmitters to the tissues and to carry metabolic wastes such as carbon dioxide (CO_2) from the tissues. These functions are performed by a multi-phase fluid called blood. Blood is a heterogeneous multi-phase mixture of formed elements suspended in a dilute electrolytic solution (about 92% water or 55% of total human blood volume), known as plasma. Plasma contains many organic molecules, minerals, and three major proteins namely fibrinogen, globulin, and albumin. The formed elements of blood are red blood cells (RBCs or erythrocytes), white blood cells (WBCs or leukocytes), and platelets (thrombocytes). RBC accounts 45% of human blood volume, whereas other corpuscles account for less than 1%. This thesis consider RBCs dynamics and their functions in biochemical signaling.

A peculiar property of RBC is that its membrane is highly deformable, thanks to the underneath cytoskeleton. As a consequence, it squeezes through capillaries, whose diameter is in the same order of magnitude or less than that of RBC. Further, the complex dynamics of RBCs owing to their deformation and high concentration (i.e., hematocrit), the behaviour of blood is mainly ascertained by RBCs. Blood is a non-Newtonian fluid that exhibits a complex rheology. The rheology of blood is defined as the deformation and flow of blood caused by the application of external forces, such as the pressure differences or any other external sources. The rheology of blood is hard to determine in contrast to the Newtonian fluid, where the viscosity of the latter is constant. The viscosity of blood depends on various factors, namely temperature, shear rate, mechanical properties of RBC, and both diameter and length of blood vessels. A small increment in the viscosity of blood ensues in a large stresses on heart. To understand the proper functioning of the heart and the physics of blood flow in the circulatory system, it is necessary to consider RBC dynamics and

its effect on blood rheology. Over the past two decades, however, the focus, both experimentally and numerically, has been given on RBC dynamics and its effect on blood viscosity.

With the advent of microfluidics devices, high resolution cameras, and microscopes, the study of blood has been further expanded to understand other functions of RBC, such as the transfer of biochemical signals or nutrients from blood to the vascular wall. A pioneering work by [Forsyth et al., 2011], laid the foundation in elucidating an important function of RBC. RBC synthesizes adenosine triphosphate (ATP), an energy carrier for internal functioning of the cell. However, it behaves as a signaling molecule when released into the extracellular environment attributable to external stimuli. ATP in the extracellular space, i.e., in plasma, helps maintain vascular tone by synthesizing a vasodilator, nitric oxide (NO). NO regulates blood perfusion to meet the metabolic needs of cells or tissues in, or around, the vessel wall by increasing vessel diameter. Although biochemical signals play an essential role in blood perfusion, the research community has not focused enough on this area. Throughout the thesis, we have delved how RBCs communicate with the vascular wall and how cellular homeostasis is preserved within the vascular wall.

1.0.1 Blood Vessel Wall, Structures, and Functions

Blood is essentially pushed from the heart to various parts of the body by the pressure gradient, which is generated by the expansion and contraction of the heart's muscle cells. It is mainly propelled from the heart's left ventricle and then passes through blood vessels of various diameters, such as the aorta, arteries, arterioles, capillaries, venules and veins as shown in Figure 1.1(a). The function and pumping speed of the heart are affected by the condition of the blood vessels, such as lipid deposition (atherosclerosis), thrombosis formation and vessel defects like stenosis and aneurysms. As a result, blood perfusion of tissues is affected.

A blood vessel with a diameter of less than 100 μm is mainly referred to as a microcirculation [Popel and Johnson, 2005]. Arterioles, capillaries, and venules are the basic units of microcirculation. Microcirculation plays an important physiological role in maintaining vascular tone. As blood flows from the arterioles into the capillaries, the arterioles expand into numerous smaller vessels, each smaller in diameter than the arterioles. Capillaries converge again to form venules, which in turn form veins. When blood passes through the microcirculation, the large surface area of the vessel to its volume and the slow movement of the blood render the microcirculation an ideal candidate for the diffusion of nutrients, oxygen and stimuli to tissues.

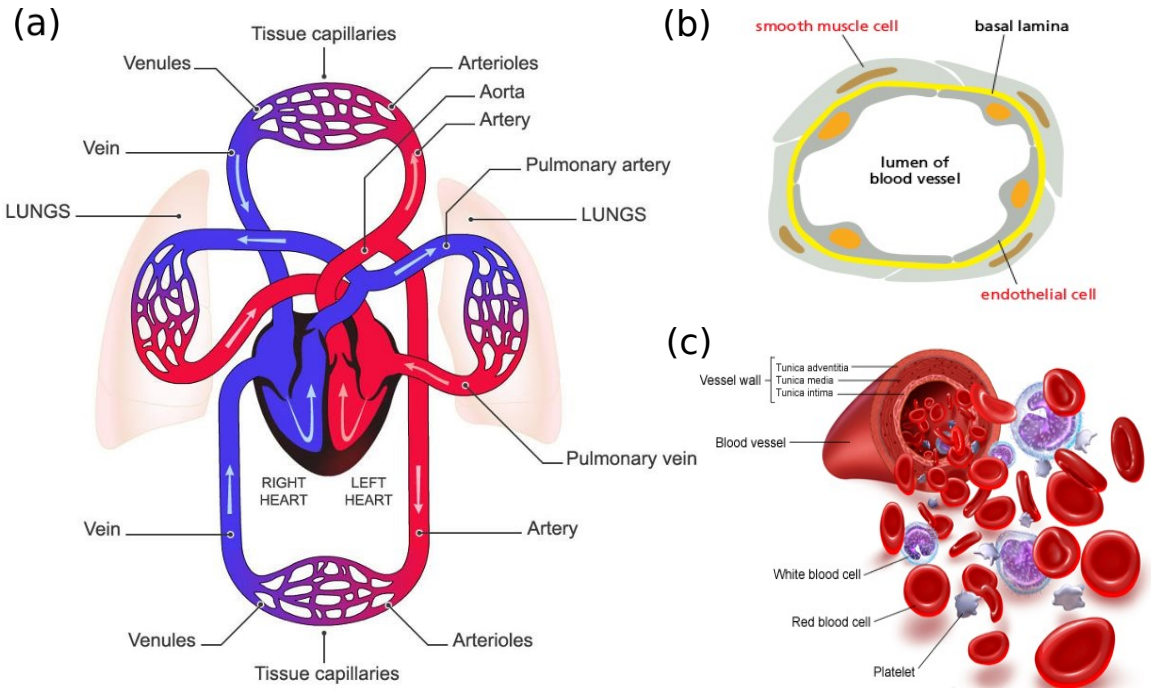

Figure 1.1: Schematic shows: (a) the flow of blood in a closed circulatory system in which different components of blood traverse through vessels with different diameters and lengths; (b) the cells, such as endothelial cells (ECs) and smooth muscle cells (SMCs), in the inner two layers of blood vessel wall [Alberts, 2017]; and (c) the blood flowing in a vessel segment that is covered with three layers, such as tunica intima, tunica media, and tunica adventitia. Figure (a) and (c) are taken from journey-through-the-circulatory-system and slideplayer, respectively.

Stimuli, such as hormones, neurotransmitters, and growth factors react to receptors on the surface of endothelial cells (ECs) (a layer of ECs forms the inner lining of a blood vessel wall, known as the endothelium as shown in Figure 1.1(b)). As a result, a ubiquitous ion, calcium, is released from the endoplasmic reticulum (ER). The calcium ion activates numerous proteins and enzymes to perform various cellular functions such as vasodilation, cell proliferation, and gene regulation [Berridge et al., 2003].

Except capillaries, other blood vessel walls are made up of three layers of fibres: tunica intima, tunica media, and tunica adventitia or externa as shown in Figure 1.1(c). ECs are situated in the inner layer of the vessel known as the tunica intima. Vascular smooth muscle cells (VSMCs) and elastic and connective tissues are arranged circumferentially around the vessel in the tunica media. VSMCs relax in response to the vasodilator, NO (as shown in Figure 1.2(a)). As a result, local changes in blood vessel diameter increase blood supply to a specific organ or location in the

circulatory system. In addition, microcirculation also plays an important role in determining blood rheology. For example, the apparent viscosity of blood decreases with a reduction in the inner diameter of glass tube from 1000 μm upto 7.5 μm and increases again with a further reduction in tube diameter as shown in Figure 1.2(b). This effect is known as Fåhærus Lindqvist effect [Fahraeus and Lindqvist, 1931]. The formation of a cell free layer (CFL), i.e., the area close to the blood vessel wall devoid of RBCs (as shown in Figure 1.2(c)), has an impact on blood viscosity. The ascertainment of CFL is a key element in determining the transport process across vessel diameter under physiological and pathological conditions [Kim et al., 2009, Balogh and Bagchi, 2019, Yin et al., 2013].

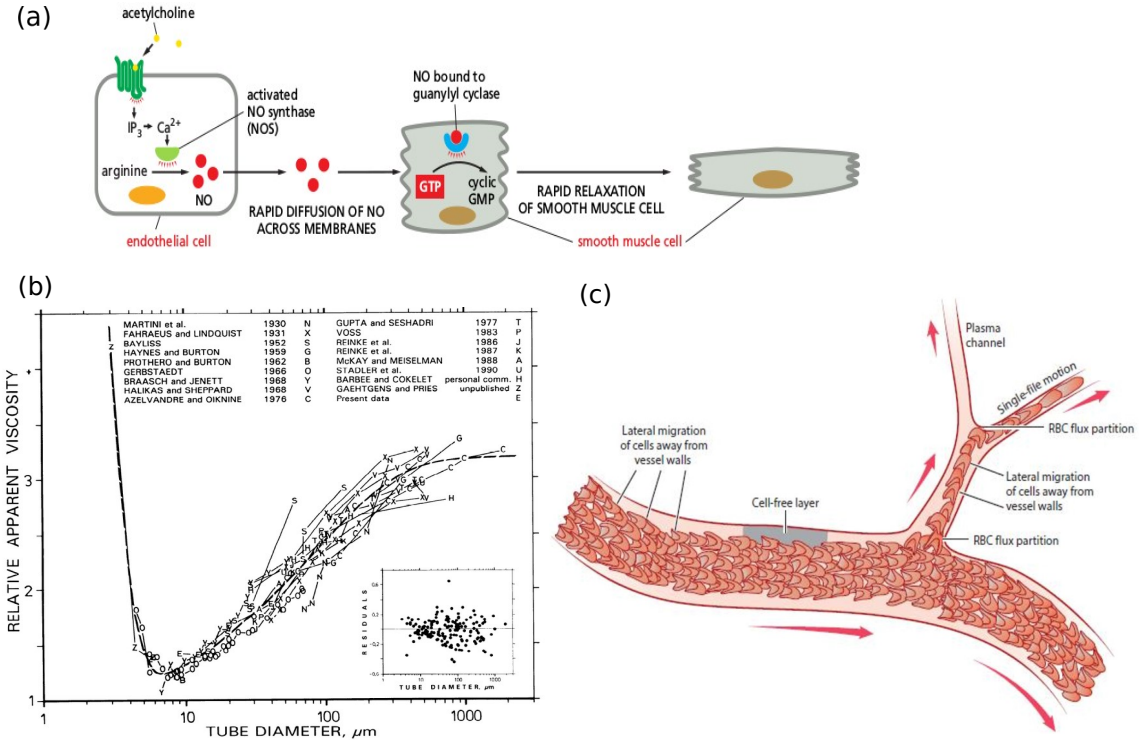

Figure 1.2: Schematic shows: (a) the external stimulus-dependent vasorelaxation of smooth muscle cells (SMCs) [Alberts, 2017]; (b) the relative viscosity of red blood cell suspensions with a hematocrit of 45% perfused through a glass tube with internal diameters between 3.3 μm and 1.978 mm [Pries et al., 1992]; and (c) the formation of cell free layer (CFL) as red blood cells (RBCs) migrate away from vessel walls [Secomb, 2017].

1.0.2 Formed Elements

1.0.2.1 RBCs

RBCs constitute 95% of the total volume of the formed element and 45% of human blood volume. The equilibrium shape of an RBC is biconcave discoid, with an average diameter of 7.5 μm and a membrane thickness of 2.5 μm [Diez-Silva et al., 2010] (Figure 1.3(a)). The mean volume and surface area of an RBC are around 90 μm^3 and 130 μm^2, respectively [Tomaiuolo, 2014]. The function of RBC is to exchange gases, such as O_2, CO_2 between blood and cells, as shown in Figure 1.3(b). In order to perform these functions properly, a mature RBC lacks internal organelles. As a result, RBCs do not repair themselves and produce proteins. An adult RBC is equipped with an internal biochemical apparatus that enables it to synthesize hemoglobin (Hb) proteins. These proteins bind efficiently to gases, helping to transport gases from the tissues to the lungs and vice versa, as shown in Figure 1.3(c).

In addition to its transport function, Hb is responsible for providing the red colour to RBCs. Because of the excess surface area of RBCs compared with the surface area of a sphere of the same volume, they squeeze through the capillaries, even if the diameter of the RBCs is greater than that of the capillaries. The life span of a RBC in the circulatory system is 120 days. During this period, it approximately travels 300 miles (equivalent to 170000 closed-circulation loops) in the circulatory system before being destroyed by macrophages in the spleen. .

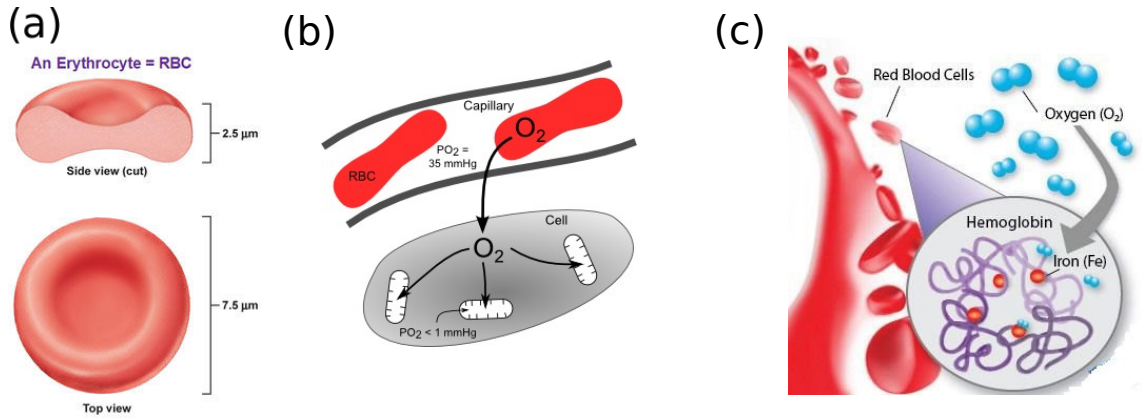

Figure 1.3: Schematic shows: (a) the equilibrium shape of red cell; (b) the transport and dispersion of oxygen at cells by red cells; and (c) the binding of oxygen molecules to hemoglobin and transportation by red cells to a location of high metabolic needs. The figures are taken from rbc, microcirculation, and hemoglobin, respectively.

1.0.2.2 Origin of RBC

Bone marrow is the production house of erythrocytes. It is a spongy tissue located in the center of the bone. RBCs are produced from pluriopotent haemopoietic cells. These cells are found in the bone marrow. Upon the appropriate stimuli such as hormones or cytokines, a young erythrocyte undergoes several maturation steps before becoming a fully functional RBC. For example, the hormone Epo, secreted by kindeys, leads to the production of RBCs in the bone marrow [Klinken, 2002]. The process of producing RBC in the bone marrow is known as erythropoiesis.

Burst forming unit-erythroid (BFU-E) cells are precursor cell that differentiate into a colony of 200 erythroblasts in a haemopoietic assay colony. These cells express receptors for stem cell factors (SCF) and low-levels of Epo receptors. The next stage is the colony-forming unit-erythroid (CFU-E), morphologically not developed. Each colony contains 8-200 erythroblasts. The CFU-E expresses fewer SCF receptors and more Epo receptors. After the CFU-E stage, erythroid cells are morphologically distinct from one another. Proerythroblasts (Pr) are large cells, 20-25 μm in diameter, with a nucleus-to-cytoplasm volume ratio of $\sim$ 80%.

Hb (Hemoglobin) synthesis begins in these cells, and the cytoplasm is basophilic in nature. Basophilic erythroblasts (BEs) are highly basophilic (16-18 μm in diameter), and have a clock face nucleus. In the next stage, polychromatic erythroblasts (PoEs) (12-15 μm in diameter) develop in which a pinkish tinge appears due to increased hameoglobin levels. In orthochromatic erythroblasts (OEs) (10-15 μm in diameter), the nucleus is reduced to $\sim$ 25% and the cytoplasm becomes pinker. In the last stage of maturation, the nucleus of reticulocytes (Rs) is extruded before entering onto the circulation. Erythrocytes then mature and synthesize Hb proteins over the next 24 to 48 hours. It is pertinent to mention that the erythrocyte cytoskeleton changes during the morphological development of the erythroblast [Klinken, 2002]. The different stages of erythroid cell differentiation are shown in Figure 1.4.

1.0.2.3 WBCs

WBCs represent a smaller fraction of the total volume of the formed elements in a healthy human being. The function of WBCs is to protect cells against foreign invaders, such as bacteria and viruses. WBCs fight against invaders by producing antibody proteins, which bind to the receptors of foreign invader and destroy it. WBCs circulate in the bloodstream, crossing blood vessel walls and tissues to locate the site of an infection. The movement of WBCs in the bloodstream towards blood

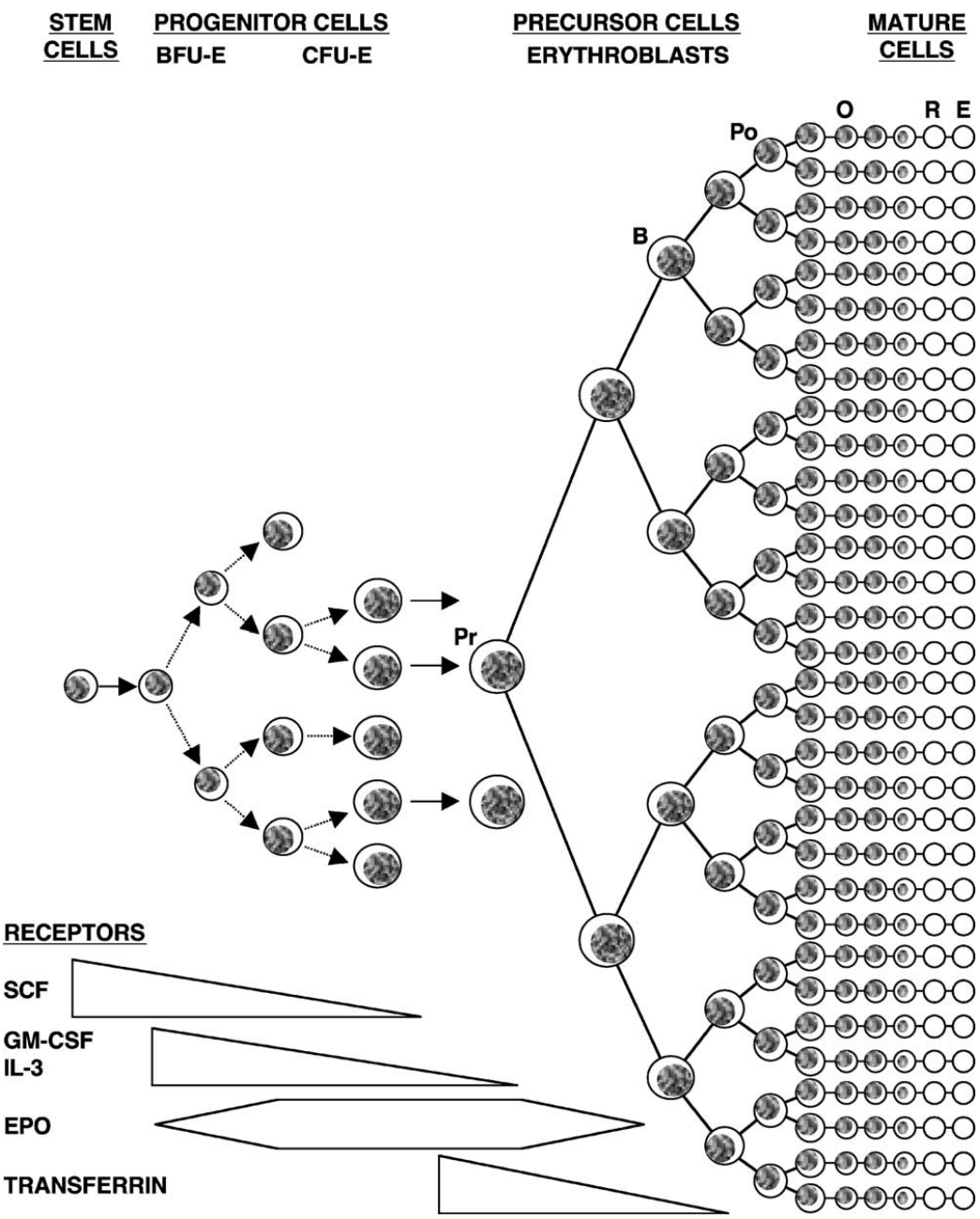

Figure 1.4: Haemopoietic stem cells proliferate and differentiate, a process regulated mainly by the activity of cell-type-specific transcription factors, through a series of stages culminating in the generation of mature red blood cells (RBCs). Morphological changes are accompanied by alterations in cell surface receptors [Klinken, 2002].

vessel walls is known as margination. On account of the low fractions of WBCs in blood, their effect on blood rheology is negligible. In addition, WBCs are stiffer and larger (size varies from 12-17 μm in diameter) than RBCs, making it difficult for them to pass through vessels .

1.0.2.4 Platelets

Platelets are activated in the event of injury or bleeding in the body. Normal platelets size varies from 1.5-3 μm in diameter. They contribute to blood coagulation. A minimal concentration of platelets in the blood can lead to significant blood loss during a hemorrhage. Conversely, a maximum concentration of platelets can lead to thrombosis.

1.1 ATP energy-cum-messenger

ATP (Adenosine Triphosphate or Adenosine 5'-(tetrahydrogen triphosphate)) is known as the currency of biological energy. It plays a key role in driving biological processes such as cell motility, maintenance of calcium ion homeostasis, muscle contraction, and nerve impulse propagation in living organisms. From a biochemical point of view, ATP consists of an adenine attached by nitrogen atom 9 to carbon atom 1' of a ribose, which in turn is attached to carbon atom 5' of the ribose to a triphosphate group. During physiological biological processes, a phosphate bond hydrolyzes from phosphate groups and produces adenosine diphosphate (ADP). Similarly, the breaking of other bonds leads to the formation of other derivatives such as adenosine monophsophate (AMP) and adenosine. The energy stored in the phosphate bond is converted into useful energy for biological functions. The phosphate derivative, ADP, is recycled to ATP in the mitochondria. In living cells, the concentration of ATP remains five times higher than the concentration of ADP. More importantly, a circulating erythrocyte contains $\sim$ mM ATP [Xu et al., 2019].

1.1.1 Erythrocyte and ATP

A mature circulating erythrocyte or RBC has no internal organelles, including the nucleus, mitochondria, and other organelles. Consequently, RBCs produce ATP by membrane bound glycolytic pathways in the absence of oxygen, and this process is known as anaerobic process. The absence of organelles in RBC has both advantages and disadvantages. One advantage is that RBCs free up space for Hb, whose main

function is oxygen transport. The disadvantage is that they cannot synthesize, divide, and self-repair RNA in the absence of a nucleus. ATP production in cells with mitochondria is 10 times higher than in cells without. Since mitochondria are absent from RBCs, the latter cannot use their own oxygen to produce the ATP they carry.

Erythrocytes release ATP in response to external stimuli such as hypoxia, pH, pharmacological stimuli, hypercapnia, and osmotic pressure. According to Ellsworth et al. [Ellsworth et al., 2009], RBCs serve as oxygen sensors, enabling them to release ATP potentially via Pannexin1 (Px1) hemichannel or voltage-gated ion channels in response to hypoxia conditions. Consequently, the hypoxia condition may be the potential onset of direct oxygen delivery to a local area in metabolic need. Hypoxia refers to a state in which there is insufficient oxygen available at tissue level to support normal cellular functions. This situation results from an insufficient supply of oxygen to the tissues due to a low blood supply or a low oxygen content in the blood (hemoglobin desaturation). When RBCs are exposed to low oxygen tension (pO_2), membrane-bound hemoglobin releases ATP. The conformational change associated with its desaturation in membrane-bound hemoglobin molecules results in a local change in membrane deformation. As a result, the ATP release pathway linked to G_i is activated, as shown in Figure 1.5(a).

In addition, RBCs release ATP under mechanical stress induced by blood flow, which is the main contributor to extracellular ATP concentration when variations in oxygen tension are not significant. In an experiment carried out in the mid-1990s, ATP release was detected when RBCs were forced through a filter paper whose size was smaller than the diameter of the RBC. In a recent microfluidic experiment, ATP release was observed from RBCs that were allowed to pass through a variable-width microfluidic channel [Wan et al., 2008]. Furthermore, in an another experiment, two different mechanisms of ATP release were observed when RBCs were exposed to both hypoxia and flow conditions. They reported that ATP release below 25% oxygen saturation (SO_2) depended mainly on hypoxia, while above 25% SO_2 ATP release depended on flow [Faris and Spence, 2008], where SO_2 is the measure of how much Hb is bound to oxygen relative to how much Hb remains free.

1.1.2 ATP-dependent conducted response

ATP, released from RBCs into the extracellular fluid, reacts with purinergic receptors on the endothelium. This enables signal transduction in the form of an increase in cytoplasmic Ca^{2+} concentration. This leads to the synthesis of NO molecules, which diffuses into vessel's middle layer and lumen. NO reacts readily with formed elements

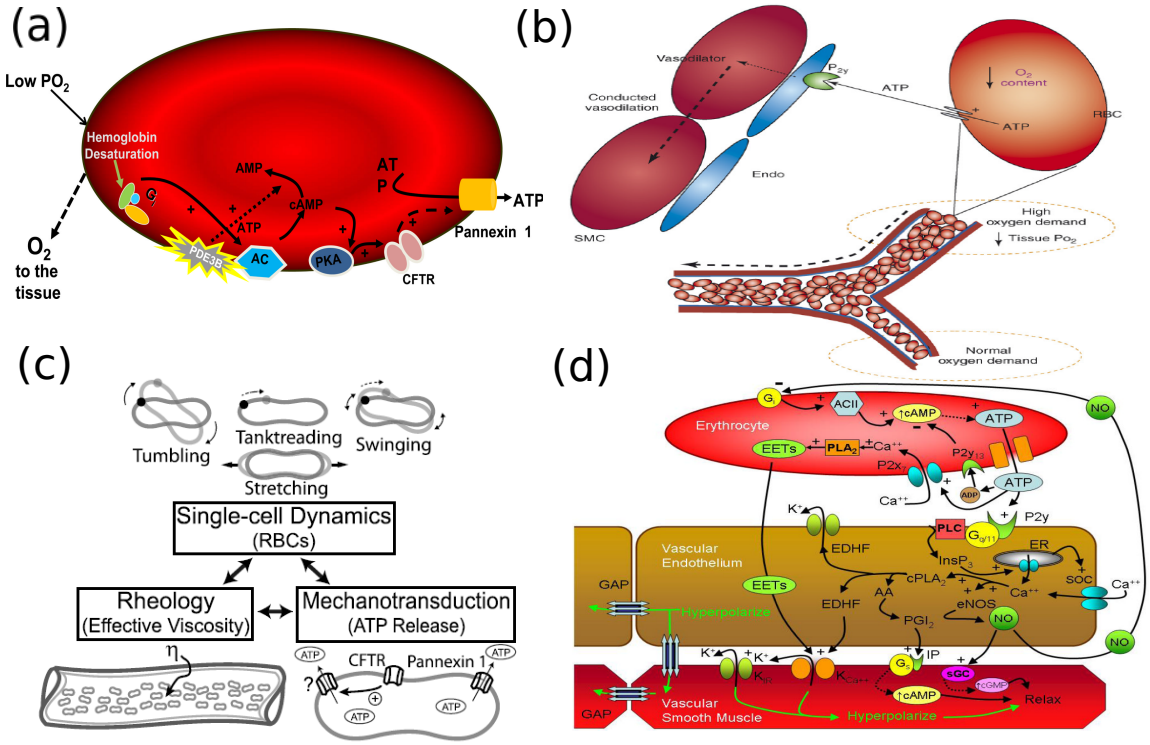

Figure 1.5: Schematic shows: (a) Exposure of RBC to low oxygen tension (pO_2) leads to hemoglobin desaturation (SO_2), which promotes ATP release via G_i signaling pathways [Sprague and Ellsworth, 2012]; (b) The ATP released from RBCs is involved in conducted vasodilation through endothelial cells (ECs) enabling selective perfusion of red blood cells in areas of high oxygen demand [Wan et al., 2011]; (c) ATP release from RBCs activates Ca^{2+} signaling in ECs. Subsequently, Ca^{2+} contributes to the production of nitric oxide (NO), prostacyclin (PGI_2), and endothelium-derived hyperpolarizing factors (EDHF). Each of these factors has its own functions. NO contributes to smooth muscle cells (SMCs) relaxation and prevents excessive ATP release from RBCs by inactivating G_i signaling pathways. EDHF controls the activation of calcium-activated potassium channels (K_{Ca}), resulting in the propagation of hyperpolarization signals in vessel walls [Ellsworth et al., 2009]; and (d) an illustration, how red cells rheology, due to different RBC dynamics, can affect ATP release from a RBC [Forsyth et al., 2011].

in the blood. For example, RBCs act as NO scavengers, while NO interacts with RBCs and serves as negative feedback for ATP release from RBCs [Olearczyk et al., 2004, Ellsworth et al., 2009]. On the other hand, NO triggers VSMC relaxation, thereby increasing blood flow to the region where metabolic activity and functional demand require oxygen, as shown in Figure 1.5(b).

Increased cytoplasmic Ca^{2+} in ECs stimulates Ca^{2+}-activated potassium (K_{ca}) channels. This leads to the egress of K^+ from the cytoplasm into the extracellu-

lar space, resulting in endothelium-derived hyper-polarization (EDHP). This is conducted to neighboring EC and spreads to the underlying SMCs to help vasorelaxation, as shown in Figure 1.5(d) [Ellsworth et al., 2009]. In an experiment with a vascular bed comprising arterioles, capillaries, and venules, ATP was applied to the lumen of collecting venules at levels similar to those released by RBCs. Local stimulation resulted in an increase in the diameter of upstream arterioles. Interestingly, the signal from the venules, where EC was stimulated, crossed the capillary bed to reach the arterioles [McCullough et al., 1997, Ellsworth et al., 2016]. Note that the signal was conducted through the ECs of the capillary blood vessel lacking SMCs.

1.1.3 Deformation-induced ATP release pathway

Although the molecular mechanism behind ATP release is still unclear, Forsyth et al. [Forsyth et al., 2011] have conclusively found that two pathways work synergistically in ATP release from RBCs when subject to flow. Firstly, RBCs sense shear stress and translate it into ATP release via Px1 hemichannels. Higher shear stress implies greater ATP release. Secondly, RBC deformation produces defects in the spectrin network and actin filaments. These filaments can bind to the freely diffusing CFTR (cystic fibrosis transmembrane conductance regulator). The binding of filaments to CFTR activates the latter and up-regulates ATP release via Px1 channels (Figure 1.5(c)). These two hydrodynamic stress sensing pathways activate ATP release via a specific channel, namely Px1. ATP release via these pathways is well documented by the chemical treatment of RBCs. Treatment of RBCs with carbenoxolone, which inhibits Px1 hemichannels, virtually ceased ATP release at any value of shear stress. Similarly, inhibition of CFTR from glibenclamide-treated RBCs did not result in ATP release.

1.2 Calcium ion: An effective messenger

Calcium is a ubiquitous ion that controls/regulates various cellular functions such as cell proliferation, vasodilation, secretion, phototransduction, reproduction, and permeability of cations such as potassium (K^+) and sodium (Na^+) (Figure 1.6(a)). Other calcium functions include forming the structural basis of cell membranes, cell-cell communication, and so on [Rasmussen, 1985]. Calcium ions are mainly stored in internal reserves such as the endoplasmic reserve (in non-excitable cells) or the sarcoplasmic reserve (in excitable cells) and the Golgi apparatus. The physiological (resting) concentration of cytoplasmic calcium is maintained at around 100 nM in

all animal cells. This is because cells avoid the formation of insoluble calcium phosphatase (Ca_2 $(PO_4)_3$) in the cell cytoplasm. As a result, the cell can use inorganic phosphate to form of energy currency, ATP. In addition, inorganic phosphate is used in kinase/phosphatase signaling and in the synthesis of lipids, carbohydrates and nucleic acids.

As Ca^{2+} has numerous second messenger functions, each of these activities is independently regulated and can occur in different parts of the same cell at the same time. This is why Ca^{2+} signal is both temporal and spatial in nature. It is worth noting that calcium signaling in many animal and plant species is strikingly similar. The question is how these second messenger functions are carried out within the cell. In the following sections, we will briefly find the answers to this question.

1.2.1 Calcium ion signal detection

The important aspect of second messenger function is a cell's ability to detect Ca^{2+} signals. To do this, cells must possess certain Ca^{2+}-sensing proteins that can detect changes in Ca^{2+} signals in the physiological range (10^{-7}-10^{-5} M) (Figure 1.6 shows the internal structure of ECs where Ca^{2+}-signals are measured; Figures 1.6(b)-(d)). Theses proteins are calmodulin and troponin-C, located in the cytoplasm. These Ca^{2+}-regulating proteins possess certain Ca^{2+}-binding sites that wrap Ca^{2+}. For example, the calmodulin protein has 4-binding sites. The binding of Ca^{2+} ions to these proteins leads to a change in their conformation, and this structural change results in activating enzymes such as eNOS. After activation of the regulatory molecules, Ca^{2+} signals must be interrupted to prevent phosphate molecules from being converted into Ca^{2+}-phosphatases [Rasmussen, 1985].

1.2.2 Calcium ion signal termination

The binding sites of the Ca^{2+}-sensing protein are limited in relation to the Ca^{2+} released from the ER. In order to maintain intracellular homeostasis, i.e., cytoplasmic Ca^{2+} concentration at its physiological Ca^{2+} concentration (10^{-7} M), other mechanisms have evolved for longer duration and higher Ca^{2+} buffering capacity of intracellular reservoirs (stores). These reservoirs have a high storage capacity for Ca^{2+}, and are capable of rapidly releasing Ca^{2+} when cells are activated. These stores are known as endoplasmic reticulum (ER), sarcoplasmic reticulum (found in excitable cells such as muscle cells), mitochondria, and Golgi apparatus. Of all stores, the ER has the largest number of Ca^{2+}. In addition, cells use other mechanisms to egress

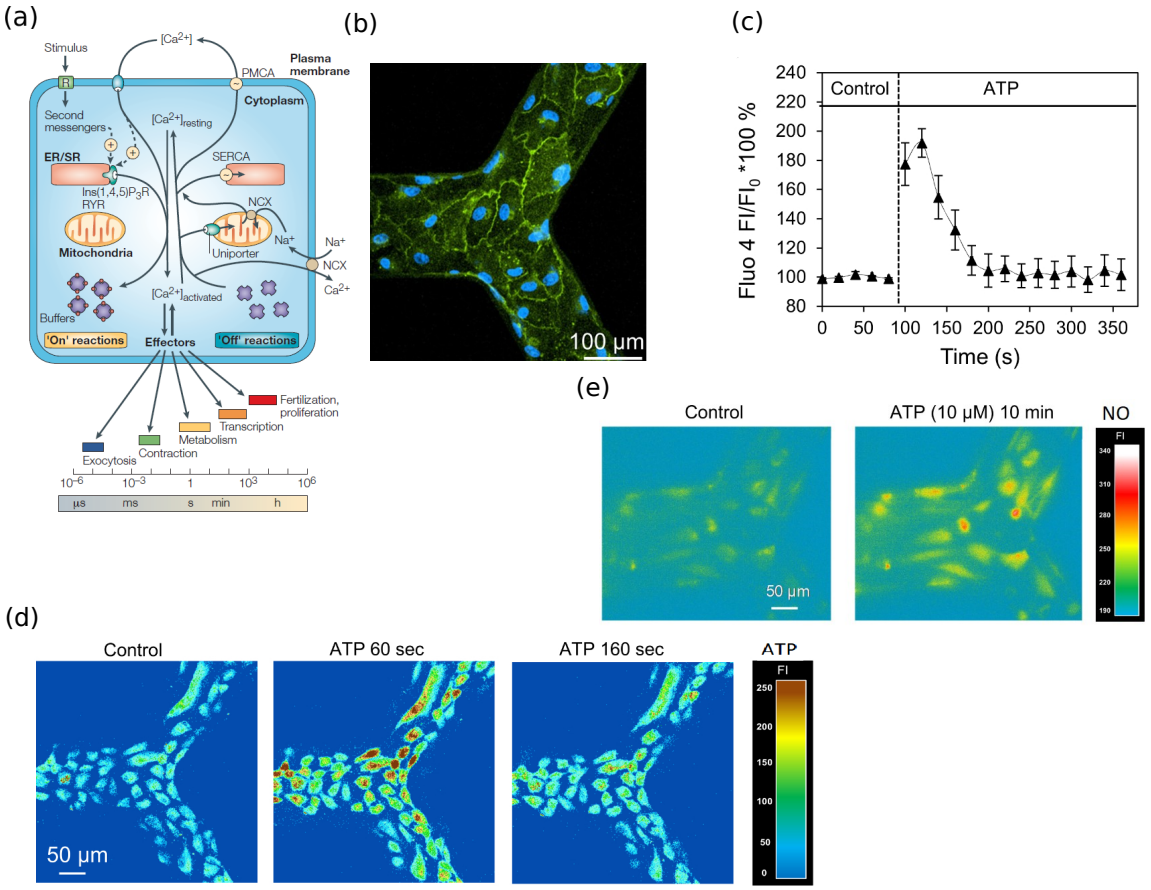

Figure 1.6: Schematic shows: (a) activation of Ca^{2+} pathways leads to the activation of effectors that perform cellular functions [Berridge et al., 2003]; (b) endothelial cells (ECs) cultured in a bifurcated microfluidic channel showing the boundary of EC (green) and nucleus (blue) [Xu et al., 2016]; (c) the normalized fluorescent response of EC to ATP in a particular region [Xu et al., 2016]; (d) spatio-temporal response (Ca^{2+}-signals) in the presence of ATP in a microfluidics channel [Xu et al., 2016]; and (e) spatio-temporal response (NO-signals) in the presence of ATP in a microfluidics channel [Xu et al., 2016].

Ca^{2+} from the cytoplasm into the extracellular space. Some of these mechanisms are driven by ATP molecules. For instance, the Ca^{2+}-ATPase uses the energy of ATP molecules to pump Ca^{2+} to the ER/SR and extracellular space. Cells also rely on other mechanisms to remove Ca^{2+} from the cytoplasm such as electrochemical gradients across the PM, ion-exchanger, and activation of a special mechanism due to the depletion of intracellular store. Another mechanism that helps maintaining intracellular homeostasis within the cell is the in-activation of surface receptors, such as $P2Y_2$, responsible for activating Ca^{2+} signaling pathways.

1.2.3 Historical aspects of calcium

In the late of nineteenth century, British clinician, physiologist and pharmacologist Sydney Ringer found by chance that sodium chloride mixed with tap water was more effective than distilled water in maintaining cardiac contractility. Furthermore, Ringer concluded in his experiment that the calcium present in distilled water acted as an antagonist to the role of sodium. Locke and others have furthered the understanding of the role of calcium in Ringer's experiment. They found that motor nerves exposed to pure sodium chloride lost their stimulatory effects on muscle contractility, and that these effects were restored by adding calcium (and potassium) at appropriate concentrations. In the early twentieth century, following Ringer's discovery, the role of calcium, sodium, and potassium concentrations in biological activity was established, although their mechanisms were not clearly understood at that time. Another experiment carried out by George Ralph Mines, an English pioneer of cardiac electro-physiology, observed phenomena on the frog gastrocnemius similar to those observed by researchers at the end of the nineteenth century. Mines inferred from his experiment that this was not electric charge, but rather a special chemical property of calcium capable of selectively interacting with unknown constituents within tissues. He thus laid the foundations for understanding the role of calcium in biological functions. Subsequently, other roles of calcium in biological activities have been studied, for example, McCutcheon and Lucke found that the presence of calcium in water decreases cell membrane permeability than magnesium [Rubin, 1985].

1.2.4 What is special about calcium ion in biology?

Why is the calcium ion an effective signal transduction ion in biology? Among other abundant ions such as K^+, Na^+, Mg^{2+}, and Cl^-, Ca^{2+} plays the role of a second messenger in the cell. Ca^{2+} is a divalent ion with atomic number and ionic radius having the values 20 and 1.06 Å, respectively. Due to Ca^{2+}'s atomic size and charge density, it is particularly preferable to bind its high-Ca^{2+} affinity binding-sites to Ca^{2+}-dependent modulators, Ca^{2+} buffers, Ca^{2+} carriers, or Ca^{2+}-selective channels. Ca^{2+} is preferred over Mg^{2+} for its versatile nature and second messenger functions, even though both are divalent [Blaustein, 1985]. The reasons lie in the difference in surface charge density and hydration energy. The surface charge density of Mg^{2+} is twice that of Ca^{2+}. As a result, Mg^{2+} forms moderately soluble salts with phosphate and remains partially hydrated. Due to its low surface charge density, Ca^{2+} forms

sparingly soluble salts with phosphates [Collins, 1997]. Furthermore, the high hydration energy of Mg^{2+} means that ions move on and off binding-sites more slowly than Ca^{2+}. Thus, Ca^{2+} is more effective to selectively bind calcium-binding proteins with dissociation constants in the range of 10^{-7}-10^{-5} M.

Table 1.1: Essential metals and their oxidation states, ligand binding properties, mobility, and function in biological systems [Jomova et al., 2022]

Metal ion	Ligand binding property	Mobility	Biological functions
Na^{+}	Weak	High	Regulatory function: osmotic pressure, membrane potential, enzyme activity
K^{+}	Weak	High	Nerve action, osmotic pressure
Mg^{2+}	Intermediate	Semi-mobile	Energy metabolism ATP → ADP, chlorophyll
Ca^{2+}	Intermediate	Semi-mobile	Signalling, enzyme regulation, muscle contraction, skeletal system (Bones, teeth)
Zn^{2+}	Intermediate/ Strong	Intermediate	Lewis acid (carbonic anhydrase, carboxypeptidase), structural roles–zinc fingers, repair enzymes
$Co^{2+,3+}$	Strong	Low	Vitamin B12 co-enzyme
$Cu^{+,2+}$	Strong	Low	Electron transfer (copper blue proteins), oxygen storage, transport proteins, ceruloplasmin
$Fe^{2+,3+}$	Strong	Low	Oxygen storage (hemoglobin, hemerythrin, electron transfer Fe–S proteins, cytochromes)
$Mn^{2+,3+,4+}$	Strong	Low	Enzyme (phosphatase, mitochondrial Mn-SOD, photoredox activity PS II
$Mo^{2+,3+,4+,5+,6+}$	Strong	Low	Enzymes (nitrogenase, reductases, hydroxylases)

1.3 Vasodilator nitric oxide

Nitric oxide (NO) is an important vasodilator that is produced by ECs in response to wall shear stress (caused by blood flow) and the binding of ATP (released from RBCs

and ECs) to purinergic receptors. NO synthesis is triggered by activation of eNOS due to increased cytoplasmic Ca^{2+} (as shown in Figures 1.2(a) and 1.6(e)). NO synthesis in the circulatory system has several implications. NO molecules can diffuse freely from the EC into neighboring SMCs and the vascular lumen. Under physiological conditions, NO molecules inhibit platelets aggregation, leukocytes adherence to the endothelium, SMCs relaxation, and NO preservation (as deoxy-Hb in RBCs). As a result, NO molecules counteract the effects of vasoconstrictors such as endothelin-I and angiotensin-II [Davignon and Ganz, 2004, Levine et al., 2012]. Vascular tone is thus maintained in the circulatory system.

Nature has chosen NO as a more important molecule for maintaining vascular tone in the human body than other molecules such as CO, O_2, or other ligands for the following reasons. These reasons are: (1) its ability to react with heme and non-heme iron proteins, (2) its ease of oxidation or reduction which allows its concentration to be controlled, and (3) the free diffusion of haemoglobin-NO (heme-NO) out of the protein or solution [Traylor and Sharma, 1992].

NO bioavailability in SMCs is influenced by the presence of RBCs and hemoglobin concentration. NO molecules are readily diffused into the vascular lumen and are strongly oxidized by hemoglobin to stable NO metabolites such as nitrite and nitrate. Hemoglobin-NO interaction leads to the formation of methemoglobin under oxygenated conditions and nitrosylhemoglobin (HbNO) under deoxygenated conditions, while NO molecules are converted to nitrite and nitrate. RBCs can also preserve NO bioactivity in the form of S-nitrosohemoglobin (SNOHb) and deoxygenated hemoglobin (deoxy-Hb), which can reversibly form NO [Deonikar et al., 2014]. These molecules are then transported to the hypoxic region, where they cause vasodilatation of vessels for improved erythrocyte supply [Buerk et al., 2017].

1.3.1 Historical aspects of nitric oxide and its applications

NO has a fascinating and colourful history. Joseph Priestley, a British theologian and chemist, named NO as nitrous oxide in 1772 [Habib and Ali, 2011, Levine et al., 2012]. NO was initially considered a colorless and toxic gas. Until 1987, NO gas was known as a poisonous gas and an air pollutant [Bruckdorfer, 2005, Habib and Ali, 2011]. After 1987, NO was recognized as an important molecule responsible for controlling blood pressure and alleviating many heart related ailments, such as angina pectoris, hypertension, and atherosclerosis. In 1987, RMJ Palmer and Louis J. Ignerro both proposed that the endothelium-derived relaxing factor (EDRF), which was responsible for vasodilation, was in fact NO [Rodeberg et al., 1995]. In the

middle of the nineteenth century, the research group of French chemist Théophile-Jules Pelouze laid the foundations for the discovery of NO. Later, Italian chemist Ascanio Sobrero, born in a small town of Casale Monferrato in the southern foothills of the Italian Alps, joined Pelouze's group as a student [Marsh and Marsh, 2000]. In a serendipitous discovery, Sobrero had synthesized nitroglycerine (NG). Later, Sobrero's research led to the discovery of the detonator, i.e., dynamite. He observed that the exposure to a minute quantity of NG caused a severe headache that lasted for several hours. The importance of NG's medical use was highlighted by an accidental observation. Workers at a factory, involved in NG production, suffering from angina pectoris (chest pain and discomfort) saw their health improve over the course of their working days. Surprisingly, their health deteriorated on Sundays. At that time, NG was known as "Monday's disease" [Levine et al., 2012]. Alfred Nobel, another student of Pelouze, learned about the discovery of NG and its commercial viability while he was in Paris. In 1867, he patented a stable compound, dynamite, made by mixing NG with Kieselguhr [Marsh and Marsh, 2000].

In 1879, British physician William Murrell introduced NG as a therapy for angina pectoris patients. Interestingly, Alfred Nobel, at the last stages of his life, was suffering from angina pectoris. His doctor prescribed NG as a medication which he refused to take. In 1977, Fried Murad confirmed the pharmacological benefits of NG on SMCs and confirmed the release of NO from SMCs [Levine et al., 2012]. In 1992, NO was named as "Molecule of the Year". The importance of this molecule graced front pages of different newspaper in 1998 when Louis J. Ignerro, Robert F. Furchgott and Ferid Murad were awarded the Nobel Prize in Medicine and Physiology for identifying NO as a signaling molecule [Habib and Ali, 2011]. In addition to its pharmacological benefits, NO is also used in the food industry. It is used to give dried meat an aesthetic red color, and to protect meat from oxidation and spoilage. This is because iron-nitrosated myoglobin (prevents spoilage of meat) is formed when NO reacts with muscle myoglobin.

1.4 Contributons of the thesis

Over the past two decades, much work has been done on deformable particles in creeping flow where viscous forces dominate. One such deformable particle is the RBC. There has been considerable interest in understanding the interactions between RBCs, the interactions between RBCs and vessel walls, and the individual dynamics of RBCs. Above all, this work has led to an understanding of blood rheology.

In addition, to understand blood flow in the human body, RBC flow was extended from a straight channel to a complex vascular network. As a result, several new phenomena have been observed, such as the persistence of RBCs at bifurcations and the reverse partitioning of RBCs in child vessels. In addition, several studies were carried out on whole blood containing RBCs, WBCs, and platelets. With the deepening understanding of RBC dynamics from numerical and modeling point of view, further knowledge on RBCs has been enriched by *in vitro* experiments in mircrofluidic chips with blood from different donors and *in vivo* experiments with animals [Tovar-Lopez et al., 2010, Forsyth et al., 2011, Tomaiuolo et al., 2011, Tomaiuolo and Guido, 2011, Shen et al., 2016, Kihm et al., 2021, Merlo et al., 2023, Xu et al., 2017].

To date, there has been little work on the vascular wall and its dynamics, or on how the vascular wall perceives information from blood flow. To better understand the physical phenomena occurring in the blood vessel wall, we need to consider a coupled system, i.e., blood flow in the vascular lumen and biochemical signalling in the blood vessel walls. ATP molecules released by RBCs and ECs, under the effect of flow, form the link between the two systems. Our group [Zhang et al., 2018] has recently developed a phenomenological model of ATP release from RBCs. ATP molecules released into plasma are transported and diffused to the blood vessel wall, where they trigger biochemical signals such as activation of Ca^{2+} signaling and NO synthesis. The biochemical signals that occur in vessel walls are directly linked to various (patho)physiological conditions such as thrombosis, atherosclerosis, stroke, and so on. It is therefore essential to investigate a direct link between RBC dynamics and biochemical signals occurring in blood vessel walls. The main aim of this thesis is to understand the role of RBC in the activation of biochemical signals, and to determine how and which biochemical pathways are responsible for maintaining vascular tone. As a preliminary study, we performed all simulations in a two-dimensional (2-D) straight channel. However, it is easy to extend this study to a three-dimensional (3-D) geometry. Furthermore, this thesis will contribute to the following chapters for a better understanding of the physiological processes occurring in the human body.

1.4.1 Calcium homeostasis modeling

Due to the relevance of Ca^{2+} signaling in various physiological processes, many experimental works have been carried out on Ca^{2+} signaling over the last three decades. In the same spirit, several mathematical models have been developed to understand the nature of the Ca^{2+} signals obtained during experiments. These mathematical models focused primarily on reproducing the Ca^{2+} oscillations that occur in many cells. In

addition, other models have been developed which produce a cytoplasmic Ca^{2+} peak and then attains a steady concentration [Plank et al., 2006]. However, the steady concentration is higher than the initial physiological concentration (Ca^{2+} concentration prior to application of ATP). Consequently, steady intracellular concentrations of important variables such as store Ca^{2+} and inositol trisphosphate (IP_3) are affected. Intracellular homeostasis is therefore not maintained in the EC. In an experiment by [Carter et al., 1990], they inferred that the most ECs exhibit the characteristic Ca^{2+} signal, in which Ca^{2+} was returns to its initial after attaining a peak in the presence of a given concentration of ATP. This type of signal is due to the desensitization of surface receptors, which are responsible for activating Ca^{2+} signaling.

Taking these experimental facts into account, we developed a mathematical model. The main ingredient of the model is the receptor dynamics. The Ca^{2+} signal obtained in the model quantitatively agrees with the experimental result. In addition, the model is able to capture other experimental observations such as the effect of stimulating ECs with ATP for a fixed time before washing out the stimulus, extracellular Ca^{2+}-dependent ER Ca^{2+} refilling, the reason for varying Ca^{2+} transients in different experiments in the same EC, and cytoplasmic Ca^{2+} saturation with increasing ATP concentration.

1.4.2 Coupling of RBC and calcium dynamics

In the previous chapter, we developed a single EC Ca^{2+} dynamics model in which a constant ATP concentration was used to trigger Ca^{2+} release from the ER. However, in actual scenario, ATP is released by RBCs and ECs when they are subjected to hydrodynamic stress. ATP concentration in plasma varies spatially and temporally as a function of vessel diameter, the hematocrit, and the external flow strength. Zhang et al. [Zhang et al., 2018] proposed a phenomenological model for ATP release from RBCs. We used this model to find the distribution of ATP in plasma as well as on the surface of the enodthelium wall (which forms the inner lining of the blood vessel). We performed 2-D lattice Boltzmann method (LBM) simulations in a straight channel lined with endothelium on the upper and lower walls of the channel.

We found a steady ATP concentration in plasma by incorporating the effects of endothelium. The enzymes on the endothelium layer hydrolyze ATP (incessant ATP release from RBCs and ECs). A steady ATP concentration is maintained due to by balancing the flux of ATP release and hydrolysis. Furthermore, We found that ATP concentration on the endothelium wall surface depends on variables such as channel width, flow strength, and RBC concentration. To understand Ca^{2+} signals inside the

endothelium, we solved Ca^{2+} dynamics modeling equations, providing ATP concentration as an input. We found an interesting observation that the Ca^{2+} peak time decreases with increase in ATP concentration. This peak time is highly dependent on the variables mentioned above. Because of the difference in peak times, if we have a vascular network, it is possible that Ca^{2+} propagates from a region of high Ca^{2+} concentration to a region of low Ca^{2+} concentration. This simplistic idea of Ca^{2+} propagation will be useful for understanding local vasodilation, and consequently blood perfusion and nutrient distribution in a vascular network.

1.4.3 Nitric oxide modeling and its bioavailability

In the previous chapters, we developed a Ca^{2+} dynamics model and later coupled it directly to RBC dynamics. ATP released by RBCs and ECs triggers the mobilization of Ca^{2+} from the ER. The rise of Ca^{2+} concentration in EC cytoplasm regulates NO synthesis. The NO produced in ECs diffuses into SMCs, which are located in the tunica media, and the vascular lumen. This NO has two consequences in the vasculature: (i) it contributes to the relaxation of SMCs, thereby increasing blood perfusion by expanding the vessel diameter to a location where metabolic requirements are high, and (ii) NO is scavenged at a high rate by RBCs to stable metabolites such as nitrite and nitrate, enabling NO to be delivered by RBCs into the hypoxia region to facilitate blood supply.

To better understand the physical phenomena occurring in the vascular wall, we first developed a model for agonist (ATP)-dependent NO generation by coupling cytoplasmic Ca^{2+} and the shear stress (experienced by ECs due to the blood flow) -dependent pathways into the model. The model results are qualitatively consistent with experimental observations. Secondly, we intricately coupled RBC dynamics, ATP release from ECs and RBCs, Ca^{2+} signaling, NO generation, and its diffusion and scavenging by RBCs for a two-dimensional (2-D) straight channel. This simulation is carried out by varying the width of the channel and for different concentrations of RBC in order to establish a link with a microvascular network. Some of the most interesting results are (i) increased RBC concentrations lead to increased ATP and cytoplasmic Ca^{2+} concentrations ("faster-is-faster" response) for all variation in width of the channel, however, NO concentration shows "faster-is-slower" response, (ii) NO availability depends on RBC distribution, at least in confined channel like capillaries, (iii) two phases of NO availability have been observed in different regions of the vessel, a phase of high NO concentration at low RBC concentration and a phase with no change in NO concentration at high RBC concentration for all confinements,

and (iv) NO availability in weakly confined channels, although there is no significant changes in its concentration, is greater than in strongly confined channel at high RBC concentration.

Chapter 2

Model Equations and Numerical Methods

2.1 Introduction

In this chapter, we briefly introduce the numerical methods used in this thesis. We carried out simulations using Lattice Boltzmann method (LBM) throughout this thesis. We used LBM to solve the fluid flow problem. LBM has an advantage over other numerical methods. Due to the local nature of the information and the ease of implementation, it is possible to implement parallel coding, which makes the simulation faster than other numerical methods. To deal with interaction between fluid and solid structures, for example flexible structures such as red blood cells (RBCs), we used the immersed boundary method (IBM). This method satisfies the no-slip conditions between interfaces by means of a singular Delta function. Over the past decade, continuous efforts have been made to simulate laboratory-scale *in vivo* conditions in order to understand physical phenomena using microfluidic setups. The problem involves fluid flows, advection diffusion transports and chemical reactions (e.g. the case of ATP in plasma). We will thus have to solve advection-diffusion-reaction equations (ADREs). For solving both fluids and chemicals, we used LBM. In the following sections, we briefly introduce methods such as IBM, basic structure of LBM used to solve fluid flow and solute concentrations, modeling of RBC membrane, and algorithm used to solve the fluid-structure interaction problem.

2.2 Lattice Boltzmann method for fluid flow

Today, parallel computing has undergone a profound evolution with the development of new technologies in the semiconductor industry. At the same time, computing

power has evolved rapidly, increasing computational efficiency, speed and ease of solving complex problems with high degrees of freedom. One of the numerical methods used to solve fluid flow problem is the LBM. The LBM algorithm has become quite popular because it is relatively easy to implement, even for very complex geometry. Moreover, the implementation is local in nature, making it an ideal candidate for parallel computing. Instead of dealing directly with physical quantities in real-world problems or continuum physics, LBM describes the motion and density of a group of fictitious particles using the distribution function, i.e., the probability of finding particles in a certain range of velocities at a certain locations at a given time. In the numerical solution, the Boltzmann equation reads generally as

$$\frac{\partial f}{\partial t} + \mathbf{c} \cdot \nabla f = \Omega \,, \tag{2.1}$$

where f is the distribution function, $\mathbf{c}$ is the velocity of a group of molecules (a small element of fluid, say of the order of a fraction of a micrometer), and Ω is the collision operator. The implementation of LBM comprises two important steps: the collision step (calculation of information at lattice nodes; given on the right-hand side of Equation (2.1)) and the streaming step (sharing of information between neighboring lattice nodes; the left-hand side of Equation (2.1)). These steps are expressed mathematically below in the discretized form of Equation (2.1). The time evolution of the discretized distribution function, $f_i(\mathbf{x}, t)$, is described in two steps below (also shown in Figure 2.1).

1. Collision step
$$f_i^{\star}(\mathbf{x}, t) = f_i(\mathbf{x}, t) + \Delta t(\Omega_i + F_i) \,, \tag{2.2}$$

2. Streaming step
$$f_i(\mathbf{x} + \mathbf{c}_i \Delta t, t + \Delta t) = f_i^{\star}(\mathbf{x}, t) \,, \tag{2.3}$$

where $\mathbf{c}_i$ is the lattice velocity vector for distribution function i, Δt is the time step, and Ω_i is the Bhatnagar-Gross-Krook (BGK) collision operator and is written as follows [Mohamad, 2011]

$$\Omega_i = -\frac{1}{\tau} \left[f_i(\mathbf{x}, t) - f_i^{eq}(\mathbf{x}, t) \right] \,, \tag{2.4}$$

where τ is the single-relaxation time (SRT) and is related to the kinematic viscosity of the fluid. The shear kinematic viscosity of the fluid, obtained while recovering the

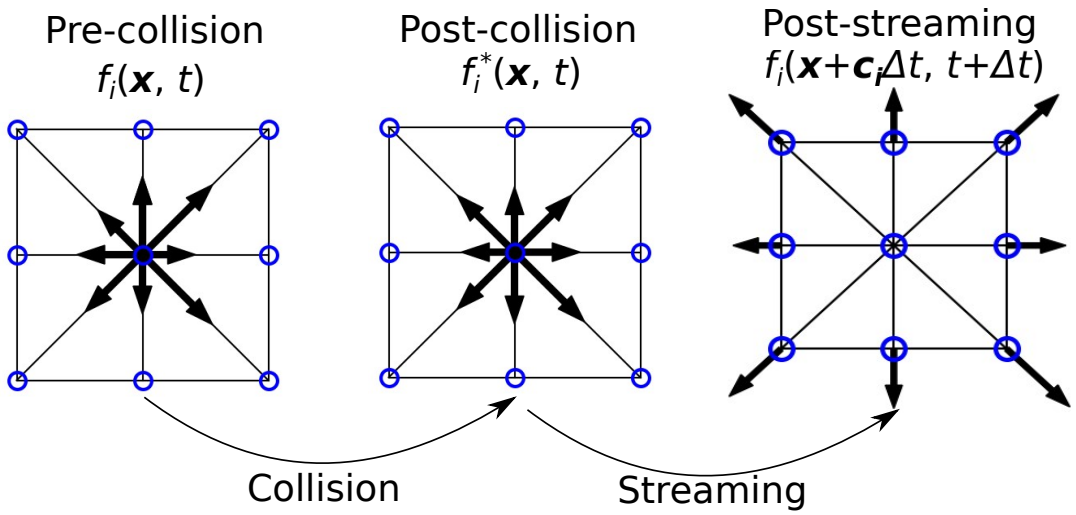

Figure 2.1: Schematic showing the collision and streaming of distribution functions in the D2Q9 model. The length of the arrow indicates the strength of the distribution function.

Navier-Stokes equations (NSEs) from the LBE using the Chapman-Enskog multiscale approach, is expressed as follows

$$\nu = \frac{1}{2} c_s^2 \Delta t \left(2\tau - 1\right) , \tag{2.5}$$

where $c_s = \frac{1}{\sqrt{3}} \frac{\Delta x}{\Delta t}$ is local speed of sound. This acts as a constraint to LBM's application to a strongly compressible flow. A compressible or incompressible fluid is known by its Mach number (Ma), which is defined as the speed of flow to the speed of sound in the same medium. It must be less than 0.3 to simulate an incompressible flow.

Navier-Stokes equations (NSEs) for incompressible flows is defined as follows,

$$\nabla . \mathbf{v} = 0 \, , \tag{2.6}$$

$$\rho \left(\frac{\partial \mathbf{v}}{\partial t} + \mathbf{v} . \nabla \mathbf{v} \right) = -\nabla p + \nabla . (\mu \nabla \mathbf{v}) + \mathbf{F} \, . \tag{2.7}$$

where ρ is the density of the incompressible fluid, p is the pressure field, $\mathbf{v}$ is the fluid velocity field, and μ is the dynamic viscosity of the fluid. To distinguish dynamic viscosity of the fluids inside and outside of RBCs, we define a dimensionless number called the viscosity contrast, λ. λ is defined as the ratio between the dynamic viscosity of interior, μ_{in} and that of exterior, μ_{ex} fluids of RBC. In this thesis, we keep the viscosity contrast constant at a physiological value. The viscosity contrast and dynamics viscosity of fluid inside RBC are $\lambda = 6$ and $\mu_{\text{in}} = 0.012$ Pa.s, respectively [Forsyth et al., 2011].

The discrete form of the equilibrium distribution function, f_i^{eq}, is obtained from an approximation of Maxwell's probability function and is expressed as functions of the local lattice velocity as well as the macroscopic fluid velocity [Mohamad, 2011],

$$f_i^{\text{eq}} = \omega_i \rho \left[1 + \frac{1}{c_s^2}(\mathbf{c}_i \cdot \mathbf{v}) + \frac{1}{2c_s^4}(\mathbf{c}_i \cdot \mathbf{v})^2 - \frac{1}{2c_s^2}(\mathbf{v} \cdot \mathbf{v}) \right], \tag{2.8}$$

where ω_i is the weight factor for discrete velocity i and i takes a value from 0 to 8. The D2Q9 model, which represents two-dimensional (2-D) flow and having 9 discrete velocities (as shown in Figure 2.2(a)), is used for the fluid flow solution in this thesis. D2Q5 (2-D, 5 discrete velocities; shown in Figure 2.2(b)) is another available model used for 2-D simulation, employed for the ADRE solution. Similarly, D3Q15 (3-D, 15 discrete velocities), D3Q19 (3-D, 19 discrete velocities), and D3Q27 (3-D, 27 discrete velocities) are used for the study of three-dimensional flow [Krüger et al., 2017]. The main constraint for the selection of lattice and number of nodes is to obtain in the continuum limit the Navier-Stokes equations (recovering isotropy is a main constraint) [Krüger et al., 2017]. The weighting factors used in Equation (2.8) are obtained by satisfying symmetry conditions, detailed in [Mohamad, 2011]. These values for the D2Q9 model, employed in this thesis, are

$$w_i = \begin{cases} \frac{4}{9}, & i = 0, \\ \frac{1}{9}, & i = 1, 2, 3, 4, \\ \frac{1}{36}, & i = 5, 6, 7, 8. \end{cases} \tag{2.9}$$

The nine discrete velocity vectors are

$$\mathbf{c}_i = \begin{cases} (0, 0), & i = 0, \\ (\cos[i-1]\frac{\pi}{2}, \sin[i-1]\frac{\pi}{2})\frac{\Delta x}{\Delta t}, & i = 1, 2, 3, 4, \\ (\cos[2i-9]\frac{\pi}{2}, \sin[2i-9]\frac{\pi}{2})\frac{\Delta x}{\Delta t}, & i = 5, 6, 7, 8. \end{cases} \tag{2.10}$$

External flow fields such as pressure-driven flow and the external force field imparted by solid objects in the form of a volumetric force are incorporated into LBM through Equation (2.11). The discrete form of the bulk force is expressed as follows

$$F_i = \left(1 - \frac{1}{2\tau}\right) \omega_i \left[\frac{\mathbf{c}_i - \mathbf{v}}{c_s^2} + \frac{(\mathbf{c}_i \cdot \mathbf{v})\mathbf{c}_i}{c_s^4} \right] \cdot \mathbf{F}, \tag{2.11}$$

where $\mathbf{F}$ is the bulk force term in NSEs (Equation (2.7)). All the bulk force can be mathematically stated as $\mathbf{F} = \mathbf{F}^b + \mathbf{F}^f$, where $\mathbf{F}^b$ is the body force equivalent to the pressure drop required to obtain the desired velocity field and $\mathbf{F}^f$ is the force exerted by solid objects on fluids.

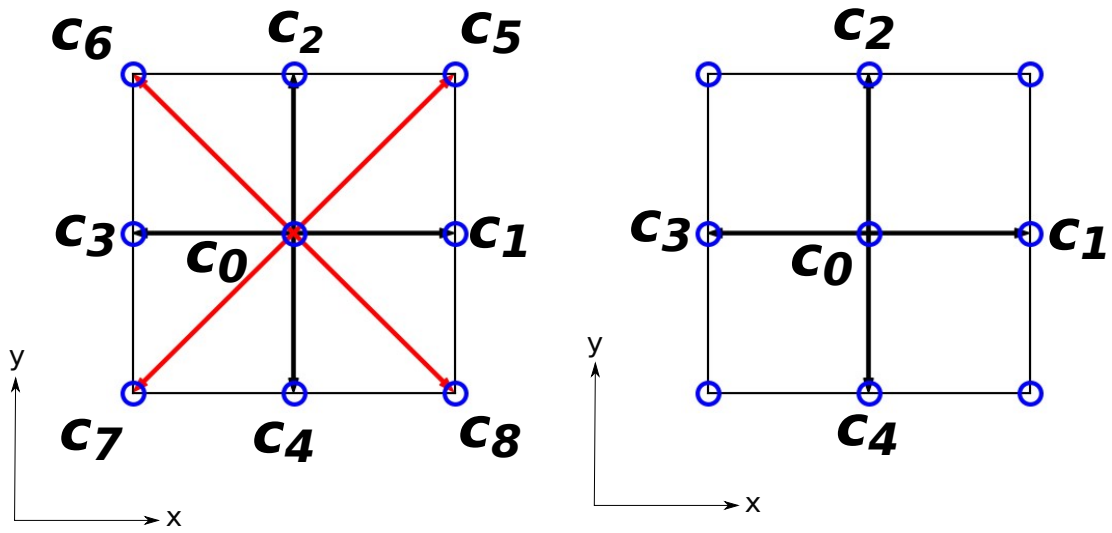

Figure 2.2: Schematic showing discrete velocities for model (a) D2Q9 and (b) D2Q5. These velocities are represented in the Cartesian coordinate system.

The physical variables for fluid, such as density (ρ), velocity ($\mathbf{v}$), and pressure (p), are obtained from the distribution function and are given as [Guo and Zhao, 2002]

$$\rho = \sum_{i=0}^{9} f_i \,, \tag{2.12}$$

$$p = \rho c_s^2 \,, \tag{2.13}$$

$$\rho \mathbf{v} = \sum_{i=0}^{9} \mathbf{c}_i f_i + \frac{\Delta t}{2} \mathbf{F} \,. \tag{2.14}$$

2.3 Treatment of boundary conditions for fluid flow

There are two main types of boundary we have to deal with when solving fluid flow problems : static and moving boundaries. In addition, we use periodic boundary conditions along the flow direction. The periodic boundary condition is managed in such a way that unknown distribution functions from the outlet boundary enter the inlet boundary and vice versa, as shown in Figure 2.3.

To enforce the no-slip boundary condition to the static boundary, we have used the half-way bounceback method. In this method, the physical boundary is located half-way distance between the fluid and solid lattice nodes. The unknown distribution functions at the boundary nodes are obtained in three steps: (a) distribution functions at $t = t_0$ propagate to neighbouring nodes after the collision step, (b) at $t = t_0 + \Delta t/2$ some of the distribution functions from the boundary nodes (lattice nodes close to the

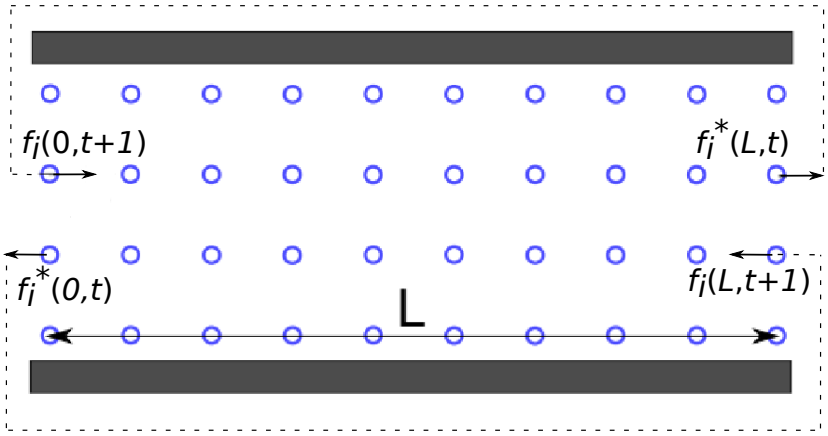

Figure 2.3: Schematic shows the implementation of periodic boundary condition in the LBM.

physical boundary) collide with the physical wall and change their direction by 180°, with no change in magnitude, and (c) at $t = t_0 + \Delta t$, they return to their original lattice nodes, and at the same time, other unknown distribution functions at the same nodes are obtained from the stream of distribution functions from their neighbouring fluid lattice nodes. These steps are illustrated in Figure 2.4. For understandable reasons of implementing the half-way bounceback method, we have not shown the streaming of populations from their neighbouring nodes in this figure.

2.3.1 Immersed Boundary Method

A common way of dealing with moving boundaries in the fluid flow is to use the so-called immersed boundary method (IBM). In IBM, rather than treating a boundary as a sharp interface, a thin strip is considered around the interface. Around this thin strip, the fluid and immersed structure (like deformable RBC membrane) interact with each other. To study fluid-structure interaction (FSI) problem numerically, two types of grid are employed without meshing the domain at each time step, namely Eulerian nodes for fluids and Lagrangian nodes for RBC. It should be noted that the positions of Eulerian nodes are fixed for the duration of the simulation, while the positions of Lagrangian nodes may or may not change over time; for RBCs, which is a deformable entity, the positions of the Lagrangian nodes changes over time. The main idea of IBM is that the RBC imparts forces on the fluid nodes in the thin strip, thereby modifying the local fluid velocities. In turn, the velocities of the RBC nodes are extrapolated from the velocities of the fluid nodes around the interface,

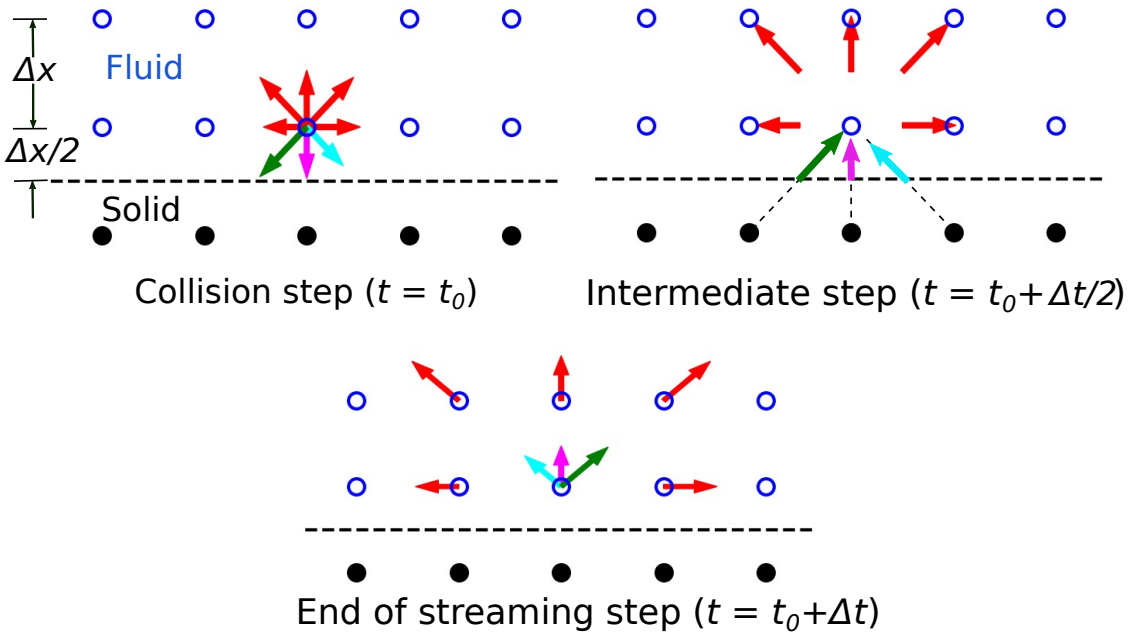

Figure 2.4: Schematic showing the finding of unknown populations at lattice nodes close to the solid wall. This figure illustrates the implementation of no-slip impermeability boundary condition in three steps. These steps are presented sequentially in time.

and subsequently, the positions of Lagrangian nodes are updated. Peskin [Peskin, 2002] proposed IBM (singular functions) to couple these two grids together. Three important steps are performed in IBM, which are

1. The elastic forces, obtained by solving the membrane deformation, are distributed to the surrounding fluid nodes using the smeared delta function. These forces are added to the body forces in the collision Equation (2.2).

2. The surrounding velocity of the fluid nodes are interpolated to the Lagrangian node using the same smeared function. This step is performed after the calculation of Eulerian velocities following the streaming step.

3. The position of the Lagrangian nodes is updated at $t + \Delta t$ using the forward Euler method.

The first step of IBM's implementation can be written mathematically as follows

$$\mathbf{F}^f = \oint_\Gamma \mathbf{f}(s).\delta(\mathbf{x} - \mathbf{X}(s))ds\,, \tag{2.15}$$

where $\mathbf{x} \in [0, L] \times [-W/2, W/2]$ (L and W are the length and width of the computational fluid domain, respectively), Γ represents integration along the contour of a

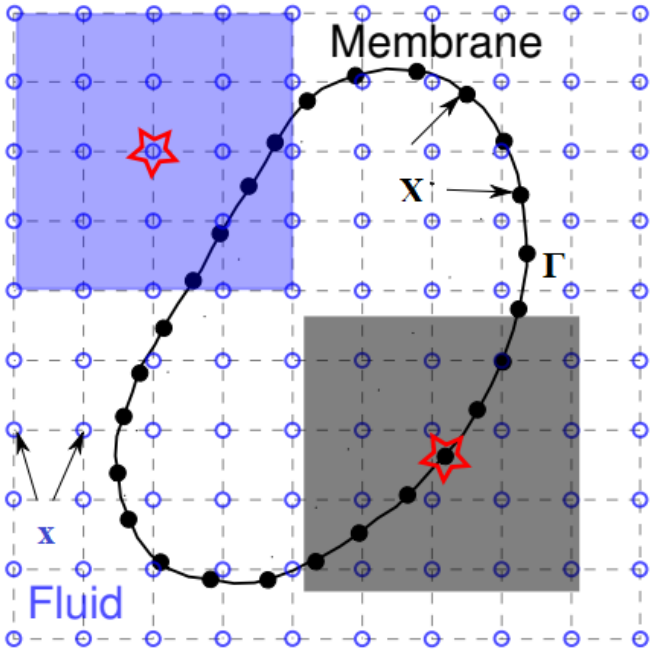

Figure 2.5: Schematic showing the force spreading and velocity interpolation in the IBM. The fluid is represented by the hollow blue nodes, and the membrane is denoted by the filled black nodes. This Figure is adopted from [Shen, 2016].

immersed object, $\mathbf{X}(s)$ is a set of points on the surface of the immersed object in the x-y plane (shown in Figure 2.5), s is the local arc-length, δ is the smeared Dirac delta function, and $\mathbf{f}$ is the force at the Lagrangian node. The force in Equation (2.15) is numerically calculated as

$$\mathbf{F}^f = \sum_{\mathbf{X}} D(\mathbf{x} - \mathbf{X})\mathbf{f}(s)\,, \tag{2.16}$$

where $D(.)$ represents the 2-D discrete-delta function. Similarly, the second step can be mathematically expressed as

$$\frac{\partial \mathbf{X}}{\partial t} = \mathbf{V}(s) = \int_y \int_x \delta(\mathbf{x} - \mathbf{X}(s))\mathbf{v}(\mathbf{x})dxdy\,, \tag{2.17}$$

where $\mathbf{V}$ is the Lagrangian velocity. Equation (2.17) is numerically solved as follows

$$\mathbf{V} = \sum_{\mathbf{x}} D(\mathbf{X} - \mathbf{x})\mathbf{v}(f)\,, \tag{2.18}$$

where the integration is performed over the neighbouring fluid nodes, $\mathbf{x}$. The final step of the IBM's implementation is expressed as follows

$$\mathbf{X}(t + \Delta t) = \mathbf{X}(t) + \mathbf{V}\Delta t\,. \tag{2.19}$$

The 2-D discrete delta function at point (x, y) is given as

$$D(x,y) = \phi(x)\phi(y)\,, \tag{2.20}$$

where ϕ is the smeared function. There are various forms of smeared function. The classic smeared function is

$$\phi(x) = \begin{cases} \frac{1}{4}\left(1+\cos(\frac{\pi x}{2})\right), & |x| \le 2, \\ 0, & 2 \ge |x|. \end{cases} \tag{2.21}$$

Yang et al. [Yang et al., 2009] proposed three- and four-point smoothing smeared functions to avoid nonphysical body force oscillations in moving boundary simulation. These functions are

$$\phi(x) = \begin{cases} \frac{17}{48} + \frac{\sqrt{3}\pi}{108} + \frac{|x|}{4} - \frac{x^2}{4} + \frac{1-2|x|}{16}\sqrt{-12x^2+12|x|+1} \\ -\frac{\sqrt{3}}{12}\arcsin\left(\sqrt{3}|x| - \frac{\sqrt{3}}{2}\right), & |x| \ge 1, \\ \frac{55}{48} + \frac{\sqrt{3}\pi}{108} + \frac{13|x|}{12} + \frac{x^2}{4} + \frac{2|x|-3}{48}\sqrt{-12x^2+36|x|-23} & \\ +\frac{\sqrt{3}}{36}\arcsin\left(\sqrt{3}|x| - \frac{3\sqrt{3}}{2}\right), & 1 \le |x| \le 2, \\ 0, & 2 \ge |x|, \end{cases} \tag{2.22}$$

$$\phi(x) = \begin{cases} \frac{3}{8} + \frac{\pi}{32} - \frac{x^2}{4}, & |x| \le 0.5, \\ \frac{1}{4} + \frac{1-|x|}{8}\sqrt{-4x^2+8|x|-2} - \frac{1}{8}\arcsin\left(\sqrt{2}|x| - \sqrt{2}\right), & 0.5 \le |x| \le 1.5, \\ \frac{17}{16} - \frac{\pi}{64} - \frac{3|x|}{4} + \frac{x^2}{8} + \frac{|x|-2}{16}\sqrt{-4x^2+16|x|-14} & \\ +\frac{\sqrt{1}}{16}\arcsin\left(\sqrt{2}|x| - 2\sqrt{2}\right), & 1.5 \le |x| \le 2, \\ 0, & 2 \ge |x|. \end{cases} \tag{2.23}$$

The term n-point is related to the degree of interpolation. In our simulation, we have used three-point smoothed smearing function.

2.3.2 Membrane Modeling

Throughout this thesis, we have carried out 2-D simulations. We modelled the membrane of a vesicle as a contour, having bending resistance to deformation. However, in three-dimensional (3-D), RBC and vesicle have differences in their structures. One of the differences is the existence of shear resistance in the former compared to the latter, thanks to the underlying cytoskeleton. The latter lacks of shear resistance due to the free in-plane diffusion of lipid molecules. Nevertheless, shear resistance could affect RBC dynamics. We adopt a 2-D model to enhance numerical efficiency, building upon our prior demonstration that this model effectively captures the fundamental attributes of the three-dimensional (3-D) RBC model. These attributes

encompass various aspects such as shapes under flow, as illustrated by Kaoui et al. [Kaoui et al., 2011]; cross-streamline noninertial migration velocity, as explored by Kaoui et al. [Kaoui et al., 2008] and Coupier et al. [Coupier et al., 2008]; inclination angle of cells concerning flow direction, as discussed by Beaucourt et al. [Beaucourt et al., 2004b] and Kantsler et al. [Kantsler and Steinberg, 2006]; as well as ATP release under flow, as outlined in the work of Gou et al. [Gou et al., 2021].

According to the Helfrich model, the energetic contribution originates from the change in local mean curvature. In addition, there is no fluid flow through RBC membrane, as a result, the area of the vesicle is conserved. The energy contribution of the local incompressiblity of the membrane is added to Helfrich equation. It is enforced using the Lagrange multiplier, which is akin to a tension. However, unlike surface tension for drop, which is an intrinsic quantity, here ζ is related to bending, to the size of the vesicle, etc... Thus, the total Helfrich energy of the RBC membrane can be written as the function of arc length of the membrane [Helfrich, 1973],

$$E(\mathbf{X}(s)) = \frac{\kappa}{2} \oint_{\Gamma} c^2 ds + \oint_{\Gamma} \zeta ds \,, \tag{2.24}$$

where κ is the bending modulus of the membrane, c is the curvature, ζ is the Lagrange multiplier enforcing the local inextensibility of the membrane length, and Γ is the contour of the membrane. The membrane force is obtained from Equation (2.24) by taking the functional derivative [Kaoui et al., 2008]

$$\mathbf{f}(s) = \frac{\delta E}{\delta \mathbf{X}(s)} = \kappa \left(\frac{\partial^2 c}{\partial s^2} + \frac{c^3}{2} \right) \mathbf{n} - \zeta c \mathbf{n} + \frac{\partial \zeta}{\partial s} \mathbf{t} \,, \tag{2.25}$$

where $\mathbf{n}$ and $\mathbf{t}$ are the local normal and tangential unit vectors on the membrane contour, respectively.

2.3.2.1 Spring energy

The membrane force Equation (2.25) can be alternatively represented using a spring model. The vesicle contour is discretized into a finite number of springs, as shown in the Figure 2.6. According to the spring model, the Helfrich energy Equation (2.24) is equivalently converted into bending energy (E_b), stretching energy (E_l), and areal energy (E_s) forms. Actually, the fluid area inside the vesicle should remain constant, due to the fluid incompressibility condition. However, numerically, there is always a drift of the area, that has to be enforced. This is what the areal energy is intended for. To enforce the area and perimeter change to constant, we use high spring constants

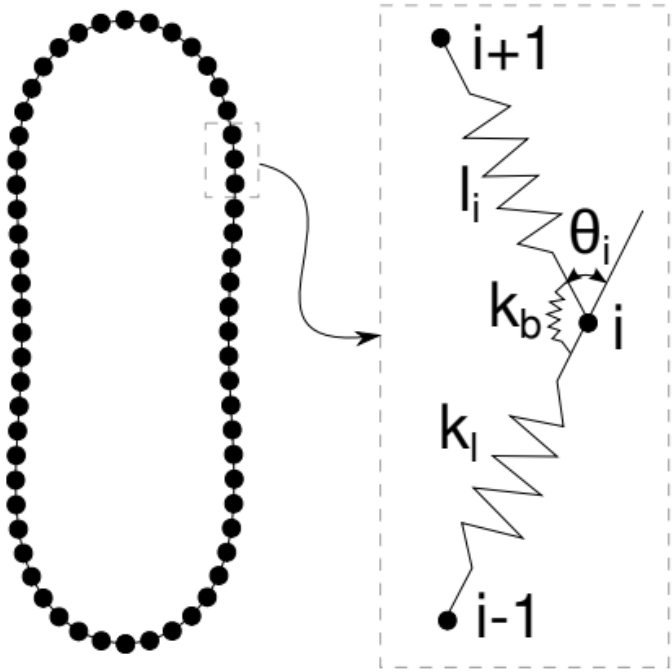

Figure 2.6: Schematic shows that the vesicle membrane is discretized using springs. These springs have a stretching and bending modulus, k_l and k_b, respectively. The angle between two springs l_i and l_{i-1} at node i is defined as θ_i. This Figure is taken from [Shen, 2016].

in the corresponding energy terms. Note that these values must be high enough to enforce above conditions, but not so high as to cause numerican instability.

These three contributions to the energy are written as follows. The energy stored in a linear spring due to extension relative to its initial length is called the stretching energy. It is defined as follows

$$E_l = \frac{1}{2} k_l \sum_{j=1}^{N} \left(\frac{l_i - l_i^0}{l_i^0} \right)^2 , \tag{2.26}$$

where k_l is the spring stretching constant (N/m), l_i and l_i^0 are stretch and initial length of the spring whose node i is connected to node $i+1$, and N is the total number of springs. We assume that the initial lengths of N springs are equal. The length of spring is expressed as $l_i^0 = \sqrt{(x_{i+1}^0 - x_i^0)^2 + (y_{i+1}^0 - y_i^0)^2}$, $l_i = \sqrt{(x_{i+1} - x_i)^2 + (y_{i+1} - y_i)^2}$, where (x_{i+1}^0, y_{i+1}^0), (x_i^0, y_i^0), (x_{i+1}, y_{i+1}), and (x_i, y_i) are the Cartesian coordinates of nodes $i+1$ and i, in 2-D setting, at time $t = 0$ (the reference configuration) and $t = t_1$ (the current configuration), respectively.

Similarly, the energy of a vesicle due to variation in its shape is written as follows

$$E_s = \frac{1}{2} k_s \sum_{i=1}^{N} \left(\frac{s_i - s_i^0}{s_i^0} \right)^2 , \tag{2.27}$$

where s_i^0 and s_i are the equilibrium and current areas of the triangles whose co-

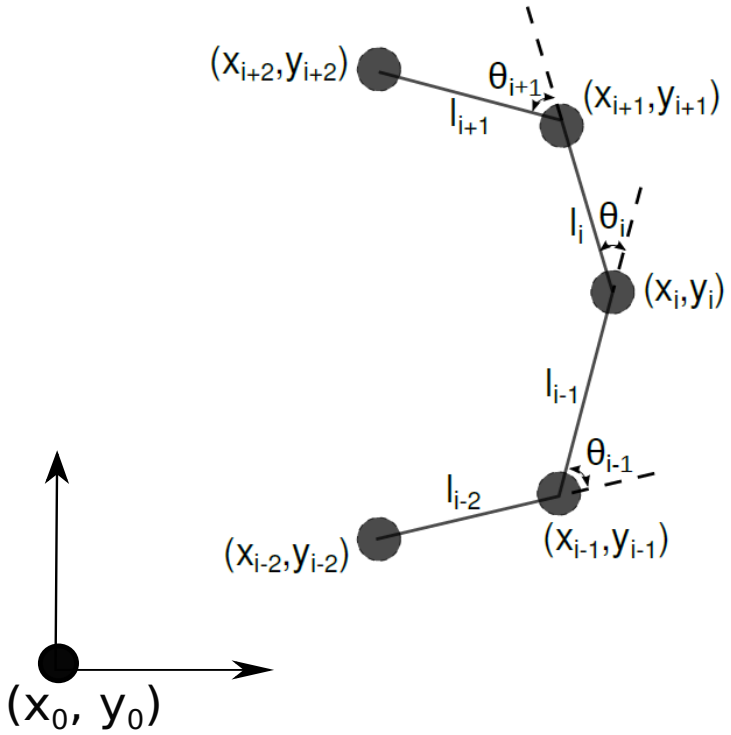

Figure 2.7: Schematic shows that co-ordinates of spring nodes used for force calculations. The origin of the system is located at x_0 and y_0, which are 0 and 0. This Figure is adopted from [Shen, 2016].

ordinates are (x_0, y_0), (x_i^0, y_i^0), and (x_{i+1}^0, y_{i+1}^0) and (x_0, y_0), (x_i, y_i), and (x_{i+1}, y_{i+1}), respectively, at time $t = 0$ and $t = t_1$ (as shown in Figure 2.7; the current configuration); x_0 and y_0 are the origin of Cartesian co-ordinate system, which are 0 and 0; and k_s is the area constant.

The bending energy is written as follows

$$E_b = \frac{1}{2} k_b \sum_{i=1}^{N} \tan^2 \left(\frac{\theta_i - \theta_i^0}{\theta_i^0} \right)^2 , \tag{2.28}$$

where k_b is the bending modulus of the spring, θ_i is (Appendix A) angle between two adjacent springs at $\mathbf{r}_i$, and θ_i^0 is the spontaneous angle (which would provide a spontaneous curvature) which is set to 0 in this thesis. The tangent of the angle is

used in Equation (2.28) in order to avoid springs folding. The force applied at $\mathbf{r}_i$ is calculated by taking the derivative of the total energy stored in the system, i.e.,

$$\mathbf{f} = -\frac{\partial(E_l + E_s + E_b)}{\partial \mathbf{r}} \,. \tag{2.29}$$

where $\mathbf{r}$ is position vector of a node i whose Cartesian coordinates are x_i and y_i. The contribution of individual forces to the total force is derived in Appendix A.

2.4 Lattice Boltzmann Method for solute field

The primary function of the RBC is to transport gases through the vascular system. In addition, RBC synthesizes and releases ATP molecules (a second messenger) to perform a plethora of cellular functions. These molecules diffuse and move through the plasma to reach the surface of the blood vessel wall, which then trigger biochemical signals. To understand how ATP distribution generates or synthesizes other molecules (such as Ca^{2+} signaling and NO availability) and change in their concentration in the vasculature, we couple fluid flow and species transport equations together. Mathematically, we solve NSEs (Equations (2.6)-(2.7)) for fluid flow and advection-diffusion-reaction equations (ADREs) for species concentrations. To leverage LBM's dependence on local information while solving NSEs, we employ LBM for the solution of ADREs with the same spirit. ADRE for any solute concentration, c, whose desired solution can be either ATP, NO or any other molecule, is given as follows,

$$\frac{\partial c}{\partial t} + \mathbf{v} \cdot \nabla c = \nabla \cdot [D(\mathbf{x}, t) \nabla c] + R(c, \mathbf{x}, t) \,, \tag{2.30}$$

where $\mathbf{v}$ is the fluid velocity, and is obtained from the LBM fluid solver; D is the diffusion coefficient and it may vary with position and time; and R is the contribution of chemical reactions and is required while dealing with molecules/ions in endothelial cells (ECs).

Let us focus on boundary conditions. The 2-D contour is parameterized by a single parameter, namely the arc length (s), and time. The membrane position is defined as $\mathbf{B}(s,t) = [X(s,t), Y(s,t)]$, where X and Y are the Cartesian components of the membrane. The local membrane velocity, which is equal to that that of adjacent fluid, is obtained (using IBM) as $\frac{\partial \mathbf{B}}{\partial t} = \mathbf{V}(\mathbf{B}, t)$. An important point is that the solute concentration is, in general, discontinuous across the membrane. Thus, on each side of the membrane the boundary values are different. Let us consider a generalized

Robin boundary conditions. Its expressions at the memrane has the form [Zhang and Misbah, 2019],

$$\alpha_1^+ c^+ + \alpha_2^+ \mathbf{n} \cdot \nabla c^+ = \alpha_3^+ \,, \tag{2.31}$$

$$\alpha_1^- c^- + \alpha_2^- \mathbf{n} \cdot \nabla c^- = \alpha_3^- \,, \tag{2.32}$$

where α_1^+, α_2^+, and α_3^+, which can be a constant or a variable, are the constants prescribed on the outer side of the membrane. Similarly, α_1^-, α_2^-, and α_3^- are constants prescribed on the inner side of the membrane. The unit normal vector pointing towards fluid is $\mathbf{n}$, and c^+ and c^- are the concentrations in the inner and outer side of the membrane, respectively. These generalized boundary condition Equations (2.31)-(2.32) can be converted to Dirichlet or Neumann boundary condition depending on the physical requirements of the problem.

We will now focus on the numerical approach (LBM) for solving Equation (2.30), subject to conditions (2.31)-(2.32). The approach to obtain the solution of Equation (2.30) is rather similar to that of fluid flow (Equation (2.1) is discretized in the LBM fluid solver, we discretize here the same equation by replacing g for f). We use D2Q5 (2-D, 5 discrete velocities, and single relaxation time) to solve Equation (2.30). The solute distribution function, g_i, is obtained in two steps, namely collision and streaming. These steps are illustrated in Figure 2.8 and are mathematically expressed as follows [Zhang and Misbah, 2019]

1. Collision step

$$g_i^\star(\mathbf{x}, t) = g_i(\mathbf{x}, t) - \frac{1}{\tau_g}\left[g_i(\mathbf{x}, t) - g_i^{eq}(\mathbf{x}, t)\right] + w_i \Delta t R \,, \tag{2.33}$$

2. Streaming step

$$g_i(\mathbf{x} + \mathbf{c}_i \Delta t, t + \Delta t) = g_i^\star(\mathbf{x}, t) \,, \tag{2.34}$$

where $\tau_g = 3D\left(\frac{\Delta t}{\Delta x^2}\right) + 0.5$ is a dimensionless relaxation time and is obtained from the Chapman-Enskog analysis. The discrete velocities and weights are given below [Zhang and Misbah, 2019]

$$w_i = \begin{cases} \frac{1}{3}, & i = 0, \\ \frac{1}{6}, & i = 1, 2, 3, 4. \end{cases} \tag{2.35}$$

$$\mathbf{c}_i = \begin{cases} (0, 0), & i = 0, \\ (\cos[i-1]\frac{\pi}{2}, \sin[i-1]\frac{\pi}{2})\frac{\Delta x}{\Delta t}, & i = 1, 2, 3, 4. \end{cases} \tag{2.36}$$

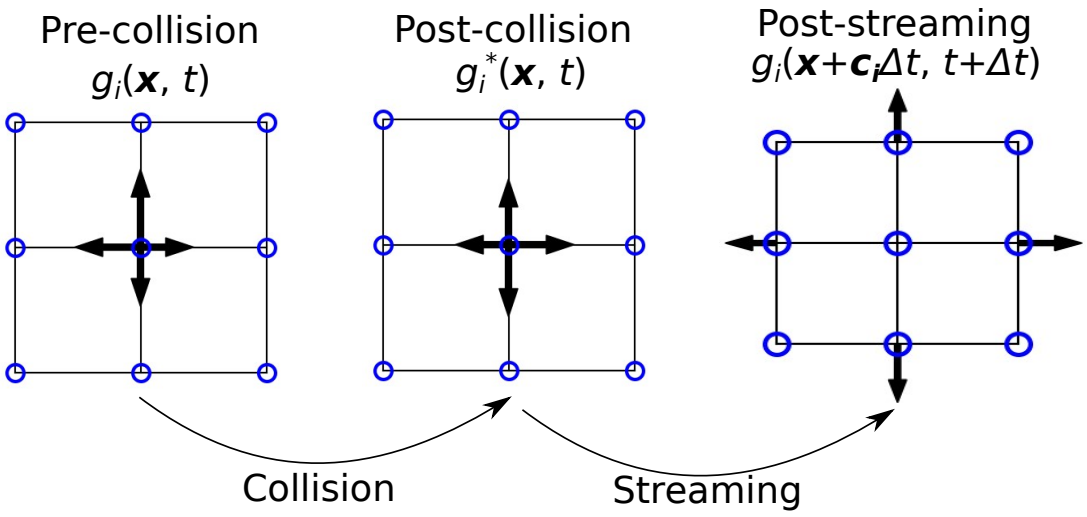

Figure 2.8: Schematic shows collision and streaming of distribution functions in the D2Q5 model. The length of the arrow indicates the strength of the distribution function.

The discrete form of the equilibrium distribution function, g_i^{eq}, is expressed as [Zhang and Misbah, 2019]

$$g_i^{\text{eq}} = w_i c \left(1 + \frac{\mathbf{c}_i \cdot \mathbf{v}}{c_s^2}\right) \tag{2.37}$$

The relationship between the physical solute concentration and the distribution function is given as

$$c = \sum_{i=0}^{4} g_i \,. \tag{2.38}$$

2.4.1 Treatment of boundary condition

We present treatment of prescribed boundary conditions such as solute concentration and its derivative along the normal direction. Note that at a particular boundary, we prescribe either the solute concentration or its derivative or the sum of the two. Once this has been done, the implementation of the general boundary condition (i.e., Robin boundary condition) is carried out by adding them together. To implement these boundary conditions for a general curved boundary, we approximate the boundary as zigzag staircase, as shown in Figure 2.9. This boundary intersects the lattice mesh segments (contains the physical boundary) in the middle of the mesh segments, as shown in Figure 2.9. This makes it possible to implement the halfway bounceback method. When dealing with boundaries, we tackle two types of boundary as in the fluid solver. The concentrations or its derivatives are prescribed on either static

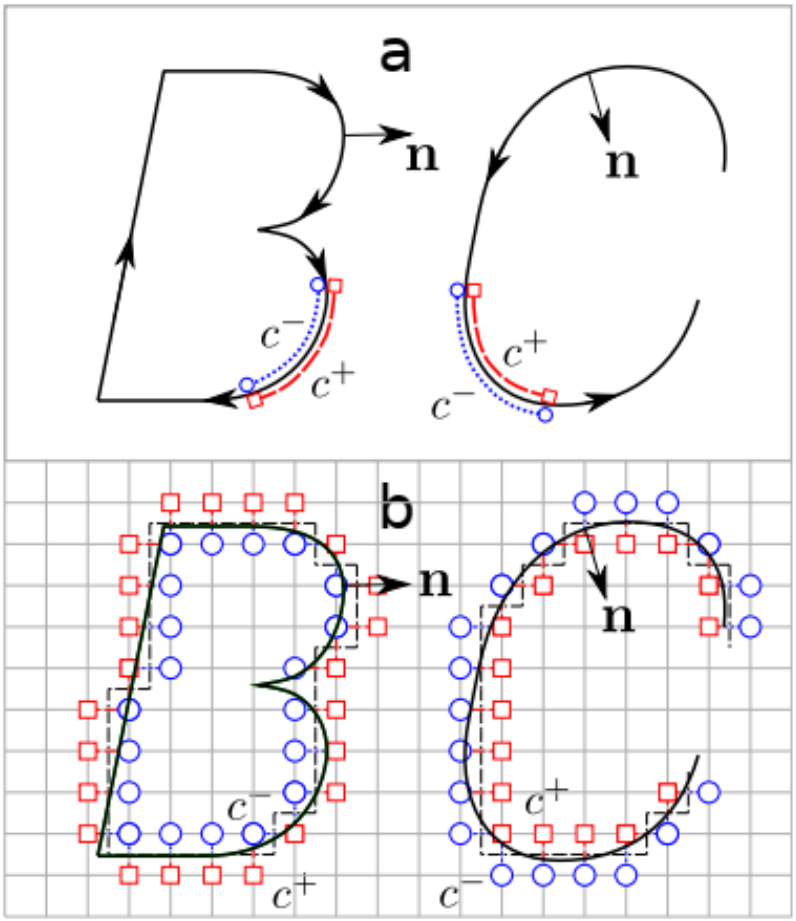

Figure 2.9: Approximation of a curved boundary and implementation of a discontinuous concentration, c across the boundary: (a) physical boundary having normal vector $\mathbf{n}$ pointing outward to the fluid and the concentration on the inner and the outer sides of the physical boundary, i.e., c^- and c^+. The arrows along the curve indicate he direction of the monotonic increase in arc length, s, and (b) the physical boundary is defined by a series of boundary pairs (a square and a circle which are located on the nearest lattice nodes from the boundary). The physical boundary is approximated as zigzag (dash-dot) lines. This Figure is adopted from [Zhang and Misbah, 2019]

boundary, such as the wall of a stationary channel or a moving boundary, such as the flow of a deformable vesicle. To handle the discontinuous concentrations across a thin boundary, we create a pair of lattice nodes for each boundary node, i.e., on the inner side and the outer side of the boundary, as shown in Figure 2.9(b).

In the simulation, we first calculate the collision distribution function, $g_i^\star$ at $\mathbf{x}$. These functions are advected to neighbouring lattice nodes by the velocity, $\mathbf{c}_i$. However, some functions at lattice nodes near to the physical boundary (which we call boundary nodes) are not advected to neighbouring nodes due to the presence of a

physical boundary, as shown in Figure 2.10. Consequently, a special treatment is required to obtain unknown populations at boundary nodes. We use bounceback method for the general boundary. Unknown functions at boundary nodes are returned after hitting the physical boundary with certain modifications, depending on the prescribed boundary conditions. However, some of them may or may not reach the boundary nodes after bounce backing the physical boundary at time, Δt. For a better understanding, let us consider the implementation of bounceback boundary condition for a prescribed zero solute concentration on a straight boundary. For the implementation for a straight boundary, the wall is located halfway between the lattice nodes. In this case the implementation is straightforward: the distribution functions return to their corresponding boundary nodes after hitting the physical boundary at time, Δt, without any modification. However, this type of implementation is not straightforward for a curved boundary.

One approach to deal with this type of boundary is to apply the Bouzidi approximation. According to Bouzidi's approximation [Bouzidi et al., 2001], the distribution functions traveling from $\mathbf{x}$ (blue hollow circle) move in the desired directions, they will return to $\mathbf{x}$ with some modifications depending on the exact location of the physical boundary from the boundary nodes if they collide with the boundary, B. If the distance between two points, $\mathbf{x}$ and P is not exactly $\Delta x/2$, the distribution functions may not reach or may overshoot $\mathbf{x}$. To determine unknown distribution functions exactly (in approximated sense) at $\mathbf{x}$, the streaming functions from neighboring lattice nodes are extrapolated or interpolated.

Bouzidi's approximation is inherently non-local due to its dependency on neighboring lattice nodes [Bouzidi et al., 2001]. In order to exploit the intrinsic local characteristics of LBM, we approximate the physical boundary as zigzag staircase boundary. In this approach, the distribution functions of the boundary node, $\mathbf{x}$ travel in their desired directions and return to the their corresponding boundary node with changes in magnitude (time, Δt) if they hit the zigzag boundary (time, $\Delta t/2$). Note that the actual boundary conditions are prescribed on the physical boundary node, P (as shown in Figure 2.10). To enforce the boundary condition accurately (in the precise second-order sense), we extrapolate concentration, α_3^{mid} from the physical boundary node, P to the zigzag node, M (as shown in Figure 2.10). This extrapolation depends on the normalized distance between the physical node and the boundary node, which is defined as $p = \frac{|\mathbf{x}_\text{P} - \mathbf{x}|}{\Delta x}$, $\mathbf{x}_\text{P}$ is the position vector of the physical boundary node (designated by P). Based on this distance, the approximate value is found at the zigzag node. Therefore, the mathematical expressions for Dirichlet or Neumann boundary

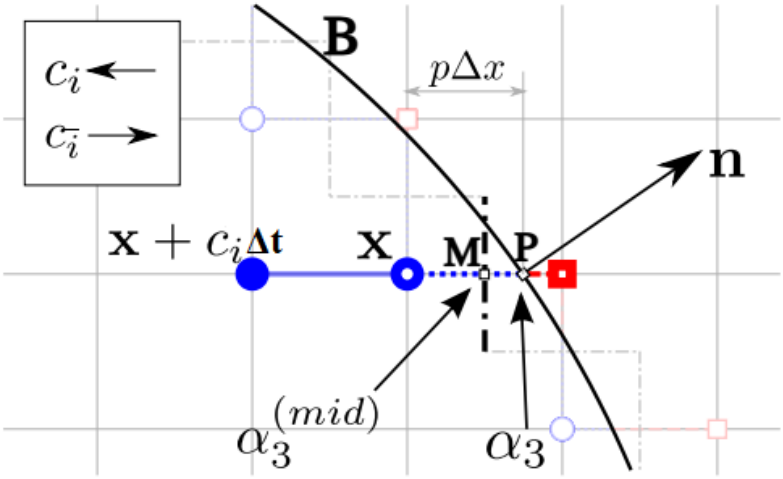

Figure 2.10: Implementation of bounceback boundary condition in a curved boundary. The physical boundary is approximated by zigzag lines (dashed-dotted line). Unknown distribution function g_i(**x**,t) is calculated at the boundary node, **x** (hollow blue circle). The concentration, α_3^{mid} is extrapolated onto the zigzag boundary (dashed-dotted line, M is the representative point) from the physical boundary concentration, α_3 (P is the representative point). c_i is the unit vector, $c_{\bar{i}}$ = - c_i. This Figure is adopted from [Zhang and Misbah, 2019]

condition at the zigzag node is given below. In addition, the detailed derivations and their accuracy are found in [Zhang and Misbah, 2019].

2.4.1.1 Dirichlet boundary condition

$$\alpha_3^{\text{mid}} = \begin{cases} \alpha_3 + \left(p - \frac{1}{2}\right)\Delta x \mathbf{c}_i \cdot \nabla c(\mathbf{x}, t), & \text{if} \quad p \le \frac{1}{2}, \\ \frac{\alpha_3}{2p} + \left(1 - \frac{1}{2p}\right) c(\mathbf{x}, t), & \text{if} \quad p > \frac{1}{2}, \end{cases} \tag{2.39}$$

where

$$\nabla c = \frac{1}{\Delta t c_s^2}\left[\mathbf{v}c - \sum_{i=0}^{4} \mathbf{c}_i g_i\right].$$

2.4.1.2 Neumann boundary condition

$$\begin{aligned} \alpha_3^{\text{mid}} &= \frac{\partial c}{\partial \mathbf{c}_{\bar{i}}} \\ &= \mathbf{c}_{\bar{i}} \cdot \mathbf{n} \left.\frac{\partial c}{\partial \mathbf{n}}\right|_{\text{M}} + \mathbf{c}_{\bar{i}} \cdot \mathbf{t} \left.\frac{\partial c}{\partial \mathbf{t}}\right|_{\text{M}} \end{aligned} \tag{2.40}$$

$$\left.\frac{\partial c}{\partial \mathbf{n}}\right|_{\text{M}} = \begin{cases} \alpha_3 + \left(p - \frac{1}{2}\right)\left(\left.\frac{\partial c}{\partial \mathbf{n}}\right|_{\mathbf{x}} - \left.\frac{\partial c}{\partial \mathbf{n}}\right|_{\mathbf{x}+\mathbf{c}_i\Delta t}\right), & \text{if} \quad p \le \frac{1}{2}, \\ \frac{\alpha_3}{2p} + \left(1 - \frac{1}{2p}\right)\left.\frac{\partial c}{\partial \mathbf{n}}\right|_{\mathbf{x}}, & \text{if} \quad p > \frac{1}{2}, \end{cases} \tag{2.41}$$

$$\left.\frac{\partial c}{\partial \mathbf{t}}\right|_{\mathrm{M}} = \left.\frac{\partial c}{\partial \mathbf{t}}\right|_{\mathbf{x}} + \frac{1}{2}\left(\left.\frac{\partial c}{\partial \mathbf{t}}\right|_{\mathbf{x}} - \left.\frac{\partial c}{\partial \mathbf{t}}\right|_{\mathbf{x}+\mathbf{c}_i\Delta t}\right) \tag{2.42}$$

2.4.1.3 Refiling unknown populations for moving boundary

As already mentioned, the solute concentration across the membrane is discontinuous due to the sharp geometric interface, while the velocity field is continuous across the membrane. When it comes to a moving boundary (such as RBC flow), after it has been treated with the desired solute boundary conditions at time, t, the membrane position is updated at time, $t + \Delta t$ thanks to IBM (shown in Figure 2.11). However, special attention is required for the newly formed lattice node (empty square in magenta colour, as shown in Figure 2.11(b)) due to flipping of lattice nodes from one side of the interface, Ω^+ to the other side, Ω^- when the membrane is advected with velocity, $\mathbf{V}$. The distribution function of the newly formed lattice node is obtained using so-called refiling procedure [Lallemand and Luo, 2003]. We used the approach proposed by Zhang et al. [Zhang and Misbah, 2019]. According to Zhang et al. [Zhang and Misbah, 2019], a first or second order linear extrapolation method is used based on the number of valid lattice nodes (empty square in red colour, as shown in Figure 2.11) in the set S^{ref} for the newly formed nodes. S^{ref} refers to a set of lattice nodes, which flipped from Ω^+ to Ω^- in time, $t + \Delta t$ (shown in Figure 2.11(b)). The refiling equation (filled square in magenta colour as shown in Figure 2.11(c)) proposed by Zhang et al. [Zhang and Misbah, 2019], is given as follows,

$$g_k = \frac{\sum_{k\in S^{\mathrm{ref}}} w_k \left[2g_k\left(\mathbf{x}+\mathbf{c}_k\Delta t, t\right) - g_k\left(\mathbf{x}+2\mathbf{c}_k\Delta t, t\right)\right]}{\sum_{k\in S^{\mathrm{ref}}} w_k}, \tag{2.43}$$

where an index k belongs to S^{ref} only if $\mathbf{x} + \mathbf{c}_k\Delta t$ and $\mathbf{x} + 2\mathbf{c}_k\Delta t$ belong to $\Omega^-(t)$ and $\Omega^-(t + \Delta t)$ at the previous and current time step. The weighting factors, w_k for lattice nodes extrapolated in the x- and y-directions are 4, while they are assigned to 1 in the diagonal directions.

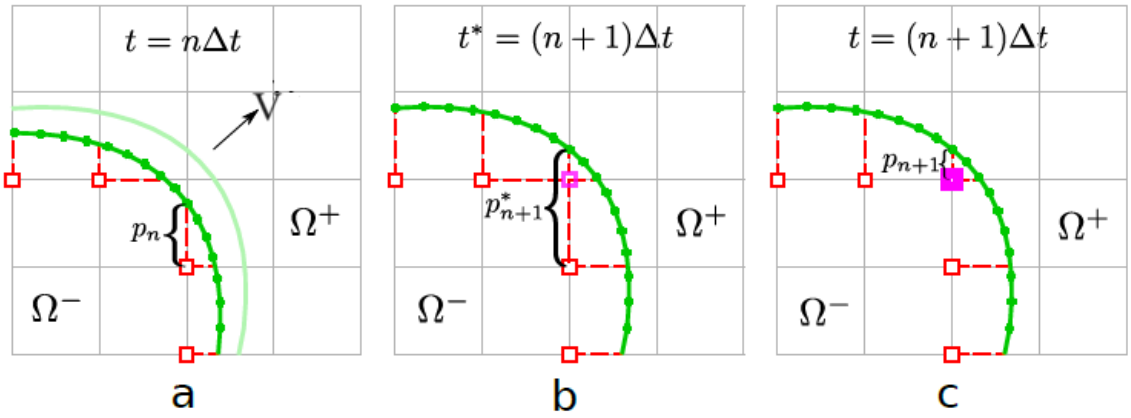

Figure 2.11: The diagram shows the refiling procedure adopted in this thesis. (a) It shows the position of the interface position at $t = n\Delta t$. (b) The updated position of the membrane at $t = (n+1)\Delta t$ after being transported with velocity, $\mathbf{V}$. Meanwhile, a new lattice node (empty square in magenta colour) is formed due to the flipping of the interface from Ω^+ to Ω^-. (c) Finally, the newly formed lattice node is refilled by extrapolating the distribution function information from neighboring lattice nodes (empty square in red colour). This figure is adopted from [Zhang and Misbah, 2019].

Chapter 3

Mathematical Modeling of Intracellular Calcium in Presence of Receptor: A Homeostatic Model for Endothelial Cell

In this chapter, we develop a homeostatic calcium model for the endothelial cell (EC). Calcium ion is omnipresent inside humans, animals, and plants. This also forms the structural basis of bone. Moreover, calcium is an important signaling element in the human body. It explicitly controls/regulates numerous cellular functions on different time-scales. The Ca^{2+} signaling pathway is activated in the EC when it responds to external stimuli called ligands, such as hormones, neurotransmitters, and mechanical stress. The detection of an external stimulus by the EC leads to an increase in the cytoplasmic Ca^{2+} concentration. There are three main types of Ca^{2+} response typically observed in experiments. (i) The first response of the EC is an increase of cytoplasmic Ca^{2+} from its physiological concentration ($\sim$ 100 nM) to a peak of $\sim$ 0.3-2 μM and then returns to a concentration that is significantly higher than its physiological concentration (more than twice the physiological concentration). (ii) In the second type of response, cytoplasmic Ca^{2+} of the EC attains a peak, then returns to its physiological concentration in the presence of ligands. This experimental result is so-called return to homeostasis, even when the ligands are still present in sufficient concentrations. The return to physiological concentration has physiological relevance. The concentration of cytoplasmic Ca^{2+} in the cell must be tightly regulated, otherwise it can become harmful or toxic. (iii) The third response is a complex oscillation whose frequency varies depending on the concentration of the stimulus. Several models have been proposed in the literature to understand Ca^{2+} signaling of the first and third responses. However, no mathematical model has been proposed to predict the return

to homeostatic concentration. In Section 3.2, we develop a mathematical model that guarantees intracellular homeostasis. In Section 3.3, it is shown that the proposed model is in agreement with experimental results. In addition, the model is also in agreement with several other well-known experimental facts (to be described later). A model novelty of the model is to account for receptor dynamics in which reaction of ligands with receptors leads to receptor desensitization. We find that receptor inactivation is an essential ingredient in maintaining Ca^{2+} homeostasis. This model will also be employed in a blood vessel (in later chapters), where the vascular wall is lined with a finite number of ECs, to understand the response of ECs to ATP released by red blood cells (RBCs) and ECs in the presence of flow.

3.1 Introduction

Ca^{2+} is a ubiquitous ion and second messenger that regulates many cellular functions ranging from exocytosis to cell proliferation occurring on different time scales [Berridge et al., 2003]. Ca^{2+} is known to directly regulate several proteins, thereby implicitly controlling many cellular functions such as gene transcription, fertilization, and arterial vasodilation [Berridge et al., 2003]. The sudden rise in cytoplasmic Ca^{2+} occurs due to the release of intracellular stored Ca^{2+} from the endoplasmic reticulum (ER), which accounts for 75% of the intracellular stored Ca^{2+} concentration [Tran et al., 2000]. Ca^{2+} is released from the ER due to the action of inositol 1,4,5-trisphosphate (IP_3) on inositol trisphosphate receptors (IP_3R) present on the ER membrane. This is preceded by a sequence of events in the plasma membrane (PM) in order to transduce the extracellular information to the second messenger IP_3.

We are interested here in intracellular Ca^{2+} dynamics in endothelial cells (ECs), which form the inner lining of all blood vessels. Ca^{2+} release from the ER of ECs may be triggered by different stimuli including shear stress [Shen et al., 1992], hormones [Sage et al., 1989], and extracellular adenosine triphosphate (ATP) [Carter et al., 1990]. The effect of ATP released by red blood cells (RBCs) on intracellular Ca^{2+} generation is particularly important because of ATP's crucial role in regulating blood flow and vascular tone [Xu et al., 2017]. RBCs release ATP under shear stress and cell deformation. ATP released by RBCs reacts with purinergic EC receptors ($P2Y_2$) (a class of membrane receptors that mediates vascular reactivity) to elicit the calcium reaction cascade in ECs. Subsequently, ECs release vasodilators such as nitric

oxide (NO), which maintains vascular tone by countering the effects of endothelium-derived vasoconstrictors, such as endothelin and angiotensin-II [Davignon and Ganz, 2004]. In addition, NO inhibits platelet adherence and aggregation, proliferation of vascular smooth muscle cells (VSMC), and leukocyte adhesion and infiltration. Thus, understanding EC Ca^{2+} kinetics is of major interest.

There is a general consensus that the calcium pathway involves three main steps: (i) reaction of a ligand with a receptor on the EC surface, (ii) generation of IP_3 due to ligand-receptor binding, and (iii) IP_3-induced channel opening on the ER membrane to release calcium from internal stores into the cytoplasm. The three main variables are thus (besides ATP) IP_3 concentration, store calcium concentration, and cytoplasmic calcium concentration, denoted, respectively, by $IP_3(t)$, $Ca_s(t)$, $Ca_c(t)$, which are all time-dependent variables. Several models are available that take into account the kinetics of these three quantities [Meyer and Stryer, 1988, Wiesner et al., 1996, Wiesner et al., 1997, Plank et al., 2006, Plank et al., 2007, Silva et al., 2007, Comerford et al., 2008, Li et al., 2015]. These models have successfully accounted for several experimental features, such as cytoplasmic Ca^{2+} peak amplitude, duration of peak, and the elevated resting Ca^{2+} concentration from its initial concentration. Additionally, some of these models have introduced several new variables into the model such as cytoplasmic Ca^{2+}-calmodulin(CaM)-activated endothelial nitric oxide synthase (eNOS) [Plank et al., 2007, Comerford et al., 2008] and transmembrane potential [Silva et al., 2007] across the PM. The authors in Refs. [Plank et al., 2007, Comerford et al., 2008] have further extended their model to include inhomogeneous distribution of ATP due to advection and diffusion and have suggested that atherosclerosis development is highly dependent on cytoplasmic Ca^{2+} concentration.

A main question is how do ECs manage to achieve intracellular homeostasis in the presence of ATP in the bloodstream. The concentration of ATP in blood plasma is maintained typically at a value of a few μM. This would mean that ECs are constantly in contact with ATP with different local ATP concentration, meaning that IP_3 would be constantly activated, not enabling the ER to be fully refilled by calcium. In addition, experiments have shown [Carter et al., 1990] that ECs produce a single calcium peak in the presence of ATP (Figure 3.1). When ATP is removed after the calcium response from the plasma and then reintroduced after a few minutes later, no calcium cellular response was observed; a response is only observed after a certain period of time (about 5-20 minutes is allowed to elapse). However, the same EC responds to a different agonist, histamine, immediately. This clearly highlights the fact of desensitization or inactivity of membrane receptors to ATP for a period

of time (as shown in Figure 3.1(d)). It is worthwhile to bring attention that most of ECs in that experiment responded to ATP (1-500 μM concentrations) with a single transient peak before returning to resting Ca^{2+} concentration. Moreover, in the same experiment, a few number of ECs have complex oscillations as well as transient peak with elevated resting Ca^{2+} concentration (as shown in Figure 3.1(b)-(c)). In addition, Felix et al. [Felix et al., 1996] observed that epithelial cells subjected to sustained stretching resulted in a transient IP_3 concentration, as shown in Figure 3.2 (a). In an independent experiment, Malli et al. [Malli et al., 2007] measured store Ca^{2+} concentration in human umbilical-vein endothelial cell (HUVEC). Under control condition, they found that in the presence of histamine store Ca^{2+} refilled to its initial concentration (shown in Figure 3.2 (b)). To ensure the source of Ca^{2+} needed to replenish store, they depolarized PM with a high K^+ concentration (130 mM) in the extracellular medium. As a result, Ca^{2+} influx through the PM is reduced, resulting in depletion of store Ca^{2+} (shown in Figure 3.2 (b)). Thus, the extracellular Ca^{2+} is needed to refill the store Ca^{2+} in the presence of an agonist.

In literature [Meyer and Stryer, 1988, Dupont and Goldbeter, 1993, Atri et al., 1993, Shen and Larter, 1995, Dupont and Erneux, 1997, Borghans et al., 1997, Marhl et al., 2000, Kummer et al., 2000, Schuster et al., 2002, Politi et al., 2006], most of Ca^{2+} models have been developed to understand the mechanism behind the cytoplasmic Ca^{2+} oscillations to agonists in various cells. These Ca^{2+} oscillations are generated due to two main pathways: (i) the participation of cytoplasmic Ca^{2+} in activating or deactivating the IP_3R channels in the presence of constant IP_3 concentration and (ii) Ca^{2+}-induced IP_3 generation and degradation due to positive or negative effects of rising cytoplasmic Ca^{2+} concentration. Furthermore, certainly, another way of possible Ca^{2+} oscillation is due to the phosphorylation and dephosphorylation of surface receptors by the protein kinase C (PKC), which is either activated due to the rising of diacylglycerol (DAG) concentration [Dupont et al., 2011] or both DAG and cytoplasmic Ca^{2+} [Cuthbertson and Chay, 1991, Wang et al., 2007] concentrations. Thus, the essential ingredients in these models to have oscillation must contain at least a downstream positive or negative feedback pathway which could affect the upstream biochemical reactions. Additionally, these models can be considered as a homeostatic model if all primary variables oscillate about their resting concentrations.

Calcium evolution in time is not always oscillatory in nature. For example, in in most ECs a single calcium peak is observed in the presence of agonist (e.g., ATP) [Carter et al., 1990]. Several attempts [Wiesner et al., 1996, Plank et al., 2006, Silva et al., 2007] have been made to understand the occurrence of a single peak

of Ca^{2+}. Because of the strategic location of ECs in vascular wall and its functions to maintain vascular homeostasis, the modeling of Ca^{2+} in ECs require much more attentions to understand the detail kinetics of the Ca^{2+} dynamics. Several attempts have been made in past years to develop and understand the single peak cytoplasmic Ca^{2+} dynamics without including the surface receptor dynamics into their model [Wiesner et al., 1996, Plank et al., 2006, Silva et al., 2007]. These models have basically been focused on the cytoplasmic Ca^{2+} peak as observed in experiments, and able to reproduce the homeostasis only in the absence of agonist concentration, but not when agonist is still present (like ATP in the blood stream). However, when these models are tested in the presence of agonists, a major deviation from post-response homeostatic conditions is revealed for cytoplasmic Ca^{2+}, as well as for store Ca^{2+}, and IP_3. These facts, as well as the above experimental observations according to which cells do not respond to agonists after their immediate reintroduction [Carter et al., 1990] may point to the fact that membrane receptors activation/deactivation can play a significant role. Along this line some authors [Lemon et al., 2003] proposed a detailed ligand-activated receptor dynamics model in which they considered a closed cell model. This model was able to produce a robust transient peak. However, the post-response plateau of Ca^{2+} is found to be higher that the resting Ca^{2+} concentration (i.e., lack of homeostasis). This is due to positive feedback of cytoplasmic Ca^{2+} on IP_3 generation (see below). In addition, this model considered some simplifications (i) a closed cell model was adopted, meaning that there is no exchange with the external environment. However, the refilling of store Ca^{2+} [Putney Jr, 1986, Putney et al., 2001] must be achieved thanks to Ca^{2+} coming from the extracellular environment and (ii) the phosphorylated receptors, free surface receptors which are phosphorylated due to the binding of ligands, were unable to recycle to free receptors when the ligands were washed out from the plasma. It is noteworthy to mention that we are exclusively aimed to develop a robust single Ca^{2+} peak homeostatic model.

Another model [Cuthbertson and Chay, 1991] also took into account the phosphorylation and dephosphorylation of G-proteins and free surface receptors (due to the negative feedback from the PKC enzyme activated by the action of both DAG and cytoplasmic calcium). The results obtained from this model, after mimicking agonist washing out from the plasma, are as follows: (i) the Ca^{2+} response from the cell was immediate with the same magnitude when the ligands were reintroduced again just after the occurrence of the calcium peak (1 to 50 seconds). This differs from experimental observations showing that a cell takes a minimum of 5 minutes to several hours to express a full response [Carter et al., 1990, Garrad et al., 1998] and (ii) the number

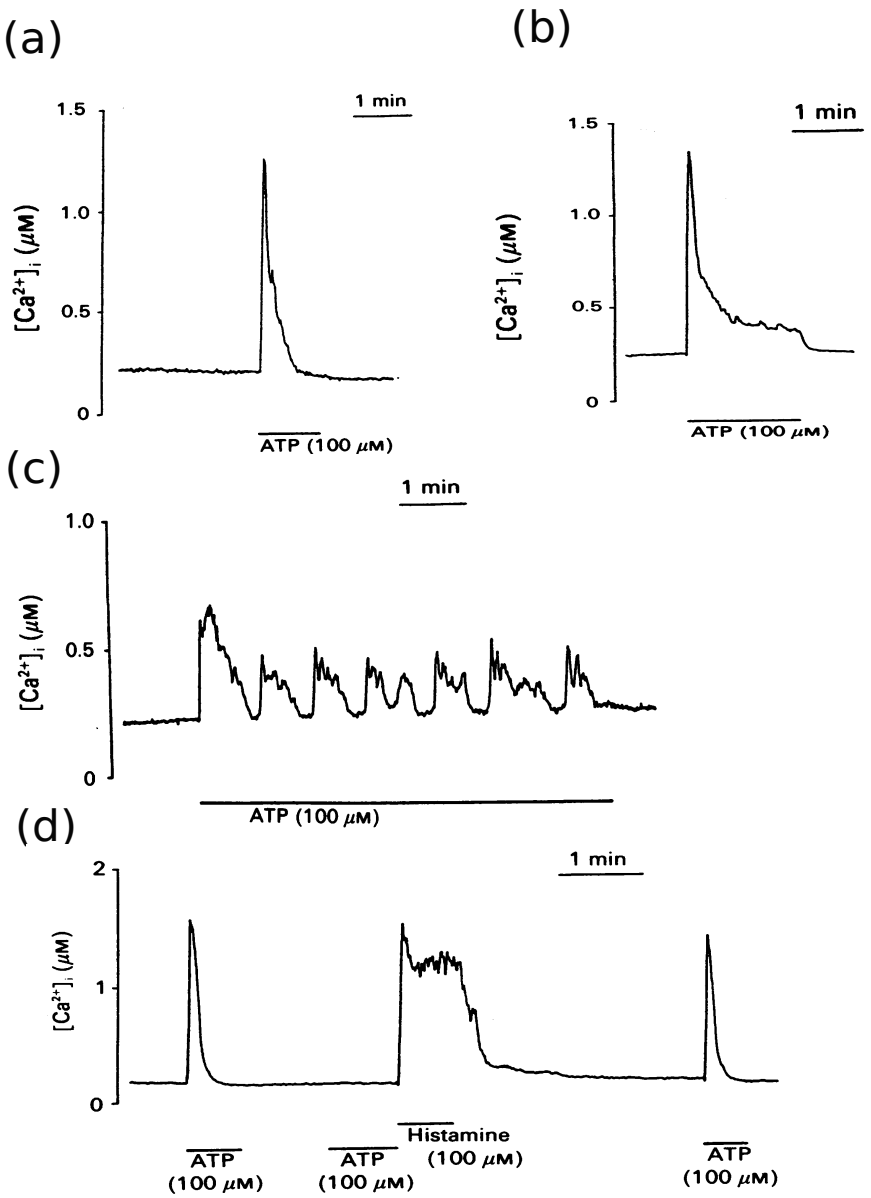

Figure 3.1: Experimental results showing the cytoplasmic Ca^{2+} concentration (or intracellular calcium $[Ca^{2+}]_i$) in a single human umbilical-vein endothelial cell (HUVEC). (a), (b), and (c) show three distinct responses from HUVEC when it is subjected to ATP (100 μM) for 1 min. (d) shows intracellular Ca^{2+} when HUVEC is sequentially stimulated with ATP (< 1 min; dose-1), ATP (2 min after dose-1; dose-2), histamine (immediately after dose-2; dose-3), and ATP (5 mins after dose-3; dose-4) [Carter et al., 1990].

of free receptors do not reach initial concentration (concentrations of free receptors prior to ligands application) even after a quite long simulation time. We expect that under physiological conditions the phosphorylated receptors must be recycled to their initial concentration when ligands are removed from the plasma. Inspired by these

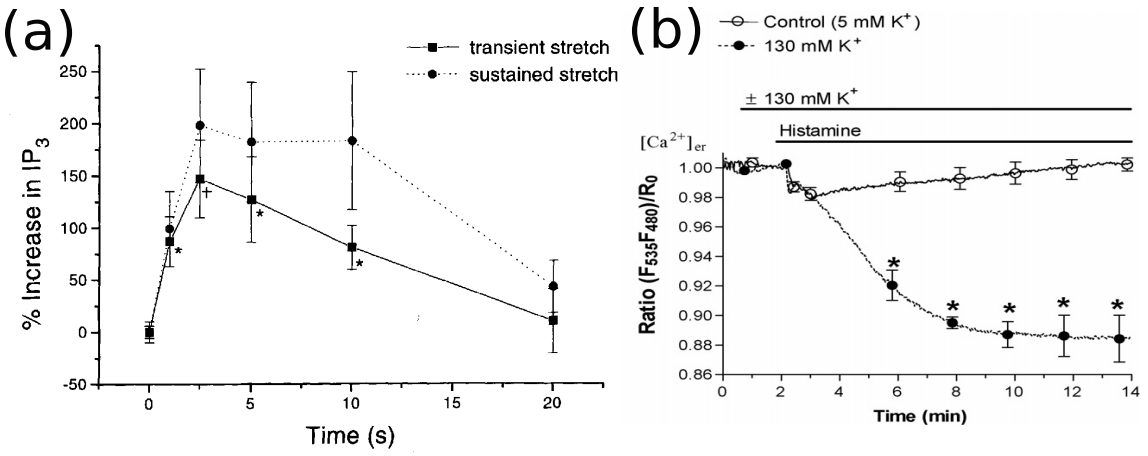

Figure 3.2: Figure shows the results of two different experiments: (a) Percentage increase in inositol trisphosphate concentration (IP_3) from its basal concentration when epithelial cells are stretched transiently or sustained way [Felix et al., 1996] and (b) endoplasmic reticulum Ca^{2+} concentration ($[Ca^{2+}]_{er}$) in normalized measured experimental unit when HUVEC is stimulated with sustained histamine in two different conditions 5 mM K^+ (control condition) and 130 mM K^+ [Malli et al., 2007].

models, we propose a further development in order identify how recycling of receptors can be incorporated, and how a time delay of cell response, after reintroducing agonist just after calcium peak, can be modeled. Our improved version is able to provide answers in favor of the above experimental facts. We will make several direct comparisons with experimental results, showing a reasonably good agreement with the proposed model.

3.2 Method and Model Development

3.2.1 Main ingredients of the model

In this section, we will develop a minimal single EC Ca^{2+} dynamics model capable of reproducing several experimental results. A major issue accounted for this model is how an ECs can maintain Ca^{2+} homeostasis in the presence of a constant ATP supply. Since ATP is constantly released by RBCs in blood, the EC might be expected to continuously produce cytoplasmic Ca^{2+} in response to this agonist. At the same time, the EC is expected to restore intracellular Ca^{2+} homeostasis in order to protect its organelles from the toxic effects of an elevated cytoplasmic Ca^{2+} concentration. Indeed, the EC develops a protective mechanism by phosphorylating ATP-bound receptors, which means that these receptors are no longer able to activate G-proteins,

which are membrane ATP sensors. This thus leads to a decline in IP_3 generation, allowing the EC to restore intracellular homeostasis. Inspired by the study of [Lemon et al., 2003] on receptor kinetics, we develop a modified version to study membrane receptor dynamics. When coupled to Ca^{2+} and IP_3 dynamics, this model accounts for several documented responses of ECs to ligands such as ATP.

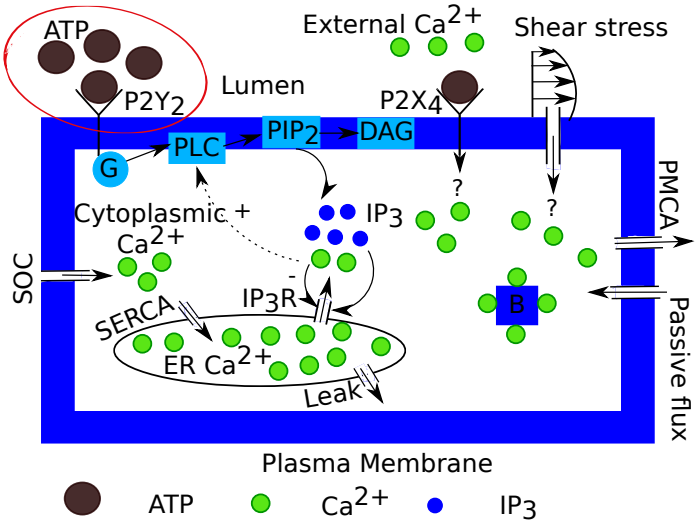

Figure 3.3: Schematic shows the Ca^{2+} homeostasis in the EC, where abbreviations are, ATP: adensoine triphosphate, G: G-protein, PLC: phospholipase-C, PIP_2: phosphatidylinositol 4,5-bisphosphate, DAG: diacylglycerol, IP_3: 1,4,5-trisphosphate, IP_3R: 1,4,5-trisphosphate receptor, SOC: store-operated channel, SERCA: sarco/endoplasmic reticulum Ca^{2+}-ATPase, PMCA: plasma membrane Ca^{2+}-ATPase, B: buffer proteins. Question marks (?) refer to the influx of extracellular Ca^{2+} into cytoplasm, due to the action of ATP on $P2X_4$ channel and shear stresses due to blood flow, that are not fully understood in experiments.

3.2.2 G-protein cascade

The first stage of calcium generation starts with the ATP reacting with the so-called purinergic (designated as $P2Y_2$, see Figure 3.3) receptors on the EC surface. This elicits a cascade of reactions. A key player is the G-protein ($P2Y_2$ is a G-protein-coupled receptor), which transmits the signal from the outside to the inside of the EC. G-proteins are deactivated due to the hydrolysis of guanosine triphosphate (GTP) into guanosine diphosphate (GDP). So, the rate of change of G-protein concentration can be expressed as,

$$\frac{d[G]}{dt} = k_a\left(\delta + \rho_r\right)\left([G_t] - [G]\right) - k_d[G]\,, \tag{3.1}$$

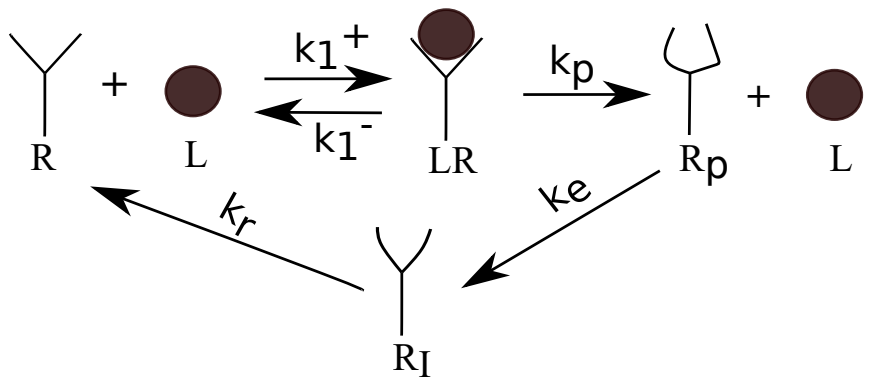

Figure 3.4: The red color enclosure in Figure 3.3 represents the receptor and ligand binding dynamics. Free receptor, R, binds with a ligand, L, reversibly and forms a ligand-receptor complex, LR. This complex is irreversibly converted into the phosphorylated receptor, R_p and ligand, L and eventually, R_p converts into internalized receptor, R_I and then R.

where $[x]$ represents the concentration of a chemical species x and k_a and k_d are the G-protein activation and deactivation rate constants, respectively. The ligand (ATP) concentration is denoted as $[L]$ and that of free receptors is denoted by $[R]$. Once ATP reacts with receptors, it gives rise to the LR complex whose concentration is denoted as $[LR]$. $[G_t]$ is the total concentration of G-protein molecules, and δ is the G-protein intrinsic activity parameter, i.e., R can independently activate G-proteins without binding to ligands. It is reported in several experiments that G-protein is able to sense and transduce shear stress-induced signals to the cytoplasm [Chachisvilis et al., 2006, Storch et al., 2012]. This explains the reason behind a non-zero basal IP_3 concentration in the cytoplasm as reported by [Felix et al., 1996] and [Nollert et al., 1990] in the absence of ligands (ATP); see below. It is important to stress that the ATP produced by ECs due to shear stress could contribute to basal IP_3 concentration. This formation of IP_3 is possible only when ATP molecules bind with free receptors.

The investigation of mechanisms that play a significant role in maintaining the basal IP_3 concentration still remains an open area. Further experiments would be needed in order to better clarify this issue. Moreover, there is no quantitative data in literature reporting on the amount of ATP released at basal shear stress. It can be perceived from the works in [Chachisvilis et al., 2006,Storch et al., 2012] that the shear induced basal IP_3 plays a vital role in maintaining basal IP_3 concentration without association of ligand-receptor. The ratio of receptors bound to ligands to the total number of $P2Y_2$ receptors is ρ_r (which will be related to receptor and ligand concentration; see Subsection 3.2.4 for more details). This is for the moment viewed as a constant before including below the receptor dynamics into the model. We can simplify Equation (3.1) by assuming that $[G]$ activation and deactivation is governed by fast kinetics [Bennett et al., 2005], so that

$$[G] = [G_t]\frac{\rho_r + \delta}{\rho_r + \delta + K_g} \equiv [G_t]\lambda\,, \tag{3.2}$$

where $K_g = k_d/k_a$ and $\lambda = \frac{\rho_r+\delta}{\rho_r+\delta+K_g}$. A remark is in order. Due to difference in the time scale of G-protein activation and deactivation, this approximation overestimates the IP_3 peak (see Appendix B, Figure S2). However, the trend remains similar to the results of the full model, i.e., without adiabatic elimination of G protein kinetics. This lends support to the fact the adiabatic elimination is reasonable. Additionally, GTP bound G-protein activates the PLC-enzyme, which then forms the IP_3 molecules by splitting PIP_2 molecules. The rate of change of IP_3 concentration, $[IP_3]$, can be defined as,

$$\frac{d\,[\mathrm{IP_3}]}{dt} = q_{\mathrm{gen}} - q_{\mathrm{deg}}\,, \tag{3.3}$$

where q_{gen} and q_{deg} are the IP_3 generation and degradation fluxes, respectively, which are defined below. There is a positive feedback from Ca^{2+} released from the ER, which triggers an increase in IP_3 formation [Meyer and Stryer, 1988], so that

$$q_{\mathrm{gen}} = \gamma\lambda\frac{[Ca_c]}{K_1 + [Ca_c]}\,, \tag{3.4}$$

with $\gamma = \alpha[G_t][(\mathrm{PIP_2})_t]/(\mathrm{N_A}V_{\mathrm{EC}})$, where, the denominator containing the product of $\mathrm{N_A}$ and V_{EC} allows to convert IP_3 generation in molar (M or mole/ltr). The entire cascade of reactions starting from G-protein activation to IP_3 generation is lumped into a single flux term given by Equation (3.4). The effective signal gain parameter is α, $\mathrm{N_A}$ is Avogadro number, V_{EC} is the EC volume, and $[(\mathrm{PIP_2})_t]$ is the total number of phosphatidylinositol 4,5-bisphosphate (PIP_2) molecules. We here assume that there is no change in the concentration of PIP_2 molecules, i.e., splitting

and replenishing of PIP_2 molecules is regulated by fast reactions [Bennett et al., 2005]. This means that the effect of G-proteins and $[(PIP_2)_t]$ enters as an effective multiplicative coefficient in this flux (in γ). The dissociation constant between the Ca^{2+} and PLC-enzyme is K_1 and is considered as an important parameter for the cytoplasmic Ca^{2+} oscillations [Meyer and Stryer, 1988]. It turns out that keeping $K_1 \neq 0$ for ECs (single peak model) precludes return to homeostasis. Based on this observation, we will in the following set $K_1 = 0$. $[Ca_c]$ is the cytoplasmic Ca^{2+} concentration. The rate of IP_3 degradation due to the formation of IP_2 or IP_4 by kinases or phosphatases is given by

$$q_{\text{deg}} = k_2 \left[\text{IP}_3\right] . \tag{3.5}$$

where k_2 is the IP_3 degradation rate.

3.2.3 Intracellular calcium

The cytoplasm of an EC is a highly complex structure due to the complex shape of organelles and their arrangement with in the cytoplasm. The governing equation for the cytoplasmic Ca^{2+} concentration, $[Ca_c]$, is obtained by balancing the fluxes across the PM and ER membrane as shown in Figure 3.5 and is given by [Plank et al., 2006]

$$\frac{d\left[Ca_c\right]}{dt} = \beta \left(q_{\text{rel}} - q_{\text{serca}} + q_{\text{leak}} + q_{\text{soc}} + q_{\text{in}} - q_{\text{pmca}}\right) , \tag{3.6}$$

where β is defined as a buffer factor for immobile buffer proteins only. The expression for β is obtained by assuming that the reaction between the buffer proteins and cytoplasmic Ca^{2+} is faster than the Ca^{2+} flux rates across the PM and ER membranes (detailed derivation and justification are given in Appendix B). Therefore, following [Wagner and Keizer, 1994], we derive the expression for β as

$$\beta = \left\{ 1 + \frac{\left[B_t\right] \frac{k_7}{k_6}}{\left(\frac{k_7}{k_6} + \left[Ca_c\right]\right)^2} \right\}^{-1} , \tag{3.7}$$

where k_6 and k_7 are the association and dissociation rates between the buffer proteins and cytoplasmic Ca^{2+}, and $[B_t]$ is the total buffer protein concentration, a constant. The fluxes q_{rel}, q_{serca}, q_{leak}, q_{soc}, q_{in}, and q_{pmca} used in Equation (3.6) are, respectively, the rates of change in the cytoplasmic Ca^{2+} concentration due to release through the IP_3R, uptake from the ER, a passive leak from the ER, ER-depleted influx from the extracellular space, a passive influx from the extracellular space, and efflux by the PM pump. The individual expressions for these fluxes are defined below. However,

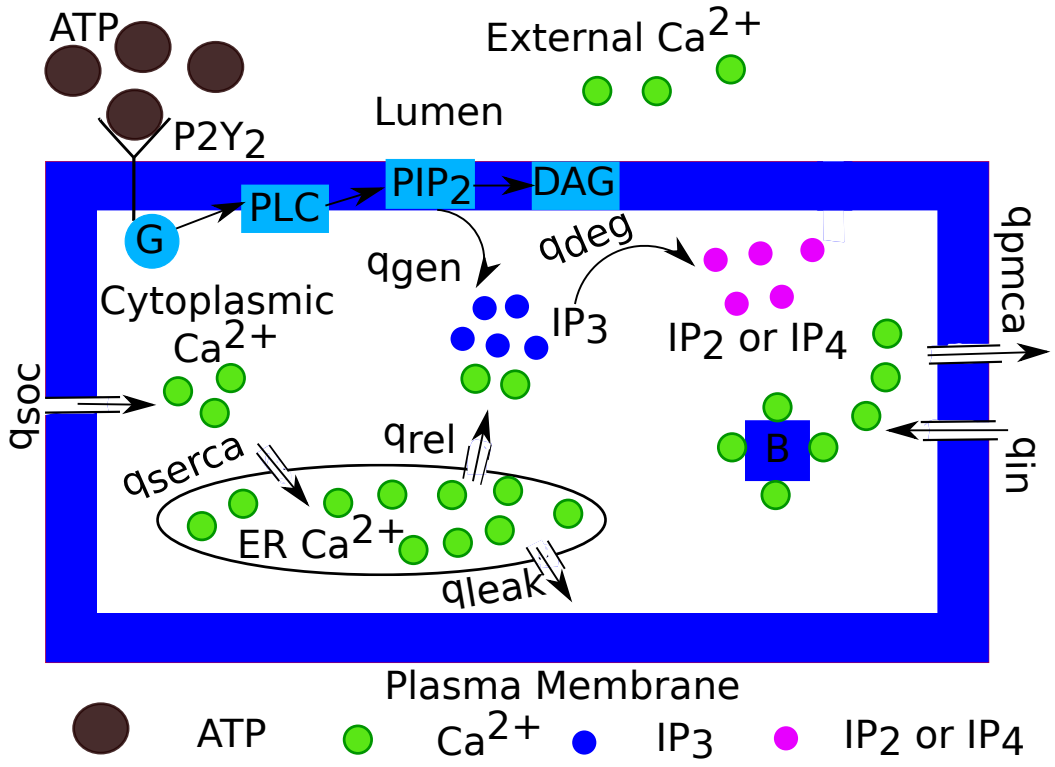

Figure 3.5: Intracellular fluxes across the plasma and ER membranes. Detailed definitions of these fluxes are given in the text.

the expression for q_{in} is given in Subsection 3.2.6, and is physically interpreted as the Ca^{2+} influx required to maintain Ca^{2+} homeostasis in the absence of ATP. The IP_3-induced Ca^{2+} releasing from the ER is defined as

$$q_{\text{rel}} = k_3 \frac{[\text{IP}_3]^3}{K_2^3 + [\text{IP}_3]^3} \frac{K_{i,Ca_c}^3}{[Ca_c]^3 + K_{i,Ca_c}^3} Ca_s \,, \tag{3.8}$$

where k_3 is the Ca^{2+} release rate from the ER, and K_2 is the IP_3 concentration at which half of the IP_3R sites are occupied by IP_3 molecules; K_{i,Ca_c} is the cytoplasmic Ca^{2+} for half-maximal inhibition of IP_3R, and $[Ca_s]$ is the ER Ca^{2+} concentration. Equation (3.8) states that the Ca^{2+} release rate from the ER is due to binding of three IP_3 molecules to the IP_3R. Moreover, several physiological IP_3R models are available in the literature in which both positive and negative effects of the cytoplasmic Ca^{2+}, i.e., calcium-induced-calcium-release (CICR) and calcium-induced-calcium-inhibition on IP_3R activation, are considered (for details see [Dupont et al., 2016]). However, here we have only considered the latter because the effects of the former are not found in vascular ECs as modeled in [Silva et al., 2007]. In particular, we assume that the

opening and closing of IP_3R channels are instantaneous. The Ca^{2+} uptake rate from the cytoplasm into the ER is defined by

$$q_{\text{serca}} = k_4 \frac{[Ca_c]^2}{K_3^2 + [Ca_c]^2}\,, \tag{3.9}$$

where k_4 is the Ca^{2+} uptake rate by sarco/endoplasmic reticulum Ca^{2+}-ATPase (SERCA) and K_3 is the Michaelis-Menten constant. The SERCA pumps cytoplasmic Ca^{2+} into the ER by using energy from ATP. The rate of passive leak of Ca^{2+} from the ER is assumed to be due to the defects in the ER membrane or may be due to the fixed capacity of ER.

$$q_{\text{leak}} = k_5[Ca_s]\,, \tag{3.10}$$

where k_5 is the Ca^{2+} leak rate from the ER. The linear dependence on $[Ca_s]$ have been verified to not be a limitation (taking for example a quadratic form, as in [Plank et al., 2006], leaves our results practically unchanged; the k_5 value will have a different dimension for the linear model adopted here; see Table 3.1).

In [Putney et al., 2001], it has been reported that a channel is only activated when the ER Ca^{2+} concentration gets depleted due to IP_3-dependent Ca^{2+} release from the ER and is termed store-operated calcium (SOC). SOC is considered one of the important channels for ER Ca^{2+} replenishment, allowing the extracellular Ca^{2+} flux into the cytoplasm. The mechanism of SOC activation is now well understood. Due to the depletion of the ER Ca^{2+}, a pathway is formed because of the interaction between the stromal interaction molecules (STIMs) and ORAIs in the ER and plasma membrane, respectively [Dupont et al., 2016]. It is noteworthy to mention that these channels are switched off, STIMs and ORAIs get separated, i.e., calcium influx is zero, when the store is completely refilled with Ca^{2+} [Thillaiappan et al., 2019, Putney Jr, 1986]. We will see that this model reproduces the Ca^{2+} homeostasis both in the presence and absence of IP_3. Thus, the rate of change of the cytoplasmic Ca^{2+} due to the SOC is written as [Su et al., 2011]

$$q_{\text{soc}} = k_{\text{soc}} \frac{1}{\left(1 + \frac{[Ca_s]}{K_{\text{soc}}}\right)^n} \left([Ca_{\text{ex}}] - [Ca_c]\right) \left([Ca_s]\,(0) - [Ca_s]\right)\,, \tag{3.11}$$

where n is a constant, k_{soc} is the maximal Ca^{2+} influx rate through the SOC, and K_{soc} is the ER Ca^{2+} for the half-activation of the SOC. $[Ca_{\text{ex}}]$ and $[Ca_s]\,(0)$ are the external and initial ER Ca^{2+} concentrations (the homeostatic one), respectively. Equation (3.11) includes three important experimental observations: (1) the probability of SOC opening, (2) the fact that the amount of Ca^{2+} influx depends on the concentration

gradient across the PM, and (3) the observation of no Ca^{2+} influx at resting conditions. The proposed model for SOC [Su et al., 2011] was modified by adding the last term in Equation (3.11) to satisfy the third observation. q_{in} is the passive influx of Ca^{2+} due to defects in the PM, a constant whose expression is obtained in Subsection 3.2.6 by satisfying the EC homeostasis condition. Note that because $[Ca_{\text{ex}}] \gg [Ca_c]$ under physiological conditions, in what follows we will make the approximation that $[Ca_{\text{ex}}] - [Ca_c] \simeq [Ca_{\text{ex}}]$.

The cytoplasmic Ca^{2+} efflux rate from the cytoplasm into the extracellular space is defined as

$$q_{\text{pmca}} = k_8 \frac{[Ca_c]^2}{K_4^2 + [Ca_c]^2} , \tag{3.12}$$

where k_8 is the maximal Ca^{2+} efflux rate through plasma membrane Ca^{2+}-ATPase (PMCA), and K_4 is the cytoplasmic Ca^{2+} concentration for the half-sites of PMCA. Note that the second power of $[Ca_c]$ is used in Equations (3.9) and (3.12) because both of these pumps transfer two Ca^{2+} ions from the cytoplasm to the ER and extracellular space, respectively, by consuming one ATP.

Similarly, the rate of change of Ca^{2+} in the ER, $[Ca_s]$, is obtained by balancing the fluxes across the ER membrane, namely

$$\frac{d\,[Ca_s]}{dt} = v_r \left(q_{\text{serca}} - q_{\text{rel}} - q_{\text{leak}}\right) , \tag{3.13}$$

where v_r is a volume scaling factor, i.e., the ratio between the cytoplasm and the ER volumes. Note that the three fluxes appearing above are the same fluxes that appear in Equation (3.6). This results simply from mass conservation (exchange between ER and the rest of cytoplasm).

3.2.4 Receptor dynamics

When solving Equations (3.3), (3.6), and (3.13) (by using the different fluxes introduced above) for a constant value of ρ_r, we obtained similar results for calcium pulses as in [Plank et al., 2006] and other similar model [Li et al., 2015] (see Figure B.1 in Appendix B). One important point is that the final steady state concentration of IP_3, cytoplasmic and ER Ca^{2+} turn out to be significantly different from their physiological concentration. In particular, the ER is not refilled, and IP_3 remains at a significantly higher level than its initial value (see Figure B.1 in Appendix B). In principle, one expects physiological systems to ensure homeostasis, i.e., different concentrations ultimately revert to their initial values before the application of a stimulus. By taking into account receptor dynamics, we can propose a model that can capture

the essential expected physiological response of calcium kinetics. The model is based on the observation that receptors R exist in 4 different states: (i) unbound receptor, R, (ii) bound receptor, LR (ligand-receptor complex), (iii) phosphorylated receptor, R_p, and (iv) internalized receptor, R_I as shown in Figure 3.4 [Lemon et al., 2003]. One important assumption here is that phosphorylated receptors are no longer able to respond to the external ligands. Moreover, it is worthwhile to mention that the increase in phosphorylated receptor concentration leads to reduction in IP_3 generation, thereby the release of Ca^{2+} from the ER. However, the actual reason for receptor phosphorylation (or desensitization) is still poorly understood. The rate of change of the total unphosphorylated receptor concentration, $[R_s] = [R] + [LR]$ becomes (this is derived using the fast kinetics approach),

$$\frac{d[R_s]}{dt} = k_r[R_t] - \left(k_r + k_p \frac{[L]}{K_r + [L]}\right)[R_s] - k_r[R_p]\,, \tag{3.14}$$

where $[R_t] = [R_s] + [R_p] + [R_I]$ is the total receptor concentration. The terms proportional to k_r sum up to $k_r[R_I]$, implying that the internalized receptor can be recycled into membrane receptors (R or LR). We have summed up $[R]$ and $[LR]$ into a single term, $[R_s]$, owing to the fact that these two unphosphorylated receptors are responsible for the activation of G-proteins and subsequently the formation of IP_3 molecules. k_r and k_p are the rate constants at which R_I is recycled to R and LR phosphorylated to R_p, respectively. $K_r = k_1^-/k_1^+$ is the unphosphorylated receptor dissociation constant, where k_1^- and k_1^+ are respectively the forward and backward constants for the reversible reaction between L and R. Similarly, using the law of mass action, we can deduce the equation for the rate of change of the phosphorylated receptor concentration, $[R_p]$, i.e.,

$$\frac{d[R_p]}{dt} = k_p \frac{[L][R_s]}{K_r + [L]} - k_e[R_p]\,. \tag{3.15}$$

This model is inspired by that of Lemon et al. [Lemon et al., 2003], which we have enriched by the fact that phosphorylated receptors R_p are converted into R in the absence of L. For that purpose, we have assumed that LR is irreversibly phosphorylated into R_p and subsequently R_p is internalized and recycled to R at rates k_e and k_r. This fact is witnessed in the second term of Equation (3.15), i.e., in the absence of ligand, $[L] = 0$, the rate of change of unphosphorylated receptor, R_p, is only dependent on the second term.

In Subsection 3.2.2, we have assumed that ρ_r is a constant because we have implicitly assumed that the concentration of LR remains constant. When taking into

account desensitization, the concentration of LR is no longer a constant as we know that LR gets phosphorylated into R_p with time. The expression of ρ_r can be obtained by assuming that the formation of LR complexes follow Michealis-Menten kinetics (rapid equilibrium approximation, i.e., dissociation of $[LR]$ to $[L]+[R]$ is faster than the formation of $[R_p]$) [Michaelis et al., 1913] and using $[R_s] = [R]+[LR]$. This allows us to determine, ρ_r, the ratio of receptors bound to ligands to the total number of $P2Y_2$ receptors (details are given in the last Section of Appendix B)

$$\rho_r = \frac{[R_s][L]}{[R_t](K_r + [L])}$$

.

3.2.5 Summary of Governing Equations

Along with Equations (3.14) and (3.15), we present the expanded form of Equations (3.3), (3.6), and (3.13) by substituting the expressions for the fluxes mentioned in Subsections 3.2.2 and 3.2.3. These equations are

$$\frac{d[R_s]}{dt} = k_r[R_t] - \left(k_r + k_p \frac{[L]}{K_r + [L]}\right)[R_s] - k_r[R_p]\,, \tag{3.16}$$

$$\frac{d[R_p]}{dt} = k_p \frac{[L][R_s]}{K_r + [L]} - k_e[R_p]\,, \tag{3.17}$$

$$\frac{d[\mathrm{IP_3}]}{dt} = \gamma\lambda \frac{[Ca_c]}{K_1 + [Ca_c]} - k_2[\mathrm{IP_3}]\,, \tag{3.18}$$

$$\begin{aligned}\frac{d[Ca_c]}{dt} = &\left\{1 + \frac{[B_t]\,\frac{k_7}{k_6}}{\left(\frac{k_7}{k_6} + [Ca_c]\right)^2}\right\}^{-1} \\ &\left\{\left(k_3 \frac{[\mathrm{IP_3}]^3}{K_2^3 + [\mathrm{IP_3}]^3} \frac{K_{i,Ca_c}^3}{[Ca_c]^3 + K_{i,Ca_c}^3} + k_5\right)[Ca_s]\right. \\ &- k_4 \frac{[Ca_c]^2}{K_3^2 + [Ca_c]^2} \\ &+ k_{\mathrm{soc}} \frac{1}{\left(1 + \frac{[Ca_s]}{K_{\mathrm{soc}}}\right)^n}\ [Ca_{\mathrm{ex}}]\left([Ca_s](0) - [Ca_s]\right) \\ &\left. + q_{\mathrm{in}} - k_8 \frac{[Ca_c]^2}{K_4^2 + [Ca_c]^2}\right\}\,,\end{aligned} \tag{3.19}$$

$$\frac{d[Ca_s]}{dt} = -v_r \left\{ \left(k_3 \frac{[IP]^3}{K_2^3 + [IP]^3} \frac{K_{i,Ca_c}^3}{[Ca_c]^3 + K_{i,Ca_c}^3} + k_5 \right) [Ca_s] - k_4 \frac{[Ca_c]^2}{K_3^2 + [Ca_c]^2} \right\} . \tag{3.20}$$

Note the right hand side of the last equation contains (with opposite signs) the same first three terms in the Equation (3.19) due to mass conservation (these terms express the exchange between the ER and the rest of the cytoplasm).

3.2.6 Homeostasis concentration

The homeostatic concentration in our simulation corresponds to the initial concentration which is maintained within the EC in the absence of ligand, $[L] = 0$. The initial concentration of the cytoplasmic Ca^{2+} ($[Ca_c](0)$) and IP_3, ($[IP_3](0)$) are assumed to have typical values of 100 nM [Billaud et al., 2014] and 10 nM [Lemon et al., 2003], respectively. The initial ER Ca^{2+} concentration ($[Ca_s](0)$) is obtained by setting Equation (3.20) to zero for the given initial cytoplasmic Ca^{2+} and IP_3 concentrations. Furthermore, setting Equations (3.16) and (3.17) to zero for $[L] = 0$, we obtain the initial concentration for the unphosphorylated receptor, $[R_s](0) = [R_t]$ and the phosphorylated receptor, $[R_p](0) = 0$. The initial concentration of all these variables are listed in Table 3.2. The value of the constant δ (we have discussed the importance of δ in Subsection (3.2.2)) is obtained by setting Equation (3.18) to zero for the given initial cytoplasmic and IP_3 concentrations at $[L] = 0$, we get

$$\delta = \frac{k_2[\mathrm{IP_3}](0)K_g}{\frac{[Ca_c](0)}{K_1+[Ca_c](0)}\gamma - k_2[\mathrm{IP_3}](0)}.$$

For the constant influx, q_{in}, we set Equation (3.19) to zero. After rearranging the obtained expression (using conditions of initial cytoplasmic and ER Ca^{2+} and IP_3), we obtain

$$q_{\mathrm{in}} = k_8 \frac{([Ca_c](0))^2}{K_4^2 + ([Ca_c](0))^2}.$$

3.2.7 Parameter values

The parameter values used in this model are listed in Table 3.1. Most of the parameter values for the intracellular Ca^{2+} modeling are taken from [Plank et al., 2006], and a few of them are slightly adjusted in order to capture the qualitative trend of the intracellular Ca^{2+} concentration observed in experiments. The parameter values for the receptor and G-protein modeling are obtained from [Lemon et al., 2003], and the

value of the parameter k_p is slightly changed in order to confine the ER Ca^{2+} refilling within a timescale of 500 s (according to [Wiesner et al., 1996]). The importance of the parameter k_e is discussed in Section 3.3. The k_{soc} value is also slightly adjusted to ensure that the refilling of ER occurs properly and within a timescale of 500 s. Taking the value of k_8 equal (or close) to that of k_4 guarantees a smooth decrease of the cytoplasmic Ca^{2+} concentration curve after the transient peak occurs. Moreover, we have slightly changed the values of K_2 and k_5 so that we can get the initial Ca^{2+} concentration of ER closer to the physiological concentration of 500 nM [Pecze et al., 2015].

3.3 Results and Discussion

We have systematically solved the set of Equations (3.16)-(3.20) and analyzed the evolution of all the relevant variables. Inspired by several experiments [Mo et al., 1991, Carter et al., 1990, Malli et al., 2005, Colden-Stanfield et al., 1987, Jacob et al., 1988, Yang et al., 2001, Zhu and He, 2005], we test our model's ability to predict specific results such as calcium signal behavior due to a blockage of extracellular calcium and the response of calcium due to the removal of agonist at a particular moment after the calcium peak occurs.

3.3.1 General discussion of the outcome of the model

In this section, we are going first to describe the main results implied by our model, while in the next section we will directly confront directly some of our predictions with existing experiments.

3.3.1.1 Receptor desensitization affects intracellular homeostasis

An interesting fact is that (see Figure 3.6) the model shows that when an EC is stimulated with a constant ATP concentration, i.e., $[L] = 300$ nM for a long period of time, the intracellular concentration of IP_3 (Figure 3.6(c)), intracellular cytoplasmic Ca^{2+} (Figure 3.6(d)), and ER Ca^{2+} (Figure 3.6(e)) return naturally back to their initial concentration (homeostasis). This behavior is related to the exponential decay of unphosphorylated receptor concentration as shown in Figure 3.6(a), which in turn causes a decrease in IP_3 generation after a transient peak at 15 s as shown in Figure 3.6(c). However, the transient peak time is dose-dependent; for example, the higher the ATP concentration, the faster are the EC response and IP_3 transient peak. Figure 3.6(d)) shows that the cytoplasmic Ca^{2+} and IP_3 peak occur approximately at the

Table 3.1: Model parameter values

Parameter	Description	Reference	Value
Receptor parameters			
k_r	Receptor recycling rate	[Lemon et al., 2003]	1.75E-4 s^{-1}
$[R_t]$	Total number of $P2Y_2$ receptors	[Lemon et al., 2003]	2E+4
K_r	Receptor dissociation constant	[Lemon et al., 2003]	2 μM
k_p	Receptor phosphorylation rate	[Lemon et al., 2003]	0.10 s^{-1}
k_e	Receptor internalized rate	[Lemon et al., 2003]	6E-3 s^{-1}
G-protein parameters			
k_a	G-protein activation rate	[Lemon et al., 2003]	0.017 s^{-1}
k_d	G-protein deactivation rate	[Lemon et al., 2003]	0.15 s^{-1}
$[G_t]$	Total number of G-protein molecules	[Lemon et al., 2003]	10^5
α	Signaling gain parameter	[Lemon et al., 2003]	2.781E-5 s^{-1}
N_A	Avogadro's number		6.02252E+23 mol^{-1}
V_{EC}	Volume of EC	[Silva et al., 2007]	1.173 pl
K_1	Michelis-Menten constant		0 μM
$[(PIP_2)_t]$	Total number of PIP_2 molecules	[Lemon et al., 2003]	5E+4
k_2	IP_3 degradation rate	[Plank et al., 2006]	0.2 s^{-1}
Ca^{2+} parameters			
k_3	Ca^{2+} release rate from the ER	[Plank et al., 2006]	6.64 s^{-1}
k_4	Ca^{2+} uptake rate to the ER	[Plank et al., 2006]	5 μM s^{-1}
k_5	Ca^{2+} leak rate from the ER	(see text)	0.000545 s^{-1}
k_{soc}	Ca^{2+} influx rate via SOC	[Su et al., 2011]	0.0086 μM^{-1} s^{-1}
n	constant	[Su et al., 2011]	1
k_8	PMCA Ca^{2+} efflux rate	[Plank et al., 2006]	5 μM s^{-1}
K_2	Michaelis-Menten constant	[Plank et al., 2006]	0.16 μM
K_3		[Plank et al., 2006]	0.15 μM
K_4		[Plank et al., 2006]	0.32 μM
K_{i,ca_c}		[Silva et al., 2007]	1.0 μM
K_{soc}		[Kapela et al., 2008]	0.1 μM
$[Ca_{ex}]$	External Ca^{2+} concentration	[Plank et al., 2006]	1500 μM
v_r	Ratio of cytoplasm and ER volumes	[Plank et al., 2006]	3.5
k_6	Association rate with buffer proteins	[Plank et al., 2006]	100 μM^{-1} s^{-1}
k_7	Dissociation rate with buffer proteins	[Plank et al., 2006]	300 s^{-1}
$[B_t]$	Total buffer protein concentration	[Plank et al., 2006]	120 μM

Table 3.2: Model initial conditions

Parameters	Description	Value
$[R_s]\,(0)$	Unphosphorylated receptors	$[R_t]$
$[R_p]\,(0)$	Phosphorylated receptors	0
$[\mathrm{IP}_3]\,(0)$	IP_3 concentration	0.01 μM
$[Ca_c]\,(0)$	Cytoplasmic Ca^{2+} concentration	0.1 μM
$[Ca_s]\,(0)$	ER Ca^{2+} concentration	711.0 μM

same time. This is a direct consequence of the fact that a maximum of IP_3 leads to a maximal release from the internal store. Another fact is that due to a prolonged presence of ligand, the concentration of unphosphorylated receptor continuously decreases to approach a minimal value, leading to desensitization of receptors, so that IP_3 concentration is able to return to its homeostatic concentration. This also triggers a decrease in Ca^{2+} release from the ER, whereas Ca^{2+} uptake from the cytoplasm (through the SERCA, as shown in Figure 3.6(e)) continues to operate allowing for a refilling of the internal store (ER). Moreover, as long as the ATP remains in the plasma, the unphosphorylated receptor concentration remains at its minimal concentration. Note that a higher unphosphorylated receptor concentration can be obtained by increasing the rate constants k_e and k_r. These constants are responsible for the conversion of phosphorylated receptors to the unbound receptors by following two steps, i.e., R_p to R_I and R_I to R. Additionally, the phosphorylated receptors reach a transient peak (as shown in Figure 3.6(b)) due to the availability of a minimal number of unphosphorylated receptors to bind with the external ATP in order to form phosphorylated receptors. From Figure 3.6(b), it is also evident that the phosphorylated receptor concentration decreases slowly due to the recycling of phosphorylated receptors to unbound receptors by undergoing an intermediate receptor state, R_I.

It is worthwhile to emphasize the main difference between the present model and previous ones [Wiesner et al., 1996, Wiesner et al., 1997, Plank et al., 2006, Plank et al., 2007, Silva et al., 2007, Comerford et al., 2008, Li et al., 2015]. One of the main criticisms is that previous models of EC Ca^{2+} do not recover the evolution with time towards intracellular homeostasis for any of the quantities at play namely, $[i(t)]$, $[Ca_c(t)]$, and $[Ca_s(t)]$), as shown in Figure B.1 (Appendix B). Figure B.1 (Appendix B) demonstrates that the intracellular concentrations remain significantly above the initial concentration when the EC is stimulated with a constant ATP, $[L] = 300$ nM. The present model is able to recover the homeostatic conditions provided the receptor desensitization is taken into account.

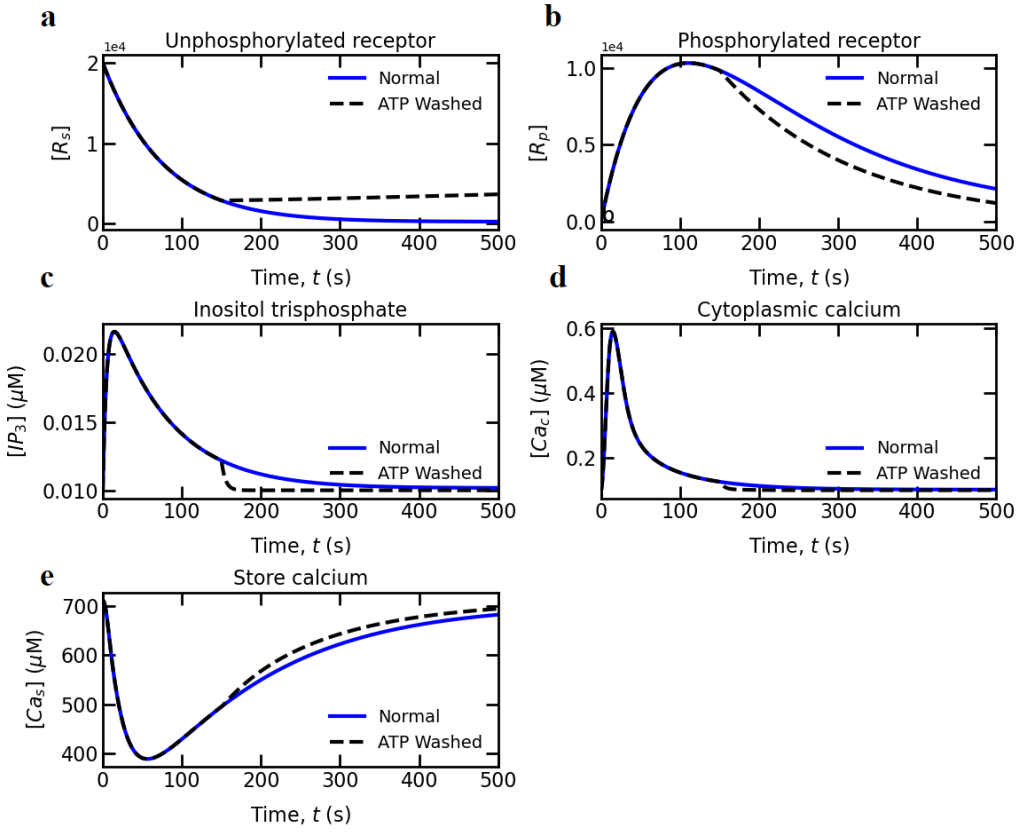

Figure 3.6: Variation of concentrations with time for a single EC stimulated by a constant ATP, $[L] = 300$ nM: (a) unphosphorylated receptor concentration; (b) phosphorylated receptor concentration; (c) inositol trisphosphate concentration; (d) cytoplasmic Ca^{2+} concentration; and (e) store Ca^{2+} concentration. **Normal** refers to the case when an EC is stimulated for 500 s, and **ATP Washed** refers to the case when an EC is stimulated for 150 s.

3.3.1.2 Faster intracellular homeostasis in absence of ATP

Most of the experiments [Mo et al., 1991, Carter et al., 1990] have been performed by stimulating ECs for a fixed period of time with a constant ligand concentration followed by washing the stimulus away in order to investigate the trailing cytoplasmic Ca^{2+} concentration in the absence of the ligand. The trailing cytoplasmic Ca^{2+} concentration refers to the concentration after the transient peak. It has been found [Mo et al., 1991] that the cytoplasmic Ca^{2+} concentration immediately returns to its initial concentration when ATP is removed after stimulating the EC for any period of time. However, no experimental data are available for the ER Ca^{2+} and IP_3 concentrations due to the experimental difficulties associated with obtaining these

values. We have simulated this experimental scenario (the return of cytoplasmic Ca^{2+} to its initial concentration) by setting the ATP concentration to zero (i.e., $[L] = 0$) after stimulating an EC for 150 s. Figure 3.6(a) (black dotted line) shows that the unphosphorylated receptor concentration increases due to the conversion of phosphorylated to unbound receptors. This increase is inevitable because of the absence of ATP and hence its inability to phosphorylate the unbound receptors. As a consequence, the IP_3 concentration immediately returns to its initial level at the time when ATP is removed from the plasma, as shown in Figure 3.6(c). Furthermore, cytoplasmic Ca^{2+} (as shown in Figure 3.6(d)) reverts to its initial concentration due to the pumping of cytoplasmic Ca^{2+} to the ER and the extracellular space. Additionally, Figure 3.6(e) shows that the ER is completely refilled to its initial concentration. This is due only to Ca^{2+} uptake from the cytoplasm rather than to Ca^{2+} release from the ER to the cytoplasm in the absence of IP_3. Thus, Figure 3.6 clearly reveals that intracellular homeostasis is achieved faster in the absence of ATP than in the case of maintaining a constant ATP for a prolonged period, which means that EC intracellular homeostasis basically depends upon the ATP stimulation time.

3.3.1.3 Extracellular Ca^{2+} is responsible for ER refilling

Some Ca^{2+} dynamics models are able to explain the oscillations in intracellular Ca^{2+} concentrations without considering Ca^{2+} fluxes across the PM [Meyer and Stryer, 1988, Sage et al., 1989]. However, in most experiments [Carter et al., 1990, Sage et al., 1989] on ECs, a single transient peak followed by a plateau has been observed. This behavior results from the balance between Ca^{2+} fluxes across the ER membrane and the PM. In order to experimentally elucidate the role of extracellular Ca^{2+} in maintaining the cytoplasmic and ER Ca^{2+} homeostatic concentrations, as well as to understand the pathways [Lückhoff and Busse, 1986, Yang et al., 2001, Malli et al., 2005] and the regulation of downstream molecules [Carter and Pearson, 1992], the Ca^{2+} chelating agent EGTA is commonly added to the extracellular solution where it binds with the free extracellular Ca^{2+}. The binding of Ca^{2+} to EGTA blocks the influx of Ca^{2+} from the extracellular environment into the cytoplasm. To understand the effect of EGTA in the simulations, we have set q_{in} and q_{soc} to zero. This has two consequences (see in Figure 3.7): (i) the trailing (or steady) cytoplasmic concentration is lower than its initial concentration, and (ii) the ER Ca^{2+} continues to be depleted, without any tendency of refilling towards its homeostatic concentration. Both facts are in agreement with experiments [Yamarnoto et al., 1995] and [Malli et al., 2007]. In conclusion of this section, the inhibition of calcium entry from the extracellular

space leads to undershooting of intracellular calcium, and the lack of refilling of ER Ca^{2+}. In both cases, the relevant pathway is associated with the SOC; as seen in Equation (3.11), the corresponding flux results from the deviation from homeostatic ER concentration, and its inhibition precludes the ER from getting back to homeostasis. We found that among the two influxes across the cytoplasmic membrane (q_{in} and q_{soc}), the SOC is dominant, in agreement with experimental findings [Malli et al., 2005, Malli et al., 2007].

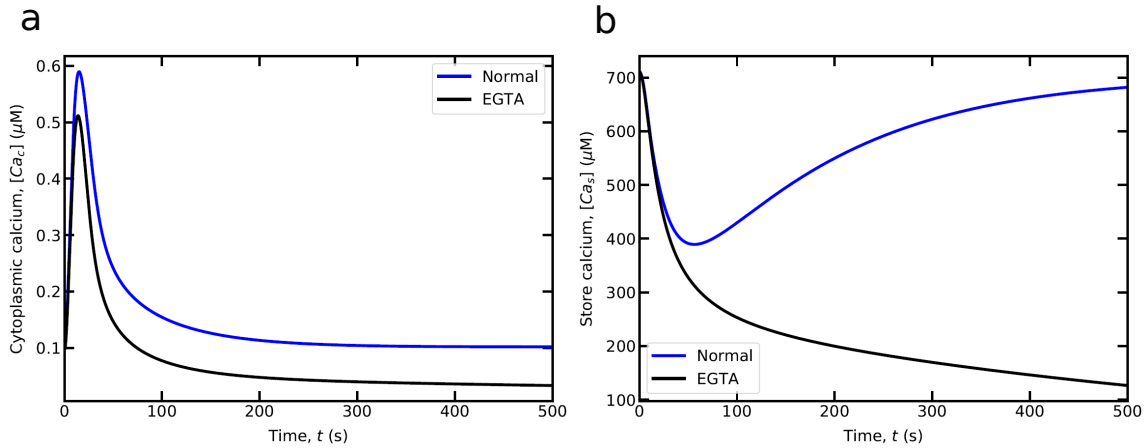

Figure 3.7: Comparison of theoretical model variable results for a single EC stimulated by a constant ATP, $[L] = 300$ nM under physiological conditions (**Normal**) and no external Ca^{2+} (**EGTA**): (a) cytoplasmic Ca^{2+} concentration; and (b) store Ca^{2+} concentration.

3.3.1.4 Variation of Ca^{2+} transient peak in ECs due to the receptor affinity

In experiments, it has been reported that a given ligand concentration can yield different amplitudes of cytoplasmic Ca^{2+} peaks for individual cells originating from the same cell line [Mahama and Linderman, 1994]. Furthermore, when considering the same origin of ECs subjected to different agonists at the same concentration, it has been observed that the Ca^{2+} peak amplitude depends on the type of ligand [Carter et al., 1990, van IJzendoorn et al., 1996]. The first observation may be explained as being due to intercellular differences in the receptor concentration, the size of the cell, PLC activity or ER Ca^{2+} capacity [Mahama and Linderman, 1994], whereas the second observation may attributable to variations in ligand affinity to their respective membrane receptors. This second observation (different agonists with the same EC) lends itself to a simpler interpretation as compared to the first one. Different

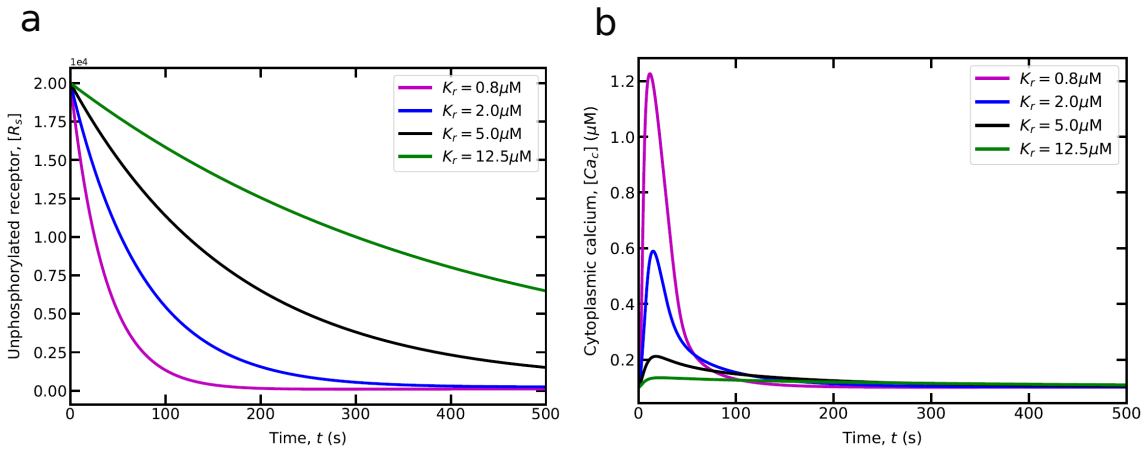

Figure 3.8: Theoretical model variable results for a single EC stimulated with $[L]$ = 300 nM and by varying the $P2Y_2$ receptor dissociation constant, K_r: (a) unphosphorylated receptor concentration; and (b) cytoplasmic Ca^{2+} concentration.

agonists are expected to have different receptor affinity. We have thus explored this scenario by varying the dissociation constant, K_r, in the range of 0.8-12.5 μM for a fixed 300 nM ligand concentration. Figure 3.8(b) displays the effect of affinity on the cytoplasmic Ca^{2+} peak. Note that increasing the receptor dissociation constant, K_r, means a weaker interaction between the $P2Y_2$ receptor and the ligand. This naturally leads to a decrease in cytoplasmic Ca^{2+} peak since this implies a slower decay of unphosphorylated receptors, resulting in fewer IP_3 molecule formation as shown in Figure 3.8(a). The first observation (i.e., different cells of the same cell line produce different amplitudes) can be explained by randomly selecting parameter values from the Gaussian distribution around the mean parameter values [Mahama and Linderman, 1994].

3.3.1.5 Saturation of transient peak with increasing ATP concentration

Figure 3.9 shows that the cytoplasmic Ca^{2+} peak concentration gets saturated with increasing of ATP concentration. The dependence of the cytoplasmic Ca^{2+} peak on ATP concentration is sigmoidal, which is commonly encountered in many biological processes. This is due to the fact that the decay of unphosphorylated receptors is fast. As a result, IP_3 formation gets saturated with the fast decay of unphosphorylated receptors. Due to the saturation of IP_3 formation, a fixed quantity of Ca^{2+} is released from the ER that leads to saturation of the cytoplasmic Ca^{2+} peak.

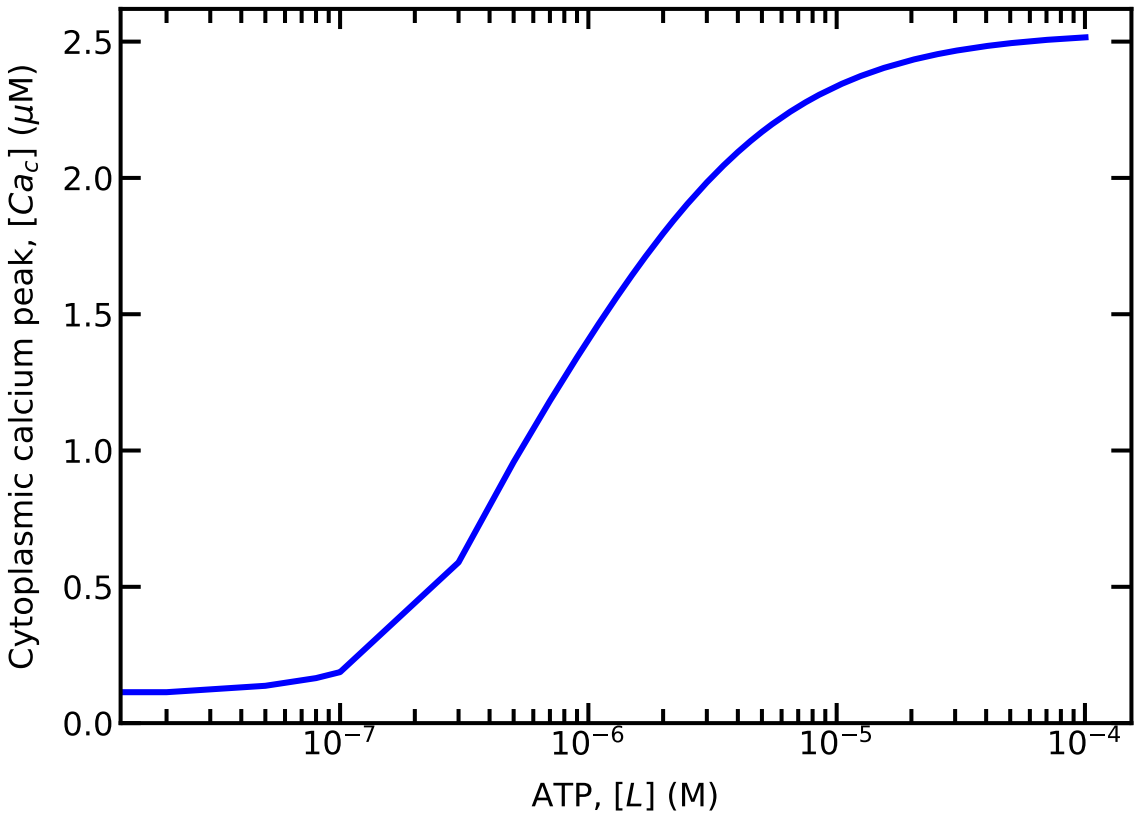

Figure 3.9: Variation of peak cytoplasmic Ca^{2+} concentration with ATP, $[L]$ concentration

3.3.1.6 Elevated cytoplasmic Ca^{2+} depends on receptor recycling rate

Many experimental studies have reported that the steady state cytoplasmic Ca^{2+} concentration (the plateau after the peak) can sometimes be more than double that of the initial concentration [Colden-Stanfield et al., 1987, Jacob et al., 1988, Yang et al., 2001, Zhu and He, 2005]. This means that the cell may not return to its homeostatic condition, as one would expect *in vivo*. We have seen before that our model can account for homeostatic recovery, provided the phosphorylated receptor recycling rate k_r is sufficiently small enough (see Figure 3.6). However, if the recycling rate is varied, our model can still capture the fact that the final Ca^{2+} concentration is higher than the homeostatic one. Figure 3.10(a) shows that an increase in k_r, results in a higher steady unphosphorylated receptor concentration. This means that the phosphorylated receptors are rapidly recycled into unphosphorylated receptors in the presence of sufficiently high ATP concentration. However, the initial decaying of unphosphorylated receptors remains unchanged with changing k_r. The cytoplasmic Ca^{2+} concentration change (as shown in Figure 3.10(b)) is due to the elevated

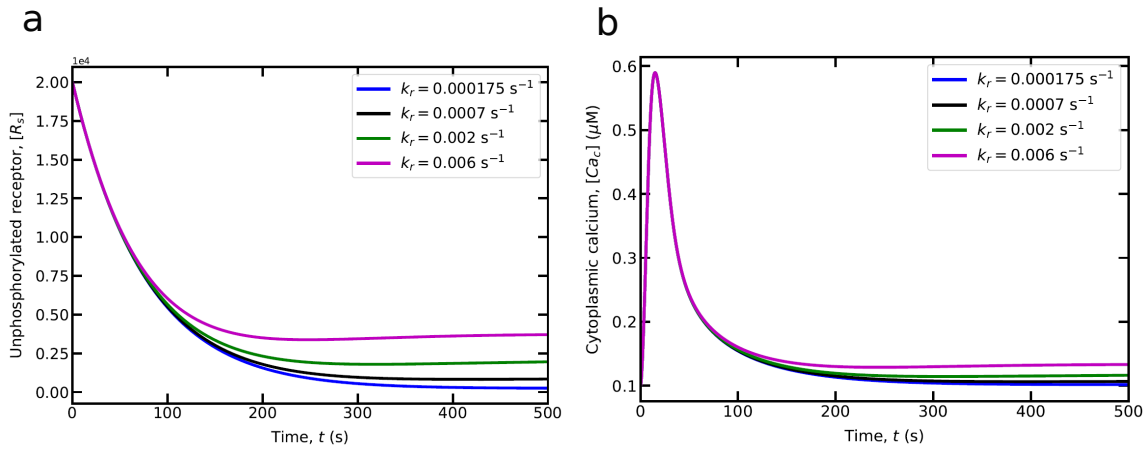

Figure 3.10: Theoretical model variable results for a single EC stimulated by a constant ATP, $[L] = 300$ nM as a function of the receptor recycling rate constant, k_r: (a) unphosphorylated receptor concentration; and (b) cytoplasmic Ca^{2+} concentration.

unphosphorylated concentration. As long as the unphosphorylated receptor concentration remains elevated, IP_3 molecules are continuously activated, triggering further release of Ca^{2+} from the ER. However, no change in the cytoplasmic Ca^{2+} transient peak is observed upon variation of k_r. In conclusion, it is tempting to speculate that the non recovery of homeostasis may be associated with an *in vitro* alteration of the recycling rate.

3.3.2 Direct model confrontation with experimental data

Here we confront our model with several experimental results. In order to make a comparison with the proposed model results, we have dimensionalized the cytoplasmic Ca^{2+} concentrations with their corresponding maximum cytoplasmic Ca^{2+} concentrations.

3.3.2.1 Calcium homeostasis recovery

In an experimental study by Carter et al. [Carter et al., 1990], the response (cytoplasmic Ca^{2+} concentration) of a human umbilical-vein EC (HUVEC) is analyzed by stimulating ECs with 100 μM concentrations of ATP. At the beginning of the stimulation, a rapid rise in the cytoplasmic Ca^{2+} concentration from its basal concentration is observed. This is due to the release of IP_3 dependent Ca^{2+} from the ER. The cytoplasmic Ca^{2+} concentration reaches a peak at ~ 6 s and subsequently, it returns to its basal concentration. Their results are reported in Figure 3.11(a) (symbols). We have confronted our model to this observation by taking the same ATP concentration as

in the experiments. Our results are shown in Figure 3.11(a) (solid line). Overall the model reproduces reasonably well the recovery towards homeostasis and the duration of the peak. It must be noted, however, that if the non-dimensionlized result of the cytoplasmic Ca^{2+} concentration of our model agrees with the non-dimensionalized experimental result, our model overestimates the amplitude of maximal calcium peak (see inset in Figure 3.11(a)), when the physical value of cytoplasmic Ca^{2+} concentration is compared (instead of dimensionalized one). Certainly more systematic adaptation of model parameters is required to have a better agreement of the model and experimental results. We have tried to find the proper parameters in order to have better agreement of the physical cytoplasmic Ca^{2+} concentration of our result with the experimental result. We have attempted to vary the values of kinetic constant k_2 (the IP_3 degradation rate constant; Equation (3.18)) from 0.2 to 0.62 s^{-1}. These value are within the range of values reported in the experiments, namely $k_2 \simeq$ 0.001-2 s^{-1} [Mahama and Linderman, 1994]. Taking for k_2 =0.62 s^{-1} provides a much better agreement (Figure 3.11(b)).

3.3.2.2 Homologous receptor desensitization

A central question concerns the response of ECs to a second ATP stimulation after a first stimulation has been applied for a certain time and then washed out. To answer this question Carter et al. [Carter et al., 1990] have performed an experimental study to answer this question. For that purpose they applied ATP to ECs for a certain time, then removed it for some time, before stimulating again with ATP. Figure 3.11(c) shows that stimulating again ECs by ATP leads to no subsequent cytoplasmic Ca^{2+} response. In fact they have shown that a second calcium response due to second ATP stimulation, is seen only if the second ATP stimulation takes place after some time (from 5 to 20 min). As anticipated when building our model, this observation is a hint to the existence of some desensitization of receptors by ATP. The result from our model also reveal the absence of calcium response after a second stimulation. This is to be contrasted with other models [Cuthbertson and Chay, 1991, Wang et al., 2007] which predict an immediate response of the cell following the application of agonist (Figure S4, Appendix B). Note, however, that a second response of ECs requires a maximum time of 20 min to respond a second ATP stimulation, whereas our model predicts about more than 2 hr (see inset Figure 3.11(c)). Here again, we did not enforce our parameters to provide a better agreement, but have selected most of parameters from several experimental estimates. Still, we believe that further

improvement will be possible in the future, by looking for best fits, as we did above for k_2. We hope to dig further into this question in a future work.

3.3.2.3 Role of the extracellular calcium on homeostasis

In another experimental validation of the proposed model, we used the experimental result of Yamamoto et al. [Yamamoto et al., 2000a] in which they measured the cytoplasmic Ca^{2+} concentration in the presence of exogenous EGTA (ethylene glycol-bis-N,N,N',N'-tetraacetic acid). EGTA binds to free extracellular calcium, preventing then extracellular calcium to enter the cytoplasm. They found that the final (Figure 3.11(d)) cytoplasmic calcium concentration is lower than the initial one (i.e., lack of homeostasis). This indicates that extracellular calcium is essential for recovery of initial cytoplasmic calcium concentration. We have simulated this experiment by setting q_{soc} and q_{in} (entered in Equation (3.19)) to zero (further discussions about the effects of EGTA on the cytoplasmic and store Ca^{2+}, has been given in Subsection 3.3.1.3). The predicted result regarding the decrease in the dimensionless cytoplasmic Ca^{2+}, after the peak of cytoplasmic Ca^{2+}, has a good agreement with the experimental result (Figure 3.11(d)).

Finally some remarks are in order. Due to the limited availability of experimental data for the ER Ca^{2+} and IP_3 concentrations, we have focused on the validation of the experimental cytoplasmic Ca^{2+} since measurement of cytoplasmic Ca^{2+} concentration with the help of fluorescence is relatively easier than the ER Ca^{2+}. Owing to difficulties in loading the Ca^{2+}-sensing fluorescent dyes in the ER [Samtleben et al., 2013], it is rarely measured in experiments. However, several new technologies [Henderson et al., 2015, Dhandapani et al., 2021] have been developed to measure the ER Ca^{2+} concentrations but it is still a matter of debate regarding the accuracy of the measured data. Similarly there are certain difficulties associated with the quantitative measurement of IP_3 molecules and tracking of PIP_2 molecules from where IP_3 molecules are formed [Miyamoto and Mikoshiba, 2017]. Therefore most reported data focus on cytoplasmic Ca^{2+} concentrations. However, the complete validation of Ca^{2+} dynamics model with all the measured intracellular Ca^{2+} dynamics variables, such as IP_3, Ca_c, and Ca_s, would be an interesting topic for future research.

3.4 Conclusions

In this work, we have developed a homeostatic Ca^{2+} dynamics model in which the intracellular EC homeostasis depends on receptor dynamics. We have shown that

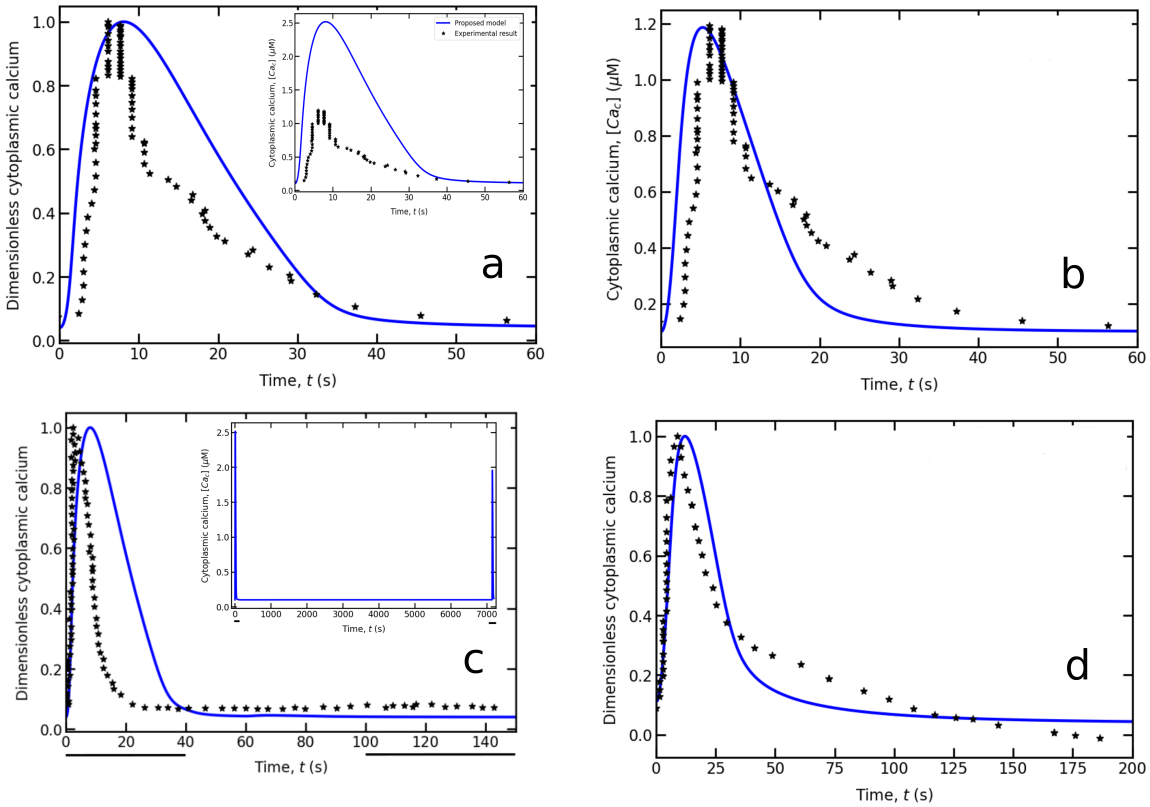

Figure 3.11: Experimental validations of the proposed Ca^{2+} dynamics model: (a) the comparison of the dimensionless cytoplasmic Ca^{2+} concentration obtained from the proposed model with the experimental result is done in the presence of 100 μM of ATP concentrations for 60 s (Experimental result: Figure 1(a) [Carter et al., 1990]). Inset represents the comparison of physical cytoplasmic Ca^{2+} concentration of the proposed model with the experimental result. (b) A better agreement result (extension of Figure 3.11(a)) between the physical cytoplasmic Ca^{2+} concentration of the proposed model and the experimental result is acquired by setting the parameter k_2 to 0.62 s^{-1} (Equation (3.18)); (c) the dimensionless cytoplasmic Ca^{2+} concentration is obtained when the EC is stimulated with 100 μM concentrations of ATP for 40 s and followed by washing out ATP from the solution and it is then applied after 60 s for 40 s (Experimental result: Figure 2 [Carter et al., 1990]). Inset shows the time taken by the EC to respond the second dose of 100 μM concentrations of ATP (model prediction). The black bold line (below x-axis) represents the time at which ATP is injected into the solution; and (d) the trailing dimensionless cytoplasmic Ca^{2+} concentration is obtained when the EC is stimulated with 500 nM of ATP concentrations in the presence of chelator, EGTA (ethylene glycol-bis-N,N,N',N'-tetraacetic acid) in the extracellular space (Experimental result: Figure 1(c) [Yamamoto et al., 2000a]).

the model is able to capture various experimental observations including the effect of stimulating ECs with ATP for a fixed time before washing the stimulus out, the extracellular Ca^{2+}-dependent ER Ca^{2+} refilling, the reason for varying Ca^{2+} transients in different experiments on even in the same EC, the saturation of cytoplasmic Ca^{2+} with increasing ATP concentration, and the cause of elevated cytoplasmic Ca^{2+} concentration levels.

The current Ca^{2+} model is primarily focused on how the EC is able to manage intracellular homeostatic concentrations in the presence of ATP. However, in the experiment of Carter et al. [Carter et al., 1990], some of the ECs exhibit oscillation of cytoplasmic Ca^{2+} concentration. It would be interesting to enrich our model in order to account for oscillations. Several models in the past have successfully accounted for Ca^{2+} oscillation in the presence of agonists as discussed at the beginning of the introduction. Inspired by several models [Cuthbertson and Chay, 1991, Dupont and Erneux, 1997, Marhl et al., 2000, Kummer et al., 2000, Schuster et al., 2002, Politi et al., 2006, Dupont et al., 2011], leading to the oscillation, we believe that incorporating additional feedback pathways (either positive or negative or both) into the model is necessary. We have in mind certain feedback pathways which would control the dynamics of receptors. For instance, the response of the present model due to ATP is controlled by the competition between the timescales of phosphorylation of the free receptors and formation of the free receptors from the phosphorylated receptors. In order to favor oscillations, these timescales must be tuned with the feedback pathways from downstream reactions as well as with the dynamics of intracellular variables. For that purpose, a well-designed experimental protocol would be needed to gain insight into the receptor controlling feedback pathways. This would lead to an interesting future research perspective.

Finally, in a recent work, Zhang et al. [Zhang et al., 2018] have proposed a phenomenological ATP release model when RBCs are subjected to flow. The concentration of ATP in fluid, bloodstream, depends on the several factors [Gou et al., 2021] such as geometry of vascular network, flow condition, hematocrit concentration, and enzymatic reaction of enzymes present on the EC surface. These ATP molecules finally lead to activation of calcium signaling in ECs. In order to understand the effects of RBC dynamics and vascular diseases such as atherosclerosis, aneurysm, and stroke on EC response, it is indispensable to study two things together. In addition, a through study, the coupling between the RBC's ATP release and EC Ca^{2+} signaling, is needed intending to understand the origin of EC related diseases.

The next natural is to study the blood flow simulation by explicitly taking into account RBCs and their ATP release as well as reaction with ECs triggering calcium for simple and complex vascular networks. This constitutes the topic of the next chapter.

Chapter 4

Calcium Dynamics due to ATP Released by Red Blood Cells

In previous Chapter 3, we developed a model for cytoplasmic Ca^{2+} in the presence of adenosine triphosphate (ATP), which guarantees intracellular Ca^{2+} homeostasis. However, in this model, the sources of ATP concentration were not known a priori. In this chapter, we have explicitly considered the sources of ATP concentration and their dynamics in the presence of flow. Red blood cells (RBCs) and endothelial cells (ECs) release ATP when subjected to hydrodynamic flow. ATP molecules react with purinergic receptors located on the inner lining of the vascular wall (the enodthelium). The activation of the purinergic receptors leads to the mobilization of Ca^{2+} from the endoplasmic reticulum (ER). Ca^{2+} is a ubiquitous ion, which controls/regulates many cellular functions as well as regulating vascular tone (expansion and contraction of the vessel wall) by triggering the synthesis of nitric oxide (NO), an important vasodilator. Because of the importance of Ca^{2+} in maintaining vascular tone in the human body, we have coupled RBC dynamics with Ca^{2+} dynamics in the context of Poiseuille flow. Numerical experiments are carried out to obtain flow velocity and ATP concentration using lattice Boltzmann method (LBM) for various flow strengths, channel widths, and RBC concentrations. To emulate blood flow in the human body, we first solve for steady ATP concentration, then introduce steady wall ATP concentration into the Ca^{2+} dynamics equations. We performed all simulations in a straight two-dimensional channel to investigate how RBC dynamics affect Ca^{2+} signaling occurring in the blood vessel wall. Furthermore, the understanding of Ca^{2+} signaling from straight channels can be extended to vascular networks where changes in length and width of a vessel can alter the local concentration of RBCs as well as the flow strength.

The detailed mathematical equations used to solve the coupled ATP and Ca^{2+} are given in Section 4.2. We have presented the main results of the study in Section 4.3.

Although ECs release ATP, we found that ATP mainly came from RBCs and that their uptake by ECs led to a steady ATP pattern in the channel. The stable concentration of ATP and the cytoplasmic concentration of Ca^{2+} in ECs depend on the concentration of RBCs, channel width and flow intensity. For example, while keeping the channel length fixed but varying its width for a given RBC concentration, the number of RBCs in the channel increases linearly with increasing the channel width. As a result, the total cumulative level of ATP release increases in channels of larger width, resulting in a higher ATP concentration than in channels of smaller width.. Similarly, we have reported that an increase in flow strength for a channel of given width and RBC concentration results in higher ATP concentration. Interestingly, we found that the amplitude of the Ca^{2+} peak per EC increases significantly with RBC concentration, while the duration of the peak decreases with RBC concentration for different flow intensities and a given channel width. Similarly, we found that the amplitude of the Ca^{2+} peak increases with channel width and the duration of the peak decreases with RBC concentration for a given flow intensity. The difference between the peak times of Ca^{2+} for variable confinement, as encountered in vascular networks, allows Ca^{2+} signals to propagate from a region of high ATP concentration to a region of low ATP concentration. At the end of Section 4.3, to illustrate Ca^{2+} propagation in the blood vessel, we locally triggered an EC within the confluent layer of EC with a given ATP concentration. This triggering leads to an increase in Ca^{2+} concentration in neighboring ECs due to diffusion of inositol trisphosphate (IP_3) from the stimulated EC to neighboring ECs via cell-cell gap junctions, resulting in release of Ca^{2+} from the ER of neighboring ECs.

4.1 Introduction

Red blood cells (RBCs) have long been recognized for their primary role in oxygen transport to tissues and the removal of metabolic wastes [Amiri and Zhang, 2023]. However, these cells serve a dual purpose by not only conveying oxygen and waste, but also acting as carriers for a crucial signaling molecule, adenosine triphosphate (ATP) [Forsyth et al., 2011, Lohman et al., 2012, Xu et al., 2017]. In the intricate landscape of cellular communication, ATP emerges as a pivotal second messenger, orchestrating the transmission of information from the extracellular environment to the endothelial cell (EC) cytoplasm. This transmission hinges on a cascade of reactions activated at the endothelial cell's plasma membrane (PM) [Pirotton et al., 1987, Song et al., 2007]. Notably, a significant consequence of ATP signaling is the liberation of sequestered

calcium ions (Ca^{2+}) from the endoplasmic reticulum (ER) of EC into the cytoplasm, perpetuating its pivotal role [Carter et al., 1990]. The systematic study of cytoplasmic Ca^{2+} resulting from ATP released by RBCs within vascular vessels constitutes the foremost objective of this chapter.

The intracellular ATP concentration within RBCs typically falls in the millimolar range [Xu et al., 2019], whereas plasma concentrations hover around the micromolar range [Gorman et al., 2007]. This implies that ATP released from RBCs might exceed plasma demands, potentially eliciting physiological concerns [Burnstock and Ralevic, 2014]. Hence, maintaining ATP concentrations within an acceptable physiological range in plasma (around micromolar levels) is crucial. This regulatory role is entrusted to ectonucleotidase, an enzyme present on the EC surface, responsible for hydrolyzing ATP into adenosine diphosphate (ADP), which then undergoes successive conversion to adenosine monophosphate (AMP) and finally to adenosine (AD). Thus, the involvement of ECs in preserving plasma ATP at physiological levels necessitates consideration. Consequently, our study examines ATP release from both RBCs (the predominant source) and ECs, alongside EC-mediated ATP hydrolysis.

The comprehension of ATP pathways originating from RBCs has been significantly enhanced through in-vitro experiments [Forsyth et al., 2011]. Zhang et al. [Zhang et al., 2018], building upon these experimental findings [Forsyth et al., 2011], have recently presented a phenomenological model that encompasses these two pathways and aligns with experimental observations. Nevertheless, the experimental work by Forsyth et al. [Forsyth et al., 2011] and the numerical exploration by Zhang et al. [Zhang et al., 2018] were conducted in a context of highly diluted RBC suspensions subjected to shear flow. In real-world blood flow scenarios within the circulatory system, the intricate interplay of Poiseuille flow and complex hydrodynamic interactions between RBCs prevails, where healthy situations can feature RBC volumes reaching up to 45% (designated as Hematocrit, Hct).

Gou et al. [Gou et al., 2021] extended Zhang et al.'s work [Zhang et al., 2018], investigating the Poiseuille flow in a two-dimensional (2-D) straight channel, accounting for different flow conditions and RBC hematocrits. Nonetheless, their investigation did not consider the role of the endothelium, encompassing ATP release from ECs, ATP hydrolysis by ectonucleotidase enzymes, and the initiation of Ca^{2+} signaling. Consequently, ATP concentrations in the channel were left to increase boundlessly over time. Clearly, the participation of ECs in maintaining stable ATP concentrations necessitates inclusion within the model. This constitutes another objective of

this chapter. Once addressed, this question will set the stage for investigating Ca^{2+} signaling within the endothelium.

In this chapter, we treat RBCs under flow as the primary source of ATP. We demonstrate that this source is contingent on the spatial arrangement of RBCs, influenced by channel width, hematocrit, and flow intensity. Moreover, we account for the crucial role of ECs, encompassing ATP release, ATP hydrolysis by ectonucleotidase enzymes, and the initiation of Ca^{2+} signaling. This is vital to establish a consistent ATP pattern. Subsequently, we integrate our recently developed model (presented in the previous chapter) [Nayak et al., 2023] for Ca^{2+} signaling, incorporating the phosphorylation of $P2Y_2$ receptors upon ATP binding, ensuring homeostasis for the three dynamic variables (IP_3, Ca_c, and Ca_s). We analyze Ca^{2+} signaling in relation to hematocrit, channel dimensions, and flow strength. Furthermore, we analyze the potential for Ca^{2+} propagation along the endothelium and determine its propagation speed. This investigation lays the foundation for comprehending Ca^{2+} signaling in the presence of blood flow along ECs, paving the way for more intricate analyses in complex vascular networks.

4.2 Methods

We recall that given our assumption of a 2-D framework, the RBC boundary is constrained to be a one-dimensional (1-D) incompressible boundary, capable of undergoing bending. The fluid dynamics both within and surrounding the RBC are characterized by the Navier-Stokes equations (NSEs) for incompressible flows. We impose a pressure-driven Poiseuille flow, with a velocity field along the $x-$direction given by

$$v_x = v_{\max}\left[1 - \left(\frac{y}{W/2}\right)^2\right],$$

where $v_{\max}$ is the maximum flow velocity at the center of the channel, of width W. We begin the numerical simulation from the equilibrium shape of the vesicle, i.e., biconcave. To do this, we define a dimensionless number called the reduced area, ν. This is the ratio between the area of the vesicle, A and the area of a circle, A_0 with the same perimeter (P), i.e.,

$$\nu = \frac{4\pi A}{P^2}$$

where $A = \pi R_0^2$. In this numerical simulation, we have taken, $\nu = 0.65$, which is the physiological value for a healthy RBC.

The bulk equations and boundary conditions for fluid flow and advection-diffusion for ATP (c_{ATP}) have been presented in Chapter 2. Note that we only solve advection-diffusion for ATP concentration outside RBCs. Indeed, the concentration of ATP in the cytoplasm of RBCs ($\sim$ 1 mM) is several folds higher than its concentration in plasma ($\sim 1\ \mu$M). Therefore, we solve the ATP concentration in plasma by considering RBCs as a source of ATP [Gou et al., 2021]. The LBM is used to solve both problems. Here, we go directly to the novelty of the modeling, namely how ATP is released from RBCs and how does it react with ECs.

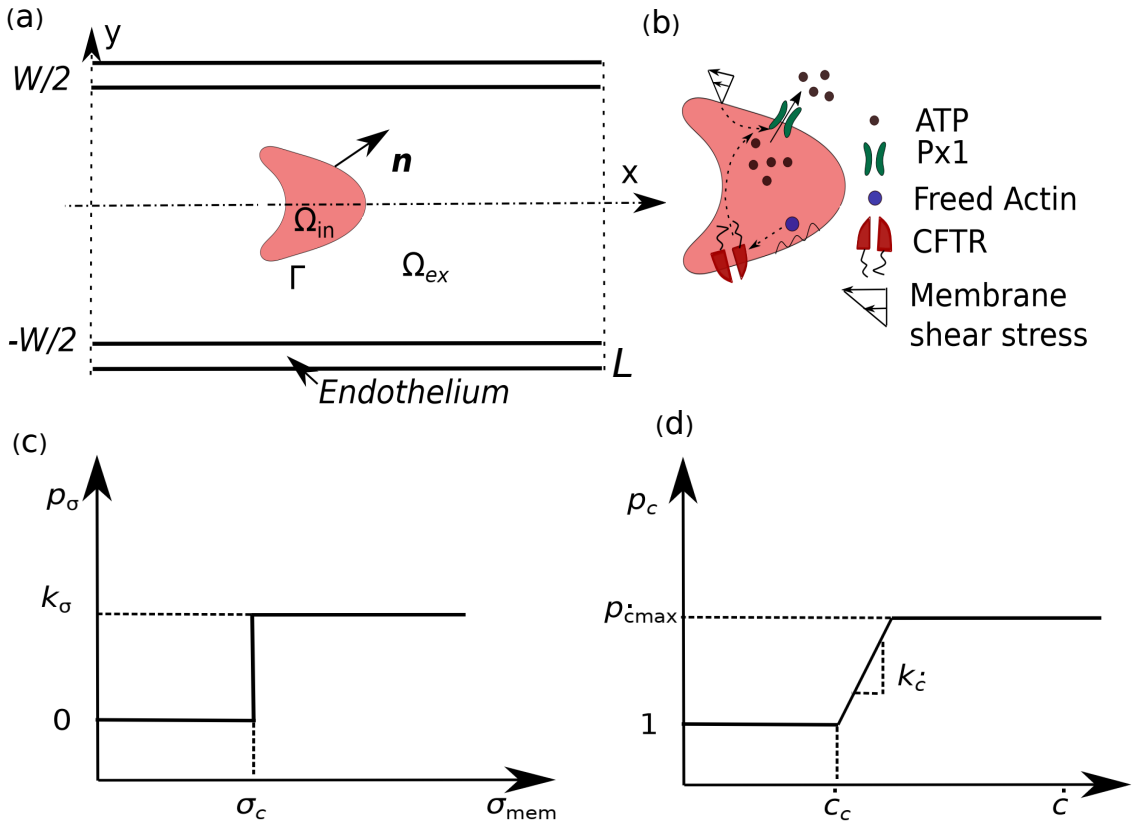

Figure 4.1: Schematic shows: (a) RBC is moving in a straight two-dimensional channel (2-D) which is lined with a layer of endothelial cells known as endothelium; (b) the pathways by which RBC releases ATP molecules when it is subjected to shear stresses; (c) the activation of Pannexin1 (Px_1) hemichannels when the membrane shear stress exceeds the critical shear stress; and (d) up-regulation of ATP release by the cystic fibrosis transmembrane conductance regulator (CFTR) through Px_1 when the curvature change rate exceeds the critical curvature change rate.

4.2.1 ATP release model

According to Zhang et al. [Zhang et al., 2018], the release of ATP from RBCs follows two pathways (shown in Figure 4.1): (i) Pannexin1 (Px_1) hemichannels are activated when the local membrane shear stress exceeds a critical value and (ii) the membrane deformation leads to activation of the CFTR, which up-regulates the Px_1 hemichannels. These two ATP pathways are mathematically expressed as

$$p_\sigma = k_\sigma H\left(\sigma_{\text{mem}} - \sigma_c\right) , \tag{4.1}$$

and

$$p_c = \min\{1 + k_{\dot{c}}\left(\dot{c} - \dot{c_c}\right) H\left(\dot{c} - \dot{c_c}\right), p_{\dot{c}\max}\} , \tag{4.2}$$

where p_σ and p_c are ATP release rates due to opening of Px_1 hemichannels and CFTR amplification factor, respectively. $H(\cdot)$ is Heaviside step function, k_σ is a phenomenological coefficient, σ_{mem} is the local membrane shear stress, and σ_c is the critical shear stress required for opening of ATP channels. $k_{\dot{c}}$ is the slope of membrane curvature change rate, $\dot{c}$ is the local curvature change rate (quantifying the degree of cell deformation), $\dot{c_c}$ is the critical curvature change rate for up-regulation of Px_1, and $p_{\dot{c}max}$ is the the maximum amount of CFTR. We define the flux on the outer surface of RBC [Zhang et al., 2018] as

$$\psi = p_\sigma \cdot p_c , \tag{4.3}$$

which postulates that no ATP is released from the RBC when $\sigma_{\text{mem}} < \sigma_c$ and is not up-regulated by cell deformation (Equation (4.2)) when $\sigma_{\text{mem}} < \sigma_c$.

4.2.2 Boundary conditions

The ATP release flux on the RBC membrane takes the form

$$D_{\text{ATP}} \frac{\partial c_{\text{ATP}}}{\partial \mathbf{n}} = -\psi , \tag{4.4}$$

where $\mathbf{n}$ denotes the local normal vector pointing outward from the boundary to fluids, and the definition of ψ is given in Equation (4.3). The concentration of ATP in the cytoplasm of RBCs ($\sim$ 1 mM) is several folds larger than the ATP concentration in the plasma ($\sim$ 1 μM). Therefore, we consider the RBC as a large reservoir of ATP [Gou et al., 2021].

Because of the strategic location of the endothelium (between the vascular lumen and tissues), it plays a critical role in maintaining the vascular tone. One of the important functions of EC is to maintain the concentration of ATP in the physiological

range. This is achieved with help of ectonucleotidase enzymes. These enzymes act as a safeguard against unwanted activation of pathways or reactions with receptor due to the presence of abnormal ATP concentration [Burnstock and Ralevic, 2014]. Another function of EC is to sense the fluid flow. It is then transmitted to the cytoplasm for synthesis and liberation of signaling molecules such as ATP [Burnstock, 1999]. Several studies have been devoted [Ando et al., 1988, Shen et al., 1992, Geiger et al., 1992] to the understanding the role shear stress on the rise of cytoplasmic Ca^{2+} concentration. One of the mechanisms may be the autocrine signaling [Burnstock, 1999, Yamamoto et al., 2003, Ando and Yamamoto, 2013], i.e., EC releases ATP in response to the flow and these ATP molecules bind to the surface receptors of the same EC to initiate the Ca^{2+} signaling reactions. These two functions of EC are mathematically expressed as the first and second terms in Equation (4.5) [John and Barakat, 2001]. The flux of ATP on the surface of endothelium is written as

$$D_{\mathrm{ATP}} \frac{\partial c_{\mathrm{ATP}}}{\partial \mathbf{n}} = \frac{V_{\max} c_{\mathrm{ATP}}}{K_m} - S_{\max} \left[1 - \left(\frac{-\tau_w}{\tau_0} \right) \right]^3 , \tag{4.5}$$

where $V_{\max}$ is the maximum enzymatic reaction velocity, K_m is the Michaelis-Menten constant, $S_{\max}$ is the maximum ATP release rate from the EC, τ_w and τ_0 are the wall and reference shear stresses on the EC surface, respectively.

Once the velocity field is obtained by solving the Navier-Stokes equations (Equations (2.6)-(2.7)), we use it to solve for ATP concentration field using the advection-diffusion equation (Equation (2.30)). The advection-diffusion equation (Equation (2.30)) is supplemented with boundary condition Equations (4.4)-(4.5). Both fluid and ATP equations are solved numerically using an in-house lattice Boltzmann method (LBM) solver. The detailed parameter values for the ATP release model are given in Table 4.1, and these values are obtained from Forsyth et al. [Forsyth et al., 2011] and John et al. [John and Barakat, 2001]. The details of the numerical procedure can be found in [Zhang et al., 2018, Zhang and Misbah, 2019].

4.2.3 Dimensionless numbers and some mathematical definitions

Dimensionless numbers are used to characterize the flow, the ATP distribution, and the ATP release level of RBCs.

(i) The capillary number is defined as the ratio between the viscous stress of fluid and bending strength of the membrane

$$Ca = \frac{\mu_{\mathrm{ex}} \dot{\gamma}_w R_0^3}{\kappa} . \tag{4.6}$$

where $\dot{\gamma}_w = 4v_{\max}/W$ refers to the wall shear rate of Poiseuille flow.

(ii) The confinement number is used to define the degree of confinement of a RBC by the gap of the channel. It is defined as

$$Cn = \frac{2R_0}{W}\,. \tag{4.7}$$

(iii) To understand the role of ECs in the lumen ATP concentration, we define the spatial-averaged ATP concentration for a given time

$$\overline{c}_{\mathrm{ATP}} = \frac{1}{LW}\int_0^L \int_{-\frac{W}{2}}^{\frac{W}{2}} c_{\mathrm{ATP}}(x,y,t)dydx\,. \tag{4.8}$$

This will allow us to follow the global ATP concentration as a function of time in order to examine the evolution towards a steady state for ATP. The time-averaged ATP concentration along the channel is defined as

$$< c_{\mathrm{ATP}} >_{\mathrm{transverse}} = \frac{1}{T}\int_0^T \frac{1}{L}\int_0^L c_{\mathrm{ATP}}(x,y,t)dxdt\,. \tag{4.9}$$

This quantity will allow us to analyze the ATP spatial distribution in the y-direction, orthogonal to the flow direction. The time-averaged ATP concentration at the wall is defined as

$$< c_{\mathrm{ATP}} >_{\mathrm{wall}} = \frac{1}{T}\int_0^T c_{\mathrm{ATP}}(x,t)\mid_{\mathrm{wall}} dt\,. \tag{4.10}$$

This is an important quantity since it is defined at the wall where ATP reacts with EC.

(iv) In a 2-D channel, the hematocrit is defined as the area occupied by RBCs to the area of the channel

$$Hct = \frac{N_c A}{LW}\,. \tag{4.11}$$

4.2.4 Ca^{2+} dynamics model of endothelial cell signaling

In a recent advancement, we have formulated a novel Ca^{2+} dynamics model that ensures return to homeostasis even when agonists are present on EC surface, as detailed in Chapter 3. A visual representation of coupling between RBC and Ca^{2+} dynamics is revisited in Figure 4.2. Notably, a distinguishing feature of this model, differentiating it from earlier literature where homeostasis was not achieved, is the incorporation of ATP-receptor desensitization as a crucial component. The homeostatic model is

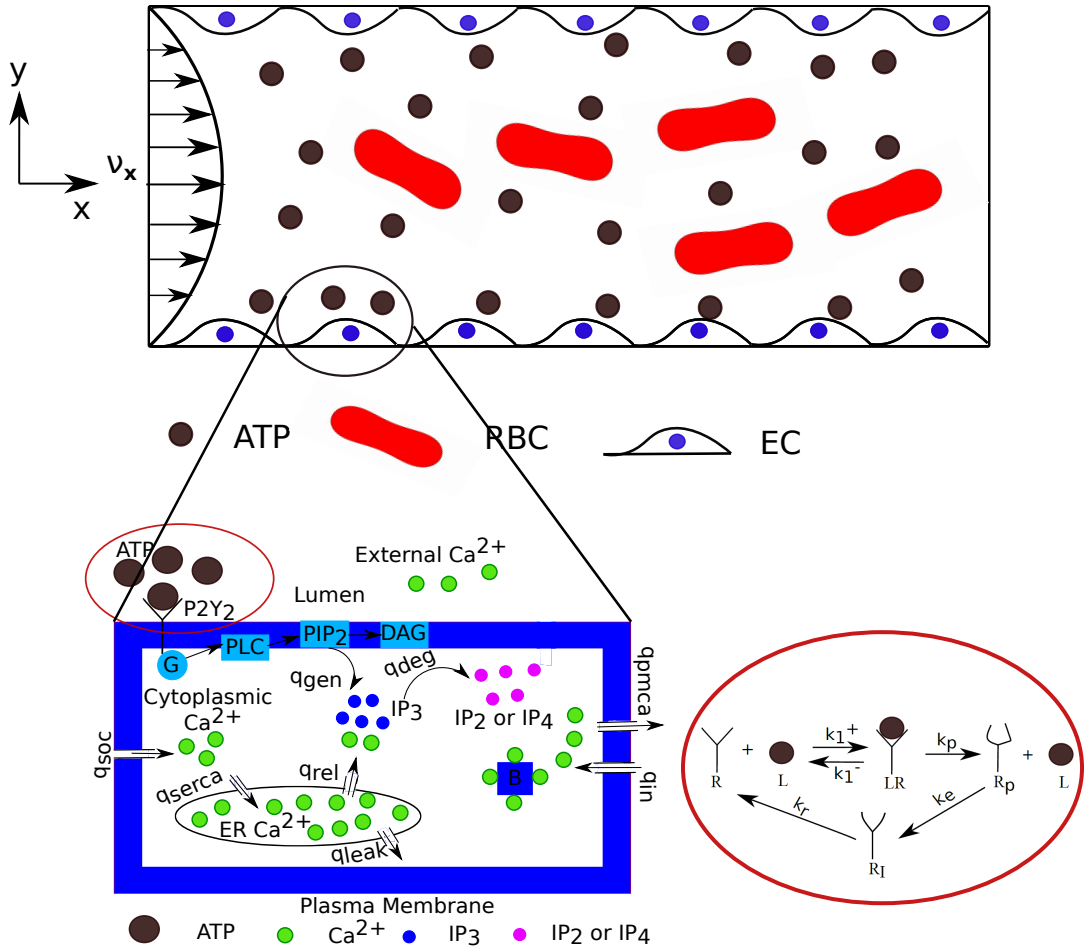

Figure 4.2: Schematic shows that red blood cells (RBCs) and endothelial cells (ECs) release adenosine triphosphate (ATP) molecules due to the application of parabolic-Poiseuille flow along x-direction. ATP is then transported to the wall-lined with ECs where ATP reacts with the surface receptors, in order to provoke the Ca^{2+} signaling. Here, both walls of the vascular lumen are lined with ECs. The activation process of Ca^{2+} signaling in an EC is shown in the enlarged Figure. This enlarged Figure depicts the activation of cascade of reactions and influx/efflux of Ca^{2+} fluxes, through the plasma membrane (PM) and the endoplasmic reticulum (ER) membrane, due to the binding of ATP molecules with the purinergic receptors ($P2Y_2$). Words starting with q represent fluxes and expression for these fluxes are reported in Chapter 3. The dynamics of $P2Y_2$ receptors is shown in the red colored enclosure. There are four states of a receptor: (a) unphosphorylated receptors, R, (b) ligand-receptor complexes, LR , (c) phosphorylated receptors, R_p, and (d) internalized receptors, R_I. ATP concentration is denoted by L. k_1^+, k_1^-, k_p, k_e, and k_r are the chemical reaction constants. Abbreviations: inositol trisphosphate (IP_3), inositol disphosphate (IP_2), inositol tetrakisphosphate (IP_4), G-protein (G), phospholipase C (PLC), phosphatidylinositol 4,5-bisphosphate (PIP_2), and diacylglycerol (DAG).

Table 4.1: ATP release parameters

Parameters	Description	Value	References
k_σ	Phenomenological constant	1.75E+2 nM μm s^{-1}	[Gou et al., 2021]
σ_c	Critical shear stress	0.05 Pa	[Zhang et al., 2018]
$k_{\dot{c}}$	Slope of curvature change rate	6E-3 μm s	[Zhang et al., 2018]
$\dot{c}_c$	Critical curvature change rate	2E+2 μm^{-1}s^{-1}	[Zhang et al., 2018]
$p_{\dot{c}max}$	Maximum amount of CFTR	2.5	[Zhang et al., 2018]
D_{ATP}	ATP diffusion constant	2.36 E-10 m ^{2}/s	[Zhang et al., 2018]
$V_{\max}$	Enzymatic reaction velocity	0.8 μmol m^{-2} s^{-1}	[John and Barakat, 2001]
K_{m}	Michaelis-menten constant	475 μM	[John and Barakat, 2001]
$S_{\max}$	Maximum ATP release rate	10^{-3} nmol m^{-2} s^{-1}	[John and Barakat, 2001]
τ_0	Reference shear stress	1 Pa	[John and Barakat, 2001]

described by 5 important variables, namely unphosphorylated receptor ($[R_s]$), phosphorylated receptor ($[R_p]$), IP_3 ($[IP_3]$), cytoplasmic Ca^{2+} ($[Ca_c]$), and store Ca^{2+} ($[Ca_s]$). The evolution of these variables is obtained based on the balance of fluxes across the membranes (PM and ER) as well as on the basis of chemical kinetics. The equations for the above mentioned variables are given in Chapter 3 (Equations (3.16)-(3.20)). Note that c_{ATP} at the boundary (is equivalent to $[L]$ in Equations (3.16)-(3.17)) is the ATP concentration on the endothelium surface, which will be used as an input to solve for Ca^{2+} dynamics equations (Equations (3.16)-(3.20)) in the endothelium.

4.3 Results and Discussion

We have delved into the impact of three pivotal parameters on the dynamics of ATP and calcium signaling, namely hematocrit (Hct) spanning from 2% to 45%, capillary number (Ca) ranging from 9 to 90, and degree of confinement (Cn) varying between 0.2 and 0.8. These parameter ranges align with those characteristic of microcirculation [Gou et al., 2021], the domain where essential transport processes such as oxygen, nutrients, ATP, and metabolic waste exchanges predominantly occur. It is important to highlight that both ATP's diffusion and advection are accounted for. While ATP originates mainly from RBCs, ECs also contribute to its release to some extent (as elaborated below). The shapes and spatial-temporal organization of RBCs are not predetermined, and we determine them by solving fluid equations under boundary conditions (refer to Equations (2.6)-(2.7)). Upon ATP release and subsequent interaction with EC receptors, the release of Ca^{2+} from ECs is triggered.

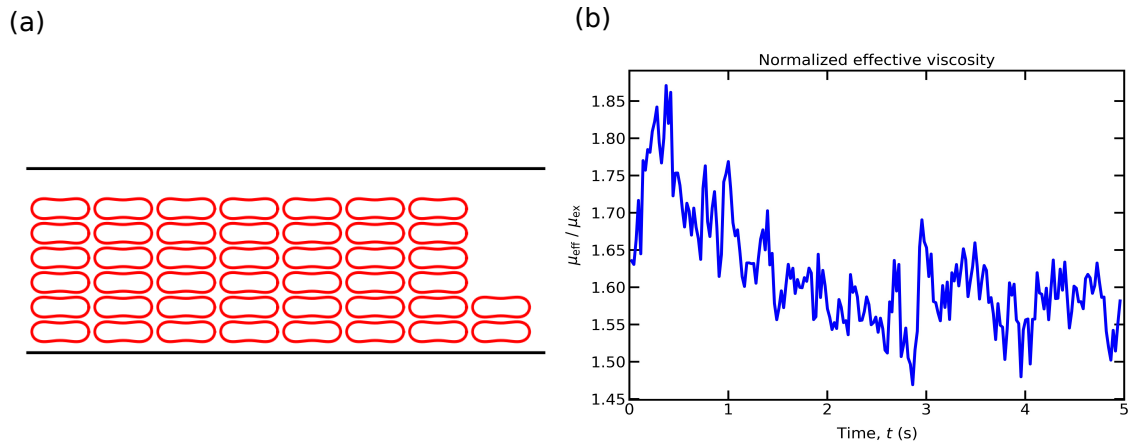

Figure 4.3: (a) Initial spatial arrangement of RBCs ($Hct = 45.9\%$) for $Cn = 0.2$; and (b) the evolution of the ratio of the effective viscosity of the suspension to the viscosity of the plasma with time corresponding to $Hct = 45.9\%$, $Cn = 0.2$, and $Ca = 90$.

Our initial focus involves establishing the distribution of ATP throughout the channel, including the endothelium surface (both bottom and top walls). To achieve this, we solve hydrodynamic equations for RBCs (Equations (2.6)-(2.7)), simultaneously coupled with advection-diffusion equations governing ATP (Equation (2.30)). The physical Reynolds number (i.e., $Re = \frac{\rho \dot{\gamma}_w R_0^2}{\mu_{ex}} \ll 1$) remains within the order of 10^{-4} at maximum. For numerical expediency without compromising precision, we set the simulation Reynolds number to 0.1 across all simulations [Kaoui and Harting, 2016]. As an arbitrary initial state, we select a regular configuration of RBCs within the channel (see Figure 4.3(a)). Notably, different initial configurations, such as random RBC positions, yield equivalent results. Our simulations achieve a steady-state configuration for blood flow in approximately 2.5 seconds (based on the parameters specified in Figure 4.3 caption).

The dynamics of RBCs evolve over time in the flow, accompanied by a corresponding change in effective viscosity. This dynamic viscosity reaches a stable state around 2.5 seconds, as depicted in Figure 4.3(b), where

$$\eta_{\text{eff}} = \frac{\mu_{\text{ex}} Q}{Q^{(\text{ssp})}},$$

where $Q^{(\text{ssp})}$ is the average vesicle suspension flux and Q is the flux of plasma (without vesicles) at the same pressure gradient as $Q^{(\text{ssp})}$. It is seen in that figure (Figure 4.3(b)) that the viscosity reaches its permanent regime in about 2.5 s. At the same time as RBCs evolve in the flow, we also determine the ATP distribution in the channel.

In contrast, the Ca^{2+} response time unfolds at a considerably slower pace compared to the time needed for RBCs to reach their steady state. The peak duration of Ca^{2+} concentrations lasts approximately 10 to 30 seconds [Nayak et al., 2023], while RBCs require approximately 2.5 seconds to stabilize. Consequently, we consider the ATP distribution on the walls after RBCs have achieved a steady-state configuration, and we employ this as input in the Ca^{2+} model (Equations (3.16)-(3.20)). We commence by analyzing the scenario where walls are spatially uniform (disregarding cell-cell junctions or intercellular communication between ECs), and we revisit this aspect later in this chapter.

Importantly, it is worth noting that the magnitude of Ca^{2+} concentrations in the blood lumen far exceeds cytoplasmic Ca^{2+} concentrations [Bisello and Friedman, 2008]. Consequently, we treat lumen Ca^{2+} concentration as a homogeneous and infinitely large reservoir of Ca^{2+}, as represented in the term within Equation (3.11).

4.3.1 Enzymatic activity of nucleotidases

In addition to conveying chemical and mechanical signals from the blood lumen into the cellular cytoplasm, ECs perform a crucial role in maintaining blood ATP concentration within the confines of physiological norms. As elaborated in Subsection 4.2.2, ECs act as a protective mechanism against the uncontrolled ATP concentration in the vascular lumen [Burnstock and Ralevic, 2014]. This safeguard is accomplished through ectonucleotidase enzymes that hydrolyze ATP into ADP, further converting ADP to AMP, and subsequently AMP into AD. This enzymatic process effectively mitigates the potential detrimental effects of elevated ATP levels. It's noteworthy that a recent study [Gou et al., 2021] did not incorporate the role of ECs, which resulted in an unbounded increase in ATP released by RBCs over time.

In our current model, we comprehensively account for the influence of ECs as a prescribed boundary condition (specifically, Equation (4.5)). To elucidate the impact of ECs on lumen ATP concentration, we conducted an analysis on the behavior of spatially-averaged ATP concentration over time. We find that ATP concentration attains a steady-state equilibrium within the lumen, as illustrated in Figure 4.4. This equilibrium arises from a delicate balance between the ATP release fluxes from RBCs and ECs and the concurrent hydrolysis of ATP catalyzed by ectonucleotidase enzymes.

Figure 4.4 also outlines the trajectory of ATP behavior in the absence of endothelium intervention. In this scenario, the simulation commences with an initial ATP concentration surpassing the eventual steady ATP concentration. This investigation

underscores the pivotal role played by ECs in maintaining homeostasis in ATP concentration within the lumen.

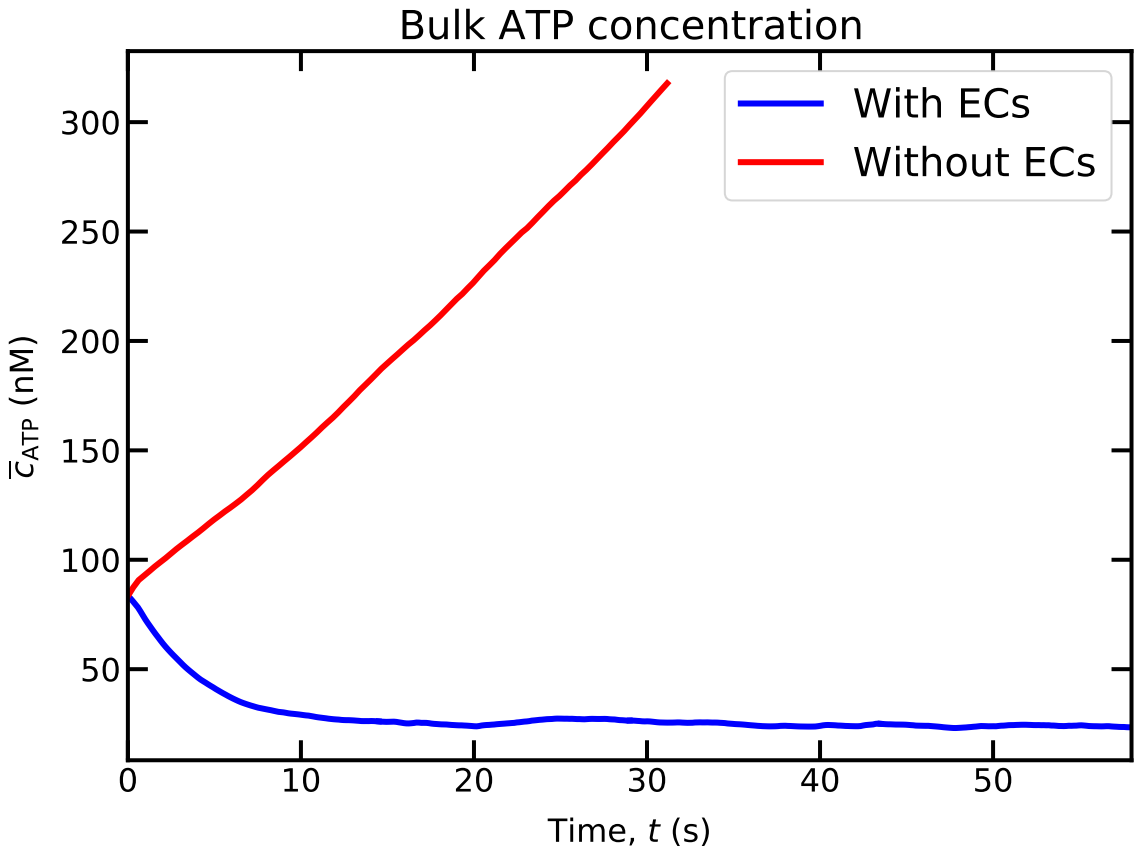

Figure 4.4: The evolution of bulk ATP concentration with time in the presence and absence of endothelium ($Ca = 22.5$, $Cn = 0.4$, and $Hct = 16.7\%$).

4.3.2 Wall ATP concentrations

Before we delve into coupling the endothelial response, specifically studying Ca^{2+} signaling, we embark on an exploration of how ATP concentrations exhibit variations along the top and bottom endothelium walls in a straight channel under different degrees of confinement (Cn). As anticipated, there emerges minimal divergence in ATP concentrations along both endothelial walls (see Figure 4.5(a)).

The discrepancy in ATP concentration between the two walls is negligible. This phenomenon can be attributed to the fact that as the simulation progresses over time, the RBCs within the channel eventually settle at equidistant positions from the walls. Consequently, RBCs adjacent to both walls experience equivalent shear stress

and ATP release, effectively leading to nearly identical ATP concentrations for both walls across all Cn values, as depicted in Figure 4.5(b).

Due to this (expected) symmetry in ATP concentration, we focus our attention on the maximum ATP concentration from the bottom wall, which serves as input for EC-mediated Ca^{2+} signaling across various Cn, Ca, and Hct configurations.

For a more comprehensive understanding of how ATP concentration varies across the channel under varying Cn values for a fixed Hct, we introduce the concept of normalized transverse average ATP concentration, as illustrated in Figure 4.5(b). In our study, we maintain a constant channel length for each Cn, leading to a reciprocal relationship between the number of RBCs and Cn while holding Hct constant. Normalizing the transverse ATP concentration to the average transverse ATP concentration of the corresponding Cn enables us to observe the variation in ATP concentration across the channel independently of the Cn effect.

A noticeable trend emerges, with higher ATP concentrations detected near the wall compared to the core region. This phenomenon can be attributed to the hydrodynamic interactions between neighboring cells, causing RBCs to spread closer to the wall. This proximity to the wall results in higher shear stress, prompting an elevated release of ATP. This concentration gradient of ATP near the wall holds significant implications for calcium signaling, a topic we shall delve into in forthcoming sections.

Interestingly, the normalized transverse ATP concentration remains fairly consistent across all Cn values. However, there is a subtle alteration in the normalized ATP concentration corresponding to variations in Cn. RBCs release a greater number of ATP molecules in highly confined channels ($Cn = 0.8$) compared to weakly confined channels. The nature of flow in highly confined channels compels RBCs to travel in a single file, closely approaching the wall. Consequently, they encounter heightened shear stress, leading to an increased ATP release compared to the scenario in weakly confined channels.

4.3.3 Effect of capillary number

We conducted a series of simulations, maintaining confinement (Cn) at 0.2, while varying capillary number (Ca) to replicate the diverse wall shear rates experienced by RBCs within microvascular networks. In actual microvascular systems, RBCs encounter distinct shear rates when navigating vessels of similar diameters. Figure 4.6(a) showcases the maximum time-averaged ATP concentration at the bottom wall. This concentration intensifies as Hct levels increase for each Ca setting. Key insights drawn from Figure 4.6(a) are as follows:

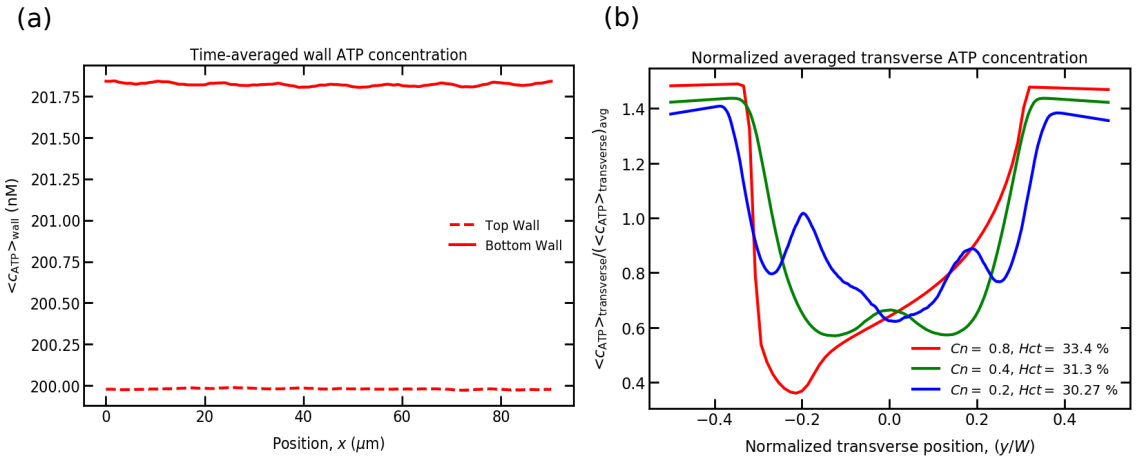

Figure 4.5: ATP concentrations are reported for $Ca = 90$. (a) Time-averaged wall ATP concentrations for $Cn = 0.8$ and $Hct = 33.4\%$; and (d) ratio between the time-and-flow direction-averaged ATP concentration to the corresponding average ATP concentration along the width of the channel for various Cn and Hct.

(i) The maximum ATP release capacity of a single RBC, as elucidated by Gou et al. [Gou et al., 2021], does not significantly determine the quasi-steady ATP concentration.

(ii) The final ATP concentration is contingent upon Hct, indicating that higher Hct values correspond to greater cumulative ATP concentration and overall ATP release.

(iii) At $Ca = 9$, the ATP concentration doesn't notably change with varying Hct, attributed to the failure to achieve the critical shear stress necessary for activating Px_1 hemichannels on the RBC membrane. Consequently, ATP concentration remains relatively constant.

(iv) As Ca increases (specifically $Ca = 22.5$ and 45), more Px_1 hemichannels open due to elevated shear stress on the RBC membrane. This opening surpasses the critical shear stress, leading to increased ATP release. EC-released ATP doesn't significantly impact lumen ATP concentration at these Ca values, and the contribution of CFTR in up-regulating Px_1 hemichannels is minor due to limited RBC membrane deformation.

(v) For higher flow strength ($Ca = 90$), almost all Px_1 hemichannels activate, assisted by CFTR up-regulation from RBC membrane deformation. Additionally, shear stress on ECs contributes to lumen ATP concentration. For elevated Hct

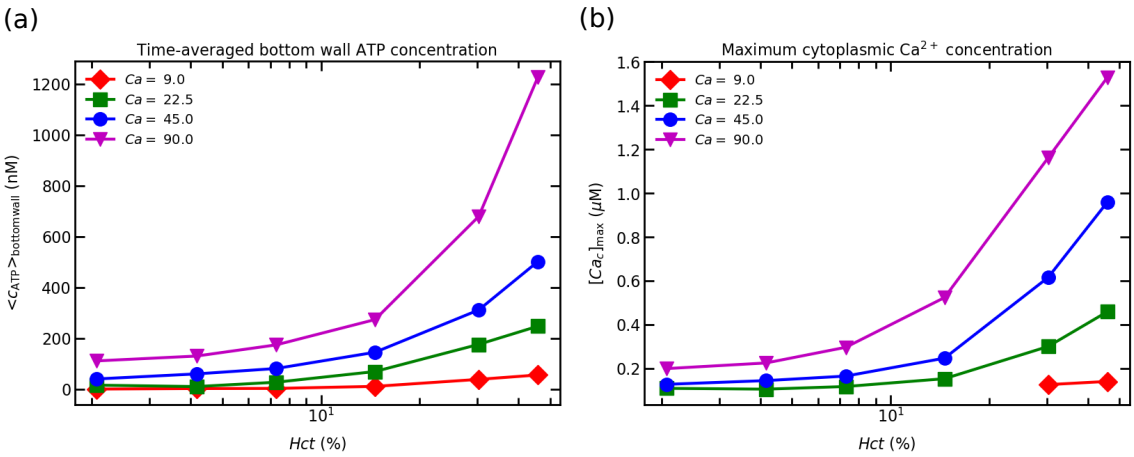

Figure 4.6: These results are obtained for $Cn = 0.2$ on the bottom wall of a 2-D channel: (a) maximum ATP concentrations on the bottom wall with varying Hct concentrations for various Ca; and (b) maximum cytoplasmic Ca^{2+} concentrations (transient peaks) obtained from the maximum ATP concentrations for different Ca.

and $Ca = 90$, more RBCs are displaced toward the wall due to cell-cell interactions, heightening shear stress, ATP release, and the ATP concentration.

(vi) ATP concentration at the wall displays linear behavior for dilute concentrations (up to 10%), transitioning into nonlinear growth as Hct increases.

Subsequently, we employ the ATP wall concentration as input to solve the Ca^{2+} signaling equations (Equations (3.16)-(3.20)). The maximum cytoplasmic Ca^{2+} concentration (Ca^{2+} peak) is presented in Figure 4.6(b). The EC response, represented by cytoplasmic Ca^{2+} concentration, follows the same pattern as the wall ATP concentration (refer to Figure 4.6(a)). The cytoplasmic Ca^{2+} concentration surpasses the homeostatic concentration of 0.1 μM for all combinations of Ca and Hct. Notably, the response at $Ca = 9$ is relatively minor compared to other Ca values. This is attributed to the low ATP concentration on the endothelial surface, insufficient for generating adequate IP_3 molecules by phosphorylating free receptors. Consequently, the concentration of IP_3 molecules required to activate IP_3R (inositol trisphosphate receptor) channels on the ER membrane is not achieved, hindering Ca^{2+} mobilization.

4.3.4 Effect of confinement

In this section, we explore the impact of varying confinement (Cn) on ATP and cytoplasmic Ca^{2+} concentration for $Ca = 45$. The results obtained with increasing

Cn generally align with observations from the preceding subsection. In addition, we deduce the following insights from Figure 4.7(a):

(i) Surprisingly, ATP concentrations for $Cn = 0.4$ and $Cn = 0.8$ are remarkably close to each other. This closeness is more pronounced within the dilute regime (up to $Hct = 10\%$). However, discernible differences become apparent beyond the dilute regime. Gou et al. [Gou et al., 2021] have reported that the ATP release level per RBC at $Cn = 0.8$ consistently surpasses that of $Cn = 0.4$ across all Hct concentrations. This discrepancy arises because, at $Cn = 0.8$, RBCs flow closely to the wall (refer to Figure 4.7(b)) in a train-like configuration for varying Hct values. Consequently, RBCs experience heightened membrane shear stress, elevating the ATP release level. However, for the same channel length, the higher number of RBCs in $Cn = 0.4$ results in an overall greater total ATP release level compared to $Cn = 0.8$.

(ii) A rapid escalation in ATP concentration is observed at $Cn = 0.2$. This phenomenon can be attributed to the emergence of complex cell-cell interactions and RBC dispersion within the channel. These factors result in heightened shear stress and membrane deformation, leading to elevated ATP concentration compared to other Cn values (specifically $Cn = 0.8$ and 0.4). Figure 4.7(c) visually illustrates that RBCs at $Cn = 0.4$ are orderly oriented and positioned closer to the channel center, while at $Cn = 0.2$, RBCs exhibit random orientation and distribution within the channel, as shown in Figure 4.7(d).

The maximum cytoplasmic Ca^{2+} concentration in an EC mirrors the ATP concentration trend (Figure 4.7(e)). It consistently rises with increasing Cn and Hct. Furthermore, higher maximum cytoplasmic Ca^{2+} concentration can facilitate the propagation of Ca^{2+} signals from regions with high cytoplasmic Ca^{2+} to those with lower concentrations.

Real vascular networks comprise diverse vessel sizes and local hematocrits. Based on the findings in Figure 4.7(e), it is plausible that ATP concentration might surpass the threshold value for calcium signaling in specific locations due to factors such as elevated Hct or significant shear stresses. This naturally prompts the question of calcium propagation within a vascular network. While this topic is reserved for future exploration, the current focus centers on addressing the transient peak time of cytoplasmic Ca^{2+} concentration. This investigation aims to illuminate the coordinated cellular mechanism governing calcium propagation within a vascular network.

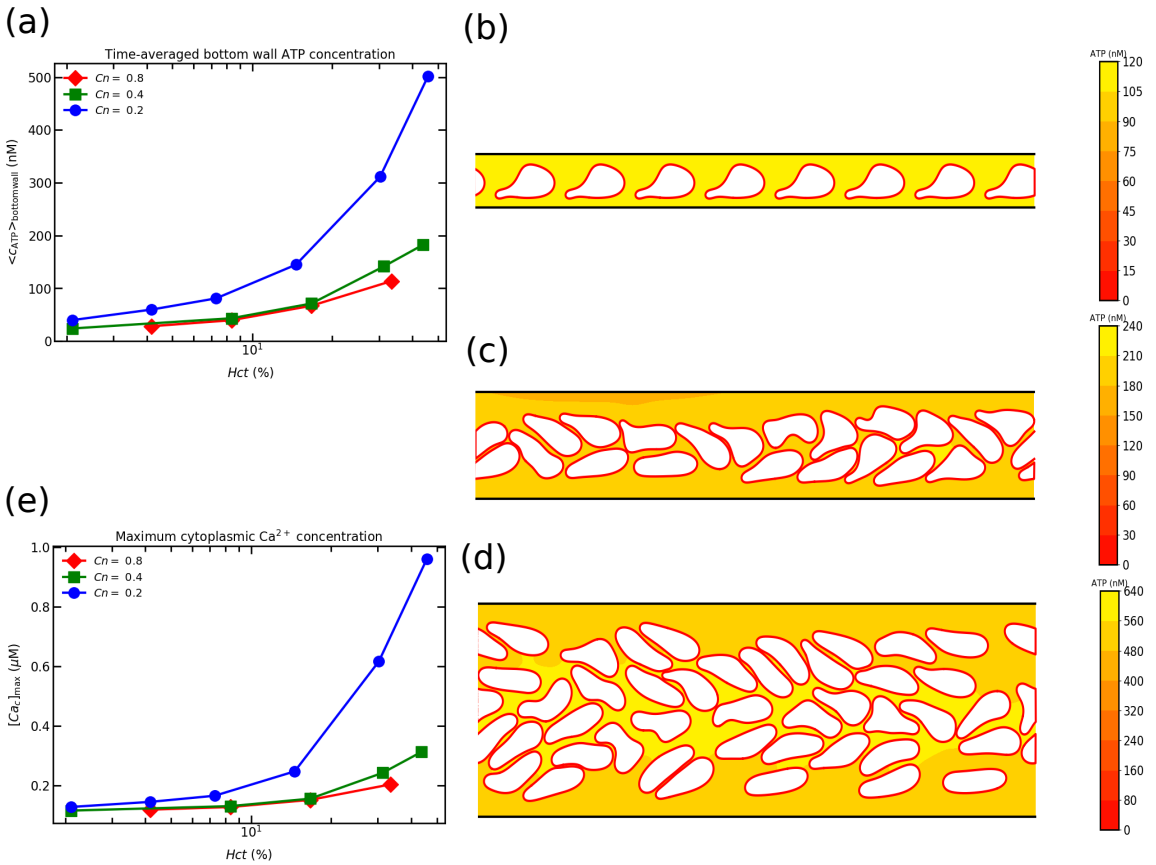

Figure 4.7: (a) Maximum ATP concentration on the bottom wall by varying Hct concentration for various Cn; (b) spatial concentration of ATP at $Cn = 0.8$, $Ca = 45$, $Hct = 33.4\%$, and $t = 18.56$ s; (c) spatial concentration of ATP at $Cn = 0.4$, $Ca = 45$, $Hct = 43.4\%$, and $t = 26.9$ s; (d) spatial concentration of ATP at $Cn = 0.2$, $Ca = 45$, $Hct = 45.9\%$, and $t = 25.87$ s; and (e) maximum cytoplasmic Ca^{2+} concentration (transient peak) obtained from the corresponding maximum ATP concentration for various Cn. All simulations are carried out for $Ca = 45$.

4.3.5 Cytoplasmic Ca^{2+} peak time

To delve into the possibility for intercellular communication within the vascular wall, we examine the transient peak time of cytoplasmic Ca^{2+}. The response of an endothelial cell (EC), indicated by the maximum cytoplasmic Ca^{2+} concentration, exhibits a dose-dependent relationship, i.e., higher ATP concentrations result in elevated cytoplasmic Ca^{2+} levels. This dependence between ATP and cytoplasmic Ca^{2+} is characterized by a sigmoidal curve [Nayak et al., 2023], primarily due to the fixed production quantity of IP_3 molecules. Furthermore, heightened ATP concentration leads to a reduction in the cytoplasmic Ca^{2+} transient time, while lower ATP concentration yields a more gradual response from ECs. This behavior is illustrated in Figure 4.8.

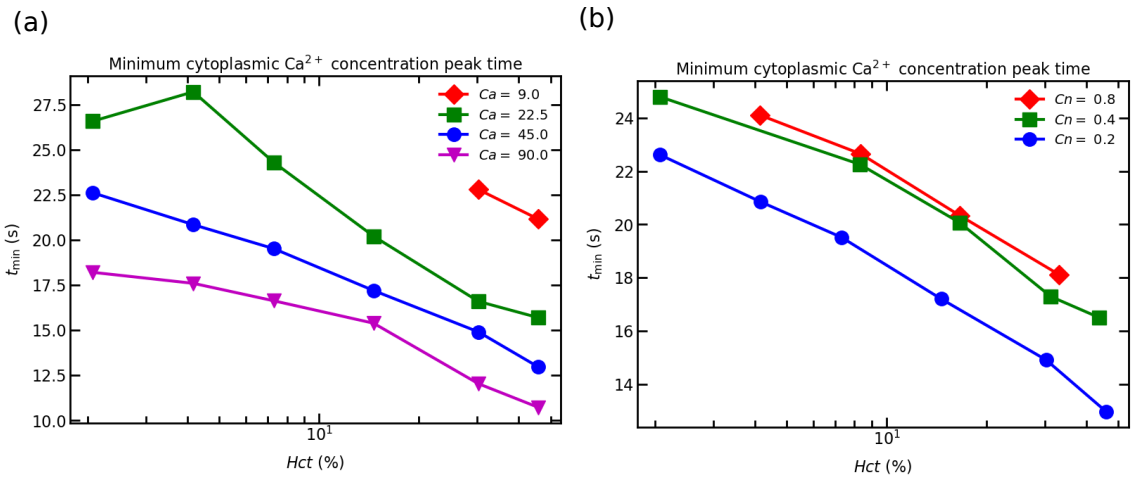

Figure 4.8: The cytoplasmic Ca^{2+} peak in an EC: (a) the peak time obtained by varying Hct concentration for different Ca and $Cn = 0.2$; and (b) the peak time obtained by varying Hct for different Cn and $Ca = 45$.

In Figure 4.8(a), we present the relationship between calcium peak time and Hct and Ca. The cytoplasmic transient time for a specific Ca diminishes as Hct concentration increases (refer to Figure 4.8(a)). Similarly, the transient peak time experiences a monotonic decrease with rising Ca. Importantly, the peak time difference between two distinct Ca values at a given Hct concentration varies between 2 to 5 seconds. This implies that calcium signals can propagate both downstream and upstream. This phenomenon is crucial for orchestrating cellular processes like cellular proliferation, wound healing, and vasodilation. However, as the propagation speed of calcium (around 10μm/s [Halidi et al., 2011, Leybaert and Sanderson, 2012, Sera et al., 2018]) is slower than blood flow velocity (in the range of mm/s in microcirculation), calcium can control vasodilation only in the upstream direction.

Figure 4.8(b) highlights that, for a given Hct concentration, there is very small difference in the cytoplasmic Ca^{2+} peak time between $Cn = 0.4$ and 0.8. In contrast, the peak time at $Cn = 0.2$ is significantly faster than those at $Cn = 0.4$ and 0.8. This discrepancy is attributed to the higher ATP concentration present at $Cn = 0.2$ (as shown in Figure 4.7(a)). Consequently, the potential for signal transfer from a wider channel (weakly confined) to narrower channels (strongly confined) exists. Experimental studies involving vascular networks stimulating a region with an agonist concentration [Uhrenholt et al., 2007, Seppey et al., 2010, Bagher et al., 2011] have observed Ca^{2+} propagation downstream to smaller vessel diameters. Our findings contribute to understanding Ca^{2+} propagation in both in-vitro and in-vivo vessel networks.

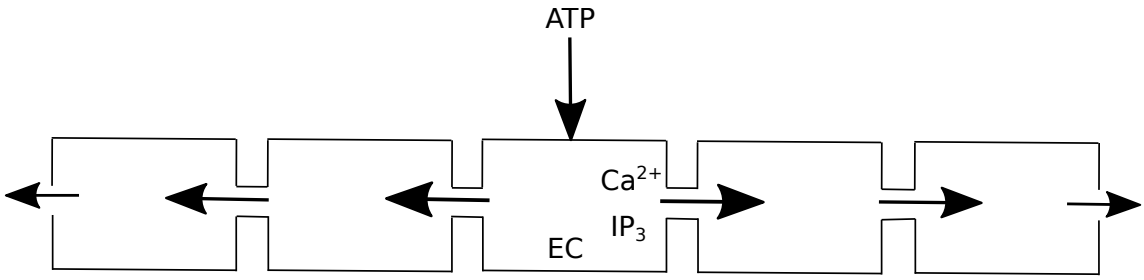

Figure 4.9: Schematic shows that a group of ECs are horizontally aligned and the middle EC is stimulated to a ATP concentration. Following stimulation, IP_3 and cytoplasmic Ca^{2+} diffuse through gap junctions into the neighboring ECs. IP_3 molecules then release sequestered Ca^{2+} from the neighboring ECs. The propagation of Ca^{2+} ions continues until IP_3 molecules are able to activate IP_3R (inositol trisphosphate receptor) present on ER membrane. The width of the arrow indicates the strength of propagation of IP_3 molecules and cytoplasmic Ca^{2+} into the neighboring ECs.

4.3.6 Calcium wave propagation

Intercellular Ca^{2+} waves orchestrate synchronized cellular activities such as cell proliferation, division, and the transmission of vasodilation signals both upstream and downstream within blood vessels [Leybaert and Sanderson, 2012]. Illustrating the propagation of a Ca^{2+} wave from an endothelial cell (EC) stimulated by a high ATP concentration to its neighboring ECs, we conduct a simple study focusing on a cluster of horizontally aligned ECs. These cells communicate through gap junctions, specialized channels that enable the transfer of Ca^{2+} and IP_3 to adjacent ECs [Sera et al., 2018]. Notably, this is just one among several mechanisms facilitating Ca^{2+} and IP_3 diffusion within the vascular wall.

Additionally, other mechanisms contribute to Ca^{2+} propagation within the vascular wall. One such mechanism involves the transmission of action potentials through ECs and smooth muscle cells (SMCs) from the stimulated site (where high ATP concentration is present) [Domeier and Segal, 2007] to nearby ECs and SMCs. Furthermore, the release of ATP from an EC into the extracellular space due to mechanical stimulation, followed by the diffusion of ATP, results in the propagation of Ca^{2+} waves across substantial distances within the vascular wall [Edwards and Gibson, 2010, Yamamoto et al., 2011]. To explore the phenomenon of intercellular Ca^{2+} waves within the present model, we initiate with the same set of model equations as described in Subsection 4.2.4. However, we extend the model by incorporating the spatial variation of IP_3 and cytoplasmic Ca^{2+} concentrations. This extension is achieved by introducing the diffusion of IP_3 and cytoplasmic Ca^{2+} into Equations (3.18)-(3.19).

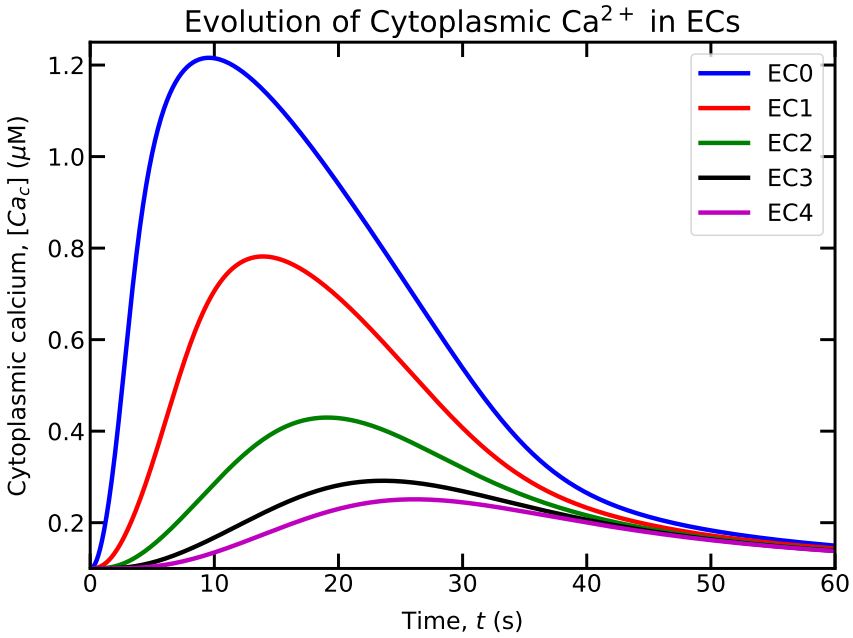

Figure 4.10: Evolution of cytoplasmic Ca^{2+} concentration for the stimulated EC as well as ECs on the right hand side of that EC. The stimulated EC is treated with 1 μM concentration of ATP.

Thus, the modified equations (Equations (3.18)-(3.19)) take on the following form:

$$\frac{\partial\,[\mathrm{IP_3}]}{\partial t} = D_{\mathrm{IP_3}}\frac{\partial^2[\mathrm{IP_3}]}{\partial x^2} + q_{\mathrm{gen}} - q_{\mathrm{deg}}\,, \tag{4.12}$$

$$\frac{\partial\,[Ca_c]}{\partial t} = D_{\mathrm{ca}}\frac{\partial^2[Ca_c]}{\partial x^2} + \beta\left(q_{\mathrm{rel}} - q_{\mathrm{serca}} + q_{\mathrm{leak}} + q_{\mathrm{soc}} + q_{\mathrm{in}} - q_{\mathrm{pmca}}\right)\,, \tag{4.13}$$

where $D_{\mathrm{IP_3}}$ is the diffusion coefficient of $\mathrm{IP_3}$ (i.e., 280 $\mu\mathrm{m}^2/\mathrm{s}$ [Sera et al., 2018]), and D_{ca} is the effective cytoplasmic diffusion coefficient of Ca^{2+} (i.e., 20 $\mu\mathrm{m}^2/\mathrm{s}$ [Sera et al., 2018]). The boundary conditions at the EC-EC interface are

$$D_{\mathrm{IP_3}}\frac{\partial\,[\mathrm{IP_3}]}{\partial x} = P_{\mathrm{IP_3}}\left([\mathrm{IP_3}]_+ - [\mathrm{IP_3}]_-\right)\,, \tag{4.14}$$

$$D_{\mathrm{ca}}\frac{\partial\,[Ca_c]}{\partial x} = P_{\mathrm{ca}}\left([Ca_c]_+ - [Ca_c]_-\right)\,, \tag{4.15}$$

where $P_{\mathrm{IP_3}}$ and P_{ca} are the permeability rate constants for $\mathrm{IP_3}$ and cytoplasmic Ca^{2+}, which are estimated to 0.05 μm/s and 5.0 μm/s, respectively [Sera et al., 2018]. $[\mathrm{IP_3}]_+$ and $[\mathrm{IP_3}]_-$ are $\mathrm{IP_3}$ concentrations on either sides of the boundary, and $[Ca_c]_+$ and $[Ca_c]_-$ are cytoplasmic Ca^{2+} concentrations on either sides of the boundary. The concentration variation in the lateral direction is smaller than that in the longitudinal direction, implying that molecular diffusion occurs more rapidly in the lateral

direction. For the purpose of demonstration, we limit our investigation to a cluster of 9 endothelial cells (ECs). Specifically, there are 4 ECs on each side of the stimulated EC. For instance, we locally stimulate the middle EC (indicated by the downward arrow in Figure 4.9) with a concentration of 1 μM ATP. This localized stimulation triggers signal propagation on both sides of the stimulated EC. The stimulated EC is designated as "EC0", and the ECs to its right are labeled as "EC1", "EC2", "EC3", and "EC4". Similarly, the ECs to its left are named "EC5", "EC6", "EC7", and "EC8". We maintain the constants as provided in Table 3.1, with the exception of altering the values of K_r and k_2 to 0.5 μM and 0.02 s^{-1} respectively, to assess their impact on the speed of Ca^{2+} wave propagation.

Because of the symmetry of the problem, we present the evolution of cytoplasmic Ca^{2+} (shown in Figure 4.10) for ECs on the right hand of the stimulated EC ("EC0") such as "EC1", "EC2", "EC3", and "EC4". As we move away from "EC0", we find variations in cytoplasmic Ca^{2+} peak magnitude as well as in peak time in the neighboring ECs. The increase in Ca^{2+} concentration in ECs neighboring to "EC0" is due to the fact that IP_3 molecules diffuse from "EC0" to "EC1" and eventually to other ECs. As a consequence, the action of these molecules on IP_3R channels results in release of Ca^{2+} from the ER. In Figure 4.10, we find that the Ca^{2+} peak in "EC1" occurs approximately 2 s after that in "EC0". Therefore, in the average sense, the Ca^{2+} signal moves at a speed of 5 μm/s. As we move further away from "EC1", the speed of the Ca^{2+} signal decays. This is due to the fact that the concentration of IP_3 decreases as it moves away from "EC0" because of passive diffusion of IP_3 molecules between ECs (Equation (4.14)) and the degradation of its concentration in ECs (third term in Equation (4.12)). Consequently, a decline in the cytoplasmic Ca^{2+} peak concentration is observed (shown in Figure 4.10).

In experiments [Halidi et al., 2011, Leybaert and Sanderson, 2012, Long et al., 2012, Sera et al., 2018], it has been reported that the Ca^{2+} wave can propagate at a speed of 10 μm/s or more, which compares well with the above order of magnitude. However, an important remark is in order. We have not observed in our simulations a Ca^{2+} wave front movement, strictly speaking, in contrast to experiments [Halidi et al., 2011, Leybaert and Sanderson, 2012, Long et al., 2012, Sera et al., 2018]. It is likely that for wave front propagation to occur, an active generation of Ca^{2+} or IP_3 would be required in the neighboring cells while Ca^{2+} or IP_3 spreads from the stimulated cell through cell-cell junction [Schuster et al., 2002, Leybaert and Sanderson, 2012, Long et al., 2012]. This effect will be thoroughly investigated in the future in order to have a complete picture of wave propagation.

4.4 Conclusions

In this chapter, we have successfully integrated the dynamic behavior of red blood cells (RBCs) within a parabolic flow with the intricate dynamics of calcium ions (Ca^{2+}). While the primary function of RBCs is to facilitate gas exchange between lungs and tissues, they also play a crucial secondary role. RBCs release ATP as a signaling molecule in response to flow conditions. These ATP molecules act as messengers, transmitting signals from the external environment to the endothelial cells (ECs), initiating the release of ubiquitous Ca^{2+} ions. The presence of Ca^{2+} ions plays a pivotal role in regulating numerous enzymatic functions. Notably, Ca^{2+} governs the production of nitric oxide (NO), a vasodilator crucial for maintaining vascular tone and overall cellular function. Consequently, this intricate system occurring in the vascular wall plays a vital role in both cellular regulation and vascular homeostasis.

To delve into the intricate relationship between RBC dynamics and biochemical signaling, we conducted a series of numerical simulations. By systematically varying parameters such as channel width (Cn), flow strength (Ca), and RBC concentrations (Hct) in a straight channel, we sought to uncover the underlying mechanisms. Employing the Immersed Boundary Lattice Boltzmann Method (IBLBM), we solved fluid-RBC interactions and ATP release mechanisms. Our investigation addressed a range of unanswered questions, including the impact of maximum ATP release levels on wall ATP concentration, the variation of ATP concentrations on vascular walls, the interplay between flow strength and confinement, and the potential existence of Ca^{2+} wave propagation within a vascular network.

While our study was conducted within a straight channel, it establishes a solid foundation for comprehending RBC dynamics in the context of biochemical signaling under diverse (patho)physiological conditions. Our work can be extended to more complex vascular networks where RBCs experience varying shear rates, local variations in Hct concentrations, ATP concentrations across different branches, and the propagation of Ca^{2+} signals throughout upstream and downstream vessel branches. These expansions would contribute significantly to our understanding of localized blood flow regulation in real-world scenarios.

Moreover, beyond ATP release, RBCs are also recognized as potential scavengers of NO, a vasodilator [Wei et al., 2019]. Therefore, a comprehensive investigation is warranted to unveil the intricate interplay between factors such as the cell-free layer (CFL), ATP concentration, RBC concentrations, Ca^{2+} concentration, and their combined effects on the bioavailability of NO within the vascular wall. Such endeavors

would not only advance our scientific knowledge but also provide insights into the multifaceted mechanisms governing vascular health and function. The next chapter deals with NO kinetics.

Chapter 5

Nitric Oxide Modeling and its Bioavailability Influenced By Red Blood Cells

In Chapter 4, we carried out simulations by coupling the release of ATP from red blood cells (RBCs) and endothelial cells (ECs) when subjected to shear stress and followed by the activation of biochemical signals, triggering the release of Ca^{2+} from the endoplasmic reticulum (ER). The rise of Ca^{2+} concentration in cytoplasm of ECs regulates an effector known as endothelial nitric oxide synthase (eNOS). This effector helps in synthesizing nitric oxide (NO), an important vasodilator. NO acts on smooth muscle cells (SMCs), which lie one layer below ECs, to relax them and thus control local blood perfusion by increasing vessel diameter. As a result, more blood flows to a location where tissue metabolic needs are high. In addition, RBC can also convert NO into stable metabolites, such as nitrite and nitrate at higher rates, affecting the bioavailability of NO in blood vessels. It therefore affects vascular homeostasis.

To understand how RBC affects NO availability in the microvascular network, a mathematical model that accounts for different pathways that lead to NO generation in ECs is developped. Although there have been several proposed models for NO in the literature [Koo et al., 2013, Kirby et al., 2016, Sriram et al., 2016], we are not aware of a model which accounted for agonist (ATP)-dependent NO generation. In this Chapter, we have developed a NO model by incorporating Ca^{2+} dynamics model proposed in Chapter 3. In addition, we have also taken into account pathways related to shear stress-dependent NO synthesis in EC (discussed in Subsections 5.2.1.1 and 5.2.1.2). The proposed model results are qualitatively consistent with experimental observations.

Later in this Chapter (Subsection 5.2.2), we have explicitly considered RBC dynamics, ATP release from ECs and RBCs, Ca^{2+} signaling, NO generation, and its diffusion and scavenging by RBCs. This intricately coupled system has been studied for a two-dimensional (2-D) straight channel by varying its channel width and for different RBC concentrations. The main results are reported in Section 5.3. Some of the intriguing results are (i) increased RBC concentrations lead to increased ATP and cytoplasmic Ca^{2+} concentrations ("faster-is-faster" response) for all variation in width of the channel, however, NO concentration shows "faster-is-slower" response, (ii) NO availability depends on RBC distribution, at least in confined channel like capillaries, (iii) two phases of NO availability have been observed in different regions of the vessel, a phase of high NO concentration at low RBC concentration and a phase with no change in NO concentration at high RBC concentration for all confinements, and (iv) NO availability in weakly confined channels, although there is no significant changes in its concentration, is greater than in a strongly confined channel at high RBC concentration.

5.1 Introduction

Red blood cell (RBC) is a major component that flows through the circulatory system. Its primary function is to transport oxygen from the lungs to the tissues and carbon dioxide from the tissues to the lungs. Another important function of RBC is to synthesize adenosine triphosphate (ATP) from glucose without oxygen intervention through the process of glycolysis. It should be noted that, due to the absence of nuclei and mitochondria, RBCs are unable to utilize oxygen molecules bound to hemoglobin proteins for the synthesis of ATP molecules. RBC releases ATP molecules into the extracellular space under the influence of external flow [Forsyth et al., 2011, Zhang et al., 2018]. ATP molecules diffuse from the lumen to the inner surface of the vascular wall. The inner layer of a blood vessel is lined with endothelium, an assembly of endothelial cells (EC). The endothelium acts as a semi-permeable membrane, allowing nutrients to pass from the vascular lumen to the surrounding tissues. Recall that ATP molecules bind to purinergic receptors, $P2Y_2$, present on the surface of ECs. As a result, a cascade of biochemical reactions is activated to trigger Ca^{2+} mobilization from the endoplasmic reticulum (ER) [Tran et al., 2000]. [Berridge et al., 2003]. The mobilization of Ca^{2+} from the ER occurs due to reaction of neurotransmitters or hormones to their respective receptors available on the cell surface [Dubyak and El-Moatassim, 1993]. The transmission of signal from the extracellular space to the

release of Ca^{2+} from the ER follows a series of intermediate biochemical reactions, as described in the previous chapter. For instance, the reaction of ATP with purinergic receptor $P2Y_2$ leads to production of inositol trisphosphate (IP_3) from hydrolysis of Phosphatidylinositol 4,5-bisphosphate (PIP_2) and subsequent action of IP_3 on the IP_3 receptors (IP_3R) on the membrane of the ER leads to release of sequestered Ca^{2+} [Dull and Davies, 1991].

The cytoplasmic free Ca^{2+} binds to the calmodulin protein to form a calcium-calmodulin complex. This complex activates caveolin-bound endothelial nitric oxide synthase (eNOS). eNOS contributes to the synthesis of an important vasodilator, nitric oxide (NO), from its precursor, L-arginine (L-Arg) [Davignon and Ganz, 2004]. In addition, shear stresses experienced by ECs can produce NO in the presence of physiological Ca^{2+} [Cai et al., 2000]. However, the pathways leading to NO production is still unclear. Nevertheless, shear stresses are involved in cell remodeling and signal transduction. Sriram et al. [Sriram et al., 2016] presented a shear-dependent NO production model in which they took into account shear-dependent Ca^{2+} release from the ER, and ultimately this leads to NO synthesis from L-Arg. In their model, Ca^{2+} is released from the ER due to G-protein activation by shear stress. In addition, ECs sense shear stress via integrins, enabling them to bind to extracellular matrix proteins and leading to the activation of enzymes such as protein kinase-B (PKB/Akt) and protein kinase-C (PKC). Consequently, NO production is augmented. It is worth mentioning that the activation of these enzymes is both Ca^{2+}-dependent and Ca^{2+}-independent [Fleming and Busse, 1999, Boo et al., 2003, Xu et al., 2017]. Moreover, the pathways involving NO production are unclear, being either Ca^{2+}-dependent or independent in the presence of shear stress.

In addition to the work of Sriram et al. [Sriram et al., 2016], other NO models proposed in the literature have considered NO production rate as a function of shear stress [Koo et al., 2013, Kirby et al., 2016]. Other studies [Yang et al., 2005, Kapela et al., 2009] have examined the impact of NO (supplied by an exogenous or endogenous source) on biochemical pathways, occurring in smooth muscle cells (SMCs). Chen et al. [Chen and Popel, 2006] analyzed the biochemical pathways of NO synthesis and formulated a model to estimate NO production from the L-Arg source. In these models, NO production due to agonist, such as ATP and bradykinin, dependent Ca^{2+} dynamics is not incorporated. However, agonist-dependent NO production is observed experimentally in [Blatter et al., 1995, Dong et al., 2004, Xu et al., 2017]. Furthermore, the response time of NO production is faster in agonist-dependent NO production than in shear-dependent NO production. This must therefore be reckoned into

account when developing a NO model, in order to emulate a rapid NO response from the EC. To account for agonist-dependent Ca^{2+} dynamics, Dormanns et al. [Dormanns et al., 2016] have proposed a NO model in which they consider agonist-dependent NO production. This model does not contemplate the homeostasis of cytoplasmic Ca^{2+} concentration in the presence of agonist. Therefore, we have recently developed a homeostatic Ca^{2+} model in which intracellular homeostasis of cytoplasmic Ca^{2+} [Ca_c], IP_3 [IP_3], and ER Ca^{2+} [Ca_s] concentrations is maintained in the presence of stimulus (ATP) [Nayak et al., 2023], a model described in the previous chapter. The first and foremost aim of the present study is to use the Ca^{2+} homeostatic dynamics model in the development of an NO model for an EC. Secondly, we incorporate shear-dependent NO generation into the Ca^{2+} dynamics model. For this, we will use the model proposed by Sriram et al. [Sriram et al., 2016]. Using this model, we will obtain a minimized model that reproduces exactly the same results as those produced in the full scale model proposed by Sriram et al. [Sriram et al., 2016]. We have taken into account both agonist (ATP) and shear stress-dependent pathways for completeness of NO modeling, but we limit our study to small time scales ($\sim$ 5s) where ATP-dependent NO production plays an important role. Furthermore, Sriram et al. [Sriram et al., 2016] have reported NO production at $\sim 10^5$ s time scales, which is difficult to simulate in our simulation.

Our final objective is to use NO modeling equations for a large-scale simulation, a vessel several orders of length long, to study NO bioavailability in the presence of realistic blood flow conditions. NO diffuses into the vascular lumen as well as into the adjacent SMC layer. The SMC relaxes under the action of NO. As a result, the diameter of the vessel increases, promoting oxygen delivery to an area of high metabolic demand. Meanwhile, NO molecules diffuse into the vascular lumen and are scavenged by the RBCs. There are two possible tasks for RBC during NO scavenging: (i) they convert NO to nitrite or nitrate, which acts as a reservoir to deliver NO to the hypoxic region by converting nitrite to NO [Buerk et al., 2017] and (ii) they excrete excess NO in the form of urine to prevent the negative health effects of NO [Ånggård, 1994]. NO bioavailability means that it escapes being scavenged by RBCs at the rate of 10^6 s^{-1} [Wei et al., 2019] and are available for SMCs relaxation. Most studies have not explicitly taken into account RBC dynamics to understand NO bioavailability in a vessel [Kavdia et al., 2002, Deonikar and Kavdia, 2010, Ong et al., 2012, Deonikar and Kavdia, 2013, Deonikar et al., 2014, Qian et al., 2020]. [Ong et al., 2012, Deonikar et al., 2014, Wei et al., 2019], found that an increase in hematocrit concentration leads to a decrease in NO bioavailability. This is due to a decrease

in the cell free layer (CFL) which pushes RBCs closer to the endothelium. As a result, the rate of NO scavenging increases regardless of flow strength. However, its bioavailability increases as resistance to NO diffusion across the RBC membrane increases. A similar study was carried out by [Wei et al., 2019] in the presence of RBCs. They found the same behaviour as in previous studies [Deonikar and Kavdia, 2010, Ong et al., 2012, Deonikar and Kavdia, 2013] where RBCs dynamics were not explicitly taken into account. However, for a given flow strength, it is unclear whether increasing hematocrit concentration will affect NO bioavailability, given that ATP concentration increases with increasing hematocrit concentration. ATP concentration, which triggers NO signaling, comes mainly from RBCs and ECs when they are subjected to shear stress [John and Barakat, 2001, Zhang et al., 2018]. We delve into how NO bioavailability varies with changes in RBC confinement, as RBC traverses vessels of different diameters. The effect of confinement will give an idea about the control of local blood supply in a realistic microvascular network.

5.2 Methods

We impose a pressure-driven Poiseuille flow, with a velocity field along the $x-$direction given by

$$v_x = v_{\max}\left[1 - \left(\frac{y}{W/2}\right)^2\right],$$

where $v_{\max}$ is the maximum flow velocity at the center of the channel, of width W, as shown in Figure 5.1 and $y = [-W/2, W/2]$. We start the numerical simulation from the equilibrium shape of the vesicle, i.e., biconcave, using the following definition for the reduced area,

$$\nu = \frac{4\pi A}{P^2},$$

where $A = \pi R_0^2$, and P is the perimeter of the vesicle. In this numerical simulation, we have taken, $\nu = 0.65$, which is the physiological value for a healthy RBC.

The bulk equations and boundary conditions for fluid flow and advection-diffusion for ATP (c_{ATP}) have been presented in Chapter 2. In addition, the modeling of ATP release and the boundary conditions used for obtaining ATP concentration in plasma have been presented in Chapter 4 (Subsections 4.2.1 and 4.2.2). The elicitation of Ca^{2+} dynamics in the EC, following the reaction of ATP molecules with $P2Y_2$ receptors have been given in Chapter 4 (Subsection 4.2.4). In following section, we will elaborately detail the modeling of NO production in the EC.

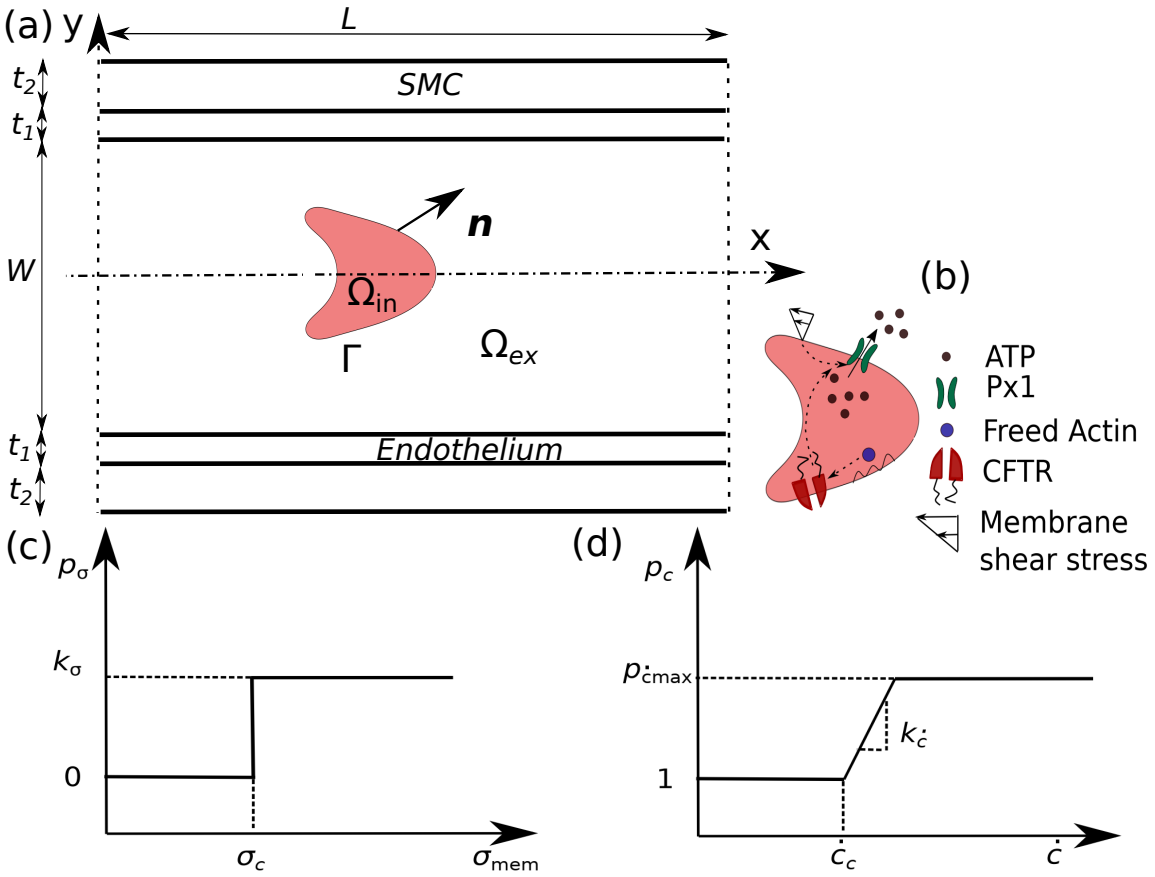

Figure 5.1: Schematic shows: (a) RBC moves in a straight two-dimensional channel (2-D) whose lower and upper walls are lined with two layers such as endothelium and SMC. The thicknesses of layers are t_1 and t_2, respectively. Note that in the text, we study a case where the vascular wall has no SMC layer, which is very close to the study of capillaries; (b) pathways by which RBC releases ATP molecules when subjected to shear stresses; (c) opening of Pannexin1 (Px_1) hemichannels when membrane shear stress exceeds critical shear stress; and (d) Px_1 is up-regulated by the cystic fibrosis transmembrane conductance regulator (CFTR) when the rate of curvature change surpasses the critical rate of curvature change.

5.2.1 Nitric oxide dynamics model of endothelial cell

5.2.1.1 ATP-mediated NO dynamics modeling

After the release of Ca^{2+} sequestered from the ER following the reaction of ATP with $P2Y_2$ receptors, free cytoplasmic Ca^{2+} forms a complex with the protein calmodulin (CaM). This complex contributes to NO production by activating caveolin-bound eNOS as shown in Figure 5.2. The reaction between cytoplasmic Ca^{2+} and CaM is much faster than the time scale of Ca^{2+} dynamics [Sriram et al., 2016]. Therefore, we can mathematically write the reaction between cytoplasmic Ca^{2+} and CaM as an

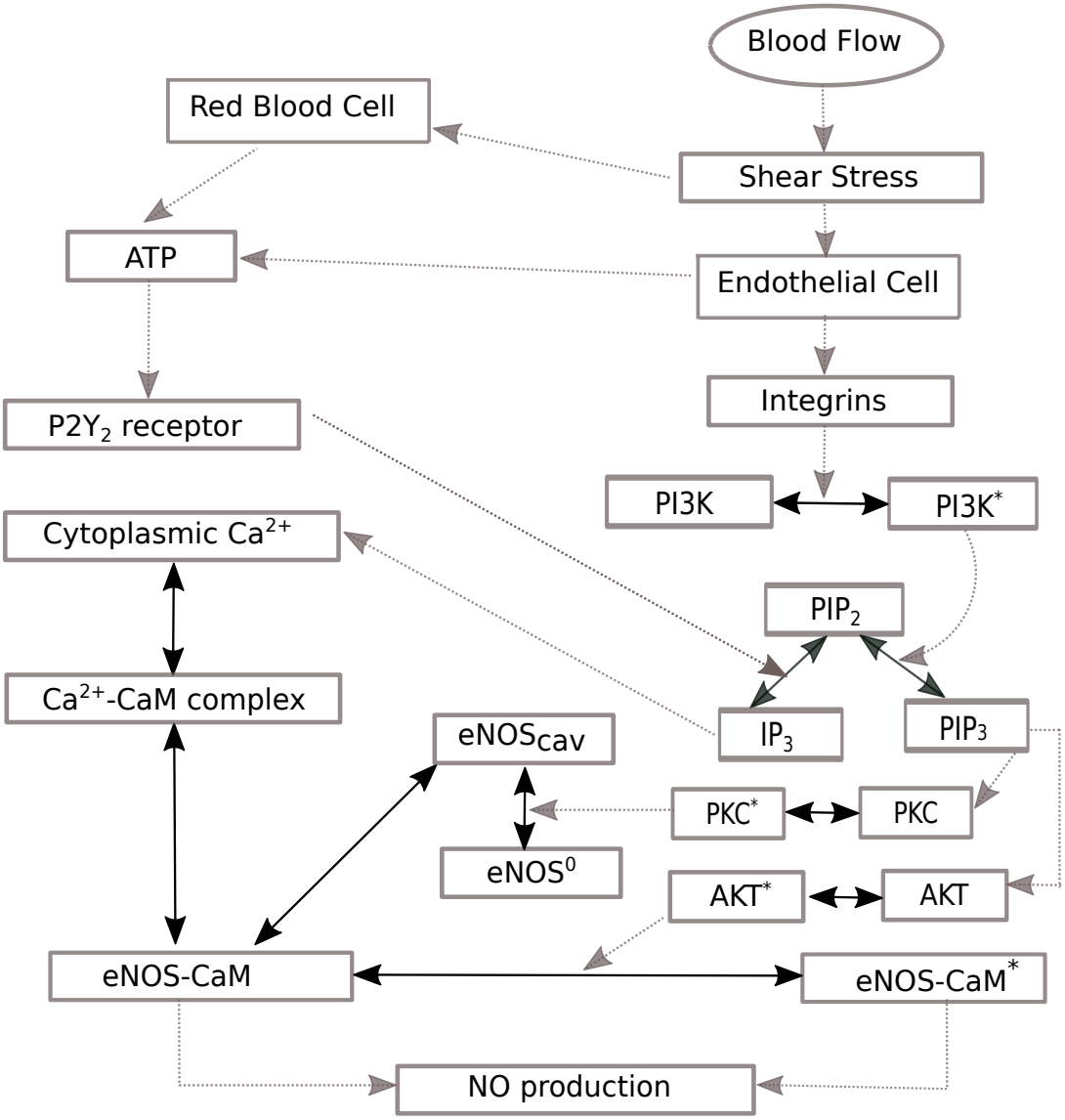

Figure 5.2: This diagram shows the reaction network for NO production pathways in an endothelial cell (EC). Adenosine triphosphate (ATP) released by red blood cells (RBCs) and ECs under flow reacts with $P2Y_2$ receptors, resulting in the mobilization of Ca^{2+} from the endoplasmic reticulum (ER). The increase in cytoplasmic Ca^{2+} concentration forms a Ca^{2+}-CaM complex and subsequently activates endothelial nitric oxide synthase (eNOS) from an inactivated form of caveolin-bound eNOS ($eNOS_{cav}$). At the same time, the shear stress-mediated integrin protein pathway is activated. As a result, protein kinase A (Akt) and protein kinase C (PKC), i.e., the AKT* and PKC* enzymes, are activated. The AKT* and PKC* enzymes increase and decrease NO production respectively. A straight line with a double arrow represents a reversible reaction, while a straight line with a single arrow regulates upstream and downstream reactants or products. The full form of the abbreviations is detailed in the modeling section. This network diagram is adopted from Sriram et al. [Sriram et al., 2016] and modified by including flow-dependent ATP release from RBCs and ECs, triggering activation of NO pathways.

algebraic equation, i.e.,

$$[\text{Ca-CaM}] = \Theta \frac{[Ca_c]^{\beta}}{K_{\text{dCaM}}^{\beta} + [Ca_c]^{\beta}} [\text{CaM}]_{\text{t}} \,, \tag{5.1}$$

where Θ is a limiting factor, β is the Hill coefficient, K_{dCaM} is the apparent Ca-CaM dissociation constant, and $[\text{CaM}]_{\text{t}}$ is the total number of CaM proteins. Formation of Ca-CaM complex leads to activation of the caveolin-bound eNOS (eNOS_{cav}) enzyme [Fleming and Busse, 1999], resulting in formation of the eNOS-CaM complex. Thus, the rate of change of eNOS-CaM concentration ([eNOS-CaM]) becomes [Sriram et al., 2016]

$$\frac{d[\text{eNOS-CaM}]}{dt} = k_{\text{CaM}}^{+} \frac{[\text{Ca-CaM}]}{K_{\text{Ca-CaM}} + [\text{Ca-CaM}]} [\text{eNOS}_{\text{cav}}] - k_{\text{CaM}}^{-} [\text{eNOS-CaM}] \,, \tag{5.2}$$

where k_{CaM}^{+} and k_{CaM}^{-} are the forward and backward rate constants, $K_{\text{Ca-CaM}}$ is the Michaelis-Menten constant, and $[\text{eNOS}_{\text{cav}}]$ is the concentration of caveolin-bound eNOS enzyme. From the conservation of mass for eNOS concentration, the total eNOS concentration ($[\text{eNOS}]_{\text{t}}$) is derived as $[\text{eNOS}_{\text{cav}}] + [\text{eNOS-CaM}] = [\text{eNOS}]_{\text{t}}$. The formation of an eNOS-CaM complex results in the production of NO from the oxidation of L-arginine (L-Arg) in the presence of eNOS-CaM complex [Snyder, 1992]. The NO produced in an EC diffuses into SMC and vascular lumen. NO molecules diffusing into the SMC are scavenged by soluble guanylate cyclase (sGC), resulting in the phosphorylation of cyclic guanosine monophosphate (cGMP) to guanosine triphosphate (GTP) [Zhao et al., 2015]. As a result, the SMC relaxes from the state of contraction to relaxation. Similarly, NO molecules diffused into the vascular lumen are scavenged by RBCs [Su et al., 2020]. Thanks to this NO molecule scavenging mechanism, excessive NO concentration is eliminated, otherwise it can be fatal to human health [Ånggård, 1994]. Taking them into account in the NO modelling, we obtain the following equation for NO

$$\frac{d[\text{NO}]}{dt} = Q_{\text{NO}} - Q_{\text{sGC}} - \lambda_{\text{NO}} [\text{NO}] \,, \tag{5.3}$$

where Q_{NO} is the rate of NO production, Q_{sGC} is the rate of NO scavenging in the SMC by sGC, and λ_{NO} is the rate at which NO molecules are scavenged by RBC. The expanded forms of Q_{NO} and Q_{sGC} are therefore as follows

$$Q_{\text{NO}} = \Psi [\text{eNOS-CaM}] \,, \tag{5.4}$$

and

$$Q_{\text{sGC}} = R_{\text{NO}}^{\max} \frac{[\text{NO}]^2 + b_1 [\text{NO}]}{a_0 + a_1 [\text{NO}] + [\text{NO}]^2} [\text{sGC}] \,, \tag{5.5}$$

where Ψ is the rate constant for NO production in the presence of a constant supply of oxygen and L-Arg; $R_{\mathrm{NO}}^{\max}$, b_1, a_0, and a_1 are constants; [sGC] is the concentration of sGC, which is assumed to be constant in the numerical simulation.

5.2.1.2 Coupling shear-induced NO

In the last subsection, we did not consider the role of shear stress in NO synthesis. Shear stress-dependent NO production is both dependent on and independent of cytoplasmic Ca^{2+} concentrations [Kuchan and Frangos, 1994, Frangos et al., 1996, Ungvari et al., 2001, Xu et al., 2017]. For example, chelation of extracellular Ca^{2+} by EGTA does not release any NO [Kanai et al., 1995], proving that NO synthesis is Ca^{2+}-dependent. In some experiments [Kuchan and Frangos, 1994, Frangos et al., 1996], a two-phase response (NO synthesis) to shear stress has been observed. A rapid increase in the NO production rate has been observed, which is similar to bradykinin dependent-NO synthesis. The second sustained phase is independent of cytoplasmic Ca^{2+} concentration. The latter phase is due to direct phosphorylation of eNOS-sites [Sandoo et al., 2010]. The former operates on a shorter time scale, whereas the latter operates on a longer time scale [Berk et al., 1995]. Although NO release in a rapid phase is dependent on the cytoplasmic Ca^{2+} concentration, the question about pathways that involves an increase of the cytoplasmic Ca^{2+} remains unanswered. There are enough evidences to support the hypothesis of shear stress dependent ATP release to the extracellular space [Berk et al., 1995, Yamamoto et al., 2000a, Hong et al., 2006, Kawai et al., 2010]. ATP molecules activate the G-protein pathway to release Ca^{2+} from the ER [Shen et al., 1992]. We have already modeled ATP-dependent NO release from the EC in the previous subsection. In this subsection, we will include shear-dependent sustained NO release phase (slower time scale) into the ATP-dependent NO release model.

Integrin senses the fluid shear stress due to blood flow [Tzima et al., 2001]. It rapidly phosphorylates phosphoinositide 3-kinase (PI3K) into an activated form of PI3K (PI3K*). Activation of PI3K leads to the production of phosphatidylinositol (3–5)-trisphosphate (PIP_3) from PIP_2, as shown in Figure 5.2. The rate of change of PIP_3 concentration ([PIP_3]) is given by the following Equation [Sriram et al., 2016]

$$\frac{d[\mathrm{PIP_3}]}{dt} = k^{+}_{\mathrm{PIP_2}}[\mathrm{PIP_2}]_{\mathrm{t}} - k^{-}_{\mathrm{PIP_2}}[\mathrm{PIP_3}]\,, \tag{5.6}$$

where $k^{+}_{\mathrm{PIP_2}}$ and $k^{-}_{\mathrm{PIP_2}}$ are the forward and backward reaction constants for the formation/degradation of PIP_3 from PIP_2, respectively. We assume that the concentration

of PIP_2 remains constant. The rate of PIP_3 production depends on the shear stress, so we can express the rate constant, $k^{+}_{PIP_2}$ as follows [Sriram et al., 2016]

$$k^{+}_{PIP_2} = \frac{k_{1p}}{1 + a_{PI3K}} \left[1 + a_{PI3K} e^{-\eta t} \tanh\left(\frac{\pi\tau}{\Delta}\right)\right] + k_{2p}\,, \tag{5.7}$$

where k_{1p} and k_{2p} are the rate constants, a_{PI3K}, η, and Δ are the constants obtained from fitting experimental data [Go et al., 1998, Katsumi et al., 2005], and τ is the shear stress experienced by the EC. Following phosphorylation of PIP_3, it recruits and phosphorylates protein kinase-C (PKC) and protein kinase-B (PKB/Akt). The concentration of phosphorylated forms of Akt ([AKT*]) and PKC ([PKC*]) is obtained on basis of time scale analysis [Sriram et al., 2016]. These equations are therefore represented mathematically as follows

$$[\text{AKT}^\star] = k^{+}_{\text{AKT}} \frac{[\text{AKT}]_t}{k^{+}_{\text{AKT}} + k^{-}_{\text{AKT}}}\,, \tag{5.8}$$

$$[\text{PKC}^\star] = k^{+}_{\text{PKC}} \frac{[\text{PKC}]_t}{k^{+}_{\text{PKC}} + k^{-}_{\text{PKC}}}\,, \tag{5.9}$$

where $[\text{AKT}]_t$ and $[\text{PKC}]_t$ are the total concentrations of AKT and PKC, respectively; k^{-}_{AKT} and k^{-}_{PKC} are the rate constants, while k^{+}_{AKT} and k^{+}_{PKC} are the time-dependent rate constants. These time-dependent rate constants can be written as follows [Sriram et al., 2016]

$$k^{+}_{\text{AKT}} = 0.1 k^{-}_{\text{AKT}} \frac{[\text{PIP}_3] - [\text{PIP}_3]_{\min}}{[\text{PIP}_3]_{\max} - [\text{PIP}_3]_{\min}}\,, \tag{5.10}$$

$$k^{+}_{\text{PKC}} = 0.1 k^{-}_{\text{PKC}} \frac{[\text{PIP}_3] - [\text{PIP}_3]_{\min}}{[\text{PIP}_3]_{\max} - [\text{PIP}_3]_{\min}}\,, \tag{5.11}$$

where $[\text{PIP}_3]_{\max} = 0.031[\text{PIP}_2]_t$ and $[\text{PIP}_3]_{\min} = 0.0031[\text{PIP}_2]_t$. Some of the recruited eNOS-CaM complexes are phosphorylated by Akt at Ser-1197, resulting in the formation of a stabilized form of the eNOS-CaM complex, i.e., [eNOS-CaM]*. The equation (5.2) and the rate of change of [eNOS-CaM]* are expressed as [Sriram et al., 2016]

$$\frac{d[\text{eNOS-CaM}]}{dt} = k^{+}_{\text{CaM}} \frac{[\text{Ca-CaM}]}{k_{\text{Ca-CaM}} + [\text{Ca-CaM}]} [\text{eNOScav}] - k^{-}_{\text{CaM}} [\text{eNOS-CaM}] - \frac{d[\text{eNOS-CaM}^\star]}{dt}\,, \tag{5.12}$$

$$\frac{d[\text{eNOS-CaM}^\star]}{dt} = k^{+}_{\text{eAKT}} [\text{eNOS-CaM}] - k^{-}_{\text{eAKT}} [\text{eNOS-CaM}^\star]\,, \tag{5.13}$$

where $k^{+}_{\text{eAKT}} = k^{\max}_{\text{eAKT}} [\text{AKT}^\star]/[\text{AKT}]_t$, $k^{\max}_{\text{eAKT}}$ and k^{-}_{eAKT} are the rate constants. The PKC enzyme phosphorylates caveolin-bound eNOS (eNOS_{cav}) at Thr-495, resulting

in a decrease in the formation of eNOS-CaM complexes. Thus, the rate of formation of inactive form of eNOS_{cav} ($[\text{eNOS}^0_{\text{cav}}]$) is written as follows [Sriram et al., 2016]

$$\frac{d[\text{eNOS}^0_{\text{cav}}]}{dt} = k^+_{\text{eThr}}[\text{eNOS}_{\text{cav}}] - k^-_{\text{Thr}}[\text{eNOS}^0_{\text{cav}}]\,, \tag{5.14}$$

where $k^+_{\text{eThr}} = k^+_{\text{Thr}}[\text{PKC}^\star]/[\text{PKC}]_{\text{t}}$, k^+_{Thr} and k^-_{Thr} are the forward and backward rate constants. From the point of view of mass conservation, the total concentration of eNOS must remain constant. The eNOS conservation equation is therefore expressed as follows

$$[\text{eNOS}_{\text{cav}}] + [\text{eNOS}^0_{\text{cav}}] + [\text{eNOS-CaM}^\star] + [\text{eNOS-CaM}] = [\text{eNOS}]_{\text{t}}\,, \tag{5.15}$$

where $[\text{eNOS}]_{\text{t}}$ is the total concentration of the eNOS enzyme. Since eNOS-CaM* participates in L-Arg oxidation, considering the contribution of eNOS-CaM* into Equation (5.3), we obtain the modified form of Equation (5.4)

$$Q_{\text{NO}} = \Psi\left(\phi[\text{eNOS-CaM}^\star] + [\text{eNOS-CaM}]\right)\,, \tag{5.16}$$

where ϕ represents the increase in eNOS activity in the presence of the heat-shock protein (Hsp90).

5.2.2 Modeling NO bioavailability in the presence of RBCs

To investigate the bioavailabilty of NO in the microcirculation, we solve its advection-diffusion-reaction equation using LBM. In this two-dimensional (2-D) study, we consider a straight channel with two continuous cell layers, namely endothelium layer and SMC layer, coated on bottom and upper walls. The thickness of endothelium layer and SMC layer is 2 μm and 6 μm, respectively. To study NO concentration in capillaries, where no SMC layer is found, we consider only the enodthelium layer where NO production takes place. We further assume that the membrane thickness of the EC and SMC is negligible, so that NO produced in the EC layer can diffuse without any resistance from the membrane into the lumen and SMC. We set no-flux condition boundary conditions on the upper and bottom wall surfaces of the SMC layer. We prescribe periodic boundary conditions along the flow direction. In addition, we assume zero fluid velocity in the endothelium layer and SMC layer. The spatio-temporal NO equations in the endothelium layer and SMC layer are expressed as follows

$$\frac{\partial[\text{NO}_{\text{EC}}]}{\partial t} = (D_{\text{NO}})_{\text{EC}}\nabla^2[\text{NO}_{\text{EC}}] + Q_{\text{NO}}, \tag{5.17}$$

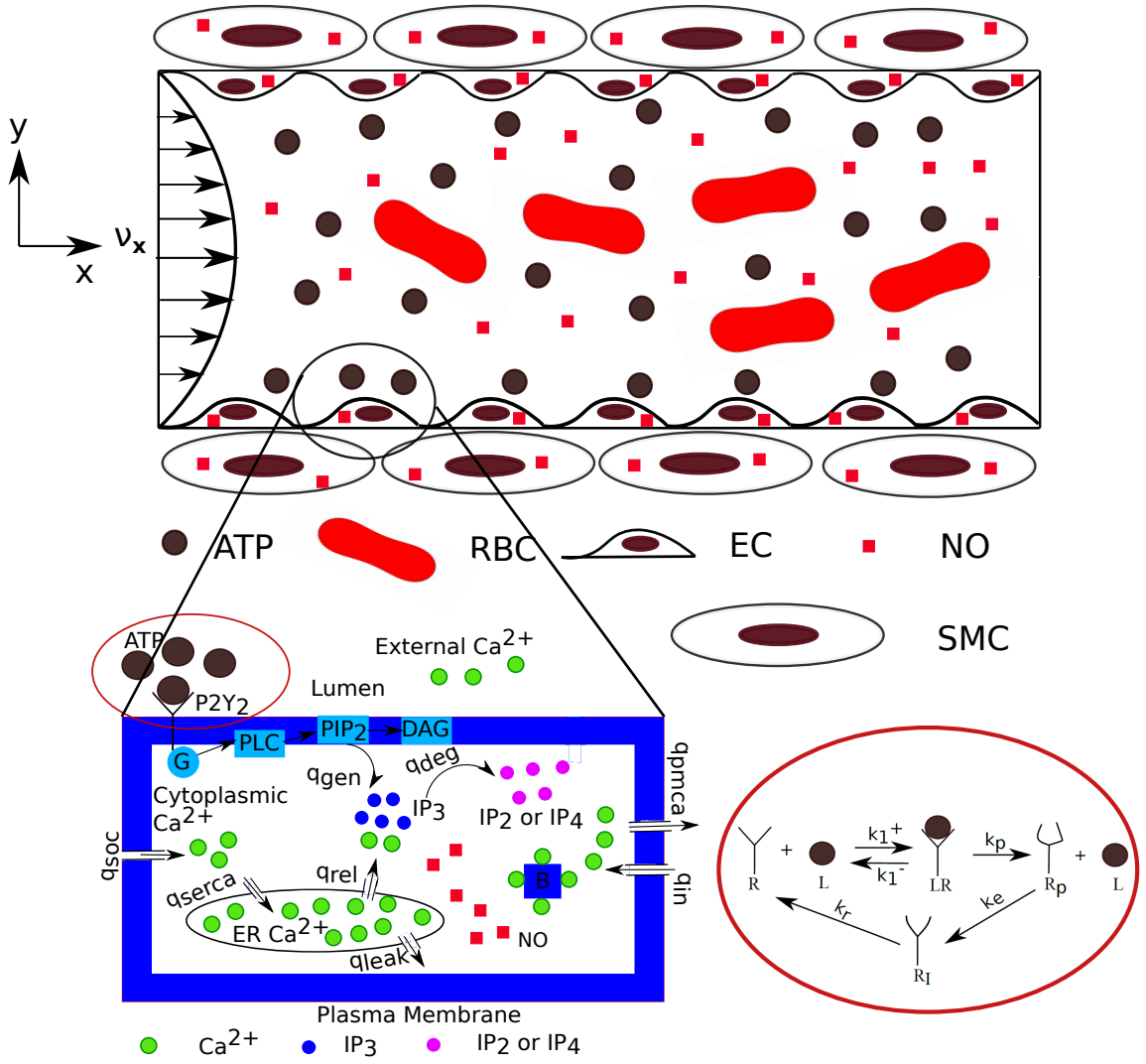

Figure 5.3: Schematic shows the distribution of ATP and NO concentrations in a two-dimensional channel. The channel comprises of the SMC layer, the EC layer, and the lumen. ATP released mainly from RBCs, due to Poiseuille flow, activates the Ca^{2+}-dependent NO production in the EC. The cytoplamic Ca^{2+} concentration is maintained at physiological levels, due to the desensitization of $P2Y_2$ receptors when ATP molecules react with $P2Y_2$ receptors, as shown in the oval enclosure. The concentration of NO in the SMC layer depends on the concentration of ATP and the rate at which it is converted to nitrites or nitrates. This figure is for illustrative purposes only. In the simulation, we assume a continuous layer of EC and SMC so that diffusion of NO molecules between EC-EC, SMC-SMC, EC-SMC and EC-lumen occur without any physical barrier.

$$\frac{\partial[\mathrm{NO_{SMC}}]}{\partial t} = (D_{\mathrm{NO}})_{\mathrm{SMC}}\nabla^2[\mathrm{NO_{SMC}}] - Q_{\mathrm{sGC}}, \tag{5.18}$$

where $(D_{\mathrm{NO}})_{\mathrm{SMC}}$ and $(D_{\mathrm{NO}})_{\mathrm{EC}}$ are the diffusion coefficients of NO in SMC layer and endothelium layer, respectively. NO produced in the endothelium layer diffuses into the lumen and permeates into the cytoplasm of RBCs, where it reacts with heme proteins to form nitrites and nitrates. As a result, NO concentration in the vascular lumen and RBC cytoplasm is expressed in the following forms

$$\frac{\partial[\mathrm{NO_{Plasma}}]}{\partial t} + \mathbf{v}\cdot\nabla[\mathrm{NO_{Plasma}}] = (D_{\mathrm{NO}})_{\mathrm{Plasma}}\nabla^2[\mathrm{NO_{Plasma}}], \tag{5.19}$$

$$\frac{\partial[\mathrm{NO_{RBC}}]}{\partial t} + \mathbf{v}\cdot\nabla[\mathrm{NO_{RBC}}] = (D_{\mathrm{NO}})_{\mathrm{RBC}}\nabla^2[\mathrm{NO_{RBC}}] - k_{\text{Hb-NO}}[\mathrm{NO_{RBC}}], \tag{5.20}$$

where $(D_{\mathrm{NO}})_{\mathrm{Plasma}}$ and $(D_{\mathrm{NO}})_{\mathrm{RBC}}$ are the diffusion coefficients of NO in the plasma and the cytoplasm of RBC, respectively; $k_{\text{Hb-NO}}$ the rate at which hemoglobin scavenged NO in RBC. We assume here, for simplicity, that NO diffusion coefficients in endothelium layer, SMC layer, and plasma have the same value. In the literature [Deonikar and Kavdia, 2013, Wei et al., 2019], it is reported that RBC membrane provides resistance to the diffusion of NO molecules before they are scavenged by RBC. As a result, its concentration in plasma is affected. To incorporate this fact into the model, we prescribe the following boundary conditions on inner and outer surface of RBC.

$$(D_{\mathrm{NO}})_{\mathrm{RBC}}\frac{\partial[\mathrm{NO}]^-}{\partial\mathbf{n}} = -(D_{\mathrm{NO}})_{\mathrm{Plasma}}\frac{\partial[\mathrm{NO}]^+}{\partial\mathbf{n}} = P_{\mathrm{NO}}\left([\mathrm{NO}]^- - [\mathrm{NO}]^+\right), \tag{5.21}$$

where the concentration along the inner and outer sides of RBC membrane are denoted as $[\mathrm{NO}]^-$ and $[\mathrm{NO}]^+$, respectively, and P_{NO} is the RBC membrane permeability constant.

5.2.3 Dimensionless numbers

Dimensionless numbers are used to characterize the flow, ATP distribution, Ca^{2+} concentration and NO distribution.

(i) The capillary number is defined as the ratio between the viscous strength of fluid and bending strength of the RBC membrane.

$$Ca = \frac{\mu_{\mathrm{ex}}\dot{\gamma_w}R_0^3}{\kappa}, \tag{5.22}$$

where $\gamma_w = 4v_{\max}/W$ denotes the wall shear rate for Poiseuille flow.

(ii) Since we are primarily concerned in how the change in confinement would affect the distribution of NO concentration in the channel, we therefore define the degree of confinement of a RBC by the boundary of the channel. The confinement is defined as the ratio of twice the radius of a RBC to the width of the channel.

$$Cn = \frac{2R_0}{W}\,, \tag{5.23}$$

(iii) In 2-D, the hematocrit is defined as the area occupied by RBCs relative to the area of the channel.

$$Hct = \frac{N_c A}{LW}\,. \tag{5.24}$$

(iv) To understand the variation of the concentration of interest (ATP, cytoplasmic Ca^{2+}, and NO for example) in different areas of the straight channel, we define the average concentration in space and time as follows

$$< \text{conc} >_{\text{domain}} = \frac{1}{T}\int_0^T \frac{1}{L(y_2 - y_1)} \int_0^L \int_{y_1}^{y_2} \text{conc}(x, y, t) dy dx dt\,, \tag{5.25}$$

where "conc" can be defined as ATP, cytoplasmic Ca^{2+}, and NO; the domain refers to the lumen, the endothelium layer, and the SMC layer; y_1 and y_2 are the integration constants of interest along the y-direction; and T is the total simulation time. This quantity will allow us to calculate the variation of the global concentration of interest in the domain of interest for different Hct as well as for different Cn. Similarly, the time-averaged concentration (conc, for instance) across the channel is defined as follows

$$< \text{conc} >_{\text{transverse}} = \frac{1}{T}\int_0^T \frac{1}{L} \int_0^L \text{conc}(x, y, t) dx dt\,, \tag{5.26}$$

where the term "conc" can be defined as ATP, cytoplasmic Ca^{2+}, and NO. This quantity will help us to analyze the distribution of the concentration of interest in the y-direction for different Hct at a given Cn.

5.3 Results and Discussion

Before investigating the direct coupling between variables such as fluid flow, ATP, cytoplasmic Ca^{2+}, and NO in the explicit presence of RBC, we first present the results of ATP-stimulated NO production for an EC in the absence of fluid flow. Here, We focus on modeling ATP-dependent NO generation, as shear stress-dependent NO synthesis has already been modeled by Sriram et al. [Sriram et al., 2016]. We therefore

solve Equations (3.16)-(3.20) and (5.2)-(5.3) for a given ATP concentration. Next, we extend this study to RBC dynamics in two-dimensional (2-D) straight channels, whose lower and upper walls are lined with endothelium and SMC layers (with the exception to capillaries, where no SMC layers are found). We performed numerical simulations for $Ca = 90$ to investigate agonist (ATP)-dependent NO bioavailability. By fixing Ca, we ensure that NO concentration changes in the channel due to variation in ATP concentration rather than shear stress. This is one of the objectives of the study. We varied Hct (7-46%) and Cn (0.2-0.8) to study their effect on the availability of NO concentration in the channel. The physical Reynolds number, defined as the ratio between the viscous strength and the inertial strength (i.e., $Re = \frac{\rho \dot{\gamma_w} R_0^2}{\mu_{ex}} \ll 1$), is of the order of 10^{-4}. Consequently, the inertia term in the left hand side of Equation (2.7) is neglected. Therefore, we set the computational Reynolds number to 0.1 in order to accelerate the speed of simulations without compromising accuracy of the results. We therefore solve Equations (2.6)-(2.7), (2.30), (3.16)-(3.20), (5.6), (5.12)-(5.14), and (5.17)-(5.20), supplemented by the appropriate boundary conditions. These equations are solved using LBM. It is worth mentioning that when solving Equations (3.16)-(3.20), (5.6), (5.12)-(5.14), and (5.17) in the endothelium layer, the boundary shear stress and ATP concentration are required from plasma (i.e., information from the lattice nodes neighboring to the endothelium layer). We assume that the boundary shear stress and ATP concentration on the endothelial layer are the same to all lattice nodes present in this layer. Consequently, cytoplasmic Ca^{2+} in endothelium layer nodes perpendicular to the boundary node is the same.

5.3.1 ATP-dependent NO dynamics

As already discussed in Subsection 5.2.1.1, cytoplasmic Ca^{2+} concentration augmentation plays an important role in the activation of eNOS, leading to NO synthesis. It has already been shown that the agonist (ATP) is capable of generating NO signal without shear stress [Xu et al., 2016], we therefore focus solely on ATP-dependent NO generation in this subsection . Nevertheless, flow-dependent NO generation has already been modelled in the literature [Sriram et al., 2016], which we will include in the following subsections. We solve Equations (3.16)-(3.20) and (5.2)-(5.3) for an ATP concentration of 500 nM. The parameter values for solving these equations are obtained from Tables 5.1 and 3.1.

Figure 5.4 (a) shows that a transient response of cytoplasmic Ca^{2+} is observed when the EC is subjected to a stimulus (ATP). Notably, cytoplasmic Ca^{2+} returns to its physiological concentration from its peak concentration even in the presence

of ATP. It has already been reported that the return to homeostasis is achieved by desensitizing $P2Y_2$ receptors (Chapter 3). The increase of cytoplasmic Ca^{2+} concen-

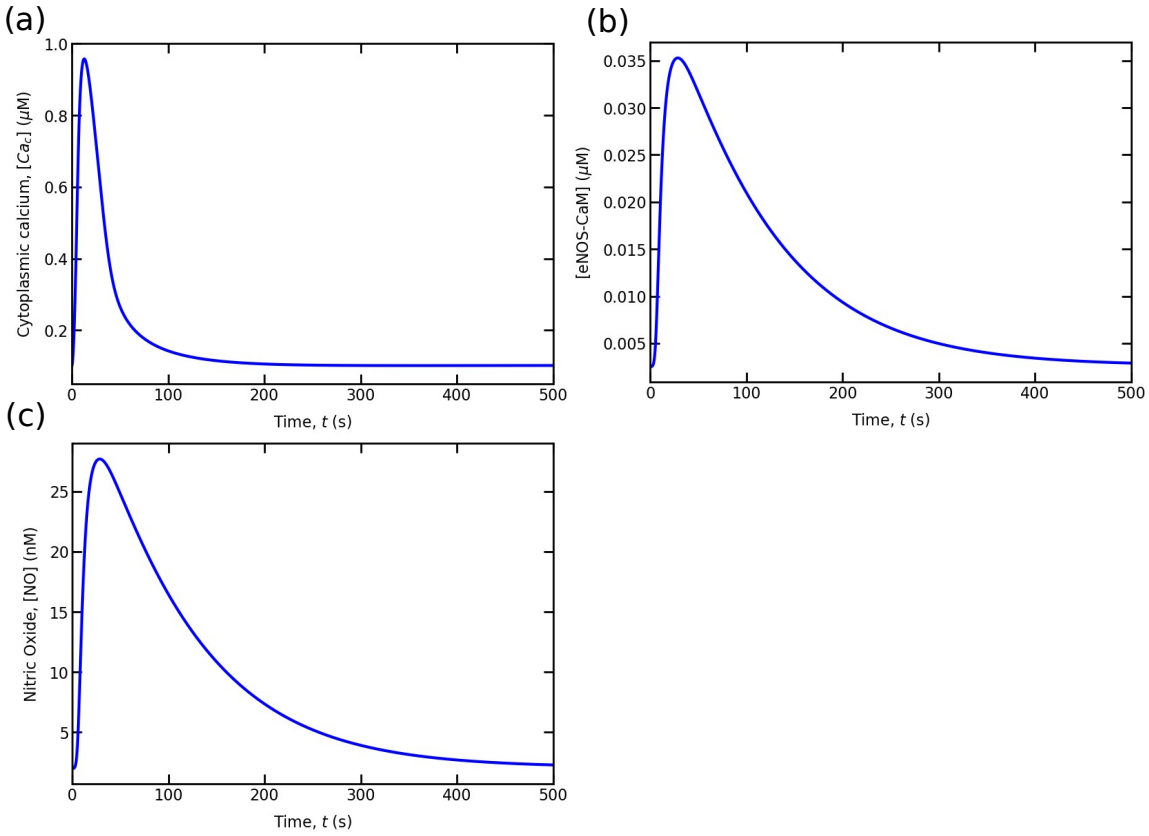

Figure 5.4: Endothelial cell (EC) response to 500 nM ATP concentration: (a) cytoplasmic Ca^{2+} concentration; (b) endothelial nitric oxide synthase-calmodulin (eNOS-CaM) concentration; and (c) nitric oxide (NO) concentration.

tration from its physiological concentration leads to binding of Ca^{2+} with calmodulin proteins, triggering the formation of eNOS-CaM complexes. Figure 5.4 (b) shows that the dynamics of the eNOS-CaM complex is similar to that of cytoplasmic Ca^{2+}. However, the peaks appear at different times, i.e., the cytoplasmic Ca^{2+} peak appears first. This is due to the fact that the conversion of eNOS-CaM complexes to $eNOS_{cav}$ is slower than vice versa (Equation 5.2). Therefore, the time scale of eNOS-CaM complex determines the NO peak time, as shown in Figure 5.4 (c). However, the time scale of the eNOS-CaM peak can be adjusted according to that of cytoplasmic Ca^{2+} by increasing the value of k^{-}_{CaM}. The difference in time scale between cytoplasmic Ca^{2+} and NO has already been reported in experimental results [Blatter et al., 1995, Xu et al., 2016]. Furthermore, Figure 5.4 shows an interesting observation, namely that NO production continues even cytoplasmic Ca^{2+} concentration has reached its basal

concentration.This is because, due to the slow conversion of eNOS-CaM complex to $eNOS_{cav}$, eNOS-CaM complex has accumulated before the cytoplasmic concentration of Ca^{2+} has reached its basal concentration. Thus, the last phase of NO production is independent of the increase in cytoplasmic Ca^{2+} concentration. Moreover, eNOS-CaM and NO concentrations stabilize to their basal concentrations over time. These results, agonist-dependent NO generation, are qualitatively aligned with the experimental observations in the literature [Blatter et al., 1995, Xu et al., 2016].

5.3.2 NO concentration distribution in confined channels

We will now study NO bioavailability in a straight channel lined with endothelial layer only, whereas the effect of SMC layers will be analyzed later. At the beginning of this study, we will focus on a confined channel, which mimics a capillary devoid of SMC layers. The main motivation for starting with a confined channel is that the lateral distance between the RBC membrane and the walls remains the same for all values of Hct (as shown in Figures 5.8) while RBCs move in single file (as shown in Figures 5.5 - 5.7). As a result, this eliminates the importance of CFL on NO concentration. After understanding the distribution of NO in a highly confined channel ($Cn = 0.8$), we will study its distribution in weakly confined channels in which we will include additional layers of SMC.

5.3.2.1 Hematocrit affects distribution of NO concentration

Figure 5.5 shows ATP, cytoplasmic Ca^{2+} and NO concentrations at time, $t = 4.12$ s and $Hct = 8.35\%$. A uniform ATP concentration is observed in the lumen (Figure 5.5 (a)). It is worth reiterating that RBCs and ECs contribute to a stable ATP concentration in lumen. Let us recall (from the last chapter) that ECs contribute more to ATP hydrolysis than to production of ATP, a stable ATP concentration is achieved thanks to the balance between ATP release by RBCs and its hydrolysis by ECs (Figure 4.4). These ATP molecules on the endothelium layer trigger a cascade of reactions to mobilize Ca^{2+} from the ER. Due to the uniform concentration of ATP in the endothelium layer, the cytoplasmic Ca^{2+} concentration is invariable in nature, as shown in Figure 5.5 (b)). The concentration of Ca^{2+} in the lumen ($\sim 1500\mu M$) is several orders of magnitude higher than the concentration of cytoplasmic Ca^{2+}($\sim 1 - 2\mu M$) [Bisello and Friedman, 2008]. Consequently, the influx and efflux of Ca^{2+} through the EC membrane to and from the lumen will not affect its distribution in the lumen. We therefore assume that the concentration of Ca^{2+} in the lumen is a

homogeneous and infinitely large source of Ca^{2+}, as represented $[Ca_{ex}]$ in Equation (3.11). Figure 5.5 (c) demonstrates the non-uniform distribution of NO concentration, particularly around RBCs, despite the fact of uniform ATP and cytoplasmic Ca^{2+} concentrations. This is due to the fact that RBCs immediately scavenged the NO released by the endothelial layers. As a result, NO concentration is lower in the vicinity of RBCs and higher away from them.

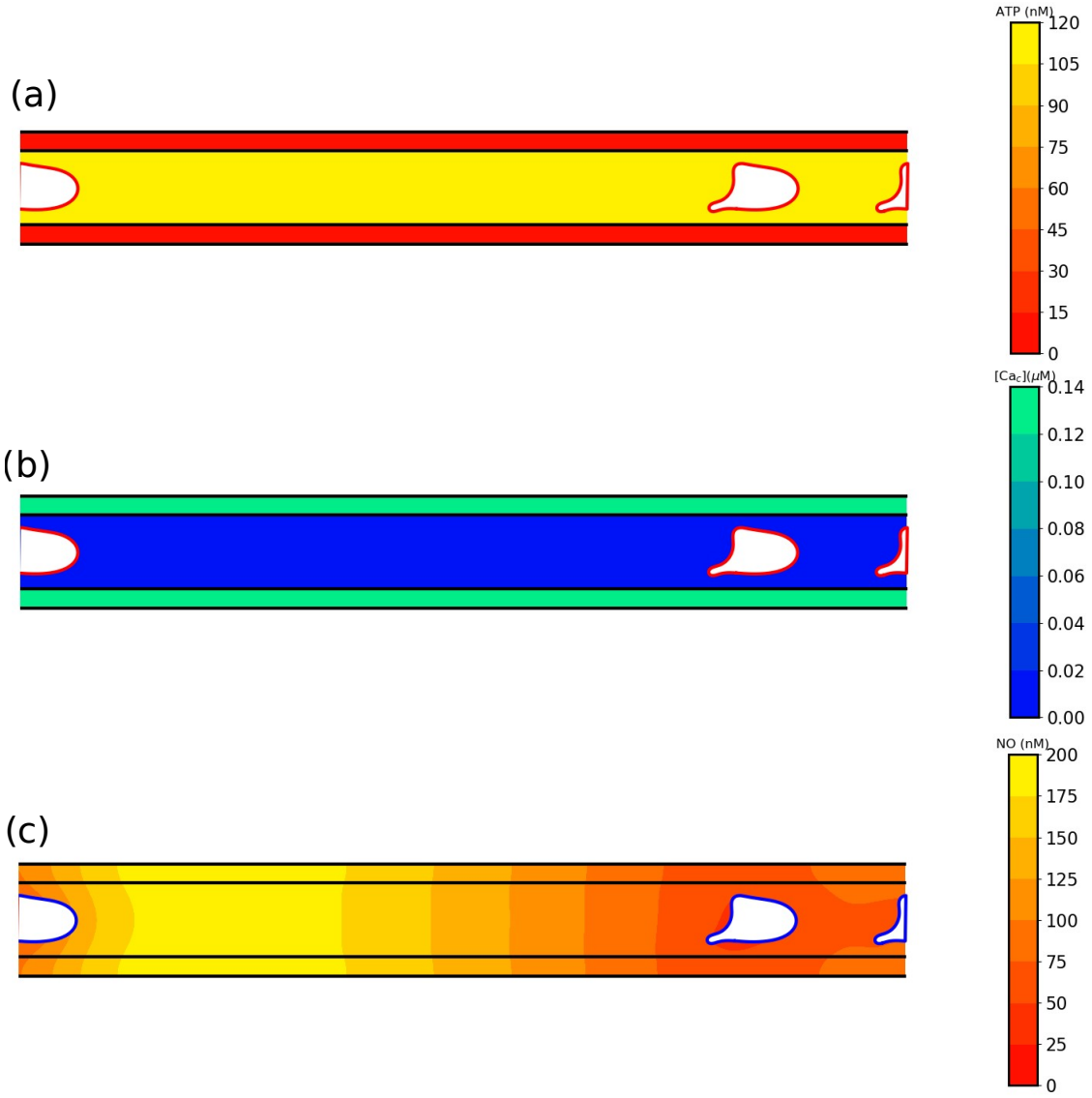

Figure 5.5: Concentration distribution contours at $t = 4.12$ s, $Cn = 0.8$, $Ca = 90$, and $Hct = 8.35\%$: (a) ATP concentration; (b) cytoplasmic Ca^{2+} concentration; and (c) NO concentration. This geometry is similar to that of a capillary where only the endothelium layer is present.

Figure 5.6 shows ATP, cytoplasmic Ca^{2+}, and NO concentrations at time, $t =$

4.12 s and $Hct = 16.7\%$. With increasing Hct concentration, ATP and cytoplasmic Ca^{2+} concentrations increase, but NO concentration decreases further as compared to $Hct = 8.35\%$ (as shown in Figure 5.6 (a)-(c)). The NO concentration around RBCs becomes uniform in comparison with $Hct = 8.35\%$. When Hct concentration increased to 33.4%, RBCs move in single train at equal distance from each other (shown in Figure 5.7). Figures 5.7(a)-(b) shows the uniform distribution of ATP and cytoplasmic Ca^{2+} concentrations in the channel, as well as increasing their concentrations. Moreover, Figure 5.7(c) shows a uniform pattern of NO concentration around RBCs as well as at the channel wall. The concentration of NO decreases further due to higher RBC concentration, resulting in more NO scavenging compared to $Hct = 8.35\%$ and 16.7%.

5.3.2.2 Hematocrit influences transverse ATP, cytoplasmic Ca^{2+}, and NO concentrations

To delve into how concentrations, such as ATP, cytoplasmic Ca^{2+} evolve over time for different Hct concentrations changes across the channel width, we calculated time and space-averaged values of these quantities across the channel width (i.e., perpendicular to the direction of applied flow) in order to understand how the presence of RBC influences the distribution of NO at the center of the channel and on the wall. Figures 5.8 (a)-(c) manifest the time-averaged concentrations of ATP, cytoplasmic Ca^{2+}, and NO across the channel. With increasing Hct, ATP concentration near the wall increases relative to away from it. This is due to the fact that RBCs in confined channels are very close to the wall, as a result, they experience high shear stress, leading to greater ATP release [Gou et al., 2021]. Moreover, ATP concentration in the channel increases with increase in Hct, as shown in Figure 5.8 (a). This change in ATP concentration leads to an increase in cytoplasmic Ca^{2+} concentration in the endothelium layers (Figure 5.8 (b)). Here, we call this response "faster-is-faster". However, a contradictory response is observed in the case of NO concentration, which we call "faster-is-slower", as shown in Figure 5.8 (c). Increasing Hct increases the cytoplasmic concentration of Ca^{2+}, followed by higher NO generation in endothelial cells. However, a high Hct simultaneously increases the rate of NO scavenging. Consequently, NO concentration in the lumen decreases with increasing Hct.

A similar observation to ours, i.e., with increasing Hct leads to decreasing NO concentration was reported in [Wei et al., 2019]. However, they only considered shear stress-induced NO production, whereas in our study we took into account both ATP (from RBCs and ECs) and shear stress-induced NO production . Furthermore,

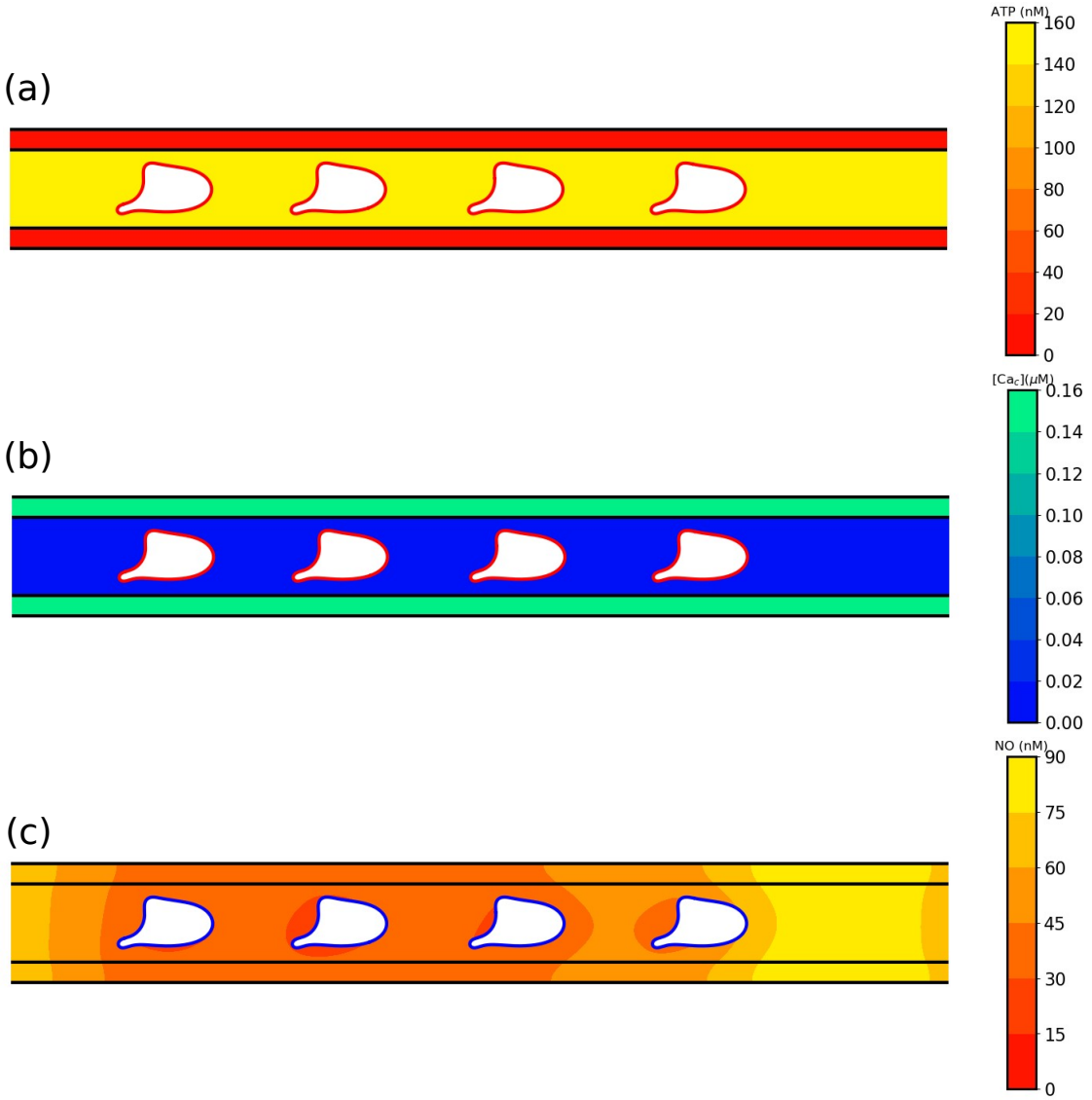

Figure 5.6: Concentration distribution contours at $t = 4.12$ s, $Cn = 0.8$, $Ca = 90$, and $Hct = 16.7\%$: (a) ATP concentration; (b) cytoplasmic Ca^{2+} concentration; and (c) NO concentration. This geometry is similar to that of a capillary where only the endothelium layer is present.

in their result, NO concentration in the channel is limited to 1-2 nM, which is a very small compared to the concentration required for vasodilation (higher than $\sim$ 5 nM [Chen et al., 2008]). In our study, NO concentration is of the order of 10^2 nM. Furthermore, NO bioavailability concentration in blood vessels depends on RBC membrane resistance and the rate of NO scavenging by RBCs [Deonikar and Kavdia, 2010, Deonikar and Kavdia, 2013, Wei et al., 2019]. It might be possible that NO response "faster-is-slower" becomes "faster-is-faster" with a decrease in RBC mem-

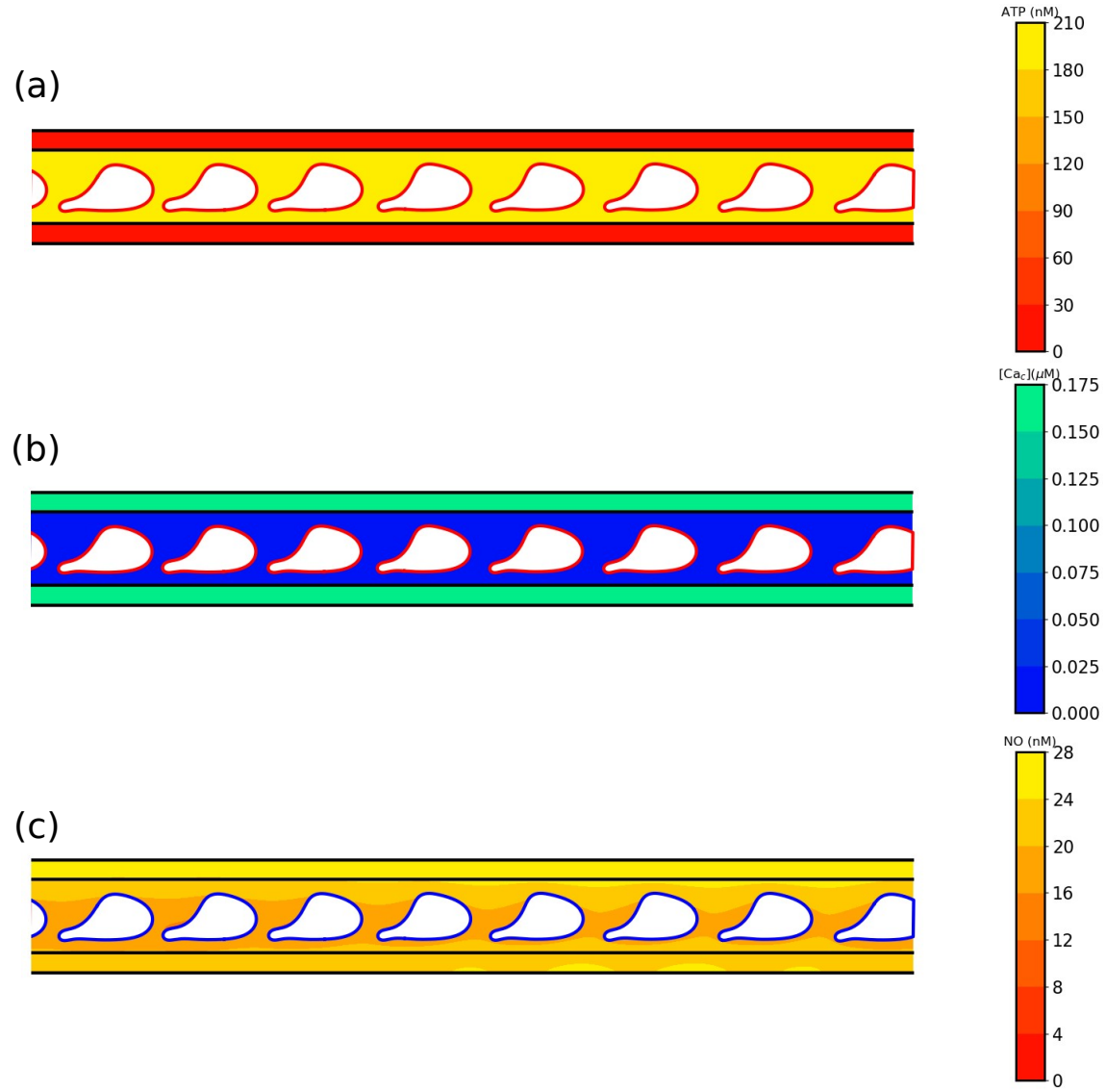

Figure 5.7: Concentration distribution contours at $t = 4.12$ s, $Cn = 0.8$, $Ca = 90$, and $Hct = 33.4\%$: (a) ATP concentration; (b) cytoplasmic Ca^{2+} concentration; and (c) NO concentration. This geometry is similar to that of a capillary where only the endothelium layer is present.

brane permeability and NO scavenging rate. There are two possible explanations: (a) firstly, a higher Hct means a higher concentration of ATP, leading to a high cytoplasmic Ca^{2+} concentration and NO production and (b) secondly, due to the decrease in RBC membrane permeability and NO scavenging rate, the NO gradient in plasma decreases, leading to a higher accumulation of NO. This hypothesis will be explored in greater detail in a future work.

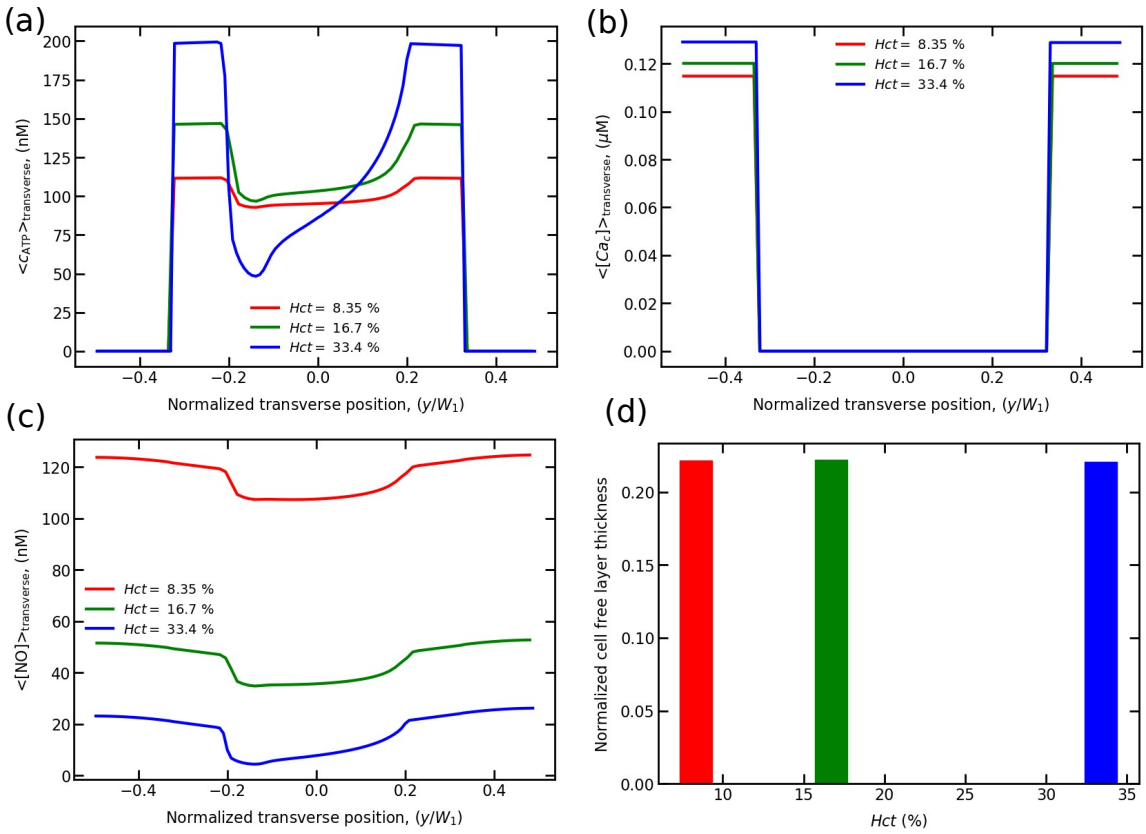

Figure 5.8: Time-averaged concentration across the channel for different Hct concentrations: (a) ATP concentration; (b) cytoplasmic Ca^{2+} concentration; and (c) NO concentration. Figure (d) shows the average cell free layer (CFL) normalized by the width of the lumen (W). These results are obtained for $Cn = 0.8$, and $Ca = 90$. The integration time varies between $t = 0$ to 4.12 s. Here $W_1 = W + 2t_1 + 2t_2$.

5.3.2.3 Hematocrit determines longitudinal concentrations variation

We further investigated the longitudinal NO concentration, to understand whether CFL plays a crucial role, at least in confined channels. In a confined channel, Cn = 0.8, CFL, the distance between the RBC membrane and the inner side of the endothelium layer, remains the same (shown in Figure 5.8(d)). We first present the time-averaged NO concentration in the upper wall for all Hct concentrations in Figure 5.9(a). We find that there is no variation in NO concentration along the flow direction. However, the NO concentration decreases with increase in the Hct. This is due to the fact that higher Hct concentration means that more NO scavenging than NO generation. Further, to understand the local variation in NO concentration with increase in the Hct, we present concentrations of ATP, cytoplasmic Ca^{2+}, and NO at a given time, $t = 4.12$ s on the upper wall of the channel.

Figure 5.9(b)-(c), we observe the "faster-is-faster" response for ATP and cytoplasmic Ca^{2+} with increase in the Hct. Similarly, in Figure 5.9(d), NO concentration exhibits a "faster-is-slower" response with increase in the Hct. In addition, Figure 5.9(d) reports that NO concentration and its gradient on the upper wall along the flow direction depend strongly on Hct as well as on RBC distribution. Figure 5.9(d) shows that NO concentration at $Hct = 8.35\%$ is not uniform, which agrees to our observation in previous section. The region proximity to RBCs shows a strong NO gradients in the axial direction due to their scavenging capabilities. At this Hct, due to the low number of RBCs, NO concentration accumulates in RBC free region. However, as Hct increases to higher values, such as 16.7% and 33.4%, the NO concentration along the flow direction attenuates relative to $Hct = 8.35\%$. For instance, at $Hct = 33.4\%$ (RBCs are equidistant from each other, i.e., the spacing is small, as shown in Figure 5.7(c))m a strong NO gradient is created in the lateral direction. As a result, NO concentration at $Hct = 33.4\%$ decreases relative to other Hct. In addition, there is no NO concentration gradient along the flow direction, leading to no variation in NO concentration, as shown in Figure 5.9(d). Therefore, we can conclude that NO concentration is strongly dependent on the axial arrangement of RBC and its concentration at least in confined channels.

5.3.3 Role of SMC on NO concentration

In this subsection, we reduce Cn from 0.8 to 0.4 (equivalent to moving wide channel) and closely resembles the arterioles and venules of the microcirculation. These vessels are composed of layers of endothelium and SMC. To mimic blood in these vessels in our simulation, we consider endothelium and SMC layers of thickness 2 μm and 6 μm, respectively. The NO generated in the endothelium layers, due to stimulation by ATP, diffuses into the SMC layers. The SMC layers play an important role in muscle cell relaxation and contraction, thereby controlling blood perfusion. To investigate the role of SMCs on NO concentration in the endothelium layer and lumen, we carried out simulations in the presence and absence of SMC layers. We found no differences in NO distribution in the endothelium layers as well as in the lumen, as shown in Figure 5.10(a)-(b). As there are no SMC layers in the second case, there is no NO concentration in these layers, as shown in figure 5.10(b). To quantify NO concentration in the endothelium layers and in the lumen, we present the average NO concentration over space and time in Figure 5.10(c). This figure clearly shows that there is no difference in NO concentration in the endothelial layer and in the lumen

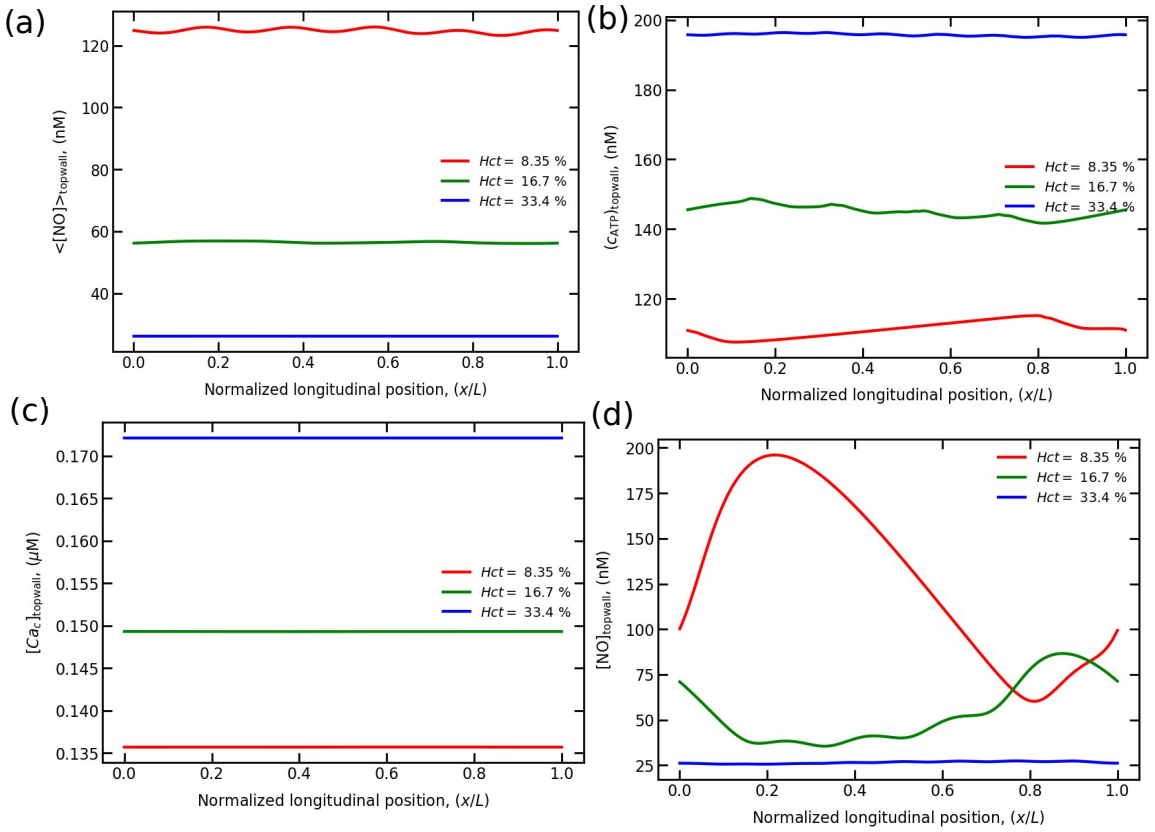

Figure 5.9: (a) Time-averaged NO concentration along the flow direction for different Hct concentrations. Concentrations along the flow direction at $t = 4.12$ s; (b) ATP concentration; (c) cytoplasmic Ca^{2+} concentration; and (d) NO concentration. These results are obtained for $Cn = 0.8$ and $Ca = 90$. The integration time for Figure (a) ranges between $t = 0$ - 4.12 s.

for both the presence and absence of SMC layers. This is due to the fact that the rate of NO consumption by sGCs is lower than that of RBCs.

5.3.4 Effect of confinement on ATP, cytoplasmic Ca^{2+}, and NO concentrations

In this subsection, we discuss the role of confinement (Cn) and hematocrit (Hct) on NO concentration in different regions, such as the endothelium layer, the SMC layer, and the lumen. The change in Cn can be intuitively thought up as RBC moving through the microvascular network of different widths. Recently, Gou et al. [Gou et al., 2023] found heterogeneous distribution of ATP in a mesentery-inspired vascular network. This is associated with the local change in Hct, as well with the local shear stress experienced by RBCs as they move through a network of channels having different Cn. In particular, they reported that a few vessels in the vascular

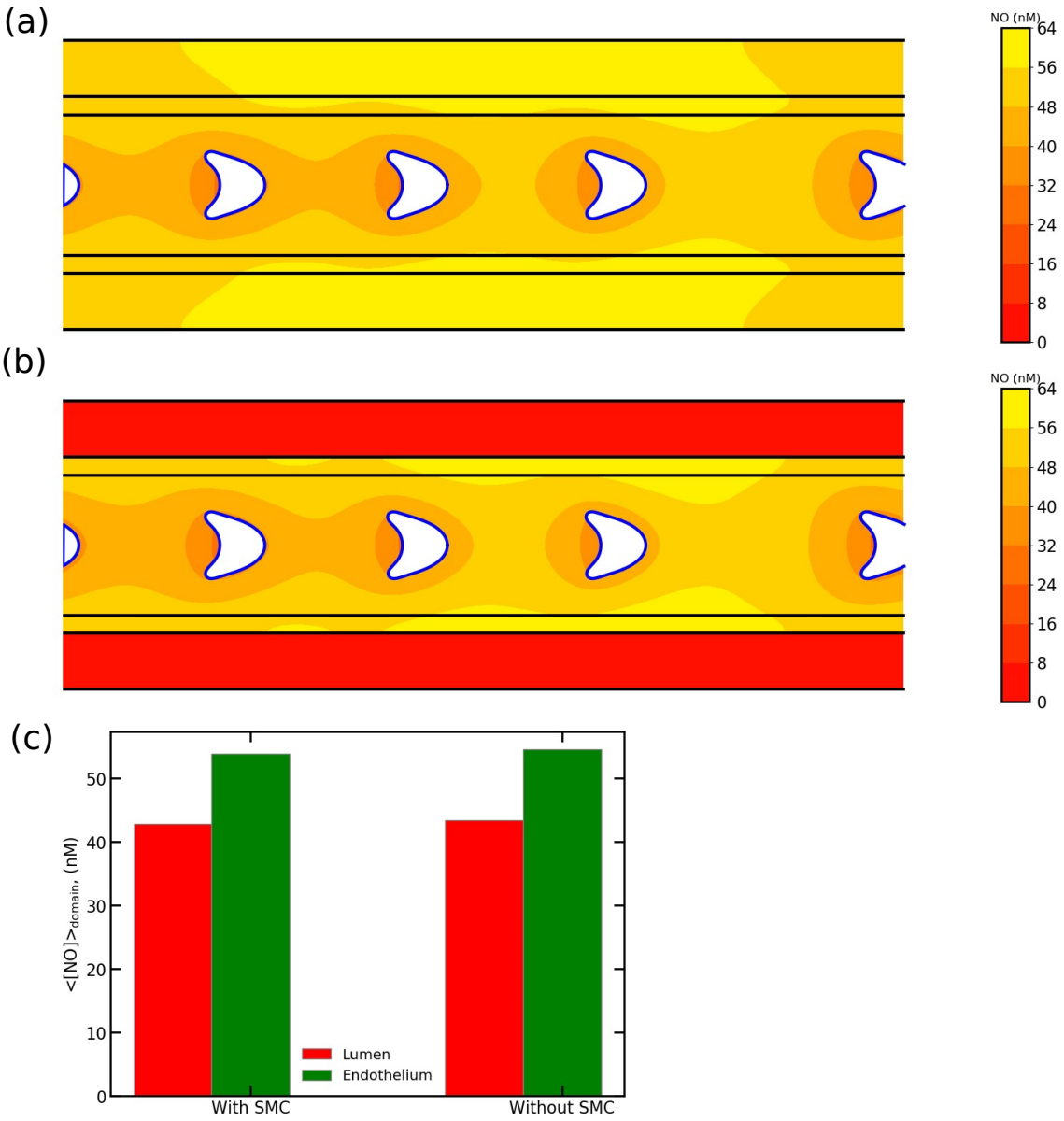

Figure 5.10: NO concentration distribution at $t = 4.12$ s, $Cn = 0.4$, $Ca = 90$, and $Hct = 8.35\%$: (a) in the presence of endothelium and SMC layers; and (b) in the presence of the endothelium layer alone. Figure (c) shows the spatio-temporal averaged NO concentration in the endothelium layer and in the vascular lumen for the above two cases. The time-averaged NO concentration is calculated between the window $t = 0$ and 4.12 s.

network receive high Hct, resulting in a higher concentration of ATP in that region. Based on this finding, this study considered the possibility of Ca^{2+} propagation from a region of high ATP concentration to a region of low ATP concentration. This can help in control of local blood perfusion in the vascular network. However, we do

not intend here to study NO production due to Ca^{2+} propagation in the vascular network. Instead, our study is limited to a straight channel of different Cn, which will help in elucidating NO bioavailability or its upstream/downstream transport in a microvascular network.

We present time and space-averaged concentrations of ATP, cytoplasmic Ca^{2+} and NO in different regions of the computational domain. Figure 5.11(a) shows that ATP concentration increases with change in Hct and channel width. This increase in ATP concentration is associated with the number of RBCs circulating at the same Hct but in different Cn. Consequently, the total ATP release increases for higher Hct [Gou et al., 2021]. Similarly, we found that cytoplasmic Ca^{2+} concentration increases linearly with increasing Hct for each channel width (5.11(b)). The response "faster-is-faster" is valid for all confinement numbers in the case of ATP and cytoplasmic Ca^{2+} concentrations. Again, the "faster-is-slower" response is applicable to NO concentration for all Cn as well as for all regions in the vessel with increase in Hct, as shown in Figure 5.11(c)-(e). In these figures, we observed two types of phase: (i) at a particular Hct limit, i.e., 7-25%, as in the current simulation, high NO concentrations are found in regions, such as the endothelium layer, the SMC layer, and the lumen and (ii) at Hct above 25%, NO concentration in all these regions is of a similar order of magnitude for all Cn. This high NO concentration in the first phase (low Hct limit) may have two implications if we have a microvascular network of different Cn: (i) even at low ATP concentration, blood vessel can increase RBC perfusion to meet its metabolic needs and (ii) NO can transport upstream and downstream in order to control local blood perfusion.

Notably, another important observation is that at higher Hct, i.e., above 20%, weakly confined channels have a higher NO concentration, although the difference is not significant, in the endothelium layer. For example, Figure 5.11(c) shows that NO concentration in the endothelium layer is of the order $0.2 > 0.4 > 0.8$. Similarly, Figure 5.11(e) shows that the NO concentration in SMC layer is of the order $0.2 > 0.4$, as $Cn = 0.8$ has no SMC layers. It is therefore important to note that, if the ATP concentration is sufficiently high in a weakly confined channel compared with a highly confined channel at a high Hct, NO bioavailability may be altered in the endothelium and SMC layers. Meanwhile, the pattern of NO concentration in the lumen remains unchanged (of the order $0.2 < 0.4 < 0.8$), as shown in Figure 5.11(d).

5.4 Conclusions

NO is an important vasodilator, helping to maintain vascular tone by counteracting the effects of vasoconstrictors. There are mainly two pathways involved in NO production: (i) the activation of agonist (ATP)-dependent pathway, which is mainly controlled by the rise of intracellular Ca^{2+} concentration and (ii) the shear stress-dependent pathway (due to blood flow experienced by ECs), which is activated with or without presence of cytoplasmic Ca^{2+}. However, there are still conflicts in the literature regarding the shear stress-dependent NO pathways. In this study, we modeled agonist (ATP)-dependent NO production. The model results are qualitatively aligned with experimental observations. For the sake of completeness, we have taken into account shear stress-dependent NO production pathway, which has already been modeled by Sriram et al. [Sriram et al., 2016]. In last section of the study, we included the source of ATP, i.e., the release of ATP from RBCs and ECs subjected to Poiseuille flow in a 2-D channel. We solved a intricately coupled system using immersed boundary lattice Boltzmann method (IBLBM), including main variables such as fluid flow, ATP, cytoplasmic Ca^{2+}, and NO by varying channel width and RBC concentration for a given flow strength. This study was focused primarily on the ATP-dependent bioavailability of NO in blood vessels. Therefore, we limited our investigation to a constant flow strength. In addition, we concentrated our numerical study on a smaller time scales (less than 5 s) rather than on a longer time scales as been carried out in by Sriram et al. [Sriram et al., 2016].

The main findings of this study are (i) NO bioavailabilty is strongly dependent on RBC concentration and its distribution in blood vessels, (ii) a phase of high NO concentration at low RBC concentration for simulations with different channel widths, (iii) a plateau of the same NO concentration for different channel widths at higher RBC concentration, and (iv) higher NO concentration at higher RBC concentration in poorly confined channels than in strongly confined channels. However, much remains to be explored by extending this study to NO bioavailability in a real microvascular network. In addition, experiments are needed to validate the current results. For this reason, appropriate experimental procedures must be adopted to quantify NO concentration in both *in vitro* and *in vivo* studies. In addition, NO is responsible for locally increasing the diameter of blood vessels by deforming them. It would be interesting if wall deformation could be incorporated into numerical simulation to reproduce blood flow conditions *in vivo*.

Table 5.1: Model parameter values for NO modeling

Parameter	Description	Reference	Value
Calcium-dependent NO			
Θ	Limiting factor	[Sriram et al., 2016]	0.0045
β	Hill coefficient	[Sriram et al., 2016]	2.7
K_{dCaM}	Ca-CaM dissociation constant	[Sriram et al., 2016]	1 μM
$[\text{CaM}]_{\text{t}}$	Total CaM concentration	[Sriram et al., 2016]	30 μM
k^{+}_{CaM}	Forward rate constant	[Sriram et al., 2016]	7.5 s^{-1}
$K_{\text{Ca-CaM}}$	Michaelis-Menten constant	[Sriram et al., 2016]	3 μM
k^{-}_{CaM}	Backward rate constant	[Sriram et al., 2016]	0.01 s^{-1}
Ψ	NO production rate	[Sriram et al., 2016]	300 s^{-1}
$R^{\text{max}}_{\text{NO}}$	NO-scavenging rate by sGC	[Sriram et al., 2016]	0.022 s^{-1}
b_1	constant	[Sriram et al., 2016]	15.15 nM
a_0			1200.16 nM^2
a_1		[Sriram et al., 2016]	37.33 nM
[sGC]	Total concentration of sGC	[Sriram et al., 2016]	0.1 μM
λ_{NO}	NO-scavenging rate by RBC	[Sriram et al., 2016]	382 s^{-1}
Shear-dependent NO			
k_{1p}	PIP_3 production rate	[Sriram et al., 2016]	0.021 s^{-1}
a_{PI3K}	constant	[Sriram et al., 2016]	2.5
η	Time scale control parameter	[Sriram et al., 2016]	0.003 s^{-1}
Δ	constant	[Sriram et al., 2016]	2.4 Pa
k_{2p}	PIP_3 production rate	[Sriram et al., 2016]	0.0022 s^{-1}
k^{-}_{AKT}	AKT dephosphorylation rate	[Sriram et al., 2016]	0.1155 s^{-1}
k^{-}_{PKC}	PKC dephosphorylation rate	[Sriram et al., 2016]	0.1155 s^{-1}
$[\text{AKT}]_{\text{t}}$	Total Akt concentration	[Sriram et al., 2016]	1 μM
$[\text{PKC}]_{\text{t}}$	Total PKC concentration	[Sriram et al., 2016]	1.0 μM
$k^{\text{max}}_{\text{eAKT}}$	Maximum eNOS-CaM* production rate	[Sriram et al., 2016]	0.004 s^{-1}
k^{-}_{eAKT}	eNOS-CaM* degradation rate	[Sriram et al., 2016]	2.2E-4 s^{-1}
k^{+}_{Thr}	$\text{eNOS}^{0}_{\text{cav}}$ production rate	[Sriram et al., 2016]	0.002 s^{-1}
k^{-}_{Thr}	$\text{eNOS}^{0}_{\text{cav}}$ degradation rate	[Sriram et al., 2016]	2.2E-4 s^{-1}
ϕ	Activity of eNOS in the presence of Hsp90	[Sriram et al., 2016]	9
NO availability			
$(D_{\text{NO}})_{\text{EC}}$	EC NO diffusion coefficient	[Wei et al., 2019]	3.3E-9 m^2/s
$(D_{\text{NO}})_{\text{SMC}}$	SMC NO diffusion coefficient	[Wei et al., 2019]	3.3E-9 m^2/s
$(D_{\text{NO}})_{\text{Plasma}}$	Plasma NO diffusion coefficient	[Wei et al., 2019]	3.3E-9 m^2/s
$(D_{\text{NO}})_{\text{RBC}}$	RBC NO diffusion coefficient	[Wei et al., 2019]	0.88E-9 m^2/s
$k_{\text{Hb-NO}}$	Reaction rate between Hb-NO	[Wei et al., 2019]	2.047E+6 s^{-1}

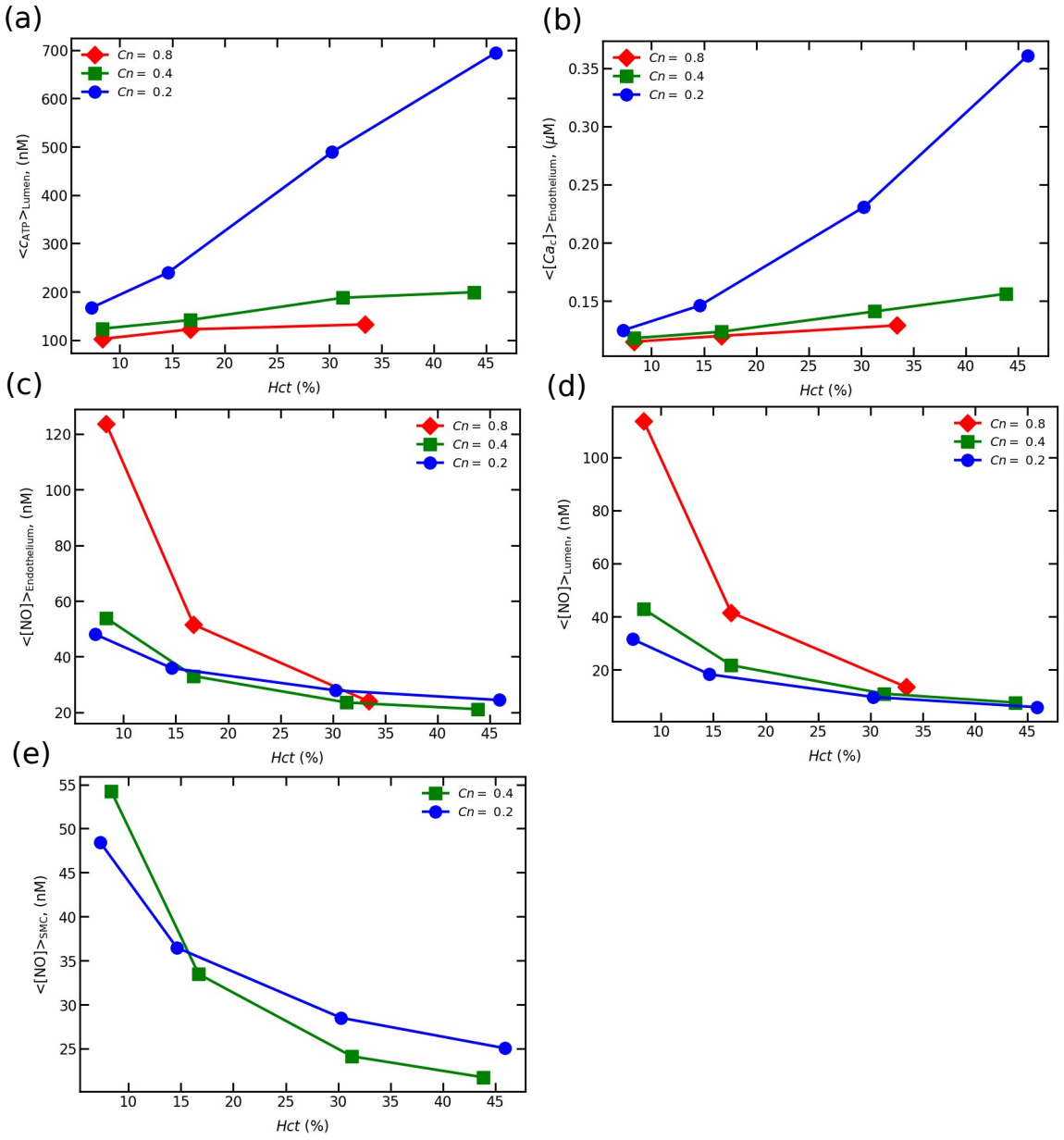

Figure 5.11: Effect of confinement on ATP, cytoplasmic Ca^{2+}, and NO concentrations for different regions, such as endothelium layer, SMC layer, and lumen, with varying Hct concentrations: (a) ATP concentration in the lumen; (b) mean cytoplasmic Ca^{2+} concentration between the upper and lower walls; (c) mean NO concentration between the upper and lower endothelium layers; (d) NO concentration in the lumen; and (e) mean NO concentration between the upper and lower SMC layers. These concentrations are obtained by integrating the spatio-temporal concentrations corresponding to the regions of interest. The time-averaged concentration is calculated between the window $t = 0$ to 4.12 s. The simulation is performed for $Ca = 90$. NO concentration in Figure (e) is compared between $Cn = 0.4$ and 0.2 as $Cn = 0.8$ has no SMC layers.

Chapter 6

Conclusions and perspectives

6.1 Summary of Chapter 3 and related perspectives

Ca^{2+} is a ubiquitous ion and a second messenger that regulates numerous cellular functions. To understand how these functions are regulated by Ca^{2+}, we essentially require to know how the behaviour of Ca^{2+} evolves over time within a cell when a cell is subjected to external stimuli. In Chapter 3, we proposed a minimal Ca^{2+} model for an EC that ensures intracellular Ca^{2+} homeostasis. The model is able to capture intracellular concentrations, such inositol trisphosphate (IP_3), cytoplasmic Ca^{2+}, and endoplasmic reticulum Ca^{2+} return to the so-called homeostatic concentration (i.e., the physiological concentration) in the presence of an agonist (stimulus). We found that receptor dynamics, in particular receptor desensitization due to prolonged exposure of $P2Y_2$ receptors to a stimulus, is a key element driving a cell to reach homeostasis in order to protect the EC from toxic effects of high cytoplasmic Ca^{2+} concentration. In addition, this model reproduces other important experimental facts such as the refiling of endoplasmic reticulum (ER) requires extracellular Ca^{2+}, the variation of the maximum cytoplasmic Ca^{2+} concentration in an EC for different stimuli, and the elevated steady cytoplasmic Ca^{2+} concentration after a transient peak.

Although this model accounts for many experimental observations, it is unable to feature Ca^{2+} oscillations that have been observed in many experiments [Cuthbertson and Chay, 1991, Dupont and Erneux, 1997, Marhl et al., 2000, Kummer et al., 2000, Schuster et al., 2002, Politi et al., 2006, Dupont et al., 2011]. This allows meticulous experiments to be carried out in a single EC in order to study whether any downstream reactions are needed to regulate the receptor dynamics that can lead to

Ca^{2+} oscillations in this model. In addition, no experiments in the literature have simultaneously measured the concentrations of inositol trisphosphate (IP_3), cytoplasmic Ca^{2+} and ER Ca^{2+}. A clear experimental picture is required to understand how these three are connected to each other and also developing a robust Ca^{2+} dynamics model. We didn't take into account another aspect, i.e., shear stress evoked Ca^{2+}

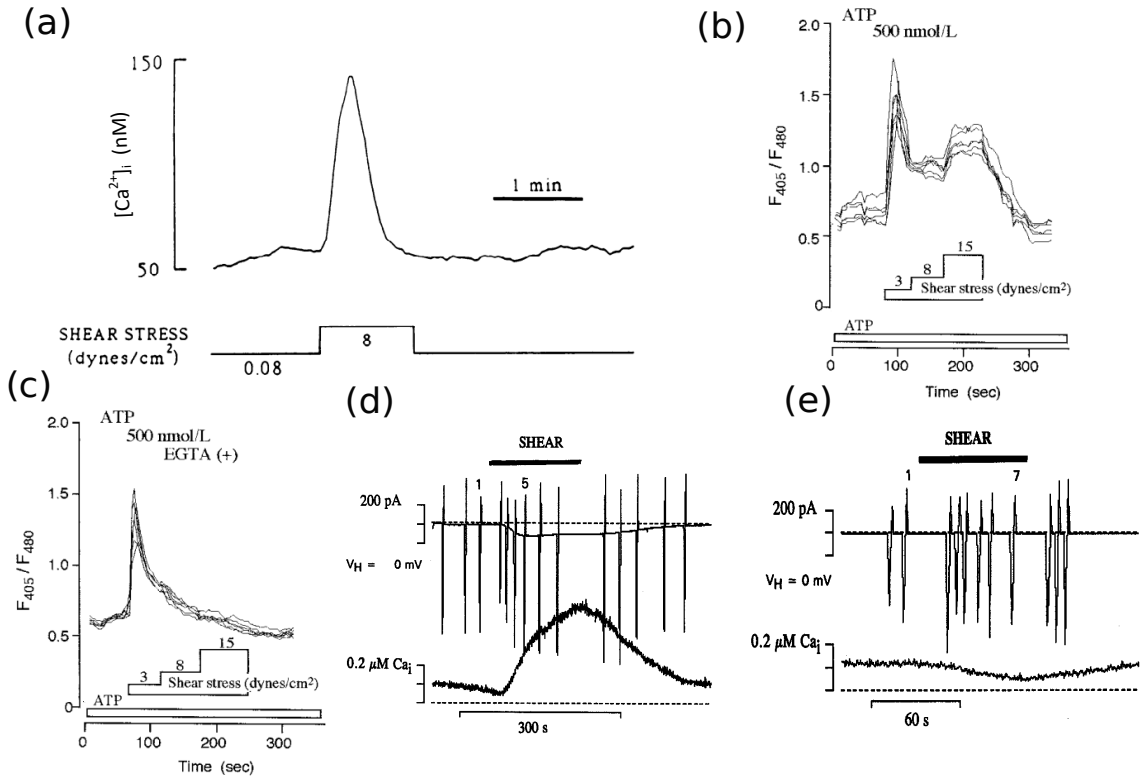

Figure 6.1: Experimental results show shear stress evokes cytoplasmic Ca^{2+} : (a) The rise of cytoplasmic Ca^{2+} concentration is observed when a confluent layer of bovine aortic endothelial cells (BAECs) are exposed to step increase in shear stress [Shen et al., 1992]; (b) and (c) The increase in cytoplasmic Ca^{2+} concentration occurs in human umbilical vein endothelical cells (HUVECs) when exposed to external ATP and step increase in shear stress. These experiments were carried out in control (b) and in the absence of extracellular free Ca^{2+} concentration using chelator (EGTA: ethylene glycol-bis(β-aminoethyl ether)-N,N,N',N'-tetra acetic acid, c) [Yamamoto et al., 2000b]; and (d) and (e) Simultaneous cytoplasmic Ca^{2+} concentration and membrane currents are measured when the human umbilical cord veins endothelial cell is subjected to shear stress ($\sim$ 1 Pa) without and with EGTA, respectively [Schwarz et al., 1992].

dynamics in ECs when developing the Ca^{2+} dynamics model. We know that ECs can sense their hemodynamic environment as they form the inner lining of blood vessels. Shear stress sensing by ECs has many physical implications, such as low-density

lipoprotein uptake, NO production, gene transcription, and proliferation. At the end of 20th century, numerous experiments were conducted to understand how the shear stress experienced by ECs transduce into an increase in cytoplasmic Ca^{2+} concentration. However, no consensus has been reached to elucidate the mechanism behind Ca^{2+} dynamics in ECs. For example, some experiments favor the hypothesis of Ca^{2+} release from the ER [Nollert et al., 1990, Shen et al., 1992, Geiger et al., 1992, James et al., 1995] (Figure 6.1(a)), while others support influx of extracellular Ca^{2+} via shear-activated Ca^{2+} channels [Ando et al., 1991, Schwarz et al., 1992, Wiesner et al., 1997] (Figures 6.1(b)-(c)) or ATP released from ECs into the extracellular environment allows influx of extracellular Ca^{2+} into the cytoplasm via ionotropic receptor, $P2X_4$ [Yamamoto et al., 2000a, Yamamoto et al., 2000b, Yamamoto et al., 2003] ((Figures 6.1(d)-(e))). Therefore, experiments must be carried out to identify the particular mechanism or pathways of Ca^{2+} signaling evoked by shear stress in different types of EC under various conditions [Hong et al., 2006]. These experimental conditions may be such as external ATP with flow or only flow or by treating ECs with suitable chemical agents to ensure that a particular pathways is or is not responsible for Ca^{2+} signaling. Hence, elucidating the mechanism of the shear stress stress-evoked increase in cytoplasmic Ca^{2+} concentration will provide a better understanding of how shear stress contributes to intracellular homeostasis in ECs.

6.2 Summary of Chapter 4 and related perspectives

Adensoine triphosphate (ATP) released by red blood cells (RBCs) and endothelial cells (ECs) into plasma triggers Ca^{2+} signaling in ECs. The increase in cytoplasmic Ca^{2+} concentration in ECs is responsible for the control/regulation of many cellular functions. One of the functions of Ca^{2+} is to regulate the synthesis of the vasodilator, nitric oxide (NO). NO helps in relaxation of blood vessels, thereby increasing their diameter and enabling local control of blood perfusion. In Chapter 4, we carried out numerical simulations using immersed boundary lattice Boltzmann method (IBLBM) by coupling RBC and Ca^{2+} dynamics for two-dimensional straight channels. The detailed studies were carried out by changing RBC concentration, flow strength, and vessel width in order to emulate blood flow conditions in microvascular network. We found that ATP and cytoplasmic Ca^{2+} concentrations depend on the number of RBCs flowing in a channel. For example, while keeping the channel length fixed but varying its width for a given RBC concentration, the number of RBCs in the

channel increases linearly with increasing the channel width. Consequently, the total cumulative level of ATP release increases in channels of larger width. This results into higher ATP and cytoplasmic Ca^{2+} concentrations in wider channels than in confined ones. In addition, a high concentration leads to a rapid cytoplasmic Ca^{2+} response. Due to the difference in response time of cytoplasmic Ca^{2+}, the cytoplasmic Ca^{2+} wave propagates from a region of high ATP concentration to a region of low ATP concentration if we think of a vascular network.

Our study was limited to straight channels, in which we assumed a homogeneous spatial distribution of cytoplasmic Ca^{2+} concentration in ECs. In reality, the distribution of cytoplasmic Ca^{2+} concentration is spatio-temporal in nature. In future, spatio-temporal Ca^{2+} dynamics model for compartments such as the cytoplasm and ER can be considered into IBLBM to understand how the distribution of Ca^{2+} concentration changes within ECs for various (patho)physiological conditions. Furthermore, we did not observe active Ca^{2+} wave propagation from a local stimulated EC to neighboring ECs in our Ca^{2+} dynamics model, as like shown in experiment [Uhrenholt et al., 2007] (Figure 6.2(b)). The development of a Ca^{2+} wave propagation model would enable us to understand how ECs perform cellular functions, such as vasodilation, in a coordinated manner. In addition, Gou et al. [Gou et al., 2023] recently observed a heterogenous distribution of ATP concentration in the mesenstric microvascular network, as shown in Figure 6.2(a). Due to the heterogeneous distribution of ATP in the network, the Ca^{2+} wave can propagate from a branch of higher ATP concentration towards branches of lower ATP concentration. As a result, the Ca^{2+} wave can raise the cytoplasmic Ca^{2+} concentration in branches of in the network with a lower ATP concentration. This means that a branch with higher ATP concentration can control the dilation of branches of lower ATP concentration, allowing more RBCs to flow through them. To understand these complex dynamics in the vascular network, it is essential to integrate the spatio-temporal dynamics of Ca^{2+} model when simulating the blood flow in the microvascular network.

6.3 Summary of Chapter 5 and related perspectives

NO is an important vasodilator, responsible for maintaining the vascular tone in our body. NO produced in vascular wall, i.e., endothelum, is diffused into the blood vessels and part of the NO concentration is scavenged by RBCs. In order to understand how RBC concentration, channel width, and ATP released by RBCs and ECs influence NO

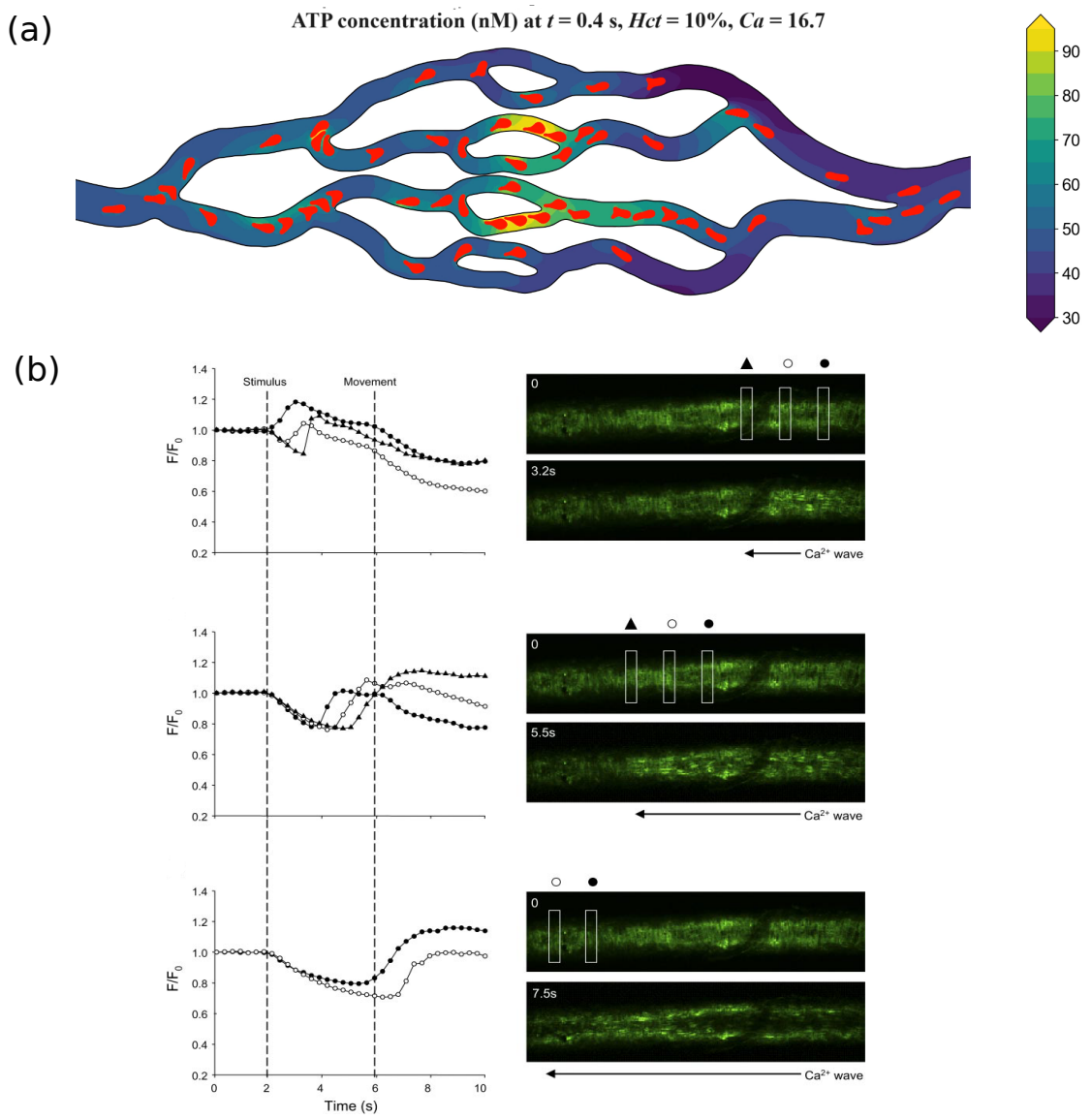

Figure 6.2: (a) The heterogeneous distribution of ATP concentration in a mescentric microvascular network at $Hct = 10\%$, $Ca = 16.7$ is obtained from numerical simulation [Gou et al., 2023]; and (b) Ca^{2+} wave propagation due course of time in hamster feed arteries following local stimulation with the agonist acetylcholine at the extreme right of the vessel (right side of top figure). The left side of the figure shows normalized fluorescence intensity over time at different locations in the vessel marked by the vertical rectangles [Uhrenholt et al., 2007].

concentration in blood vessel, we first developed a mathematical model by taking into account ATP- and shear stress-dependent NO production pathways. This model is qualitatively consistent with experimental results. Secondly, we simulated an intricate coupled system by considering main variables, namely fluid velocity, ATP, cytoplasmic

Ca^{2+}, and NO in the explicit presence of RBCs. We found that NO concentration decreases in the blood vessels with increasing Hct concentration even though ATP concentration rises with increasing Hct concentration. In addition, we found that NO concentration in highly confined channels is higher than in loosely confined channels.

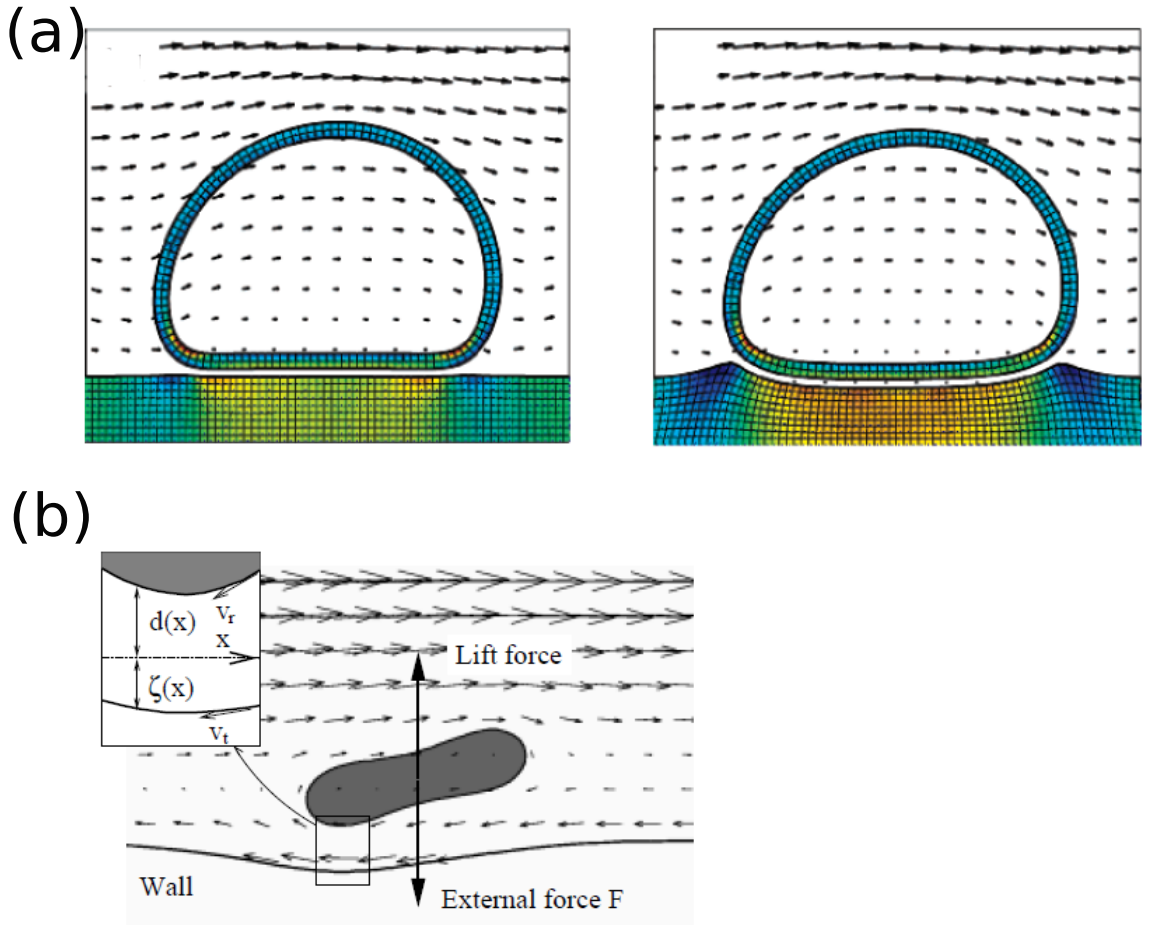

Figure 6.3: (a) Figure shows fluid-driven motion of microcapsule on a compliant surface: stiff substrate (left) and soft substrate (right) [Alexeev et al., 2005]; and (b) schematic shows deformation compressible wall alters the local fluid velcocity and lift force [Beaucourt et al., 2004a].

All the simulations carried out in this thesis concerned rigid channel walls. However, we have advocated that the local control of blood perfusion in the microvascular network is done by dilating the blood vessel through the action of NO on smooth muscle cells (SMCs). Indeed, our body's blood vessels are deformable to external stimuli such as the applied pressure gradient [Beaucourt et al., 2004a, Alexeev et al., 2005] (Figure 6.3(a)-(b)) and the external pressure around the blood vessel. In addition to

these external stimuli, NO itself can modify vessel diameter. It would be interesting to account for deformation of blood vessel walls by implementing it in a numerical simulation for a straight blood vessel or a microvascular network. This can lead to a better understanding of how blood perfusion is regulated under *in vivo* conditions.

Appendix A

Supplementary Information for Model Equations and Numerical Methods

A.1 Force calculations

We now derive the membrane force contribution for each energy separately, then add them together to obtain the total force components at the spring node in the Cartesian coordinate system. The details of the derivation are given as follows

Stretching force

The stretching force at the spring node, i, can be intuitively thought of as the force exerted by the stretching of the two neighboring springs, whose current deformed lengths are l_i and l_{i-1}, as shown in Figure 2.7. The force components (f_{lx} and f_{ly}) at the spring node, i, are obtained by taking the partial derivative of the total stretching energy of the system with respect to the position vector of the corresponding spring node, i, whose components in the Cartesian coordinate system are x_i and y_i. These definitions can be mathematically expressed as follows

$$f_{lx} = -\frac{\partial E_l}{\partial x_i}, \quad f_{ly} = -\frac{\partial E_l}{\partial y_i}, \tag{A.1}$$

where E_l is the total stretching energy of the system. Equation (2.26) can be expanded as

$$E_l = \frac{1}{2}k_l\left(\frac{l_1 - l_1^0}{l_1^0}\right)^2 + ... + \frac{1}{2}k_l\left(\frac{l_{N-1} - l_{N-1}^0}{l_{N-1}^0}\right)^2 + \frac{1}{2}k_l\left(\frac{l_N - l_N^0}{l_N^0}\right)^2, \tag{A.2}$$

where $l^0_{N-1} = \sqrt{(x^0_{N-1} - x^0_N)^2 + (y^0_{N-1} - y^0_N)^2}$, $l_{N-1} = \sqrt{(x_{N-1} - x_N)^2 + (y_{N-1} - y_N)^2}$, and in the same way, we can also write expressions for other springs. The force components in Equation (A.1) are obtained by taking the partial derivative of Equation (A.2) and using the expressions for stretched and unstretched spring lengths. Note that the contribution to the forces at the spring node, i, comes from the terms involving the i coordinates, such as x_i and y_i.

$$f_{lx} = -k_l \frac{l_i - l^0_i}{(l^0_i)^2 l_i} (x_i - x_{i+1}) - k_l \frac{l_{i-1} - l^0_i}{(l^0_i)^2 l_{i-1}} (x_i - x_{i-1}) \ , \tag{A.3}$$

$$f_{ly} = -k_l \frac{l_i - l^0_i}{(l^0_i)^2 l_i} (y_i - y_{i+1}) - k_l \frac{l_{i-1} - l^0_i}{(l^0_i)^2 l_{i-1}} (y_i - y_{i-1}) \ . \tag{A.4}$$

Similarly, the components of stretching force can be calculated for other spring nodes.

Areal force

The areal force components at a given spring node is obtained by taking the partial derivative of Equation (2.27) with respect to the position of that spring node, i.e.

$$f_{sx} = -\frac{\partial E_s}{\partial x_i}, \quad f_{sy} = -\frac{\partial E_s}{\partial y_i} \ , \tag{A.5}$$

where E_s is the total areal energy of the system due to the change in the area of a vesicle. The expanded form of Equation (2.27) is given as follows,

$$E_s = \frac{1}{2} k_s \left(\frac{s_1 - s^0_1}{s^0_1} \right)^2 + ... + \frac{1}{2} k_s \left(\frac{s_{N-1} - s^0_{N-1}}{s^0_{N-1}} \right)^2 + \frac{1}{2} k_s \left(\frac{s_N - s^0_N}{s^0_N} \right)^2 \ , \tag{A.6}$$

where $s_{N-1} = \frac{1}{2} (x_{N-1} y_N - x_N y_{N-1})$ and $s^0_{N-1} = \frac{1}{2} \left(x^0_{N-1} y^0_N - x^0_N y^0_{N-1} \right)$. Similarly, it can be done for other spring nodes. The force components in Equation (A.5) are obtained by taking the partial derivative of Equation (A.6) for the node i. The force components therefore are

$$f_{sx} = -\frac{1}{2} k_s \frac{s_i - s^0_i}{(s^0_i)^2} (-x_{i+1} + x_{i-1}) \ , \tag{A.7}$$

$$f_{sy} = -\frac{1}{2} k_s \frac{s_i - s^0_i}{(s^0_i)^2} (y_{i+1} - y_{i-1}) \ . \tag{A.8}$$

Similarly, the force components for the other spring nodes can be obtained.

Bending force

The bending force components at a spring node, i, is obtained by taking the partial derivative of Equation (2.28) with respect to its Cartesian coordinates. The force components, f_{bx} and f_{by}, at spring node, i (x_i, y_i) are

$$f_{bx} = -\frac{\partial E_b}{\partial x_i}, \quad f_{by} = -\frac{\partial E_b}{\partial y_i}, \tag{A.9}$$

where E_b is the total bending energy of the system, resulting from the change in curvature of the vesicle membrane. This equation can be further rewritten as

$$E_b = \frac{1}{2}k_b \tan^2\left(\frac{\theta_1 - \theta_1^0}{\theta_1^0}\right) + ... + \frac{1}{2}k_b \tan^2\left(\frac{\theta_{N-1} - \theta_{N-1}^0}{\theta_{N-1}^0}\right) + \frac{1}{2}k_b \tan^2\left(\frac{\theta_N - \theta_N^0}{\theta_N^0}\right). \tag{A.10}$$

Using the half-angle identity, $\tan^2(\frac{\alpha}{2}) = \frac{1-\cos\alpha}{1+\cos\alpha}$, Equation (A.10) can be rewritten as

$$E_b = \frac{1}{2}k_b \frac{1-\cos(\theta_1 - \theta_1^0)}{1+\cos(\theta_1 + \theta_1^0)} + ... + \frac{1}{2}k_b \frac{1-\cos\left(\theta_{N-1} - \theta_{N-1}^0\right)}{1+\cos\left(\theta_{N-1} + \theta_{N-1}^0\right)} + \frac{1}{2}k_b \frac{1-\cos(\theta_N - \theta_N^0)}{1+\cos(\theta_N + \theta_N^0)}, \tag{A.11}$$

By using the trigonometric identities, $\cos(\alpha \pm \beta) = \cos\alpha\cos\beta \mp \sin\alpha\sin\beta$ and $\sin(\alpha \pm \beta) = \sin\alpha\cos\beta \pm \cos\alpha\sin\beta$ in Equation (A.11) and followed by using Equation (A.9), we arrive

$$\begin{aligned} f_{bx} = &-\frac{k_b}{\left[1+\cos(\theta_{i-1} - \theta_{i-1}^0)\right]^2}\left(\cos\theta_{i-1}^0 \frac{\partial\cos\theta_{i-1}}{\partial x_i} + \sin\theta_{i-1}^0 \frac{\partial\sin\theta_{i-1}}{\partial x_i}\right) \\ &- \frac{k_b}{\left[1+\cos(\theta_i - \theta_i^0)\right]^2}\left(\cos\theta_i^0 \frac{\partial\cos\theta_i}{\partial x_i} + \sin\theta_i^0 \frac{\partial\sin\theta_i}{\partial x_i}\right) \\ &- \frac{k_b}{\left[1+\cos(\theta_{i+1} - \theta_{i+1}^0)\right]^2}\left(\cos\theta_{i+1}^0 \frac{\partial\cos\theta_{i+1}}{\partial x_i} + \sin\theta_{i+1}^0 \frac{\partial\sin\theta_{i+1}}{\partial x_i}\right) \end{aligned} \tag{A.12}$$

$$\begin{aligned} f_{by} = &-\frac{k_b}{\left[1+\cos(\theta_{i-1} - \theta_{i-1}^0)\right]^2}\left(\cos\theta_{i-1}^0 \frac{\partial\cos\theta_{i-1}}{\partial y_i} + \sin\theta_{i-1}^0 \frac{\partial\sin\theta_{i-1}}{\partial y_i}\right) \\ &- \frac{k_b}{\left[1+\cos(\theta_i - \theta_i^0)\right]^2}\left(\cos\theta_i^0 \frac{\partial\cos\theta_i}{\partial y_i} + \sin\theta_i^0 \frac{\partial\sin\theta_i}{\partial y_i}\right) \\ &- \frac{k_b}{\left[1+\cos(\theta_{i+1} - \theta_{i+1}^0)\right]^2}\left(\cos\theta_{i+1}^0 \frac{\partial\cos\theta_{i+1}}{\partial y_i} + \sin\theta_{i+1}^0 \frac{\partial\sin\theta_{i+1}}{\partial y_i}\right) \end{aligned} \tag{A.13}$$

There are three angles, such as θ_{i-1}, θ_i, and θ_{i+1} present in Equations (A.12)-(A.13) as the coordinates of node, i appear in these angles. Therefore, these angles and their derivatives are given below.

$$\cos\theta_{i-1} = \frac{(x_i - x_{i-1})(x_{i-1} - x_{i-2}) + (y_i - y_{i-1})(y_{i-1} - y_{i-2})}{l_{i-1}l_{i-2}}, \tag{A.14}$$

$$\cos\theta_i = \frac{(x_{i+1}-x_i)(x_i-x_{i-1})+(y_{i+1}-y_i)(y_i-y_{i-1})}{l_i l_{i-1}}\,, \tag{A.15}$$

$$\cos\theta_{i+1} = \frac{(x_{i+2}-x_{i+1})(x_{i+1}-x_i)+(y_{i+2}-y_{i+1})(y_{i+1}-y_i)}{l_i l_{i+1}}\,. \tag{A.16}$$

Using Equations (A.14)-(A.16) and the general relation, $\sin^2\beta+\cos^2\beta=1$, we obtain the following expressions for Equations (A.12)-(A.13)

$$\begin{aligned}\frac{\partial\cos\theta_{i-1}}{\partial x_i} &= \frac{x_{i-1}-x_{i-2}}{l_{i-1}l_{i-2}}\\ &- \frac{(x_i-x_{i-1})(x_{i-1}-x_{i-2})+(y_i-y_{i-1})(y_{i-1}-y_{i-2})}{l_{i-1}^3 l_{i-2}}(x_i-x_{i-1})\,,\end{aligned} \tag{A.17}$$

$$\begin{aligned}\frac{\partial\cos\theta_{i}}{\partial x_i} &= \frac{x_{i+1}+x_{i-1}-2x_i}{l_i l_{i-1}}\\ &- \frac{(x_{i+1}-x_i)(x_i-x_{i-1})+(y_{i+1}-y_i)(y_i-y_{i-1})}{l_i^3 l_{i-1}}(x_i-x_{i+1})\\ &- \frac{(x_{i+1}-x_i)(x_i-x_{i-1})+(y_{i+1}-y_i)(y_i-y_{i-1})}{l_i l_{i-1}^3}(x_i-x_{i-1})\,,\end{aligned} \tag{A.18}$$

$$\begin{aligned}\frac{\partial\cos\theta_{i+1}}{\partial x_i} &= \frac{x_{i+1}-x_{i+2}}{l_i l_{i+1}}\\ &- \frac{(x_{i+2}-x_{i+1})(x_{i+1}-x_i)+(y_{i+2}-y_{i+1})(y_{i+1}-y_i)}{l_i^3 l_{i+1}}(x_i-x_{i+1})\,,\end{aligned} \tag{A.19}$$

$$\begin{aligned}\frac{\partial\sin\theta_{i-1}}{\partial x_i} &= \frac{y_{i-2}-y_{i-1}}{l_{i-1}l_{i-2}}\\ &- \frac{(x_{i-1}-x_i)(y_{i-1}-y_{i-2})+(x_{i-1}-x_{i-2})(y_i-y_{i-1})}{l_{i-1}^3 l_{i-2}}(x_i-x_{i-1})\,,\end{aligned} \tag{A.20}$$

$$\begin{aligned}\frac{\partial\sin\theta_{i}}{\partial x_i} &= \frac{y_{i+1}-y_{i-1}}{l_i l_{i-1}}\\ &- \frac{(x_i-x_{i+1})(y_i-y_{i-1})+(x_i-x_{i-1})(y_{i+1}-y_i)}{l_i^3 l_{i-1}}(x_i-x_{i+1})\\ &- \frac{(x_i-x_{i+1})(y_i-y_{i-1})+(x_i-x_{i-1})(y_{i+1}-y_i)}{l_i l_{i-1}^3}(x_i-x_{i-1})\,,\end{aligned} \tag{A.21}$$

$$\begin{aligned}\frac{\partial\cos\theta_{i+1}}{\partial x_i} &= \frac{y_{i+1}-y_{i+2}}{l_i l_{i+1}}\\ &- \frac{(x_{i+1}-x_{i+2})(y_{i+1}-y_i)+(x_{i+1}-x_i)(y_{i+2}-y_{i+1})}{l_i^3 l_{i+1}}(x_i-x_{i+1})\,,\end{aligned} \tag{A.22}$$

$$\begin{aligned}\frac{\partial\cos\theta_{i-1}}{\partial y_i} &= \frac{y_{i-1}-y_{i-2}}{l_{i-1}l_{i-2}}\\ &- \frac{(x_i-x_{i-1})(x_{i-1}-x_{i-2})+(y_i-y_{i-1})(y_{i-1}-y_{i-2})}{l_{i-1}^3 l_{i-2}}(y_i-y_{i-1})\,,\end{aligned} \tag{A.23}$$

$$\begin{aligned}\frac{\partial \cos\theta_i}{\partial y_i} &= \frac{y_{i+1}+y_{i-1}-2y_i}{l_i l_{i-1}} \\ &- \frac{(x_{i+1}-x_i)(x_i-x_{i-1})+(y_{i+1}-y_i)(y_i-y_{i-1})}{l_i^3 l_{i-1}}(y_i-y_{i+1}) \\ &- \frac{(x_{i+1}-x_i)(x_i-x_{i-1})+(y_{i+1}-y_i)(y_i-y_{i-1})}{l_i l_{i-1}^3}(y_i-y_{i-1})\,,\end{aligned} \tag{A.24}$$

$$\begin{aligned}\frac{\partial \cos\theta_{i+1}}{\partial y_i} &= \frac{y_{i+1}-y_{i+2}}{l_i l_{i+1}} \\ &- \frac{(x_{i+2}-x_{i+1})(x_{i+1}-x_i)+(y_{i+2}-y_{i+1})(y_{i+1}-y_i)}{l_i^3 l_{i+1}}(y_i-y_{i+1})\,,\end{aligned} \tag{A.25}$$

$$\begin{aligned}\frac{\partial \sin\theta_{i-1}}{\partial y_i} &= \frac{x_{i-1}-x_{i-2}}{l_{i-1} l_{i-2}} \\ &- \frac{(x_{i-1}-x_i)(y_{i-1}-y_{i-2})+(x_{i-1}-x_{i-2})(y_i-y_{i-1})}{l_{i-1}^3 l_{i-2}}(y_i-y_{i-1})\,,\end{aligned} \tag{A.26}$$

$$\begin{aligned}\frac{\partial \sin\theta_i}{\partial y_i} &= \frac{x_{i-1}-x_{i+1}}{l_i l_{i-1}} \\ &- \frac{(x_i-x_{i+1})(y_i-y_{i-1})+(x_i-x_{i-1})(y_{i+1}-y_i)}{l_i^3 l_{i-1}}(y_i-y_{i+1}) \\ &- \frac{(x_i-x_{i+1})(y_i-y_{i-1})+(x_i-x_{i-1})(y_{i+1}-y_i)}{l_i l_{i-1}^3}(y_i-y_{i-1})\,,\end{aligned} \tag{A.27}$$

$$\begin{aligned}\frac{\partial \cos\theta_{i+1}}{\partial y_i} &= \frac{x_{i+2}-x_{i+1}}{l_i l_{i+1}} \\ &- \frac{(x_{i+1}-x_{i+2})(y_{i+1}-y_i)+(x_{i+1}-x_i)(y_{i+2}-y_{i+1})}{l_i^3 l_{i+1}}(y_i-y_{i+1})\,.\end{aligned} \tag{A.28}$$

Appendix B

Supplementary Information for Mathematical Modeling of Intracellular Calcium in Presence of Receptor: A Homeostatic Model for Endothelial Cell

Method and Model Development

G-protein

Intracellular calcium

In this section, we derive the mathematical expression for buffer factor, β (see Subsection 3.2.3, in the main text). We assume that the immobile buffer proteins are uniformly distributed in the cytoplasm of EC. We here ignore presence of the buffer proteins in the ER. The binding of buffer proteins, B with cytoplasmic Ca^{2+}, Ca_c reversibly forms a calcium-buffer protein complex. So the chemical reaction becomes

$$\mathrm{Ca}_c + \mathrm{B} \underset{\mathrm{k}_7}{\overset{\mathrm{k}_6}{\rightleftharpoons}} \mathrm{Ca{-}B}$$

The rate change of concentrations of the cytoplasmic Ca^{2+}, $[Ca_c]$, buffer proteins, $[B]$, and calcium-buffer protein complex, $[Ca-B]$ are obtained using the law of mass action and conservation of mass. These equations are

$$\frac{d[Ca_c]}{dt} = f - k_6[B][Ca_c] + k_7[Ca - B]\,, \tag{B.1}$$

$$\frac{d[B]}{dt} = k_7[Ca - B] - k_6[B][Ca_c]\,, \tag{B.2}$$

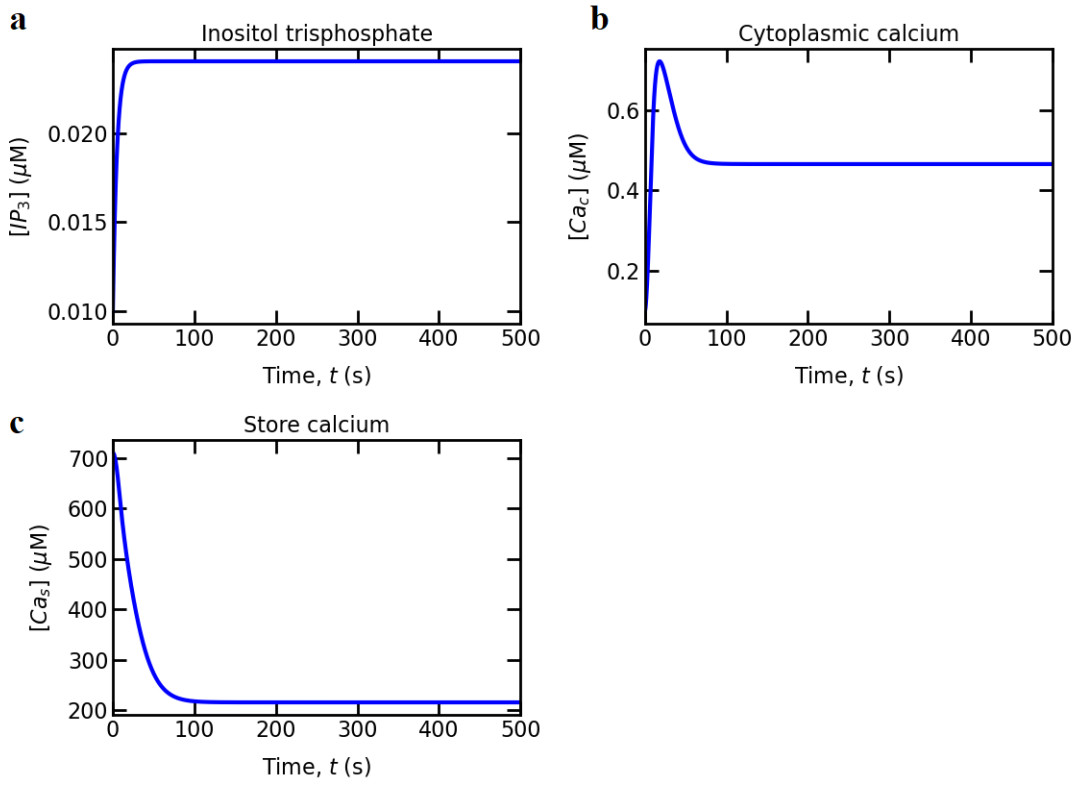

Figure B.1: Existing model variable results for a single EC stimulated by a constant ATP, $[L] = 300$ nM: (a) inositol trisphosphate concentration; (b) cytoplasmic Ca^{2+} concentration; and (c) store Ca^{2+} concentration.

$$\frac{d[Ca-B]}{dt} = k_6[B][Ca_c] - k_7[Ca-B]\,, \tag{B.3}$$

where

$$f = q_{\text{rel}} - q_{\text{serca}} + q_{\text{leak}} + q_{\text{soc}} + q_{\text{in}} - q_{\text{pmca}}$$

q_{rel}, q_{serca}, q_{leak}, q_{soc}, q_{in}, and q_{pmca} are the rates of change in the cytoplasmic Ca^{2+} concentration due to release through the IP_3R, uptake from the ER, a passive leak from the ER, ER depleted influx from the extracellular space, a passive influx from the extracellular space, and efflux by the PM pump, respectively; k_6 and k_7 are the association and dissociation rates between the buffer proteins and cytoplasmic Ca^{2+}.

We here assume that the reaction between buffer proteins and cytoplasmic calcium takes place on a faster time-scale than diffusion, influx, and efflux of the cytoplasmic Ca^{2+}. The time-scale of buffered reaction with calcium is very small comparison to the time-scale of calcium rise and return back to its basal concentration. In this

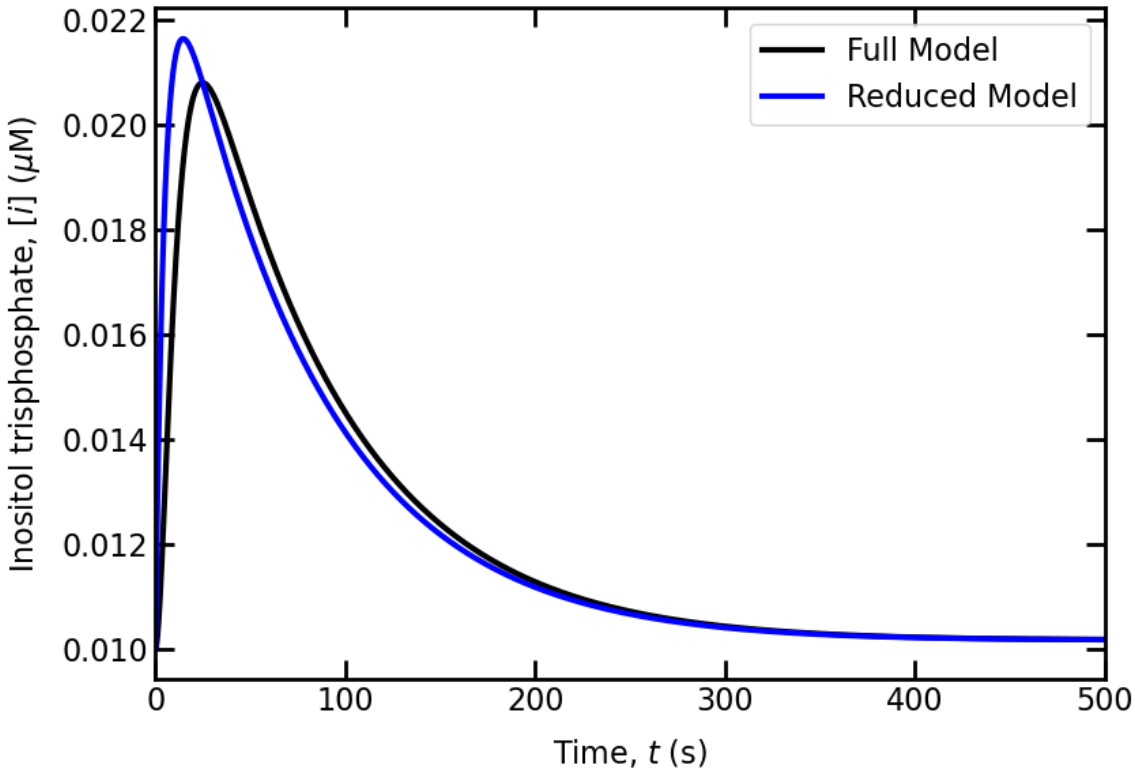

Figure S2: Variation in IP_3 concentrations when EC is stimulated with 300 nM ATP concentration. A comparison has been made between the full scale model (considering G-protein equation as an ODE) and the reduced model (as discussed in Subsection 3.2.2, Chapter 3)

study, the time-scale of reaction between buffer proteins and calcium is ,

$$\tau_i = \frac{1}{k_7 + k_6([ca_c(0)] + [B_t])}$$

$[Ca_c(0)]$ is the initial cytoplasmic calcium concentration. The time scale of reaction (τ_i) is order of 10^{-5} s which is much faster than the time-scale of calcium reaction ($\sim$ 70 s). As a consequence, we assume that formation ($Ca - B$ due to binding of Ca_c and B) and dissociation of $Ca - B$ ($Ca - B$ to Ca_c and B) is governed by the rapid equilibrium approximation. Thus, we can write it as follows

$$k_7[Ca - B] = k_6[B][Ca_c]\,. \tag{B.4}$$

To eliminate $[B]$ from Equation (B.4), we assume that the total number of buffer proteins, $[B_t]$ in the EC cytoplasm is a constant i.e., $[B_t] = [B] + [Ca - B]$. Using $[B] = [B_t] - [Ca - B]$ in Equation (B.4) and further simplifying it, we get

$$[Ca - B] = \frac{[B_t][Ca_c]}{\frac{k_7}{k_6} + [Ca_c]}.$$

Furthermore, adding Equations (B.1) and (B.3), we obtain

$$\frac{d[Ca_t]}{dt} = f\,, \tag{B.5}$$

where $[Ca_t] = [Ca_c] + [Ca - B]$. Further, taking derivative of $[Ca_t]$ with respect to time and using the expression for $[Ca - B]$, we get

$$\frac{d[Ca_t]}{dt} = \frac{d[Ca_c]}{dt} + \frac{\frac{k_7}{k_6}[B_t]}{\left(\frac{k_7}{k_6} + [Ca_c]\right)^2}\frac{d[Ca_c]}{dt}\,, \tag{B.6}$$

Plugging Equation (B.6) in Equation (B.5) and then solving for the rate of change of cytoplasmic Ca^{2+}, we obtain

$$\frac{d[Ca_c]}{dt} = \beta f\,, \tag{B.7}$$

where buffer factor,

$$\beta = \left\{1 + \frac{[B_t]\,\frac{k_7}{k_6}}{\left(\frac{k_7}{k_6} + [Ca_c]\right)^2}\right\}^{-1}.$$

Receptor dynamics

The rate of change of unbounded receptor, R, bounded receptor, LR (ligand-receptor complex), phosphorylated receptor, R_p, and internalized receptor, R_I as shown in Figure S3 concentrations are obtained using the law of mass action and conservation of mass. These equations become

$$\frac{d[R]}{dt} = k_1^-[LR] - k_1^+[L][R] + k_r[R_I]\,, \tag{B.8}$$

$$\frac{d[LR]}{dt} = k_1^+[L][R] - k_1^-[LR] - k_p[LR]\,, \tag{B.9}$$

$$\frac{d[R_p]}{dt} = k_p[LR] - k_e[R_p]\,, \tag{B.10}$$

$$\frac{d[R_I]}{dt} = k_e[R_p] - k_r[R_I]\,. \tag{B.11}$$

Adding Equations (B.8) and (B.9), we get

$$\frac{d[R_s]}{dt} = k_r[R_I] - k_p[LR]\,, \tag{B.12}$$

where $[R_s]$ ($[R_s] = [R] + [LR]$) is the unphosphorylated receptors concentration. The expression for $[LR]$ is derived at the end of this subsection. We add Equations (B.8)-(B.11) to get the total receptors concentration, $[R_t]$, i.e.,

$$[R_t] = [R] + [LR] + [R_p] + [R_I] = [R_s] + [R_p] + [R_I].$$

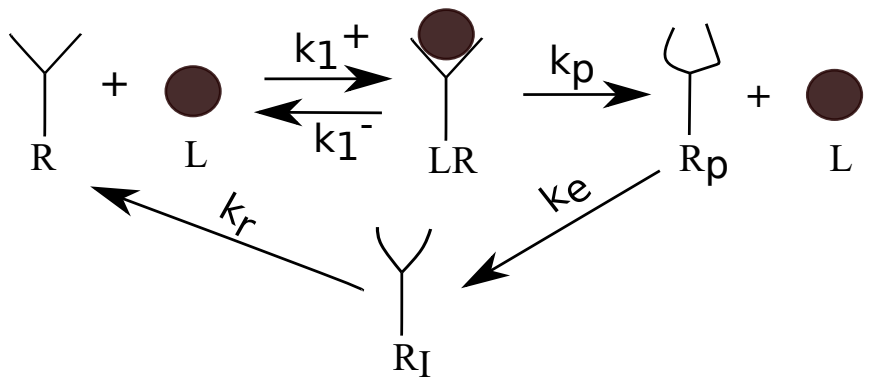

Figure S3: represents the receptor and ligand binding dynamics. Free receptor, R, binds with a ligand, L, reversibly and forms a ligand-receptor complex, LR. This complex is irreversibly converted into the phosphorylated receptor, R_p and ligand, L and eventually, R_p converts into internalized receptor, R_I and then R.

We assume that the formation (LR due to binding of L and R) and dissociation of LR (LR to L and R) is governed by the rapid equilibrium approximation i.e., $k_1^{-1} \gg k_p$. This can be mathematically stated as

$$k_1^+[L][R] = k_1^-[LR]\,, \tag{B.13}$$

Putting $[R] = [R_s] - [LR]$ and $K_r = k_1^-/k_1^+$ into Equation (B.13) and further manipulating it, we get

$$[LR] = \frac{[R_s][L]}{[K_r] + [L]}\,, \tag{B.14}$$

ρ_r, the ratio of receptors bound to ligands to the total number of $P2Y_2$ receptors is given by

$$\rho_r = \frac{[LR]}{[R_t]}.$$

So, the final expression for ρ_r can be obtained by plugging Equation (B.14) on the

above definition, we get

$$\rho_r = \frac{[R_s][L]}{[R_t](K_r + [L])} \,. \tag{B.15}$$

Results and Discussion

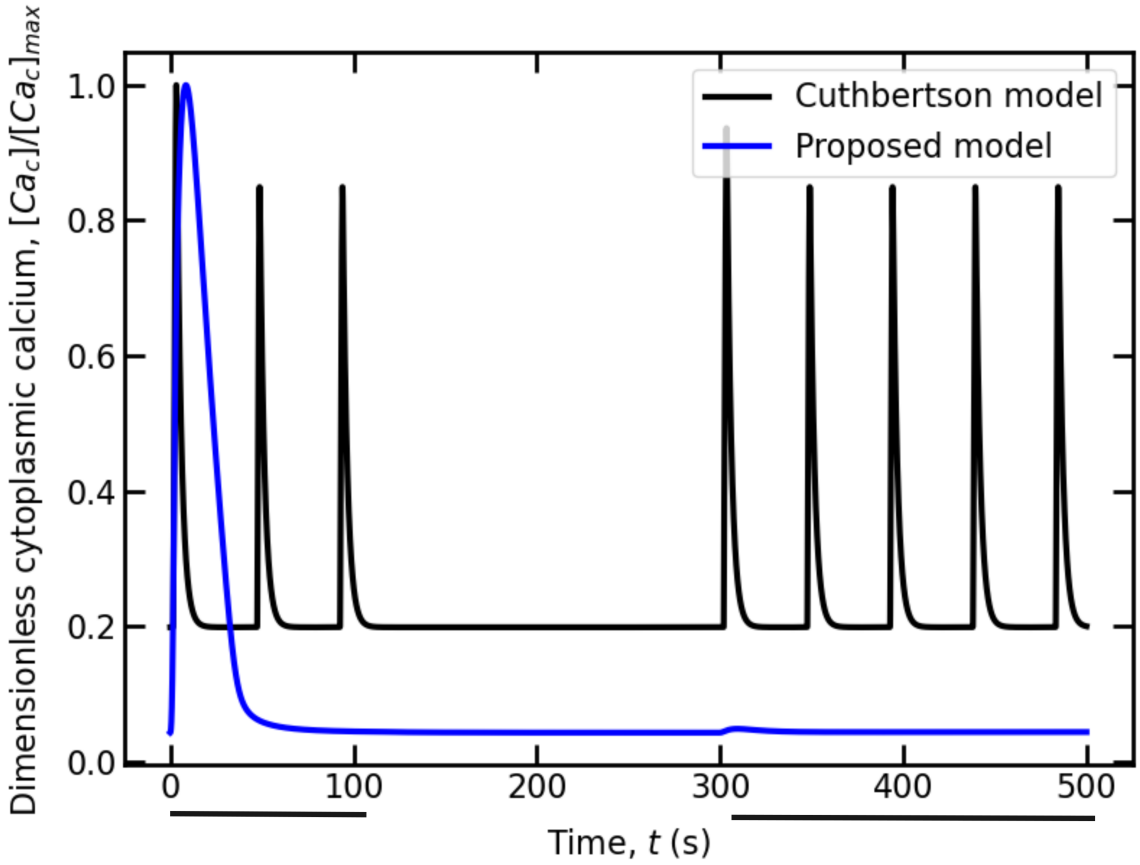

Figure S4: Comparison of results of the cytoplasmic Ca^{2+} concentration of the proposed model and the Cuthbertson model for intermittent exposure of EC with 10 μM concentrations of ATP. The black bold horizontal line represents the duration of application of ATP.

References

[Alberts, 2017] Alberts, B. (2017). *Molecular biology of the cell*. Garland science. iv, 3, 4

[Alexeev et al., 2005] Alexeev, A., Verberg, R., and Balazs, A. C. (2005). Modeling the motion of microcapsules on compliant polymeric surfaces. *Macromolecules*, 38(24):10244–10260. xv, 131

[Amiri and Zhang, 2023] Amiri, F. A. and Zhang, J. (2023). Oxygen transport across tank-treading red blood cell: individual and joint roles of flow convection and oxygen-hemoglobin reaction. *Microvascular Research*, 145:104447. 74

[Ando et al., 1988] Ando, J., Komatsuda, T., and Kamiya, A. (1988). Cytoplasmic calcium response to fluid shear stress in cultured vascular endothelial cells. *In vitro cellular & developmental biology*, 24(9):871–877. 79

[Ando et al., 1991] Ando, J., Ohtsuka, A., Korenaga, R., and Kamiya, A. (1991). Effect of extracellular ATP level on flow-induced Ca^{++} response in cultured vascular endothelial cells. *Biochemical and biophysical research communications*, 179(3):1192–1199. 128

[Ando and Yamamoto, 2013] Ando, J. and Yamamoto, K. (2013). Flow detection and calcium signalling in vascular endothelial cells. *Cardiovascular research*, 99(2):260–268. 79

[Änggård, 1994] Änggård, E. (1994). Nitric oxide: mediator, murderer, and medicine. *The lancet*, 343(8907):1199–1206. 100, 104

[Atri et al., 1993] Atri, A., Amundson, J., Clapham, D., and Sneyd, J. (1993). A single-pool model for intracellular calcium oscillations and waves in the Xenopus laevis oocyte. *Biophysical Journal*, 65(4):1727–1739. 45

[Bagher et al., 2011] Bagher, P., Davis, M. J., and Segal, S. S. (2011). Visualizing calcium responses to acetylcholine convection along endothelium of arteriolar networks in Cx40BAC-GCaMP2 transgenic mice. *American Journal of Physiology-Heart and Circulatory Physiology*, 301(3):H794–H802. 91

[Balogh and Bagchi, 2019] Balogh, P. and Bagchi, P. (2019). The cell-free layer in simulated microvascular networks. *Journal of fluid mechanics*, 864:768–806. 4

[Beaucourt et al., 2004a] Beaucourt, J., Biben, T., and Misbah, C. (2004a). Optimal lift force on vesicles near a compressible substrate. *Europhysics Letters*, 67(4):676. xv, 131

[Beaucourt et al., 2004b] Beaucourt, J., Rioual, F., Séon, T., Biben, T., and Misbah, C. (2004b). Steady to unsteady dynamics of a vesicle in a flow. *Physical Review E*, 69(1):011906. 31

[Bennett et al., 2005] Bennett, M., Farnell, L., and Gibson, W. (2005). A quantitative model of purinergic junctional transmission of calcium waves in astrocyte networks. *Biophysical journal*, 89(4):2235–2250. 51, 52

[Berk et al., 1995] Berk, B. C., Corson, M. A., Peterson, T. E., and Tseng, H. (1995). Protein kinases as mediators of fluid shear stress stimulated signal transduction in endothelial cells: a hypothesis for calcium-dependent and calcium-independent events activated by flow. *Journal of biomechanics*, 28(12):1439–1450. 105

[Berridge et al., 2003] Berridge, M. J., Bootman, M. D., and Roderick, H. L. (2003). Calcium signalling: dynamics, homeostasis and remodelling. *Nature reviews Molecular cell biology*, 4(7):517–529. v, 3, 13, 43, 98

[Billaud et al., 2014] Billaud, M., Lohman, A. W., Johnstone, S. R., Biwer, L. A., Mutchler, S., and Isakson, B. E. (2014). Regulation of cellular communication by signaling microdomains in the blood vessel wall. *Pharmacological reviews*, 66(2):513–569. 58

[Bisello and Friedman, 2008] Bisello, A. and Friedman, P. A. (2008). PTH and PTHrP actions on kidney and bone. *Principles of bone biology*, pages 665–712. 84, 113

[Blatter et al., 1995] Blatter, L. A., Taha, Z., Mesaros, S., Shacklock, P. S., Wier, W. G., and Malinski, T. (1995). Simultaneous measurements of Ca^{2+} and nitric

oxide in bradykinin-stimulated vascular endothelial cells. *Circulation Research*, 76(5):922–924. 99, 112, 113

[Blaustein, 1985] Blaustein, M. P. (1985). Intracellular Calcium as a Second Messenger: Whats so Special about Calcium? In *Calcium in biological systems*, pages 23–33. Springer. 14

[Boo et al., 2003] Boo, Y. C., Sorescu, G. P., Bauer, P. M., Fulton, D., Kemp, B. E., Harrison, D. G., Sessa, W. C., and Jo, H. (2003). Endothelial NO synthase phosphorylated at SER635 produces NO without requiring intracellular calcium increase. *Free Radical Biology and Medicine*, 35(7):729–741. 99

[Borghans et al., 1997] Borghans, J. M., Dupont, G., and Goldbeter, A. (1997). Complex intracellular calcium oscillations A theoretical exploration of possible mechanisms. *Biophysical chemistry*, 66(1):25–41. 45

[Bouzidi et al., 2001] Bouzidi, M., Firdaouss, M., and Lallemand, P. (2001). Momentum transfer of a Boltzmann-lattice fluid with boundaries. *Physics of fluids*, 13(11):3452–3459. 38

[Bruckdorfer, 2005] Bruckdorfer, R. (2005). The basics about nitric oxide. *Molecular aspects of medicine*, 26(1-2):3–31. 16

[Buerk et al., 2017] Buerk, D. G., Liu, Y., Zaccheo, K. A., Barbee, K. A., and Jaron, D. (2017). Nitrite-mediated hypoxic vasodilation predicted from mathematical modeling and quantified from in vivo studies in rat mesentery. *Frontiers in Physiology*, 8:1053. 16, 100

[Burnstock, 1999] Burnstock, G. (1999). Release of vasoactive substances from endothelial cells by shear stress and purinergic mechanosensory transduction. *The Journal of Anatomy*, 194(3):335–342. 79

[Burnstock and Ralevic, 2014] Burnstock, G. and Ralevic, V. (2014). Purinergic signaling and blood vessels in health and disease. *Pharmacological reviews*, 66(1):102–192. 75, 79, 84

[Cai et al., 2000] Cai, Z., Xin, J., Pollock, D. M., and Pollock, J. S. (2000). Shear stress-mediated NO production in inner medullary collecting duct cells. *American Journal of Physiology-Renal Physiology*, 279(2):F270–F274. 99

[Carter et al., 1990] Carter, T., Newton, J., Jacob, R., and Pearson, J. (1990). Homologous desensitization of ATP-mediated elevations in cytoplasmic calcium and prostacyclin release in human endothelial cells does not involve protein kinase C. *Biochemical journal*, 272(1):217–221. vii, ix, 19, 43, 44, 45, 46, 47, 59, 62, 63, 64, 67, 68, 70, 71, 75

[Carter and Pearson, 1992] Carter, T. and Pearson, J. (1992). Regulation of prostacyclin synthesis in endothelial cells. *Physiology*, 7(2):64–69. 63

[Chachisvilis et al., 2006] Chachisvilis, M., Zhang, Y.-L., and Frangos, J. A. (2006). G protein-coupled receptors sense fluid shear stress in endothelial cells. *Proceedings of the National Academy of Sciences*, 103(42):15463–15468. 50, 51

[Chen et al., 2008] Chen, K., Pittman, R. N., and Popel, A. S. (2008). Nitric oxide in the vasculature: where does it come from and where does it go? A quantitative perspective. *Antioxidants & redox signaling*, 10(7):1185–1198. 116

[Chen and Popel, 2006] Chen, K. and Popel, A. S. (2006). Theoretical analysis of biochemical pathways of nitric oxide release from vascular endothelial cells. *Free Radical Biology and Medicine*, 41(4):668–680. 99

[Colden-Stanfield et al., 1987] Colden-Stanfield, M., Schilling, W. P., Ritchie, A. K., Eskin, S. G., Navarro, L. T., and Kunze, D. L. (1987). Bradykinin-induced increases in cytosolic calcium and ionic currents in cultured bovine aortic endothelial cells. *Circulation research*, 61(5):632–640. 59, 66

[Collins, 1997] Collins, K. D. (1997). Charge density-dependent strength of hydration and biological structure. *Biophysical journal*, 72(1):65–76. 15

[Comerford et al., 2008] Comerford, A., Plank, M., and David, T. (2008). Endothelial nitric oxide synthase and calcium production in arterial geometries: an integrated fluid mechanics/cell model. *Journal of biomechanical engineering*, 130(1). 44, 61

[Coupier et al., 2008] Coupier, G., Kaoui, B., Podgorski, T., and Misbah, C. (2008). Noninertial lateral migration of vesicles in bounded Poiseuille flow. *Physics of Fluids*, 20(11):111702. 31

[Cuthbertson and Chay, 1991] Cuthbertson, K. and Chay, T. (1991). Modelling receptor-controlled intracellular calcium oscillators. *Cell calcium*, 12(2-3):97–109. 45, 46, 68, 71, 126

[Davignon and Ganz, 2004] Davignon, J. and Ganz, P. (2004). Role of endothelial dysfunction in atherosclerosis. *Circulation*, 109(23_suppl_1):III–27. 16, 44, 99

[Deonikar et al., 2014] Deonikar, P., Abu-Soud, H. M., and Kavdia, M. (2014). Computational analysis of nitric oxide biotransport to red blood cell in the presence of free hemoglobin and NO donor. *Microvascular Research*, 95:15–25. 16, 100

[Deonikar and Kavdia, 2010] Deonikar, P. and Kavdia, M. (2010). A computational model for nitric oxide, nitrite and nitrate biotransport in the microcirculation: effect of reduced nitric oxide consumption by red blood cells and blood velocity. *Microvascular research*, 80(3):464–476. 100, 101, 116

[Deonikar and Kavdia, 2013] Deonikar, P. and Kavdia, M. (2013). Contribution of membrane permeability and unstirred layer diffusion to nitric oxide–red blood cell interaction. *Journal of theoretical biology*, 317:321–330. 100, 101, 109, 116

[Dhandapani et al., 2021] Dhandapani, P., Dondapati, S. K., Zemella, A., Bräuer, D., Wüstenhagen, D. A., Mergler, S., and Kubick, S. (2021). Targeted esterase-induced dye (TED) loading supports direct calcium imaging in eukaryotic cell-free systems. *RSC advances*, 11(27):16285–16296. 69

[Diez-Silva et al., 2010] Diez-Silva, M., Dao, M., Han, J., Lim, C.-T., and Suresh, S. (2010). Shape and biomechanical characteristics of human red blood cells in health and disease. *MRS bulletin*, 35(5):382–388. 5

[Domeier and Segal, 2007] Domeier, T. L. and Segal, S. S. (2007). Electromechanical and pharmacomechanical signalling pathways for conducted vasodilatation along endothelium of hamster feed arteries. *The Journal of physiology*, 579(1):175–186. 92

[Dong et al., 2004] Dong, X. H., Komiyama, Y., Nishimura, N., Masuda, M., and Takahashi, H. (2004). Nanomolar level of ouabain increases intracellular calcium to produce nitric oxide in rat aortic endothelial cells. *Clinical and experimental pharmacology and physiology*, 31(5-6):276–283. 99

[Dormanns et al., 2016] Dormanns, K., Brown, R., and David, T. (2016). The role of nitric oxide in neurovascular coupling. *Journal of theoretical biology*, 394:1–17. 100

[Dubyak and El-Moatassim, 1993] Dubyak, G. R. and El-Moatassim, C. (1993). Signal transduction via P2-purinergic receptors for extracellular ATP and other nucleotides. *American Journal of Physiology-Cell Physiology*, 265(3):C577–C606. 98

[Dull and Davies, 1991] Dull, R. and Davies, P. (1991). Flow modulation of agonist (ATP)-response (Ca^{2+}) coupling in vascular endothelial cells. *American Journal of Physiology-Heart and Circulatory Physiology*, 261(1):H149–H154. 99

[Dupont and Erneux, 1997] Dupont, G. and Erneux, C. (1997). Simulations of the effects of inositol 1, 4, 5-trisphosphate 3-kinase and 5-phosphatase activities on Ca^{2+} oscillations. *Cell calcium*, 22(5):321–331. 45, 71, 126

[Dupont et al., 2016] Dupont, G., Falcke, M., Kirk, V., and Sneyd, J. (2016). *Models of calcium signalling*, volume 43. Springer. 53, 54

[Dupont and Goldbeter, 1993] Dupont, G. and Goldbeter, A. (1993). One-pool model for Ca^{2+} oscillations involving Ca^{2+} and inositol 1, 4, 5-trisphosphate as co-agonists for Ca^{2+} release. *Cell calcium*, 14(4):311–322. 45

[Dupont et al., 2011] Dupont, G., Lokenye, E. F. L., and Challiss, R. J. (2011). A model for Ca^{2+} oscillations stimulated by the type 5 metabotropic glutamate receptor: an unusual mechanism based on repetitive, reversible phosphorylation of the receptor. *Biochimie*, 93(12):2132–2138. 45, 71, 126

[Edwards and Gibson, 2010] Edwards, J. R. and Gibson, W. G. (2010). A model for Ca^{2+} waves in networks of glial cells incorporating both intercellular and extracellular communication pathways. *Journal of theoretical biology*, 263(1):45–58. 92

[Ellsworth et al., 2009] Ellsworth, M. L., Ellis, C. G., Goldman, D., Stephenson, A. H., Dietrich, H. H., and Sprague, R. S. (2009). Erythrocytes: oxygen sensors and modulators of vascular tone. *Physiology*, 24(2):107–116. v, 9, 10, 11

[Ellsworth et al., 2016] Ellsworth, M. L., Ellis, C. G., and Sprague, R. S. (2016). Role of erythrocyte-released ATP in the regulation of microvascular oxygen supply in skeletal muscle. *Acta Physiologica*, 216(3):265–276. 11

[Fahraeus and Lindqvist, 1931] Fahraeus, R. and Lindqvist, T. (1931). The viscosity of the blood in narrow capillary tubes. *American Journal of Physiology-Legacy Content*, 96(3):562–568. 4

[Faris and Spence, 2008] Faris, A. and Spence, D. M. (2008). Measuring the simultaneous effects of hypoxia and deformation on ATP release from erythrocytes. *Analyst*, 133(5):678–682. 9

[Felix et al., 1996] Felix, J. A., Woodruff, M. L., and Dirksen, E. R. (1996). Stretch increases inositol 1, 4, 5-trisphosphate concentration in airway epithelial cells. *American journal of respiratory cell and molecular biology*, 14(3):296–301. vii, 45, 48, 50

[Fleming and Busse, 1999] Fleming, I. and Busse, R. (1999). Signal transduction of eNOS activation. *Cardiovascular research*, 43(3):532–541. 99, 104

[Forsyth et al., 2011] Forsyth, A. M., Wan, J., Owrutsky, P. D., Abkarian, M., and Stone, H. A. (2011). Multiscale approach to link red blood cell dynamics, shear viscosity, and ATP release. *Proceedings of the National Academy of Sciences*, 108(27):10986–10991. v, 2, 10, 11, 18, 24, 74, 75, 79, 98

[Frangos et al., 1996] Frangos, J. A., Huang, T., and Clark, C. B. (1996). Steady shear and step changes in shear stimulate endothelium via independent mechanisms—superposition of transient and sustained nitric oxide production. *Biochemical and biophysical research communications*, 224(3):660–665. 105

[Garrad et al., 1998] Garrad, R. C., Otero, M. A., Erb, L., Theiss, P. M., Clarke, L. L., Gonzalez, F. A., Turner, J. T., and Weisman, G. A. (1998). Structural basis of agonist-induced desensitization and sequestration of the P2Y2 nucleotide receptor: consequences of truncation of the C terminus. *Journal of Biological Chemistry*, 273(45):29437–29444. 46

[Geiger et al., 1992] Geiger, R. V., Berk, B. C., Alexander, R. W., and Nerem, R. M. (1992). Flow-induced calcium transients in single endothelial cells: spatial and temporal analysis. *American Journal of Physiology-Cell Physiology*, 262(6):C1411–C1417. 79, 128

[Go et al., 1998] Go, Y.-M., Park, H., Maland, M. C., Darley-Usmar, V. M., Stoyanov, B., Wetzker, R., and Jo, H. (1998). Phosphatidylinositol 3-kinase γ mediates shear stress-dependent activation of JNK in endothelial cells. *American Journal of Physiology-Heart and Circulatory Physiology*, 275(5):H1898–H1904. 106

[Gorman et al., 2007] Gorman, M. W., Feigl, E. O., and Buffington, C. W. (2007). Human plasma ATP concentration. *Clinical chemistry*, 53(2):318–325. 75

[Gou et al., 2021] Gou, Z., Zhang, H., Abbasi, M., and Misbah, C. (2021). Red blood cells under flow show maximal ATP release for specific hematocrit. *Biophysical Journal*, 120(21):4819–4831. 31, 71, 75, 77, 78, 82, 84, 87, 89, 115, 122

[Gou et al., 2023] Gou, Z., Zhang, H., and Misbah, C. (2023). Heterogeneous ATP patterns in microvascular networks. *Journal of the Royal Society Interface*, 20(204):20230186. xiv, 120, 129, 130

[Guo and Zhao, 2002] Guo, Z. and Zhao, T. (2002). Lattice boltzmann model for incompressible flows through porous media. *Physical review E*, 66(3):036304. 26

[Habib and Ali, 2011] Habib, S. and Ali, A. (2011). Biochemistry of nitric oxide. *Indian journal of clinical biochemistry*, 26:3–17. 16, 17

[Halidi et al., 2011] Halidi, N., Boittin, F.-X., Bény, J.-L., and Meister, J.-J. (2011). Propagation of fast and slow intercellular Ca^{2+} waves in primary cultured arterial smooth muscle cells. *Cell calcium*, 50(5):459–467. 91, 94

[Helfrich, 1973] Helfrich, W. (1973). Elastic properties of lipid bilayers: theory and possible experiments. *Zeitschrift für Naturforschung C*, 28(11-12):693–703. 31

[Henderson et al., 2015] Henderson, M. J., Wires, E. S., Trychta, K. A., Yan, X., and Harvey, B. K. (2015). Monitoring endoplasmic reticulum calcium homeostasis using a Gaussia luciferase SERCaMP. *JoVE (Journal of Visualized Experiments)*, (103):e53199. 69

[Hong et al., 2006] Hong, D., Jaron, D., Buerk, D. G., and Barbee, K. A. (2006). Heterogeneous response of microvascular endothelial cells to shear stress. *American Journal of Physiology-Heart and Circulatory Physiology*, 290(6):H2498–H2508. 105, 128

[Jacob et al., 1988] Jacob, R., Merritt, J. E., Hallam, T. J., and Rink, T. J. (1988). Repetitive spikes in cytoplasmic calcium evoked by histamine in human endothelial cells. *Nature*, 335(6185):40–45. 59, 66

[James et al., 1995] James, N. L., Harrison, D. G., and Nerem, R. M. (1995). Effects of shear on endothelial cell calcium in the presence and absence of ATP. *The FASEB journal*, 9(10):968–973. 128

[John and Barakat, 2001] John, K. and Barakat, A. I. (2001). Modulation of ATP/ADP concentration at the endothelial surface by shear stress: effect of flow-induced ATP release. *Annals of biomedical engineering*, 29(9):740–751. 79, 82, 101

[Jomova et al., 2022] Jomova, K., Makova, M., Alomar, S. Y., Alwasel, S. H., Nepovimova, E., Kuca, K., Rhodes, C. J., and Valko, M. (2022). Essential metals in health and disease. *Chemico-biological interactions*, page 110173. xvi, 15

[Kanai et al., 1995] Kanai, A. J., Strauss, H. C., Truskey, G. A., Crews, A. L., Grunfeld, S., and Malinski, T. (1995). Shear stress induces ATP-independent transient nitric oxide release from vascular endothelial cells, measured directly with a porphyrinic microsensor. *Circulation research*, 77(2):284–293. 105

[Kantsler and Steinberg, 2006] Kantsler, V. and Steinberg, V. (2006). Transition to tumbling and two regimes of tumbling motion of a vesicle in shear flow. *Physical review letters*, 96(3):036001. 31

[Kaoui and Harting, 2016] Kaoui, B. and Harting, J. (2016). Two-dimensional lattice Boltzmann simulations of vesicles with viscosity contrast. *Rheologica Acta*, 55(6):465–475. 83

[Kaoui et al., 2008] Kaoui, B., Ristow, G., Cantat, I., Misbah, C., and Zimmermann, W. (2008). Lateral migration of a two-dimensional vesicle in unbounded Poiseuille flow. *Physical Review E*, 77(2):021903. 31

[Kaoui et al., 2011] Kaoui, B., Tahiri, N., Biben, T., Ez-Zahraouy, H., Benyoussef, A., Biros, G., and Misbah, C. (2011). Complexity of vesicle microcirculation. *Physical Review E*, 84(4):041906. 31

[Kapela et al., 2008] Kapela, A., Bezerianos, A., and Tsoukias, N. M. (2008). A mathematical model of Ca^{2+} dynamics in rat mesenteric smooth muscle cell: agonist and NO stimulation. *Journal of theoretical biology*, 253(2):238–260. 60

[Kapela et al., 2009] Kapela, A., Bezerianos, A., and Tsoukias, N. M. (2009). A mathematical model of vasoreactivity in rat mesenteric arterioles: I. Myoendothelial communication. *Microcirculation*, 16(8):694–713. 99

[Katsumi et al., 2005] Katsumi, A., Naoe, T., Matsushita, T., Kaibuchi, K., and Schwartz, M. A. (2005). Integrin activation and matrix binding mediate cellular

responses to mechanical stretch. *Journal of Biological Chemistry*, 280(17):16546–16549. 106

[Kavdia et al., 2002] Kavdia, M., Tsoukias, N. M., and Popel, A. S. (2002). Model of nitric oxide diffusion in an arteriole: impact of hemoglobin-based blood substitutes. *American Journal of Physiology-Heart and Circulatory Physiology*, 282(6):H2245–H2253. 100

[Kawai et al., 2010] Kawai, Y., Yokoyama, Y., Kaidoh, M., and Ohhashi, T. (2010). Shear stress-induced ATP-mediated endothelial constitutive nitric oxide synthase expression in human lymphatic endothelial cells. *American Journal of Physiology-Cell Physiology*, 298(3):C647–C655. 105

[Kihm et al., 2021] Kihm, A., Quint, S., Laschke, M. W., Menger, M. D., John, T., Kaestner, L., and Wagner, C. (2021). Lingering dynamics in microvascular blood flow. *Biophysical journal*, 120(3):432–439. 18

[Kim et al., 2009] Kim, S., Ong, P. K., Yalcin, O., Intaglietta, M., and Johnson, P. C. (2009). The cell-free layer in microvascular blood flow. *Biorheology*, 46(3):181–189. 4

[Kirby et al., 2016] Kirby, P. L., Buerk, D. G., Parikh, J., Barbee, K. A., and Jaron, D. (2016). Mathematical model for shear stress dependent NO and adenine nucleotide production from endothelial cells. *Nitric Oxide*, 52:1–15. 97, 99

[Klinken, 2002] Klinken, S. P. (2002). Red blood cells. *The international journal of biochemistry & cell biology*, 34(12):1513–1518. iv, 6, 7

[Koo et al., 2013] Koo, A., Nordsletten, D., Umeton, R., Yankama, B., Ayyadurai, S., García-Cardeña, G., and Dewey, C. F. (2013). In silico modeling of shear-stress-induced nitric oxide production in endothelial cells through systems biology. *Biophysical journal*, 104(10):2295–2306. 97, 99

[Krüger et al., 2017] Krüger, T., Kusumaatmaja, H., Kuzmin, A., Shardt, O., Silva, G., and Viggen, E. M. (2017). The lattice Boltzmann method. *Springer International Publishing*, 10(978-3):4–15. 25

[Kuchan and Frangos, 1994] Kuchan, M. and Frangos, J. (1994). Role of calcium and calmodulin in flow-induced nitric oxide production in endothelial cells. *American Journal of Physiology-Cell Physiology*, 266(3):C628–C636. 105

[Kummer et al., 2000] Kummer, U., Olsen, L. F., Dixon, C. J., Green, A. K., Bornberg-Bauer, E., and Baier, G. (2000). Switching from simple to complex oscillations in calcium signaling. *Biophysical journal*, 79(3):1188–1195. 45, 71, 126

[Lallemand and Luo, 2003] Lallemand, P. and Luo, L.-S. (2003). Lattice Boltzmann method for moving boundaries. *Journal of Computational Physics*, 184(2):406–421. 40

[Lemon et al., 2003] Lemon, G., Gibson, W., and Bennett, M. (2003). Metabotropic receptor activation, desensitization and sequestration-I: modelling calcium and inositol 1, 4, 5-trisphosphate dynamics following receptor activation. *Journal of Theoretical Biology*, 223(1):93–111. 46, 49, 56, 58, 60

[Levine et al., 2012] Levine, A. B., Punihaole, D., and Levine, T. B. (2012). Characterization of the role of nitric oxide and its clinical applications. *Cardiology*, 122(1):55–68. 16, 17

[Leybaert and Sanderson, 2012] Leybaert, L. and Sanderson, M. J. (2012). Intercellular Ca^{2+} waves: mechanisms and function. *Physiological reviews*, 92(3):1359–1392. 91, 92, 94

[Li et al., 2015] Li, L.-F., Xiang, C., and Qin, K.-R. (2015). Modeling of $TRPV_4$-C_1-mediated calcium signaling in vascular endothelial cells induced by fluid shear stress and ATP. *Biomechanics and modeling in mechanobiology*, 14(5):979–993. 44, 55, 61

[Lohman et al., 2012] Lohman, A. W., Billaud, M., and Isakson, B. E. (2012). Mechanisms of ATP release and signalling in the blood vessel wall. *Cardiovascular research*, 95(3):269–280. 74

[Long et al., 2012] Long, J., Junkin, M., Wong, P. K., Hoying, J., and Deymier, P. (2012). Calcium wave propagation in networks of endothelial cells: model-based theoretical and experimental study. *PLoS computational biology*, 8(12):e1002847. 94

[Lückhoff and Busse, 1986] Lückhoff, A. and Busse, R. (1986). Increased free calcium in endothelial cells under stimulation with adenine nucleotides. *Journal of cellular physiology*, 126(3):414–420. 63

[Mahama and Linderman, 1994] Mahama, P. A. and Linderman, J. J. (1994). Calcium signaling in individual BC3H1 cells: Speed of calcium mobilization and heterogeneity. *Biotechnology progress*, 10(1):45–54. 64, 65, 68

[Malli et al., 2007] Malli, R., Frieden, M., Hunkova, M., Trenker, M., and Graier, W. (2007). Ca^{2+} refilling of the endoplasmic reticulum is largely preserved albeit reduced Ca^{2+} entry in endothelial cells. *Cell calcium*, 41(1):63–76. vii, 45, 48, 63, 64

[Malli et al., 2005] Malli, R., Frieden, M., Trenker, M., and Graier, W. F. (2005). The role of mitochondria for Ca^{2+} refilling of the endoplasmic reticulum. *Journal of Biological Chemistry*, 280(13):12114–12122. 59, 63, 64

[Marhl et al., 2000] Marhl, M., Haberichter, T., Brumen, M., and Heinrich, R. (2000). Complex calcium oscillations and the role of mitochondria and cytosolic proteins. *Biosystems*, 57(2):75–86. 45, 71, 126

[Marsh and Marsh, 2000] Marsh, N. and Marsh, A. (2000). A short history of nitroglycerine and nitric oxide in pharmacology and physiology. *Clinical and Experimental Pharmacology and Physiology*, 27(4):313–319. 17

[McCullough et al., 1997] McCullough, W. T., Collins, D. M., and Ellsworth, M. L. (1997). Arteriolar responses to extracellular ATP in striated muscle. *American Journal of Physiology-Heart and Circulatory Physiology*, 272(4):H1886–H1891. 11

[Merlo et al., 2023] Merlo, A., Losserand, S., Yaya, F., Connes, P., Faivre, M., Lorthois, S., Minetti, C., Nader, E., Podgorski, T., Renoux, C., et al. (2023). Influence of storage and buffer composition on the mechanical behavior of flowing red blood cells. *Biophysical Journal*, 122(2):360–373. 18

[Meyer and Stryer, 1988] Meyer, T. and Stryer, L. (1988). Molecular model for receptor-stimulated calcium spiking. *Proceedings of the National Academy of Sciences*, 85(14):5051–5055. 44, 45, 51, 52, 63

[Michaelis et al., 1913] Michaelis, L., Menten, M. L., et al. (1913). Die kinetik der invertinwirkung. *Biochem. z*, 49(333-369):352. 57

[Miyamoto and Mikoshiba, 2017] Miyamoto, A. and Mikoshiba, K. (2017). Probes for manipulating and monitoring ip3. *Cell Calcium*, 64:57–64. 69

[Mo et al., 1991] Mo, M., Eskin, S. G., and Schilling, W. P. (1991). Flow-induced changes in Ca^{2+} signaling of vascular endothelial cells: effect of shear stress and ATP. *American Journal of Physiology-Heart and Circulatory Physiology*, 260(5):H1698–H1707. 59, 62

[Mohamad, 2011] Mohamad, A. (2011). *Lattice Boltzmann Method*, volume 70. Springer. 23, 25

[Nayak et al., 2023] Nayak, A. K., Gou, Z., Das, S. L., Barakat, A. I., and Misbah, C. (2023). Mathematical modeling of intracellular calcium in presence of receptor: a homeostatic model for endothelial cell. *Biomechanics and Modeling in Mechanobiology*, 22(1):217–232. 76, 84, 90, 100

[Nollert et al., 1990] Nollert, M., Eskin, S., and McIntire, L. (1990). Shear stress increases inositol trisphosphate levels in human endothelial cells. *Biochemical and biophysical research communications*, 170(1):281–287. 50, 128

[Olearczyk et al., 2004] Olearczyk, J. J., Ellsworth, M. L., Stephenson, A. H., Lonigro, A. J., and Sprague, R. S. (2004). Nitric oxide inhibits ATP release from erythrocytes. *Journal of Pharmacology and Experimental Therapeutics*, 309(3):1079–1084. 10

[Ong et al., 2012] Ong, P. K., Cho, S., Namgung, B., and Kim, S. (2012). Effects of cell-free layer formation on NO/O_2 bioavailability in small arterioles. *Microvascular Research*, 83(2):168–177. 100, 101

[Pecze et al., 2015] Pecze, L., Blum, W., and Schwaller, B. (2015). Routes of Ca^{2+} shuttling during Ca^{2+} oscillations: focus on the role of mitochondrial Ca^{2+} handling and cytosolic Ca^{2+} buffers. *Journal of Biological Chemistry*, 290(47):28214–28230. 59

[Peskin, 2002] Peskin, C. S. (2002). The immersed boundary method. *Acta numerica*, 11:479–517. 28

[Pirotton et al., 1987] Pirotton, S., Raspé, E., Demolle, D., Erneux, C., and Boeynaems, J.-M. (1987). Involvement of inositol 1, 4, 5-trisphosphate and calcium in the action of adenine nucleotides on aortic endothelial cells. *Journal of Biological Chemistry*, 262(36):17461–17466. 74

[Plank et al., 2007] Plank, M., Wall, D., and David, T. (2007). The role of endothelial calcium and nitric oxide in the localisation of atherosclerosis. *Mathematical biosciences*, 207(1):26–39. 44, 61

[Plank et al., 2006] Plank, M. J., Wall, D. J., and David, T. (2006). Atherosclerosis and calcium signalling in endothelial cells. *Progress in biophysics and molecular biology*, 91(3):287–313. 19, 44, 45, 46, 52, 54, 55, 58, 60, 61

[Politi et al., 2006] Politi, A., Gaspers, L. D., Thomas, A. P., and Höfer, T. (2006). Models of IP_3 and Ca^{2+} oscillations: frequency encoding and identification of underlying feedbacks. *Biophysical journal*, 90(9):3120–3133. 45, 71, 126

[Popel and Johnson, 2005] Popel, A. S. and Johnson, P. C. (2005). Microcirculation and hemorheology. *Annu. Rev. Fluid Mech.*, 37:43–69. 2

[Pries et al., 1992] Pries, A. R., Neuhaus, D., and Gaehtgens, P. (1992). Blood viscosity in tube flow: dependence on diameter and hematocrit. *American Journal of Physiology-Heart and Circulatory Physiology*, 263(6):H1770–H1778. iv, 4

[Putney et al., 2001] Putney, J. W., Broad, L. M., Braun, F.-J., Lievremont, J.-P., and Bird, G. S. J. (2001). Mechanisms of capacitative calcium entry. *Journal of cell science*, 114(12):2223–2229. 46, 54

[Putney Jr, 1986] Putney Jr, J. W. (1986). A model for receptor-regulated calcium entry. *Cell calcium*, 7(1):1–12. 46, 54

[Qian et al., 2020] Qian, S., Ma, T., Zhang, N., Liu, X., Zhao, P., Li, X., Chen, D., Hu, L., Chang, L., Xu, L., et al. (2020). Spatiotemporal transfer of nitric oxide in patient-specific atherosclerotic carotid artery bifurcations with MRI and computational fluid dynamics modeling. *Computers in Biology and Medicine*, 125:104015. 100

[Rasmussen, 1985] Rasmussen, H. (1985). Calcium ion: a synarchic and mercurial but minatory messenger. In *Calcium in biological systems*, pages 13–22. Springer. 11, 12

[Rodeberg et al., 1995] Rodeberg, D. A., Chaet, M. S., Bass, R. C., Arkovitz, M. S., and Garcia, V. F. (1995). Nitric oxide: an overview. *The American journal of surgery*, 170(3):292–303. 16

[Rubin, 1985] Rubin, R. P. (1985). Historical and biological aspects of calcium action. In *Calcium in biological systems*, pages 5–11. Springer. 14

[Sage et al., 1989] Sage, S. O., Adams, D. J., and Van Breemen, C. (1989). Synchronized oscillations in cytoplasmic free calcium concentration in confluent bradykinin-stimulated bovine pulmonary artery endothelial cell monolayers. *Journal of Biological Chemistry*, 264(1):6–9. 43, 63

[Samtleben et al., 2013] Samtleben, S., Jaepel, J., Fecher, C., Andreska, T., Rehberg, M., and Blum, R. (2013). Direct imaging of ER calcium with targeted-esterase induced dye loading (TED). *JoVE (Journal of Visualized Experiments)*, (75):e50317. 69

[Sandoo et al., 2010] Sandoo, A., Veldhuijzen van Zanten, J. J., Metsios, G. S., Carroll, D., and Kitas, G. D. (2010). The endothelium and its role in regulating vascular tone. *The open cardiovascular medicine journal*, 4(1). 105

[Schuster et al., 2002] Schuster, S., Marhl, M., and Höfer, T. (2002). Modelling of simple and complex calcium oscillations: From single-cell responses to intercellular signalling. *European Journal of Biochemistry*, 269(5):1333–1355. 45, 71, 94, 126

[Schwarz et al., 1992] Schwarz, G., Droogmans, G., and Nilius, B. (1992). Shear stress induced membrane currents and calcium transients in human vascular endothelial cells. *Pflügers Archiv*, 421:394–396. xiv, 127, 128

[Secomb, 2017] Secomb, T. W. (2017). Blood flow in the microcirculation. *Annual Review of Fluid Mechanics*, 49:443–461. iv, 4

[Seppey et al., 2010] Seppey, D., Sauser, R., Koenigsberger, M., Bény, J.-L., and Meister, J.-J. (2010). Intercellular calcium waves are associated with the propagation of vasomotion along arterial strips. *American Journal of Physiology-Heart and Circulatory Physiology*, 298(2):H488–H496. 91

[Sera et al., 2018] Sera, T., Komine, S., Arai, M., Sunaga, Y., Yokota, H., and Kudo, S. (2018). Three-dimensional model of intracellular and intercellular Ca^{2+} waves propagation in endothelial cells. *Biochemical and biophysical research communications*, 505(3):781–786. 91, 92, 93, 94

[Shen et al., 1992] Shen, J., Luscinskas, F. W., Connolly, A., Dewey Jr, C. F., and Gimbrone Jr, M. (1992). Fluid shear stress modulates cytosolic free calcium

in vascular endothelial cells. *American Journal of Physiology-Cell Physiology*, 262(2):C384–C390. xiv, 43, 79, 105, 127, 128

[Shen and Larter, 1995] Shen, P. and Larter, R. (1995). Chaos in intracellular Ca^{2+} oscillations in a new model for non-excitable cells. *Cell calcium*, 17(3):225–232. 45

[Shen, 2016] Shen, Z. (2016). *Blood flow in microfluidic architectures: collective behaviors of deformable particles in confined flow*. PhD thesis, Université Grenoble Alpes. vi, 29, 32, 33

[Shen et al., 2016] Shen, Z., Coupier, G., Kaoui, B., Polack, B., Harting, J., Misbah, C., and Podgorski, T. (2016). Inversion of hematocrit partition at microfluidic bifurcations. *Microvascular research*, 105:40–46. 18

[Silva et al., 2007] Silva, H. S., Kapela, A., and Tsoukias, N. M. (2007). A mathematical model of plasma membrane electrophysiology and calcium dynamics in vascular endothelial cells. *American Journal of Physiology-Cell Physiology*, 293(1):C277–C293. 44, 45, 46, 53, 60, 61

[Snyder, 1992] Snyder, S. H. (1992). Nitric oxide: first in a new class of neurotransmitters. *Science*, 257(5069):494–496. 104

[Song et al., 2007] Song, Z., Vijayaraghavan, S., and Sladek, C. D. (2007). ATP increases intracellular calcium in supraoptic neurons by activation of both P2X and P2Y purinergic receptors. *American Journal of Physiology-Regulatory, Integrative and Comparative Physiology*, 292(1):R423–R431. 74

[Sprague and Ellsworth, 2012] Sprague, R. S. and Ellsworth, M. L. (2012). Erythrocyte-derived ATP and perfusion distribution: role of intracellular and intercellular communication. *Microcirculation*, 19(5):430–439. v, 10

[Sriram et al., 2016] Sriram, K., Laughlin, J. G., Rangamani, P., and Tartakovsky, D. M. (2016). Shear-induced nitric oxide production by endothelial cells. *Biophysical journal*, 111(1):208–221. xii, 97, 99, 100, 102, 103, 104, 105, 106, 107, 110, 111, 123, 124

[Storch et al., 2012] Storch, U., Schnitzler, M. M. y., and Gudermann, T. (2012). G protein-mediated stretch reception. *American Journal of Physiology-Heart and Circulatory Physiology*, 302(6):H1241–H1249. 50, 51

[Su et al., 2020] Su, H., Liu, X., Du, J., Deng, X., and Fan, Y. (2020). The role of hemoglobin in nitric oxide transport in vascular system. *Medicine in Novel Technology and Devices*, 5:100034. 104

[Su et al., 2011] Su, J., Xu, F., Lu, X., and Lu, T. (2011). Fluid flow induced calcium response in osteoblasts: mathematical modeling. *Journal of biomechanics*, 44(11):2040–2046. 54, 55, 60

[Thillaiappan et al., 2019] Thillaiappan, N. B., Chakraborty, P., Hasan, G., and Taylor, C. W. (2019). IP_3 receptors and Ca^{2+} entry. *Biochimica Et Biophysica Acta (BBA)-Molecular Cell Research*, 1866(7):1092–1100. 54

[Tomaiuolo, 2014] Tomaiuolo, G. (2014). Biomechanical properties of red blood cells in health and disease towards microfluidics. *Biomicrofluidics*, 8(5). 5

[Tomaiuolo et al., 2011] Tomaiuolo, G., Barra, M., Preziosi, V., Cassinese, A., Rotoli, B., and Guido, S. (2011). Microfluidics analysis of red blood cell membrane viscoelasticity. *Lab on a Chip*, 11(3):449–454. 18

[Tomaiuolo and Guido, 2011] Tomaiuolo, G. and Guido, S. (2011). Start-up shape dynamics of red blood cells in microcapillary flow. *Microvascular research*, 82(1):35–41. 18

[Tovar-Lopez et al., 2010] Tovar-Lopez, F. J., Rosengarten, G., Westein, E., Khoshmanesh, K., Jackson, S. P., Mitchell, A., and Nesbitt, W. S. (2010). A microfluidics device to monitor platelet aggregation dynamics in response to strain rate microgradients in flowing blood. *Lab on a Chip*, 10(3):291–302. 18

[Tran et al., 2000] Tran, Q.-K., Ohashi, K., and Watanabe, H. (2000). Calcium signalling in endothelial cells. *Cardiovascular research*, 48(1):13–22. 43, 98

[Traylor and Sharma, 1992] Traylor, T. G. and Sharma, V. S. (1992). Why NO? *Biochemistry*, 31(11):2847–2849. 16

[Tzima et al., 2001] Tzima, E., Del Pozo, M. A., Shattil, S. J., Chien, S., and Schwartz, M. A. (2001). Activation of integrins in endothelial cells by fluid shear stress mediates rho-dependent cytoskeletal alignment. *The EMBO journal*, 20(17):4639–4647. 105

[Uhrenholt et al., 2007] Uhrenholt, T. R., Domeier, T. L., and Segal, S. S. (2007). Propagation of calcium waves along endothelium of hamster feed arteries. *American Journal of Physiology-Heart and Circulatory Physiology*, 292(3):H1634–H1640. xiv, 91, 129, 130

[Ungvari et al., 2001] Ungvari, Z., Sun, D., Huang, A., Kaley, G., and Koller, A. (2001). Role of endothelial $[Ca^{2+}]_i$ in activation of eNOS in pressurized arterioles by agonists and wall shear stress. *American Journal of Physiology-Heart and Circulatory Physiology*, 281(2):H606–H612. 105

[van IJzendoorn et al., 1996] van IJzendoorn, S., van Gool, R., Reutelingsperger, C., and Heemskerk, J. (1996). Unstimulated platelets evoke calcium responses in human umbilical vein endothelial cells. *Biochim Biophys Acta*, 1311:64–70. 64

[Wagner and Keizer, 1994] Wagner, J. and Keizer, J. (1994). Effects of rapid buffers on Ca^{2+} diffusion and Ca^{2+} oscillations. *Biophysical journal*, 67(1):447–456. 52

[Wan et al., 2011] Wan, J., Forsyth, A. M., and Stone, H. A. (2011). Red blood cell dynamics: from cell deformation to ATP release. *Integrative Biology*, 3(10):972–981. v, 10

[Wan et al., 2008] Wan, J., Ristenpart, W. D., and Stone, H. A. (2008). Dynamics of shear-induced ATP release from red blood cells. *Proceedings of the National Academy of Sciences*, 105(43):16432–16437. 9

[Wang et al., 2007] Wang, J., Huang, X., and Huang, W. (2007). A quantitative kinetic model for ATP-induced intracellular Ca^{2+} oscillations. *Journal of theoretical biology*, 245(3):510–519. 45, 68

[Wei et al., 2019] Wei, Y., Mu, L., Tang, Y., Shen, Z., and He, Y. (2019). Computational analysis of nitric oxide biotransport in a microvessel influenced by red blood cells. *Microvascular research*, 125:103878. 95, 100, 101, 109, 115, 116, 124

[Wiesner et al., 1996] Wiesner, T. F., Berk, B. C., and Nerem, R. M. (1996). A mathematical model of cytosolic calcium dynamics in human umbilical vein endothelial cells. *American Journal of Physiology-Cell Physiology*, 270(5):C1556–C1569. 44, 45, 46, 59, 61

[Wiesner et al., 1997] Wiesner, T. F., Berk, B. C., and Nerem, R. M. (1997). A mathematical model of the cytosolic-free calcium response in endothelial cells to

fluid shear stress. *Proceedings of the National Academy of Sciences*, 94(8):3726–3731. 44, 61, 128

[Xu et al., 2017] Xu, S., Li, X., LaPenna, K. B., Yokota, S. D., Huke, S., and He, P. (2017). New insights into shear stress-induced endothelial signalling and barrier function: cell-free fluid versus blood flow. *Cardiovascular research*, 113(5):508–518. 18, 43, 74, 99, 105

[Xu et al., 2016] Xu, S., Li, X., Liu, Y., and He, P. (2016). Development and characterization of in vitro microvessel network and quantitative measurements of endothelial $[Ca^{2+}]_i$ and nitric oxide production. *JoVE (Journal of Visualized Experiments)*, (111):e54014. v, 13, 111, 112, 113

[Xu et al., 2019] Xu, Z., Dou, W., Wang, C., and Sun, Y. (2019). Stiffness and atp recovery of stored red blood cells in serum. *Microsystems & Nanoengineering*, 5(1):51. 8, 75

[Yamamoto et al., 2011] Yamamoto, K., Furuya, K., Nakamura, M., Kobatake, E., Sokabe, M., and Ando, J. (2011). Visualization of flow-induced ATP release and triggering of Ca^{2+} waves at caveolae in vascular endothelial cells. *Journal of cell science*, 124(20):3477–3483. 92

[Yamamoto et al., 2000a] Yamamoto, K., Korenaga, R., Kamiya, A., and Ando, J. (2000a). Fluid shear stress activates Ca^{2+} influx into human endothelial cells via P2X4 purinoceptors. *Circulation research*, 87(5):385–391. ix, 69, 70, 105, 128

[Yamamoto et al., 2000b] Yamamoto, K., Korenaga, R., Kamiya, A., Qi, Z., Sokabe, M., and Ando, J. (2000b). $P2X_4$ receptors mediate ATP-induced calcium influx in human vascular endothelial cells. *American Journal of Physiology-Heart and Circulatory Physiology*, 279(1):H285–H292. xiv, 127, 128

[Yamamoto et al., 2003] Yamamoto, K., Sokabe, T., Ohura, N., Nakatsuka, H., Kamiya, A., and Ando, J. (2003). Endogenously released ATP mediates shear stress-induced Ca^{2+} influx into pulmonary artery endothelial cells. *American Journal of Physiology-Heart and Circulatory Physiology*, 285(2):H793–H803. 79, 128

[Yamarnoto et al., 1995] Yamarnoto, N., Watanabe, H., Kakizawa, H., Hirano, M., Kobayashi, A., and Ohno, R. (1995). A study on thapsigargin-induced calcium ion and cation influx pathways in vascular endothelial cells. *Biochimica et Biophysica Acta (BBA)-Molecular Cell Research*, 1266(2):157–162. 63

[Yang et al., 2005] Yang, J., Clark, J. W., Bryan, R. M., and Robertson, C. S. (2005). Mathematical modeling of the nitric oxide/cGMP pathway in the vascular smooth muscle cell. *American Journal of Physiology-Heart and Circulatory Physiology*, 289(2):H886–H897. 99

[Yang et al., 2001] Yang, S.-W., Lee, W. K., Lee, E.-J., Kim, K.-A., Lim, Y., Lee, K.-H., Rha, H. K., and Hahn, T.-W. (2001). Effect of bradykinin on cultured bovine corneal endothelial cells. *Ophthalmologica*, 215(4):303–308. 59, 63, 66

[Yang et al., 2009] Yang, X., Zhang, X., Li, Z., and He, G.-W. (2009). A smoothing technique for discrete Delta functions with application to immersed boundary method in moving boundary simulations. *Journal of Computational Physics*, 228(20):7821–7836. 30

[Yin et al., 2013] Yin, X., Thomas, T., and Zhang, J. (2013). Multiple red blood cell flows through microvascular bifurcations: cell free layer, cell trajectory, and hematocrit separation. *Microvascular research*, 89:47–56. 4

[Zhang and Misbah, 2019] Zhang, H. and Misbah, C. (2019). Lattice Boltzmann simulation of advection-diffusion of chemicals and applications to blood flow. *Computers & Fluids*, 187:46–59. vi, vii, 35, 36, 37, 39, 40, 41, 79

[Zhang et al., 2018] Zhang, H., Shen, Z., Hogan, B., Barakat, A. I., and Misbah, C. (2018). ATP release by red blood cells under flow: model and simulations. *Biophysical journal*, 115(11):2218–2229. 18, 19, 71, 75, 78, 79, 82, 98, 101

[Zhao et al., 2015] Zhao, Y., Vanhoutte, P. M., and Leung, S. W. (2015). Vascular nitric oxide: Beyond eNOS. *Journal of pharmacological sciences*, 129(2):83–94. 104

[Zhu and He, 2005] Zhu, L. and He, P. (2005). Platelet-activating factor increases endothelial $[Ca^{2+}]_i$ and NO production in individually perfused intact microvessels. *American Journal of Physiology-Heart and Circulatory Physiology*, 288(6):H2869–H2877. 59, 66